

Éléments finis solide-coque pour l'analyse quasi-statique et dynamique des structures minces 3d : application aux procédés de mise en forme

Peng Wang

▶ **To cite this version:**

Peng Wang. Éléments finis solide-coque pour l'analyse quasi-statique et dynamique des structures minces 3d : application aux procédés de mise en forme. Mécanique des matériaux [physics.class-ph]. Ecole nationale supérieure d'arts et métiers - ENSAM, 2017. Français. NNT : 2017ENAM0010 . tel-01540345

HAL Id: tel-01540345
https://pastel.hal.science/tel-01540345

Submitted on 16 Jun 2017

HAL is a multi-disciplinary open access archive for the deposit and dissemination of scientific research documents, whether they are published or not. The documents may come from teaching and research institutions in France or abroad, or from public or private research centers.

L'archive ouverte pluridisciplinaire **HAL**, est destinée au dépôt et à la diffusion de documents scientifiques de niveau recherche, publiés ou non, émanant des établissements d'enseignement et de recherche français ou étrangers, des laboratoires publics ou privés.

2017-ENAM-0010



École doctorale n° 432 : Science des Métiers de l'ingénieur

Doctorat ParisTech

T H È S E

pour obtenir le grade de docteur délivré par

l'École Nationale Supérieure d'Arts et Métiers

Spécialité " Mécanique - matériaux "

présentée et soutenue publiquement par

Peng WANG

le 6 avril 2017

Solid–shell finite elements for quasi-static and dynamic analysis of 3D thin structures: Application to sheet metal forming processes

Directeur de thèse : **Farid ABED-MERAIM**

Co-encadrement de la thèse : **Hocine CHALAL**

Jury

M. Jean-Philippe PONTHOT, Professeur, LTAS, Université de Liège, Belgique	Président
M. Laurent DUCHÊNE, Professeur associé, ArGEnCo, Université de Liège, Belgique	Rapporteur
M. Thomas ELGUEDJ, Maître de Conférences – HDR, LaMCoS, INSA de Lyon, France	Rapporteur
M. Olivier POLIT, Professeur, LEME, Université Paris Nanterre, France	Examinateur
M. Habibou MAITOURNAM, Professeur, IMSIA, ENSTA ParisTech, France	Examinateur
M. Farid ABED-MERAIM, Professeur, LEM3, Arts et Métiers ParisTech, France	Examinateur
M. Hocine CHALAL, Maître de Conférences, LEM3, Arts et Métiers ParisTech, France	Examinateur

T H È S E

Arts et Métiers ParisTech - Campus de Metz
Laboratoire d'Étude des Microstructures et de Mécanique des Matériaux (LEM3)
UMR CNRS 7239

To my beloved parents for their sacrifices

To my beloved sisters and brothers for their support

To my dear supervisors for their guidance

To all my dear friends for their help

Acknowledgments

This work has been realized within the team MeNu (Mécanique Numérique) of the laboratory LEM3 (Laboratoire d'Étude des Microstructures et de Mécanique des Matériaux) in Metz Campus of ENSAM (École Nationale Supérieure et d'Arts et Métiers). The study in France was a valuable and memorable experience in my life. First and foremost, I would like to thank my supervisors for their dedicated support, kind guidance and encouragement.

I sincerely thank the director of my thesis, Prof. Farid ABED-MERAIM, who kindly gave me this opportunity to study in France. I am deeply grateful for his encouragement, invaluable advices and guidance during my study. I would like to thank my co-supervisor, Dr. Hocine CHALAL, for his responsible supervision, meticulous guidance and kind assistance. Without them, it is impossible for me to complete this thesis on time. It was a really great pleasure for me to work with them for three years.

I also deeply thank Prof. Jean-Philippe PONTHOT from Université de Liège for being the president of my Ph.D. thesis committee. I would like to express my gratitude to two reporters, Prof. Laurent DUCHÊNE from Université de Liège and Assoc. Prof. Thomas ELGUEDJ from INSA de Lyon, for their insightful comments and academic reports. I am deeply grateful to Prof. Olivier POLIT from Université Paris–Nanterre and Prof. Habibou MAITOURNAM from ENSTA ParisTech for accepting the invitation and spending their precious time to attend my thesis defense. I am honored to be able to invite these famous, charming and knowledgeable professors as the referees. I sincerely appreciate their insightful, valuable and constructive comments.

I would like to thank the organization China Scholarship Council (CSC, Contract No. 201308640010), who supplied the scholarship to support my study in ENSAM, France.

I would like thank all my colleagues in our lab, Abderrahim NACHIT, Boris POITROWSKI, Dominique VINCENT, Francis ADZIMA, Francis PRAUD, Holanyo AKPAMA, Kevin BONNAY, Mohamed BEN BETTAIEB, Pascal POMAREDE, Paul DIDIER, Paul LOHMULLER, etc. and also my Chinese friends, Bin JIA, Fan LI, Haitao TIAN, Jianchang ZHU, Jianjie ZHANG, Jinna QIN, Ke WANG, Long CHENG, Qing XIA, Qiming YAO, Yanfeng YANG, Zhicheng HUANG, Zhongkai CHEN, with whom I shared the most memorable moments.

I express my sincere gratitude to all my family members, particularly my parents, my father Yuxiang WANG and my mother Zhilie WANG. There are no words for me to be able to express my utmost gratitude and thanks to them for their great sacrifices, support and encouragement.

At last, I also would like to thank all kind people who always help and encourage me.

Contents

Part I: English version

Contents.....i

List of Tables.....v

List of Figures.....vii

Part I: English version

Introduction.....1

Research background.....1

Objectives of the thesis.....3

Organization of the thesis.....3

Chapter 1 Literature review on solid–shell finite element technology.....5

Introduction.....5

1.1 Three-dimensional solid finite elements.....6

1.1.1 State of the art.....6

1.1.2 Treatment of locking phenomena.....7

1.2 Conventional shell elements.....11

1.2.1 State of the art.....11

1.2.2 Locking phenomena.....15

1.2.3 Numerical methods for alleviating locking problems.....17

1.3 Solid–shell finite elements.....18

1.3.1 State of the art.....18

1.3.2 Treatment of locking phenomena.....20

1.4 Proposed solid–shell elements (SHB family).....26

Conclusion.....28

Chapter 2 Formulation of the SHB solid–shell elements.....29

Introduction.....29

2.1 General formulation for quasi-static/implicit analysis.....29

2.1.1 Geometry and integration points.....29

2.1.2 Interpolation of the SHB elements.....30

2.1.3 Strain-displacement relationship and discrete gradient operator.....31
2.1.4 Variational principle.....33
2.2 Definition of local frames.....35
2.3 Special treatments for the linear SHB elements.....36
2.3.1 Assumed-strain projection for the SHB6 element.....37
2.3.2 Stabilization procedure and assumed-strain projection for the SHB8PS element..38
2.4 General formulation for dynamic/explicit analysis.....45
2.4.1 Velocity field interpolation.....45
2.4.2 Modeling of the mass matrix.....46
2.5 Constitutive equations.....52
2.5.1 Isotropic and anisotropic elastic material behavior.....53
2.5.2 Anisotropic constitutive equations for metallic materials.....57
Conclusion.....61

Chapter 3 Validation of the SHB family elements.....63
Introduction.....63
3.1 Linear benchmark problems.....65
3.1.1 Linear static beam problems.....65
3.1.2 Plate vibration problems.....71
3.2 Nonlinear benchmark problems.....74
3.2.1 Quasi-static analysis.....74
3.2.2 Dynamic analysis.....82
3.3 Composite multilayered structures.....92
3.3.1 Cantilever plate with ply dropoffs.....93
3.3.2 Cantilever bending of a laminated beam.....94
3.3.3 Slit laminated annular plate.....95
3.3.4 Pinched laminated semi-cylindrical shell.....97
3.3.5 Pinched laminated hemispherical shell.....98
Conclusion.....100

Chapter 4 Applications to the simulation of complex processes.....101
Introduction.....101
4.1 Simulation of impact problems.....102
4.1.1 Low velocity impact of a circular plate.....102

4.1.2 Impact of a boxbeam.....107
4.2 Simulation of sheet metal forming processes.....111
4.2.1 Deep drawing of a hemispherical cup.....112
4.2.2 Deep drawing of a cylindrical cup.....115
4.2.3 Deep drawing of a rectangular cup.....118
4.2.4 Springback simulation of U-shape deep drawing.....121
4.2.5 Deep drawing of a square cup.....124
4.2.6 Single point incremental sheet metal forming.....127
Conclusion.....131

Conclusions and future works.....133
Conclusion.....133
Future works.....134

Part II: Résumé Français

Résumé en français de la thèse.....137

References.....173

Appendix:

Appendix A Shape functions for the SHB elements.....185

Appendix B Detailed expressions of the h_α functions.....189

Appendix C Orthogonality conditions for the SHB elements.....191

List of Tables

Table 1.1. Deformation modes for beam problems.....9

Table 1.2. Comparison between different FE technologies.....19

Table 2.1. Possible permutations for subscripts i, j and k 43

Table 2.2. Definition of the commonly used isotropic hardening models and their evolution laws.....59

Table 3.1. Prismatic, hexahedral and shell finite elements used in the quasi-static analysis..64

Table 3.2. Prismatic, hexahedral and shell finite elements used in the dynamic analysis.....65

Table 3.3. Normalized deflection results for the cantilever beam under out-of-plane bending using linear elements.....66

Table 3.4. Normalized deflection results for the cantilever beam under out-of-plane bending using quadratic elements.....66

Table 3.5. Normalized deflection results for the cantilever beam under in-plane bending using linear elements.....67

Table 3.6. Normalized deflection results for the cantilever beam under in-plane bending using quadratic elements.....68

Table 3.7. Normalized deflection results for the cantilever beam under torsion-type loading using linear elements.....69

Table 3.8. Normalized deflection results for the cantilever beam under torsion-type loading using quadratic elements.....69

Table 3.9. Normalized deflection results for the elastic twisted beam under in-plane bending using linear elements.....70

Table 3.10. Normalized deflection results for the elastic twisted beam under in-plane bending using quadratic elements.....70

Table 3.11. Normalized deflection results for the elastic twisted beam under out-of-plane bending using linear elements.....71

Table 3.12. Normalized deflection results for the elastic twisted beam under out-of-plane bending using quadratic elements.....71

Table 3.13. Natural frequency coefficients for the rectangular cantilever plate using linear elements.....72

Table 3.14. Natural frequency coefficients for the rectangular cantilever plate using quadratic elements.....72

Table 3.15. Natural frequency coefficients for the clamped square plate using linear elements 73

Table 3.16. Natural frequency coefficients for the clamped square plate using quadratic elements.....74

Table 3.17. Computation details for the pinched semi-cylindrical shell problem.....80

Table 3.18. Computation details for the cantilever beam subjected to a concentrated load.....84

Table 3.19. Normalized deflection for the cantilever plate with ply dropoffs.....94

Table 4.1. Material parameters for the studied 6061-T6 aluminum alloy.....102

Table 4.2. Material parameters for the boxbeam.....108

Table 4.3. Material parameters for the hemispherical cup.....112

Table 4.4. Material parameters for the AA2090-T3 aluminum alloy.....116

Table 4.5. Material parameters associated with the anisotropic elastic-plastic model for the cold rolled steel.....118

Table 4.6. Material parameters for the aluminum and steel sheets.....122

Table 4.7. Springback angles θ_1 and θ_2 for the aluminum material.....123

Table 4.8. Springback angles θ_1 and θ_2 for the steel material.....124

Table 4.9. Draw-in distances for the aluminum cup at 15 mm punch stroke.....126

Table 4.10. Draw-in distances for the steel cup at 40 mm punch stroke.....127

Table 4.11. Material parameters for the AA3103-O aluminum alloy.....128

List of Figures

Figure 1.1. Commonly used conventional continuum solid elements.....7
Figure 1.2. Pure bending of a long beam.....8
Figure 1.3. Parasitic bending deformation mode.....9
Figure 1.4. Illustration of degenerated shell element.....12
Figure 1.5. Geometry of conventional shell elements.....13
Figure 1.6. Local coordinate system and nodal variables.....14
Figure 1.7. Illustration of a curved beam.....16
Figure 1.8. Re-interpolation of the transverse shear strain components by the ANS method 24
Figure 2.1. Reference geometry and location of integration points for the SHB solid–shell elements.....30
Figure 2.2. Illustration of the local frames used in the formulation of the SHB solid–shell elements.....36
Figure 2.3. Several approaches for computing the element mass matrix.....46
Figure 2.4. Traditional linear and substitute piecewise shape functions for a triangular shell element.....47
Figure 2.5. 8-node linear hexahedral element.....48
Figure 2.6. Schematic representation of the fiber orientations with respect to the local element frame for the SHB20 element.....55
Figure 2.7. Illustration of stacking sequence for multilayered composite materials.....57
Figure 3.1. Elastic cantilever beam subjected to out-of-plane bending forces.....65
Figure 3.2. Elastic cantilever beam subjected to in-plane bending forces.....66
Figure 3.3. Elastic cantilever beam subjected to torsion-type forces.....67
Figure 3.4. Elastic twisted beam subjected to bending forces.....69
Figure 3.5. Simple rectangular cantilever plate as proposed by Anderson et al. (1968).....71
Figure 3.6. Geometry and boundary conditions for the clamped square plate.....72
Figure 3.7. Geometry and material parameters for the simply supported square plate.....73
Figure 3.8. Load–displacement curves for the simply supported square plate.....74
Figure 3.9. Geometry and material parameters for the cantilever plate.....75
Figure 3.10. Load–displacement curves for the cantilever plate under a concentrated force...76
Figure 3.11. Geometry and material parameters for the pinched semi-cylindrical shell.....77

Figure 3.12. Load–deflection curves for the pinched semi-cylindrical shell.....78

Figure 3.13. Geometry and material parameters for the pinched hemispherical shell.....80

Figure 3.14. Illustration of the mesh nomenclature for the pinched semi-cylindrical shell.....80

Figure 3.15. Load–displacement curves for the pinched hemispherical shell.....81

Figure 3.16. Geometry and material parameters for the cantilever beam.....82

Figure 3.17. Deflection history for the cantilever beam.....83

Figure 3.18. Geometry and material parameters for the simply supported elastic beam.....84

Figure 3.19. Deflection history for the simply supported elastic beam.....85

Figure 3.20. Geometry and material parameters for the clamped circular annular plate.....86

Figure 3.21. Deflection history for the clamped circular annular plate.....86

Figure 3.22. Geometry and material parameters for the elastic twisted cantilever beam.....87

Figure 3.23. Deflection history for the elastic twisted cantilever beam.....88

Figure 3.24. Geometry and material parameters for the clamped spherical cap.....89

Figure 3.25. Deflection history for the clamped spherical cap.....89

Figure 3.26. Geometry and material parameters for the explosively loaded plate.....90

Figure 3.27. Deflection history for the explosively loaded plate.....91

Figure 3.28. Cantilever plate with ply dropoffs.....92

Figure 3.29. Geometry and material parameters for the cantilever laminated beam.....94

Figure 3.30. Load–deflection curves for the cantilever laminated beam.....94

Figure 3.31. Undeformed and deformed configurations of the slit laminated annular plate....95

Figure 3.32. Load–deflection curves for the corner point B for the slit laminated annular plate.....95

Figure 3.33. Geometry parameters for the pinched laminated semi-cylindrical shell.....96

Figure 3.34. Load–displacement curves for the pinched laminated semi-cylindrical shell.....97

Figure 3.35. Geometry of the pinched laminated hemispherical shell.....97

Figure 3.36. Load–displacement curves at points A and B for the pinched laminated hemispherical shell.....98

Figure 3.37. Undeformed and final deformed shapes of the pinched laminated hemispherical shell.....98

Figure 4.1. Schematic representation of a circular plate subjected to impact by a projectile 101

Figure 4.2. Initial in-plane mesh for the clamped circular plate under impact by a projectile 102

Figure 4.3. History of velocity (left) and impact force (right) for the projectile, obtained with the linear SHB elements and ABAQUS shell elements along with the reference

solutions for case 1.....103

Figure 4.4. History of velocity (left) and impact force (right) for the projectile, obtained with the linear SHB elements and ABAQUS shell elements along with the reference solutions for case 2.....104

Figure 4.5. History of velocity (left) and impact force (right) for the projectile, obtained with the linear SHB elements and ABAQUS solid elements along with the reference solutions for case 1.....105

Figure 4.6. History of velocity (left) and impact force (right) for the projectile, obtained with the linear SHB elements and ABAQUS solid elements along with the reference solutions for case 2.....106

Figure 4.7. Schematic representation of a boxbeam impacted by an infinite mass.....107

Figure 4.8. Coarse and fine undeformed meshes for the boxbeam using the quadratic SHB elements.....108

Figure 4.9. Deformed shape for the boxbeam, at time 0.08s, using the linear ABAQUS shell elements.....109

Figure 4.10. Deformed shape for the boxbeam, at time 0.08s, using the linear ABAQUS solid elements.....109

Figure 4.11. Deformed shape for the boxbeam, at time 0.08s, using the quadratic SHB elements.....109

Figure 4.12. Reaction force−displacement curves for the impactor using the coarse mesh...110

Figure 4.13. Reaction force−displacement curves for the impactor using the fine mesh.....110

Figure 4.14. Hemispherical deep drawing setup.....112

Figure 4.15. Initial meshes for one quarter of the circular sheet using the linear SHB elements 112

Figure 4.16. Final deformed shape for the hemispherical cup using the linear SHB elements 112

Figure 4.17. Simulation results in terms of thickness strain.....113

Figure 4.18. Final deformed mesh for the hemispherical cup using ABAQUS C3D8R solid element: illustration of the distorted mesh zone.....114

Figure 4.19. Punch force evolution during the deep drawing of the hemispherical cup.....114

Figure 4.20. Schematic view for the cylindrical cup drawing process.....115

Figure 4.21. Initial meshes for one quarter of the circular sheet.....116

Figure 4.22. Final deformed shape for a completely drawn cylindrical cup.....116

Figure 4.23. Prediction of cup height profiles.....117

Figure 4.24. Schematic view for the rectangular cup drawing setup.....118

Figure 4.25. Initial in-plane meshes for a quarter of the rectangular sheet.....119

Figure 4.26. Final deformed shape for the rectangular cup at a punch stroke of 30 mm.....119

Figure 4.27. Prediction of flange contours at different punch strokes for the deep drawing of a rectangular cup.....120

Figure 4.28. Setup of the U-bending tools.....121

Figure 4.29. Illustration of the deformed sheet in the U-shape deep drawing test (using SHB20 elements).....121

Figure 4.30. Definition of springback angles θ_1 and θ_2.....122

Figure 4.31. Schematic view for the square cup drawing process.....124

Figure 4.32. Final deformed shape for the aluminum square cup at 15 mm punch stroke....124

Figure 4.33. Final deformed shape for the steel square cup at 40 mm punch stroke.....124

Figure 4.34. Definition of the drawn-in distances for the final deformed square cup.....125

Figure 4.35. Description of the single point incremental forming test.....127

Figure 4.36. Final deformed shape for the SPIF sheet.....128

Figure 4.37. Simulation results using coarse meshes, in terms of punch force evolution for the SPIF test, along with experiments taken from Bouffioux et al. (2008).....129

Figure 4.38. Simulation results using fine meshes, in terms of punch force evolution for the SPIF test, along with experiments taken from Bouffioux et al. (2008).....130

Part I: English version

Introduction

Research background

Nowadays, thin structures are widely employed in many fields of the industry (such as automotive, aerospace, civil engineering) in order to reduce the weight of products and improve their mechanical performances. The finite element (FE) simulation of these thin structures has become an indispensable tool in the design of products and the optimization of manufacturing processes, by replacing a number of expensive and time-consuming experimental tests. Despite the significantly growing development of computational resources, reliability and efficiency of the FE analysis still remain the key features in the simulation practice. Traditionally, for the simulation of thin structures, conventional shell elements are used or alternatively low-order solid elements, when three-dimensional effects need to be accounted for. However, in some circumstances, traditional shell and solid elements suffer from various locking phenomena, such as membrane locking, thickness locking, shear locking, etc. In addition, shell elements are often not appropriate for the modeling of complex problems involving double-sided contact. To remedy these shortcomings, considerable effort has been devoted to the development of more accurate and efficient finite elements during the last few decades.

Membrane finite elements have been widely used, due to their computational efficiency in the simulation of bending as well as stretching-dominated sheet metal forming problems. In order to obtain more accurate results, particular attention has been paid in the literature to the development of shell elements for the modeling of thin structures. Compared to membrane elements, shell elements offer better accuracy for modeling bending effects in thin structures. However, the formulation of classical shell elements is typically based on the assumption of plane-stress conditions, which limits their application in sheet metal forming simulation. Further, they cannot account for thickness variations, since only the mid-plane of the sheet is modeled, which makes the double-sided contact difficult to handle.

Concurrently, continuum solid elements allow more realistic modeling for a number of structural problems thanks to their three-dimensional formulation, thus avoiding geometric (mid-plane) or kinematics assumptions as well as constitutive (plane-stress) restrictions.

However, in the simulation of thin structures, the use of solid elements involves meshes with too many elements, which is partly attributable to element aspect ratio limitations as well as locking effects in low-order formulations. In addition, several layers of solid elements are required in the thickness direction in order to accurately describe the various nonlinear phenomena, which considerably increases the computational cost of the simulations.

More recently, the concept of solid–shell elements has emerged, which represents nowadays an interesting alternative to conventional solid and shell elements, in particular for the simulation of sheet metal forming processes. In fact, solid–shell elements combine the advantages of both solid and shell formulations. Their main key features, which make them very attractive, may be summarized as follows: the use of fully three-dimensional constitutive laws, without plane-stress restrictions; easy connection with conventional solid elements, since displacements are the only degrees of freedom; direct calculation of thickness variations, as this is based on physical nodes; automatic consideration of double-sided contact; ability to accurately model thin structures with only a single element layer and few integration points in the thickness direction.

The current work contributes to the development of a family of assumed strain based solid–shell elements (SHB) for the three-dimensional modeling of thin structures. These formulations are extended to include geometric and material nonlinearities, following the earlier works on the family of SHB elements. The first solid–shell element in this family was developed by Abed-Meraim and Combescure (2002), and consists of an eight-node hexahedral element denoted SHB8PS. Its formulation was subsequently improved by Abed-Meraim and Combescure (2009), especially in terms of locking reduction, while the hourglass modes were efficiently controlled by implementing a new stabilization procedure. Then, a six-node prismatic solid–shell element denoted SHB6 was developed by Trinh et al. (2011), as a complement to the SHB8PS element for the modeling of complex geometries whose meshing requires the combination of hexahedral and prismatic elements. Although the performance of the SHB6 is good on the whole, its convergence rate remains slower than that of the SHB8PS, and it requires finer meshes to obtain accurate solutions. More recently, the quadratic counterparts of the above hexahedral and prismatic solid–shell elements have been developed by Abed-Meraim et al. (2013), in order to improve the overall performance and convergence rate. These quadratic versions consist of a 20-node hexahedral element, denoted SHB20, and

a 15-node prismatic element, denoted SHB15. Likewise, their formulation is based on a fully three-dimensional approach with an in-plane reduced-integration rule.

Objectives of the thesis

In this work, a family of SHB solid–shell elements, which includes linear prismatic and hexahedral solid–shell elements, and their quadratic counterparts, is developed for the three-dimensional modeling of thin structures. With respect to the earlier contributions of Abed-Meraim and co-workers on the SHB family elements, we summarize hereafter the main objectives of the current work:

- The SHB elements proposed in this contribution represent extensions of the previous quasi-static versions. They are formulated here with a new lumped mass matrix, in order to deal with explicit/dynamic problems and complex sheet metal forming simulations;
- In the current contribution, the formulation of the SHB elements is combined with various types of constitutive equations, including classical isotropic elastic behavior, orthotropic elastic behavior for composite materials, and anisotropic plastic behavior for metallic materials;
- In this work, all SHB elements have been implemented into the ABAQUS static/implicit and dynamic/explicit software packages, in order to extend their application range to nonlinear quasi-static and dynamic analyses;
- In contrast to previous contributions, which were restricted to academic benchmark problems, the range of application of the proposed SHB elements is enlarged in the current work to include selective dynamic and impact-type problems as well as challenging sheet metal forming processes, involving complex (nonlinear) strain paths, large-strain anisotropic plasticity and double-sided contact.

Organization of the thesis

The thesis manuscript is structured into four main chapters, which are described as follows. The first chapter introduces a literature review on the state-of-the-art of finite element technologies used for the modeling of thin structures. Then, a unified formulation for the

proposed four solid–shell elements is presented in Chapter 2. In Chapter 3, various popular benchmark tests are conducted in order to assess the performance of the SHB elements in quasi-static and dynamic analyses. To further evaluate the performance of the SHB elements in complex highly nonlinear test problems, the proposed solid–shell elements are applied in Chapter 4 to the simulation of impact-type problems as well as challenging sheet metal forming processes, involving geometric nonlinearities, anisotropic elasto-plastic behavior, and double-sided contact. Finally, the main conclusions and remarks on the current contribution as well as some prospects for future work are drawn in the conclusion part of this manuscript.

Chapter 1

Literature review on solid–shell finite element technology

Introduction

In order to save materials, reduce their weight and improve the whole mechanical performance, thin structures are nowadays increasingly used in modern industries. The rapid development of computational resources has made the finite element (FE) analysis of thin structures possible in the design and manufacturing processes. However, the reliability and accuracy of the predicted solutions still remain to be improved.

It is well known that shell theory allows developing highly efficient finite elements; in particular, through their degenerated formulations. In this regard, conventional shell elements have been most often adopted for the FE analysis of thin structures. Although shell elements involve relatively low computational costs, their degenerated formulations lead to several limitations. For instance, the formulation of classical shell elements is typically based on the assumption of plane-stress conditions, which limits their application in sheet metal forming simulation. Further, they cannot account for thickness variations, since only the mid-plane of the sheet is modeled, which makes the double-sided contact difficult to handle. Moreover, shell elements also suffer from various locking phenomena, in particular in the simulation of bending-dominated problems. Concurrently, solid elements have been developed based on fully three-dimensional formulations, which allow physical modeling of thickness variations. However, locking phenomena are also present in these conventional solid elements, in particular for low-order formulations, which cannot be avoided by just refining the mesh.

To remedy these shortcomings, considerable effort has been devoted to the development of solid–shell elements during the past few decades. The key idea behind this original concept of solid–shell elements is to combine the advantages of both solid and shell formulations. The main benefits of the resulting solid–shell concept may be summarized as follows: easier

formulation, based on a purely three-dimensional approach, with displacements as the only degrees of freedom; consideration of fully three-dimensional constitutive laws, without plane-stress restrictions; direct calculation of thickness variations; natural treatment of double-sided contact, thanks to the availability of actual top and bottom surfaces; 3D modeling of thin structures, using only a single element layer and few integration points, while accurately describing the through-thickness phenomena.

In this chapter, a literature review on the development and the use of FE technologies for the simulation of thin structures is presented. The remaining sections of this chapter are organized as follows. In a short introduction, the conventional solid and shell formulations are summarized in Subsections 1.1 and 1.2, respectively. Then, the concept of solid–shell elements and related numerical techniques are introduced in Subsection 1.3. The last Subsection is dedicated to the state-of-the-art of the solid–shell elements whose formulation will be further developed and extended in the current work.

1.1 Three-dimensional solid finite elements

1.1.1 State of the art

Continuum solid finite elements are usually used to model three-dimensional bulk structures without any geometric simplifications. The geometry of continuum solid elements is completely defined by the coordinates of the nodes, and the nodal displacements allow the interpolation of the displacements within the element in all directions. Moreover, fully 3D constitutive equations are adopted for these solid elements, which allow a realistic description of the various phenomena without the need for restrictive assumptions (e.g., plane-stress conditions). Nowadays, the most commonly used continuum elements in finite element analysis are the tetrahedral elements, prismatic elements and hexahedral elements, as illustrated in Fig. 1.1 (see, e.g., Hellen, 1972; Andersen, 1979; Hughes, 1987; Zienkiewicz and Taylor, 2000; Cao et al., 2002). These elements usually have four, six and eight nodes, respectively, in the case of linear element formulations, while they have ten, fifteen and twenty, respectively, in the case of quadratic element formulations. Generally, it is well known that the low-order hexahedral elements provide more accurate solutions than the low-order tetrahedral and prismatic elements for most nonlinear problems (see, e.g., Puso and Solberg, 2006). However, hexahedral elements are not suitable to mesh complex geometries

and, in such situations, tetrahedral or prismatic elements are useful. Also, the high-order tetrahedral and prismatic elements can be used to model nonlinear problems involving complex geometries, however, at the expense of a higher computational cost.

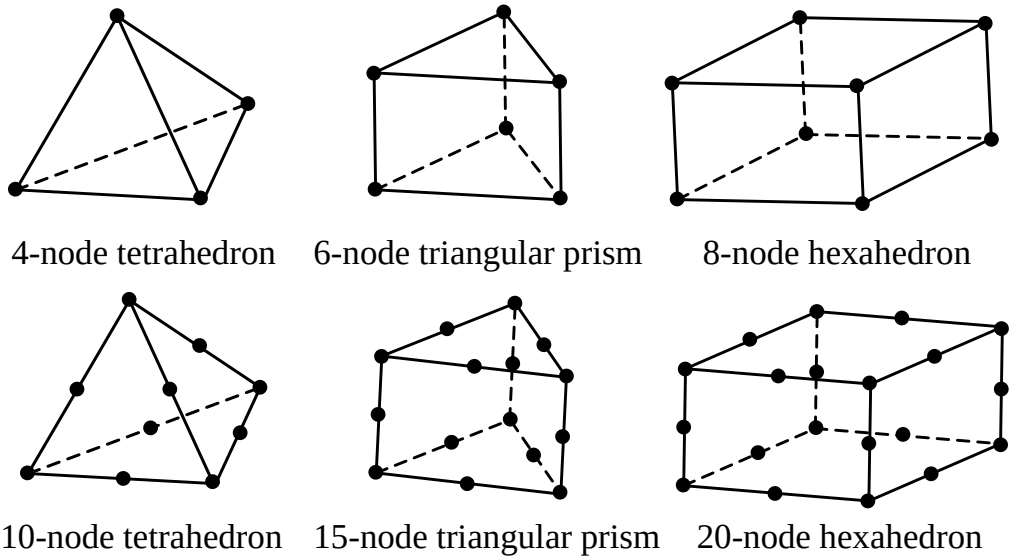


Figure 1.1. Commonly used conventional continuum solid elements.

1.1.2 Treatment of locking phenomena

As mentioned above, solid elements have many advantages, due to their fully three-dimensional formulations, and are designed to be general-purpose elements. In most nonlinear situations, the low-order solid elements are preferred due to their lower computational cost. However, they often show poor performance and suffer from several locking phenomena in simulations of thin structures, especially for bending-dominated problems (see, e.g., Adam et al., 2014, 2015a). These locking phenomena, which significantly compromise the performance of solid elements, are briefly presented in what follows.

1.1.2.1 Shear locking

The shear locking usually occurs when the elements are subjected to bending-dominated forces or moments. This shear locking is due to the fact that the finite element is not able to model pure bending situations without introducing (spurious) transverse shear strains, which results in excessive element stiffness in shear (see, e.g., Prathap, 1985; Huang, 1987; Tessler and Spiridigliozzi, 1988). Regarding this point, the following example illustrates the case of a long beam with rectangular cross section subjected to pure bending moment, as shown in Fig. 1.2.

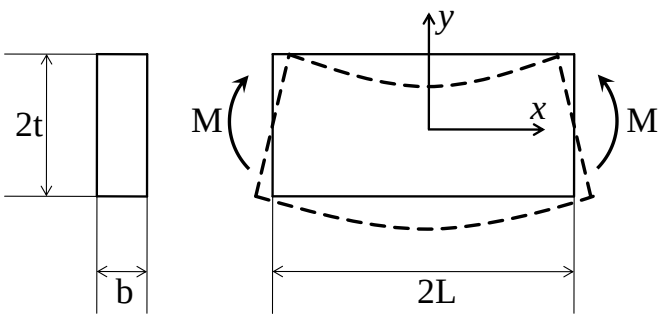


Figure 1.2. Pure bending of a long beam.

Theoretically, the analytical solution of this in-plane beam bending problem is given by the following expressions:

$$u = \frac{\mathrm{M}}{E\mathrm{I}} xy, \qquad v = \frac{\mathrm{M}}{2E\mathrm{I}}\left(\mathrm{L}^2 - x^2\right) - \frac{\nu \mathrm{M}}{2E\mathrm{I}}\left(\mathrm{t}^2 - y^2\right), \tag{1.1}$$

where u and v are the displacements in the $\vec{x}$ and $\vec{y}$ directions, respectively. The geometric dimensions $2\mathrm{t}$, b and 2L represent the thickness, the width and the length of the beam. The elastic properties are given by E for the Young modulus, and ν for the Poisson ratio. Also, in the above formulas, I denotes the inertia moment of the beam section, while M is the bending moment.

The strain components are derived from the above in-plane displacements as follows:

$$\varepsilon_x = \frac{\partial u}{\partial x} = \frac{\mathrm{M}}{E\mathrm{I}} y, \qquad \varepsilon_y = \frac{\partial v}{\partial y} = \frac{\nu \mathrm{M}}{E\mathrm{I}} y, \qquad \gamma_{xy} = \frac{\partial u}{\partial y} + \frac{\partial v}{\partial x} = 0. \tag{1.2}$$

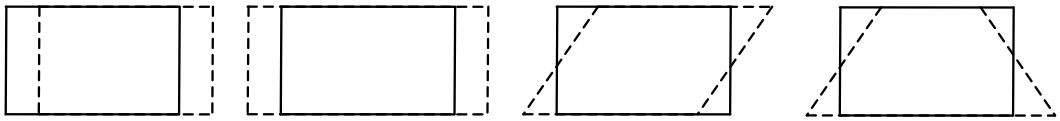
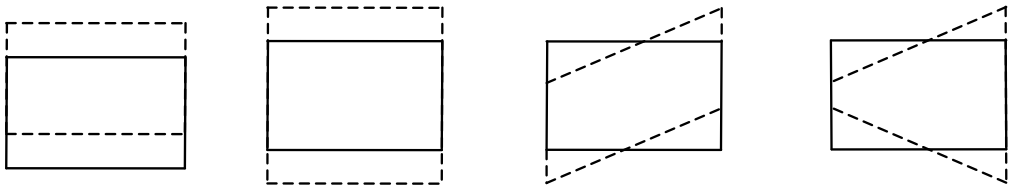
From the above expressions, it is clear that the shear strain γ_{xy} satisfies the zero-shear-strain condition, which is consistent with a beam in pure bending.

From a finite element point of view, the displacement field can be interpolated using the following classical functions:

$$\begin{cases} u = a_0 + a_1 x + a_2 y + a_3 xy \\ v = b_0 + b_1 x + b_2 y + b_3 xy \end{cases}, \tag{1.3}$$

where the eight coefficients a_i and b_i represent the eight deformation modes, as illustrated in Table 1.1.

Table 1.1. Deformation modes for beam problems.

Coefficient	$a_0 \neq 0$	$a_1 \neq 0$	$a_2 \neq 0$	$a_3 \neq 0$
Mode				
Coefficient	$b_0 \neq 0$	$b_1 \neq 0$	$b_2 \neq 0$	$b_3 \neq 0$
Mode				

Considering the pure bending condition, only the fourth mode ($a_3 \neq 0$) is active. Thus, the interpolations given in Eq. (1.3) degenerate to

$$\begin{cases} u = a_3 xy \\ v = 0 \end{cases}. \tag{1.4}$$

The strain components associated with the above displacement field are given by

$$\varepsilon_x = \frac{\partial u}{\partial x} = a_3 y, \qquad \varepsilon_y = \frac{\partial v}{\partial y} = 0, \qquad \gamma_{xy} = \frac{\partial u}{\partial y} + \frac{\partial v}{\partial x} = a_3 x. \tag{1.5}$$

The above expressions clearly show that the resulting strain components do not satisfy the zero-shear-strain condition of pure bending, which leads to a stiffer element, and thereby to a parasitic deformation mode, as shown in Fig. 1.3 (see, e.g., Belytschko and Bindeman, 1993; Li and Cescotto, 1997).

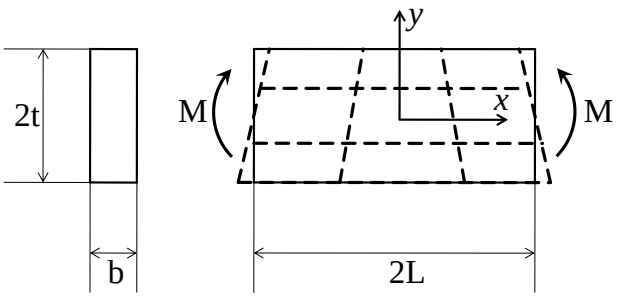


Figure 1.3. Parasitic bending deformation mode.

The parasitic shear strain that appears in Eq. (1.5) is represents the shear locking, which is well known in finite element analysis. This phenomenon appears especially for low-order finite elements, due to their particularly simple kinematics, which is not rich enough to represent the correct solution. The shear locking phenomenon can be prevented by using specific numerical treatments, such as the reduced-integration technique (see, e.g., Zienkiewicz et al., 1971), the assumed-strain method (see, e.g., Belytschko and Bindeman, 1993), or possibly the consideration of higher-order elements.

1.1.2.2 Poisson thickness locking

The Poisson thickness locking may also occur in low-order hexahedral elements. To illustrate this phenomenon, let us consider again the pure bending problem described above. According to the displacement interpolation given by Eq. (1.3), the strain components in the $\vec{x}$ and $\vec{y}$ directions can be obtained as:

$$\begin{cases} \varepsilon_x = \dfrac{\partial u}{\partial x} = a_1 + a_3 y \\ \varepsilon_y = \dfrac{\partial v}{\partial y} = b_2 + b_3 x \end{cases}. \tag{1.6}$$

Based on the elastic strain–stress relationship, the corresponding stress components are given by

$$\begin{cases} \sigma_x = \lambda\varepsilon_y + (\lambda + 2\mu)\varepsilon_x \\ \sigma_y = \lambda\varepsilon_x + (\lambda + 2\mu)\varepsilon_y \end{cases}, \tag{1.7}$$

where $\lambda = \dfrac{\nu E}{(1+\nu)(1-2\nu)}$ and $\mu = \dfrac{E}{2(1+\nu)}$.

It can be noticed that a constant approximation for the thickness strain ε_y is obtained, while the corresponding stress σ_y has a linear distribution along the $\vec{y}$ direction (for $\nu \neq 0$). Such inconsistency between the distribution of the stress and the strain in the thickness direction leads to the undesirable locking effect, denoted as the Poisson thickness locking. The latter can be alleviated by modifying the elastic constitutive matrix so that the normal stress is uniformly distributed through the thickness (see, e.g., Petchsasithon and Gosling, 2005).

1.1.2.3 Volumetric locking

When incompressible or nearly-incompressible material behavior is considered, standard fully integrated finite elements usually suffer from the so-called volumetric locking phenomenon. The latter cannot be avoided just by refining the mesh and, thus, some finite elements show poor performance when the Poisson ratio approaches the limit value of 0.5. To better illustrate this locking effect, we consider here a linear elastic material. The elastic strain can be decomposed into a deviatoric part $\boldsymbol{\varepsilon}_{\mathrm{d}}$ and a volumetric part $\boldsymbol{\varepsilon}_{\mathrm{v}} = tr(\boldsymbol{\varepsilon})$. Consequently, the elastic strain energy Π_{int} of the involved element is also partitioned into a deviatoric (distortional) part Π_{dev} and a volumetric part Π_{v} as follows:

$$\Pi_{\mathrm{int}} = \Pi_{\mathrm{dev}} + \Pi_{\mathrm{v}} = 2G\int_{\Omega_e} \boldsymbol{\varepsilon}_{\mathrm{d}} : \boldsymbol{\varepsilon}_{\mathrm{d}}\, d\Omega_e + K\int_{\Omega_e} tr(\boldsymbol{\varepsilon})^2\, d\Omega_e\,, \tag{1.8}$$

where $G = \dfrac{E}{2(1+\nu)}$ is the shear modulus, and $K = \dfrac{E}{3(1-2\nu)}$ is the bulk modulus.

For incompressible or nearly-incompressible materials, the bulk modulus K will become extremely large when the Poisson ratio ν approaches the limit value of 0.5. Consequently, the associated element becomes overly stiff, as compared to that of real incompressible materials, if $\varepsilon_{ii} = tr(\boldsymbol{\varepsilon})$ is not vanishing (see Nguyen, 2009). Generally, the selective reduced integration rule, the Galerkin mixed formulation and stabilization techniques may be used to alleviate this type of locking (see, e.g., Elguedj et al., 2008; Davim, 2012). In some cases, the volumetric locking can also be prevented by defining nodal volumes and by evaluating average nodal pressures in terms of these designed local volumes instead of using the whole element volume (Bonet and Burton, 1998).

1.2 Conventional shell elements

1.2.1 State of the art

Conventional shell elements have been specifically developed for the analysis of thin structures (i.e., when the thickness dimension is significantly smaller than the other dimensions). According to the theoretical backgrounds on which their formulations are based, shell elements can be classified into two main families: the conventional flat shells and the degenerated shells. For the conventional flat shell elements, the geometry of the shell is

approximated by a flat finite element. Some classical theories, such as the Kirchhoff theory for thin plates and the Reissner–Mindlin theory for thick plates, are generally adopted as basic theoretical models for the formulation of flat shell elements, which is well detailed in several finite element books (see, e.g., Bathe, 1996; Zienkiewicz and Taylor, 2000). For the second family of shell elements, the latter are degenerated from the formulation of three-dimensional finite elements, and commonly used to represent the mid-surface of thin structures, as illustrated in Fig. 1.4 for a 4-node shell element. In most shell theories, some basic assumptions are essentially made for the purpose of implementation. In general, the following assumptions are widely considered in shell element formulations:

- The consistent physical thickness of the simulated structure is neglected.
- The normal to the mid-surface remains straight after deformation.
- The transverse normal stress is assumed negligible.

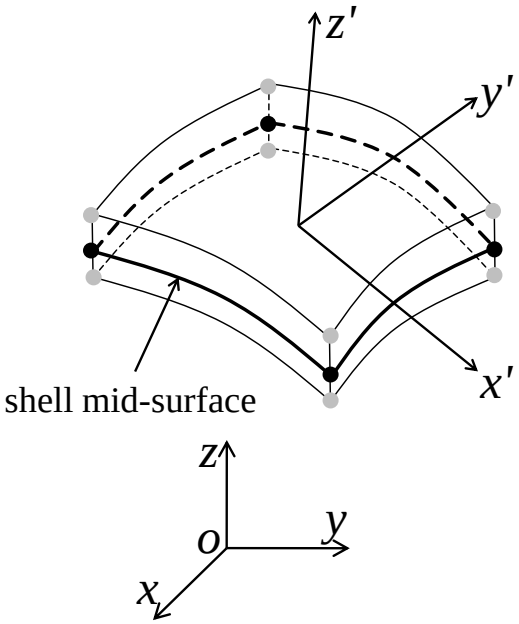


Figure 1.4. Illustration of degenerated shell element.

Neglecting the physical thickness, the plane-stress conditions are adopted in the formulation of shell elements, which allows improving the computational efficiency. Therefore, shell elements usually perform more efficiently than continuum solid elements. According to their geometric characteristics, four commonly used shell elements, including linear triangular and quadrilateral shell elements, and their quadratic counterparts, have been developed in the literature (see the illustrative Fig. 1.5).

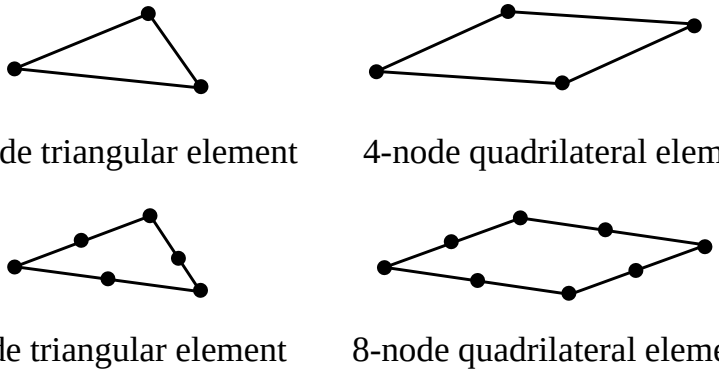


Figure 1.5. Geometry of conventional shell elements.

The widely used degenerated shell elements are derived from the pioneering work of Ahmad et al. (Ahmad et al., 1970), who developed a curved shell element for thick and thin structures. In what follows, only some basic concepts of degenerated shell elements are briefly introduced in order to subsequently compare their main features with those of solid–shell elements.

1) Geometry and kinematic interpolation

As mentioned above, the degenerated shell elements are obtained from the reduction (degeneration) of the 3D solid approach to the 2D shell approach, which has only mid-surface nodal variables. As illustrated in Fig. 1.6, a local orthogonal coordinate system ($\overline{\mathbf{V}}_{1i}, \overline{\mathbf{V}}_{2i}, \overline{\mathbf{V}}_{3i}$) associated with the shell element is defined, in which the unit vector $\overline{\mathbf{V}}_{3i}$ represents the direction normal to the mid-surface. The nodal coordinates ($\overline{x}, \overline{y}, \overline{z}$) and nodal displacements ($\overline{u}, \overline{v}, \overline{w}$) at the i-th node of the shell element can be interpolated using the three translational displacements (u, v, w) and the two rotations (α, β) at the two points i_{top} and i_{bottom}. The detailed equations are well explained in some well-established references (see, e.g., Ahmad et al., 1970; Choi and Paik, 1995; Polit and Touratier, 1999; Zienkiewicz and Taylor, 2000).

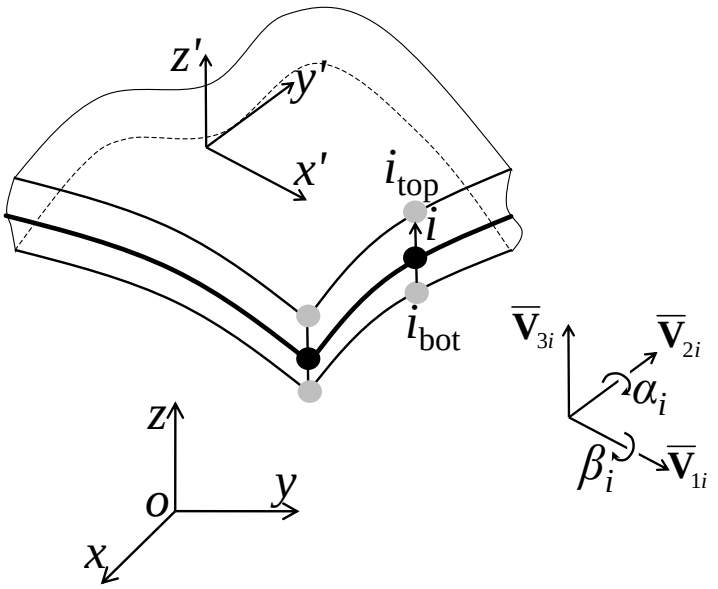


Figure 1.6. Local coordinate system and nodal variables (Ahmad et al., 1970).

2) Definition of the strain and stress fields

In the local coordinate system (x', y', z'), the strain field is derived from the expression of the displacement gradient, while the stress field is computed by the constitutive equations associated with the shell element. According to the classical shell assumptions, the stress in the thickness direction is assumed to be negligible. Hence, the strain field corresponding to the plane-stress conditions is expressed as:

$$\boldsymbol{\varepsilon} = \nabla\left(\hat{\mathbf{u}}\right) = \left[\varepsilon_{x'x'}, \varepsilon_{y'y'}, 2\varepsilon_{x'y'}, 2\varepsilon_{y'z'}, 2\varepsilon_{z'x'}\right]^T, \tag{1.9}$$

where vector $\hat{\mathbf{u}}$ is the displacement field within the shell element, which is interpolated using the nodal displacements $\bar{\mathbf{u}}\left(\bar{u}, \bar{v}, \bar{w}\right)$. The corresponding stress field is given by:

$$\boldsymbol{\sigma} = \left[\sigma_{x'x'}, \sigma_{y'y'}, \tau_{x'y'}, \tau_{y'z'}, \tau_{z'x'}\right]^T. \tag{1.10}$$

Then, the elastic stress–strain relationship is written as:

$$\boldsymbol{\sigma} = \mathbf{C}^e \cdot \boldsymbol{\varepsilon}, \tag{1.11}$$

where the plane-stress-type elasticity matrix $\mathbf{C}^e$ takes the following form:

$$\mathbf{C}^e = \frac{E}{1-\nu^2}\begin{bmatrix} 1 & \nu & 0 & 0 & 0 \\ & 1 & 0 & 0 & 0 \\ & & (1-\nu)/2 & 0 & 0 \\ & & & k(1-\nu)/2 & 0 \\ sym & & & & k(1-\nu)/2 \end{bmatrix}, \tag{1.12}$$

where the shear correction factor $k = 5/6$ is introduced to account for the parabolic shear stress distribution across the section (see, e.g., Vlachoutsis, 1992).

3) Variational principle

Finally, the variational form of the virtual work expression for the conventional shell elements writes:

$$\delta\Pi = \delta W_{\text{int}} + \delta W_{ext} = -\int_{\Omega_e} \delta\left(\nabla\left(\hat{\mathbf{u}}\right)\right)^T \cdot \boldsymbol{\sigma}\, d\Omega_e + \delta\overline{\mathbf{u}}^T \cdot \mathbf{R} = 0, \tag{1.13}$$

where vector $\mathbf{R}$ represents the equivalent external nodal force vector.

1.2.2 Locking phenomena

For the last decades, conventional shell elements have attracted much attention for the analysis of thin structures, due to their high efficiency. However, a number of locking phenomena also exist in conventional shell elements, which are especially revealed in the simulation of thin structures. In this subsection, two typical locking phenomena, i.e. the transverse shear locking and the membrane locking, which are commonly identified in conventional shell elements, are briefly presented.

1.2.2.1 Transverse shear locking

Similar to the solid elements discussed previously, the transverse shear locking is one of the most commonly encountered locking phenomena in shell elements. This locking is due to the fact that the Kirchhoff–Love hypothesis is not considered in the displacement interpolations, which does not allow reproducing the zero-transverse-shear-strain condition in pure bending problems (see, e.g., Zienkiewicz et al., 1971; Kui et al., 1985; César de Sá et al., 2002). The illustration of the specific mechanism leading to the occurrence of transverse shear locking, in relation with the resulting parasitic shear strain, is similar to what has been shown in subsection 1.1.2.1, and is not repeated here for conciseness.

1.2.2.2 Membrane locking

The membrane locking is characterized by the occurrence of parasitic membrane strains in bending-dominated problems of curved beam and shell structures. This locking phenomenon is a severe issue, which is frequently encountered in both low-order and high-order shell elements (see, e.g., Stolarski and Belytschko, 1982; Koschnick et al., 2005; Nguyen, 2009). In order to clearly explain the origin of membrane locking, we present here a simple curved beam with length L and radius R, as illustrated in Fig. 1.7. Based on the classical thin beam theory (see, e.g., Timoshenko, 1955), the displacement degrees of freedom are defined as the circumferential displacement u and the radial displacement w. The coordinate s is aligned so that to follow the middle line of the curved beam.

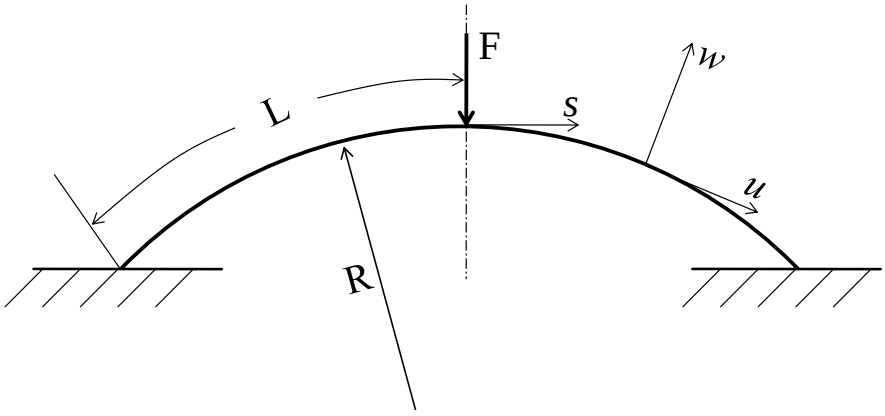


Figure 1.7. Illustration of a curved beam.

With these definitions, the membrane strain ε and the bending strain χ are derived from the displacement field as follows:

$$\begin{cases} \varepsilon = u_{,s} + w/\mathrm{R} \\ \chi = u_{,s}/\mathrm{R} - w_{,ss} \end{cases}. \tag{1.14}$$

From the above expressions, it is clearly suggested that interpolations of class C^0 and C^2 are required for the displacements u and w, respectively, which leads to the following expressions:

$$\begin{cases} u = a_0 + a_1\xi \\ w = b_0 + b_1\xi + b_2\xi^2 + b_3\xi^3 \end{cases}, \tag{1.15}$$

where $\xi = s/\mathrm{L}$, and coefficients a_i and b_j ($i = 0,1$ and $j = 0$ to 3) are expressed in terms of the nodal degrees of freedom.

According to the expressions given in Eq. (1.15), the membrane strain ε and the bending strain χ can be rewritten as:

$$\begin{cases} \varepsilon = \left(a_1/\mathrm{L} + b_0/\mathrm{R}\right) + \left(b_1/\mathrm{R}\right)\xi + \left(b_2/\mathrm{R}\right)\xi^2 + \left(b_3/\mathrm{R}\right)\xi^3 \\ \chi = \left(a_1/\mathrm{RL} - 2b_2/\mathrm{L}^2\right) - \left(6b_3/\mathrm{L}^2\right)\xi \end{cases} . \tag{1.16}$$

Considering the physical response of inextensional bending, which is usually the case for curved beams and shells, it is required that the membrane strain ε tends to vanish. In this case, the following constraints must to be satisfied:

$$\begin{cases} a_1/\mathrm{L} + b_0/\mathrm{R} = 0 \\ b_1/\mathrm{R} = 0 \\ b_2/\mathrm{R} = 0 \\ b_3/\mathrm{R} = 0 \end{cases} . \tag{1.17}$$

In the above system of equations, including the terms from both the circumferential and radial displacements, the first expression represents the true constraint and it reflects the physical condition of curved beams, for which the membrane strain $\varepsilon \to 0$. However, the remaining three constrains, $b_1 \to 0$, $b_2 \to 0$ and $b_3 \to 0$, involve the following spurious constraints: $w_{,s} \to 0$, $w_{,ss} \to 0$ and $w_{,sss} \to 0$, which will excessively increase the bending stiffness of the element and cause the so-called membrane locking (see Nguyen, 2009).

1.2.3 Numerical methods for alleviating locking problems

Locking phenomena usually occur when low-order fully integrated elements are adopted in the simulations. Therefore, the stiffness of the investigated element is overestimated due to non-physical (spurious) deformations. A number of methods and techniques have been developed in the literature to overcome these locking phenomena for both solid and shell elements. The reduced integration (RI) technique was the first numerical method to alleviate some locking phenomena (see, e.g., Hughes et al., 1978; Stolarski and Belytschko, 1982, 1983; Briassoulis, 1989; Belytschko et al., 1992; Zhu and Cescotto, 1996; Hauptmann et al., 2000; Geyer and Groenwold, 2003; Parente et al., 2006; Schwarze and Reese, 2009; Winkler, 2010; Schwarze et al., 2011; Bouclier et al., 2012; Edem and Gosling, 2013; Pagani et al., 2014). However, not all locking phenomena can be alleviated by the RI technique, which requires additional treatments to improve the performance of shell elements (see, e.g., Zienkiewicz et al., 1971; Hughes et al., 1978).

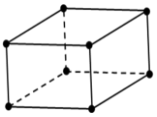
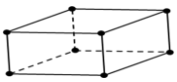
The most effective solution to prevent the occurrence of locking problems is the use of mixed formulations, in which separate (independent) interpolations are adopted for the displacements and the stresses, or by the projection of the nodal displacements so that the spurious deformations are minimized (see, e.g., Rhiu and Lee, 1987; Chang et al., 1989; Polit and Touratier, 2000; Brischetto et al., 2012). In this context, the so-called assumed strain method (ASM) has been introduced for shell elements by Bathe and Dvorkin (1986), and was extensively applied to solid elements (see, e.g., Belytschko and Bindeman, 1993; Zhu and Cescotto, 1996; Flores, 2013a). By combining the ASM with the RI technique, the resulting elements showed good performances with respect to shear and volumetric locking phenomena. The enhanced assumed strain (EAS) technique is also widely used in the formulation of low-order finite elements, which is based on the inclusion of additional deformation modes for removing locking problems (see, e.g., Simo and Rifai, 1990; Simo and Armero, 1992). The EAS technique is often combined with the assumed natural strain (ANS) method in order to prevent most locking phenomena (see, e.g., Wagner et al., 2002). The numerical techniques discussed above have been widely applied in the literature for 2D and 3D solid and shell element formulations, which ultimately motivated the efficient and accurate concept of solid–shell elements for the 3D modeling of thin structures.

1.3 Solid–shell finite elements

1.3.1 State of the art

During the past few decades, the concept of "solid–shell" elements has attracted significant attention from researchers and FE developers. The main objective of developing solid–shell elements is to allow three-dimensional modeling of thin structures, without the occurrence of locking effects, while accounting for the through-thickness phenomena. In other words, solid–shell elements are aimed to combine the advantages of both conventional shell elements and continuum solid formulations. A general comparison, in terms of advantages and drawbacks, for conventional shell elements, solid elements and solid–shell elements is proposed in Table 1.2.

Table 1.2. Comparison between different FE technologies.

	 Shell elements	 Solid elements	 Solid–shell elements
Advantages	▪ only the mid-plane is discretized ▪ low computational cost	▪ Direct modeling of thickness ▪ fully 3D constitutive equations	▪ Direct modeling of thickness. ▪ fully 3D constitutive equations ▪ only displacement DOF ▪ locking-free ▪ low computational cost (only a single layer of elements)
Disadvantages	▪ plane-stress assumptions ▪ locking problems	▪ high computational cost ▪ locking problems	

As mentioned in the above Table, the main benefits of the solid–shell concept can be summarized as follows: direct calculation of thickness variations thanks to the three-dimensional formulation, with displacements as the only degrees of freedom; consideration of fully three-dimensional constitutive laws, with no plane-stress restrictions; natural treatment of double-sided contact, which makes them more suitable for industrial applications; 3D modeling of thin structures with only a single element layer and few integration points, while accurately describing the through-thickness phenomena.

Several numerical techniques have been developed for solid–shell elements to alleviate most locking pathologies. Among them, the reduced integration (RI) technique (see, e.g., Zienkiewicz et al., 1971) or the selective reduced integration (SRI) technique (see, e.g., Hughes, 1980), which consists, for low-order solid–shell elements, in adopting a one-point in-plane quadrature rule, while considering several integration points along the thickness. Such RI techniques make the solid–shell elements very attractive in terms of computational cost, since they only require few integration points in the simulations. However, due to the low quadrature order, some elements may be subjected to spurious zero-energy modes (hourglass modes), which require specific procedures for their stabilization (see, e.g., Abed-Meraim and Combescure, 2009). Furthermore, several additional strategies have been combined with the

above techniques in order to improve the performance of solid–shell elements with regard to locking effects. The most widely used are the assumed strain method (ASM), the enhanced assumed strain (EAS) approach, and the assumed natural strain (ANS) concept (see, e.g., Cho et al., 1998; Hauptmann and Schweizerhof, 1998; Puso, 2000; Sze and Yao, 2000; Abed-Meraim and Combescure, 2002; Alves de Sousa et al., 2005; Parente et al., 2006; Reese, 2007; Cardoso et al., 2008; Abed-Meraim and Combescure, 2009; Schwarze and Reese, 2009; Moreira et al., 2010; Li et al., 2011; Edem and Gosling, 2012; Bouclier et al., 2013a, 2013b; Flores, 2013a, 2013b; Naceur et al., 2013; Pagani et al., 2014; Bouclier et al., 2015; Caseiro et al., 2015; Ben Bettaieb et al., 2015; Kpeky et al., 2015; Flores, 2016).

1.3.2 Treatment of locking phenomena

In order to eliminate the locking phenomena and to improve the overall performance, several numerical treatments are commonly adopted in the formulation of solid–shell elements. In this subsection, we briefly present the four most commonly used methods for solid–shell elements, which consist of the ASM, the EAS, the ANS, the mixed method and the NURBS-based formulation.

1.3.2.1 Assumed strain method (ASM)

Based on the variational framework, the so-called assumed strain method is frequently adopted in the formulation of solid–shell elements. In the pioneering works of Hughes (1980), the "$\mathbf{B}$-bar approach" has been introduced in order to specifically solve volumetric locking problems. This approach consists of the projection of the classical discrete gradient operator $\mathbf{B}$ into an assumed (projected) gradient operator $\overline{\mathbf{B}}$, in which the contribution of the volumetric part is reduced (see also Simo and Hughes, 1986). Later on, a number of contributions have proved that the ASM method is able to significantly enhance the performance of finite elements, including solid–shell elements (see, e.g., Belytschko and Bindeman, 1991, 1993; Stolarski and Chen, 1995; Li and Cescotto, 1997; Cho et al., 1998; Abed-Meraim and Combescure, 2002; Hong and Kim, 2002; Lee et al., 2002; Flores and Oñate, 2005; Kulikov and Plotnikova, 2006; Abed-Meraim and Combescure, 2009; Wisniewski et al., 2010).

The assumed strain method (ASM) is usually based on the well-known Hu–Washizu three-field variational principle (see, e.g., Simo et al., 1985; Simo and Hughes, 1986; Belytschko and Bindeman, 1991, 1993). The weak form of the Hu–Washizu principle is expressed by

$$\delta\Pi\left(\mathbf{v}, \dot{\bar{\boldsymbol{\varepsilon}}}, \bar{\boldsymbol{\sigma}}\right) = \int_{\Omega_e} \delta\dot{\bar{\boldsymbol{\varepsilon}}}^{\mathrm{T}} \cdot \boldsymbol{\sigma}\, \mathrm{d}\Omega_e + \delta \int_{\Omega_e} \bar{\boldsymbol{\sigma}}^{\mathrm{T}} \cdot \left(\nabla_{\mathrm{s}}\left(\mathbf{v}\right) - \dot{\bar{\boldsymbol{\varepsilon}}}\right) \mathrm{d}\Omega_e - \delta\dot{\mathbf{d}}^{\mathrm{T}} \cdot \mathbf{f}^{\mathrm{ext}} = 0, \tag{1.18}$$

where δ denotes a variation, $\mathbf{v}$ the velocity field, $\dot{\bar{\boldsymbol{\varepsilon}}}$ the assumed strain rate, $\bar{\boldsymbol{\sigma}}$ the interpolated stress, $\boldsymbol{\sigma}$ the stress evaluated by the constitutive law, $\dot{\mathbf{d}}$ the nodal velocities, $\mathbf{f}^{\mathrm{ext}}$ the external nodal forces, and $\nabla_{\mathrm{s}}\left(\mathbf{v}\right)$ the symmetric part of the velocity gradient.

As suggested by Simo and Hughes (1986), the interpolated stress $\bar{\boldsymbol{\sigma}}$ is assumed to be orthogonal to the difference between the symmetric part of the velocity gradient $\nabla_{\mathrm{s}}\left(\mathbf{v}\right)$ and the assumed strain rate $\dot{\bar{\boldsymbol{\varepsilon}}}$, which leads to the following simplified form of the Hu–Washizu variational principle

$$\delta\Pi\left(\dot{\bar{\boldsymbol{\varepsilon}}}\right) = \int_{\Omega_e} \delta\dot{\bar{\boldsymbol{\varepsilon}}}^{\mathrm{T}} \cdot \boldsymbol{\sigma}\, \mathrm{d}\Omega_e - \delta\dot{\mathbf{d}}^{\mathrm{T}} \cdot \mathbf{f}^{\mathrm{ext}} = 0. \tag{1.19}$$

The symmetric part of the velocity gradient $\nabla_{\mathrm{s}}\left(\mathbf{v}\right)$ is related to the nodal velocities $\dot{\mathbf{d}}$ by using the classical discrete gradient operator $\mathbf{B}$ as follows

$$\nabla_{\mathrm{s}}\mathbf{v}(x, t) = \sum_{1}^{n} \nabla_{\mathrm{s}}\left[N_I(x)\dot{\mathbf{d}}_I(t)\right] = \mathbf{B}(x) \cdot \dot{\mathbf{d}}(t), \tag{1.20}$$

where N_I represent the shape functions, and $I = 1, \cdots, n$, with n being the number of element nodes.

The assumed strain rate $\dot{\bar{\boldsymbol{\varepsilon}}}$ is expressed in terms of a modified matrix $\bar{\mathbf{B}}$, which is derived from the classical gradient operator $\mathbf{B}$, in order to eliminate most locking phenomena. Its expression is given by

$$\dot{\bar{\boldsymbol{\varepsilon}}}(x, t) = \sum_{1}^{n} \bar{\mathbf{B}}_I(x) \cdot \dot{\mathbf{d}}_I(t) = \bar{\mathbf{B}}(x) \cdot \dot{\mathbf{d}}(t). \tag{1.21}$$

Substituting Eq. (1.21) into the simplified form of the Hu–Washizu variational principle (see Eq. (1.19)), we obtain:

$$\delta\dot{\mathbf{d}}^{\mathrm{T}} \cdot \left(\int_{\Omega_e} \bar{\mathbf{B}}^{\mathrm{T}} \cdot \boldsymbol{\sigma}\, \mathrm{d}\Omega_e - \mathbf{f}^{\mathrm{ext}}\right) = 0. \tag{1.22}$$

Since $\delta\dot{\mathbf{d}}$ can be chosen quite arbitrarily, Eq. (1.22) leads to the following expressions of the element stiffness matrix and internal force vector:

$$\mathbf{K}_e = \int_{\Omega_e} \bar{\mathbf{B}}^{\mathrm{T}} \cdot \mathbf{C}^{\mathrm{ep}} \cdot \bar{\mathbf{B}}\, \mathrm{d}\Omega_e, \qquad \mathbf{f}^{\mathrm{int}} = \int_{\Omega_e} \bar{\mathbf{B}}^{\mathrm{T}} \cdot \boldsymbol{\sigma}(\dot{\bar{\boldsymbol{\varepsilon}}})\, \mathrm{d}\Omega_e, \tag{1.23}$$

where $\mathbf{C}^{\mathrm{ep}}$ is the fourth-order tangent modulus derived from the constitutive law.

1.3.2.2 Enhanced assumed strain (EAS) method

The enhanced assumed strain method (EAS) proposed by Simo and Rifai (Simo and Rifai, 1990) also attracted much interest for overcoming the locking deficiencies over the past two decades (see, e.g., Simo and Rifai, 1990; Puso, 2000; César de Sá et al., 2002; Areias et al., 2003; Bui et al., 2004; Pimpinelli, 2004; Valente et al., 2004; Cardoso et al., 2008; Nguyen, 2009; Li et al., 2011; Sena et al., 2011; Flores, 2013b, Ben Bettaieb et al., 2015).

The fundamental principle of the EAS method consists in the addition of an extra enhanced assumed strain field $\widetilde{\mathbf{E}}^{\alpha}$ to the displacement-based strain field $\mathbf{E}^{\text{com}}$ (also known as the compatible strain field), which leads to the following improved strain field $\mathbf{E}$:

$$\mathbf{E} = \mathbf{E}^{\text{com}} + \tilde{\mathbf{E}}^{\alpha} . \tag{1.24}$$

Substituting the modified strain field into the Hu–Washizu variational principle, the latter writes:

$$\Pi(\mathbf{u}, \mathbf{E}, \mathbf{S}) = \Pi_{\text{int}}(\mathbf{u}, \mathbf{E}, \mathbf{S}) - \Pi_{\text{ext}}(\mathbf{u}), \tag{1.25}$$

where the internal and external potentials are given by:

$$\begin{cases} \Pi_{\text{int}}(\mathbf{u}, \mathbf{E}, \mathbf{S}) = \int_{\Omega_e} W(\mathbf{E})\, \mathrm{d}\Omega_e + \int_{\Omega_e} \mathbf{S} : \tilde{\mathbf{E}}^{\alpha}\, \mathrm{d}\Omega_e \\ \Pi_{\text{ext}}(\mathbf{u}) = \int_{\Omega_e} \mathbf{u}\cdot\mathbf{b}\, \rho \mathrm{d}\Omega_e + \int_{\mathrm{S_e}} \mathbf{u}\cdot\mathbf{t}\, \mathrm{dS}_e \end{cases}, \tag{1.26}$$

where $\mathbf{u}$ is the displacement field, $\mathbf{E}$ is the enhanced strain field and $\mathbf{S}$ is the stress field. $W(\mathbf{E})$ denotes the strain energy, while $\rho\mathbf{b}$ and $\mathbf{t}$ represent the body forces and the traction forces, respectively.

As suggested by Simo and Rifai (1990), the stress field $\mathbf{S}$ is eliminated from the above equation via the following orthogonality condition:

$$\int_{\Omega_e} \mathbf{S} : \tilde{\mathbf{E}}^{\alpha}\, \mathrm{d}\Omega_e = 0 , \tag{1.27}$$

which is analogous to that considered by Simo and Hughes (1986) for the ASM approach.

Accordingly, the first variation of Eq. (1.25) writes:

$$\begin{aligned} \delta\Pi(\mathbf{u}, \mathbf{E}, \mathbf{S}) &= \delta\Pi_{\text{int}}(\mathbf{u}, \mathbf{E}, \mathbf{S}) - \delta\Pi_{\text{ext}}(\mathbf{u}) \\ &= \int_{\Omega_e} \left(\delta\mathbf{E}^{\text{com}} + \delta\widetilde{\mathbf{E}}^{\alpha}\right) : \frac{\partial W(\mathbf{E})}{\partial \mathbf{E}}\, \mathrm{d}\Omega_e - \int_{\Omega_e} \delta\mathbf{u}\cdot\mathbf{b}\, \rho \mathrm{d}\Omega_e - \int_{\mathrm{S_e}} \delta\mathbf{u}\cdot\mathbf{t}\, \mathrm{dS}_e . \end{aligned} \tag{1.28}$$

The linearization of the above simplified form of the Hu–Washizu variational principle leads to the following system of equilibrium equations:

$$\begin{bmatrix} \mathbf{K}^{uu} & \mathbf{K}^{u\alpha} \\ \mathbf{K}^{\alpha u} & \mathbf{K}^{\alpha\alpha} \end{bmatrix} \begin{Bmatrix} \Delta\mathbf{d} \\ \Delta\boldsymbol{\alpha} \end{Bmatrix} = \begin{Bmatrix} \mathbf{f}^{\text{ext}} - \mathbf{f}^{u} \\ -\mathbf{f}^{\alpha} \end{Bmatrix}, \tag{1.29}$$

where $\mathbf{d}$ denotes the nodal displacements, and $\boldsymbol{\alpha}$ the enhancing parameters. The matrices involved in Eq. (1.29) include the classical displacement-based stiffness matrix $\mathbf{K}^{uu}$, the enhanced stiffness operator $\mathbf{K}^{\alpha\alpha}$, and the coupling stiffness matrices $\mathbf{K}^{\alpha u}$ and $\mathbf{K}^{u\alpha}$. The internal forces $\mathbf{f}^{u}$ and $\mathbf{f}^{\alpha}$ are associated with the displacement field and the enhanced field, respectively.

By solving the above equilibrium equations, the final condensed element stiffness matrix $\mathbf{K}_e$ can be obtained as:

$$\mathbf{K}_e = \mathbf{K}^{uu} - \mathbf{K}^{u\alpha} \cdot \left(\mathbf{K}^{\alpha\alpha}\right)^{-1} \cdot \mathbf{K}^{\alpha u}. \tag{1.30}$$

1.3.2.3 Assumed natural strain (ANS) method

The ANS method consists in interpolating the shear strains at specific locations instead of using the standard displacement-based strain field, which allows significantly reducing the shear and volumetric locking. Such interpolation, also known as the mixed-interpolation method, can be traced back to the work of Hughes and Tezduyar (1981) for Mindlin plates, and later extended to shell elements by Dvorkin and Bathe (1984). The ANS method has been widely applied for the improvement of various finite elements (see, e.g., Bathe and Dvorkin, 1986; Militello and Felippa, 1990a, 1990b; Hauptmann and Schweizerhof, 1998; Sze and Zhu, 1999; Sze and Yao, 2000; Sze and Chan, 2001; Kim and Kim, 2002; Vu-Quoc and Tan, 2003; Lee, 2004; Kim et al., 2005; Klinkel et al., 2006; Cardoso et al., 2008; Schwarze and Reese, 2009; Nguyen, 2009; Norachan et al., 2012; Edem and Gosling, 2012, 2013; Flores, 2013b; Caseiro et al., 2014, 2015).

In order to describe the basic concept of the ANS method, an isoparametric 8-node hexahedral solid–shell element is considered here, as illustrated in Fig. 1.8. It is well known that, for solid–shell elements, only displacements are taken as degrees of freedom and, thus, the local strain field $\mathbf{E}^{loc}$ can be related to the nodal displacements $\mathbf{d}^{loc}$ by the discrete gradient operator $\mathbf{B}$ as follows:

$$\mathbf{E}^{loc} = \mathbf{B} \cdot \mathbf{d}^{loc}, \tag{1.31}$$

where the local strain field $\mathbf{E}^{loc}$ can be expressed in the following vector form:

$$\mathbf{E}^{loc} = \left\{ E_{11}, E_{22}, E_{33}, E_{12}, E_{13}, E_{23} \right\}. \tag{1.32}$$

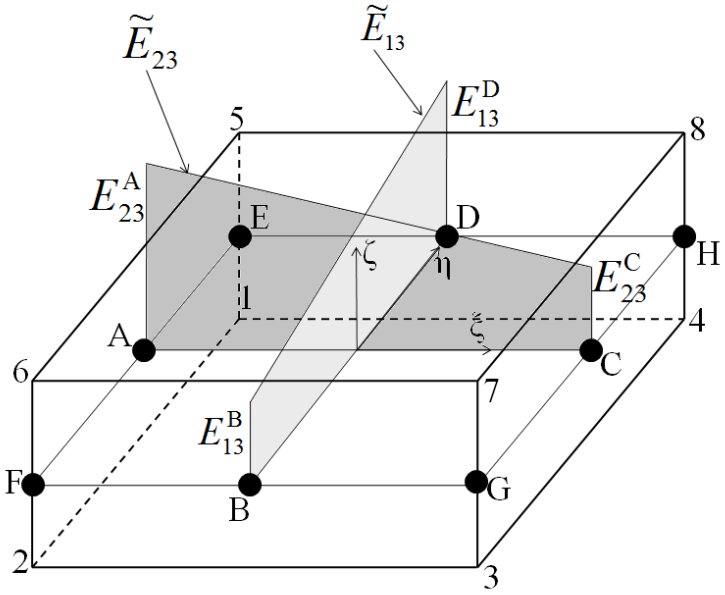


Figure 1.8. Re-interpolation of the transverse shear strain components by the ANS method (Nguyen, 2009).

Once the classical strain field is obtained using the standard displacement interpolation, it is straightforward to apply the ANS method to the current element. As shown in Fig. 1.8, a mid-plane is defined by four sampling points E, F, G and H with respect to the natural local coordinate system. To prevent the shear locking, two assumed transverse shear strains are interpolated as follows:

$$\begin{cases} \tilde{E}_{13} = P_1(\eta_B) E_{13}^{B} + P_2(\eta_D) E_{13}^{D} \\ \tilde{E}_{23} = Q_1(\xi_A) E_{23}^{A} + Q_2(\xi_C) E_{23}^{C} \end{cases}, \tag{1.33}$$

where E_{23}^{A}, E_{13}^{B}, E_{23}^{C} and E_{13}^{D} are the natural shear strains at the sampling points A, B, C and D, respectively, while P_1, P_2, Q_1 and Q_2 are the preselected interpolation functions, which can be defined using linear interpolations or higher-order polynomials (see, e.g., Dvorkin and Bathe, 1984; Kim et al., 2005; Vu-Quoc and Tan, 2003; Nguyen, 2009).

By replacing the original shear strains by the new assumed natural strains $\widetilde{E}_{13}$ and $\widetilde{E}_{23}$, the final strain vector becomes $\mathbf{E}^{loc} = \left\{E_{11}, E_{22}, E_{33}, E_{12}, \widetilde{E}_{13}, \widetilde{E}_{23}\right\}$. This new strain field leads to a new discrete gradient operator $\widetilde{\mathbf{B}}$, which aims at eliminating shear locking.

However, for curved thin structures, some particular locking effects, such as trapezoidal locking, could be caused by the transverse normal strain. Similar to the treatment of shear locking, the ANS method can also be applied to the transverse normal strain in order to eliminate such type of locking. The assumed transverse normal strain is interpolated through the natural strains at the four corner points E, F, G and H as depicted in Fig. 1.8, which writes:

$$\widetilde{E}_{33} = L_1(\xi_{\mathrm{E}}, \eta_{\mathrm{E}})E_{33}^{\mathrm{E}} + L_2(\xi_{\mathrm{F}}, \eta_{\mathrm{F}})E_{33}^{\mathrm{F}} + L_3(\xi_{\mathrm{G}}, \eta_{\mathrm{G}})E_{33}^{\mathrm{G}} + L_4(\xi_{\mathrm{H}}, \eta_{\mathrm{H}})E_{33}^{\mathrm{H}}, \tag{1.34}$$

where E_{33}^{E}, E_{33}^{F}, E_{33}^{G} and E_{33}^{H} are natural transverse normal strains at the sampling points E, F, G and H, respectively, while $L_1(\xi_{\mathrm{E}}, \eta_{\mathrm{E}})$, $L_2(\xi_{\mathrm{F}}, \eta_{\mathrm{F}})$, $L_3(\xi_{\mathrm{G}}, \eta_{\mathrm{G}})$ and $L_4(\xi_{\mathrm{H}}, \eta_{\mathrm{H}})$ are the corresponding interpolation functions (see, e.g., Vu-Quoc and Tan, 2003; Kim et al., 2005; Nguyen, 2009).

1.3.2.4 Mixed (or combined) formulations

Although the above approaches have been introduced and discussed separately (i.e., the RI or the SRI, the ASM technique, the EAS method and the ANS strategy), they are sometimes combined together in the formulation of solid–shell elements, which improves further their performance. This strategy of combination of several approaches is sometimes denoted as mixed formulation (a terminology that could be somewhat confusing, since mixed formulation may also refer to mixed variational principle, which is a different concept). As discussed above, the reduced integration technique (RI) allows improving the computational efficiency (and may also contribute to alleviating some locking effects), while the ASM, EAS and ANS methods introduce enhanced strain fields for the treatment of locking phenomena. Considerable attention has been devoted in the literature to this class of combined formulation approaches. For example, in the work of Li and Cescotto (1997), the RI method has been combined with the ASM for the development of an 8-node hexahedral element. Also, the combined approach, which couples the EAS and the ANS methods within a single formulation, has been applied to develop several locking-free solid–shell elements (see, e.g., Vu-Quoc and Tan, 2003; Cardoso et al., 2008; Nguyen et al., 2008; Nguyen, 2009; Ben Bettaieb et al., 2011; Duchêne et al., 2011; Ben Bettaieb et al., 2015). It has been shown that

these combined formulations could significantly improve the performance of solid–shell elements in the case of coarse meshes, which makes them very attractive for the 3D modeling of thin structures.

1.3.2.5 NURBS-based formulation

More recently, the Non-Uniform Rational B-Splines (NURBS) based elements, proposed by Hughes et al. (2005), have been developed by a number of researchers for the isogeometric analysis (IGA) of structures. Instead of using the conventional Lagrange polynomials, Hughes and co-workers (see, e.g., Hughes et al., 2005, 2008; Elguedj et al., 2008) introduced the NURBS functions in the finite elements to maintain exact geometry at all levels, without the necessity of subsequent communication with CAD user interface. Therefore, based on the superiority of the NURBS functions, several contributions have been devoted to the development of locking-free NURBS-based elements. For example, in order to avoid locking phenomena, Adam et al. (2014, 2015a, 2015b) combined the improved selective reduced integration technique with NURBS-based elements. Also, based on the work of Elguedj et al. (2008), Bouclier et al. (2013a, 2013b, 2015) developed NURBS-based solid–shell elements for the analysis of elastic and elasto-plastic structures under small strains. In the works of Caseiro et al. (2014, 2015), the authors combined the ANS method with NURBS functions in solid–shell elements for the nonlinear analysis of thin shell structures. Ambati and De Lorenzis (2016) applied NURBS-based solid–shell elements to the modeling of brittle and ductile fracture in shells. The literature review reveals that the NURBS-based technology can significantly improve the capabilities of finite elements and has promising prospective for future advances in solid–shell finite element formulations.

1.4 Proposed solid–shell elements (SHB family)

In the context of predictive and reliable simulations of thin 3D structures, our research group has been interested in the development of efficient solid–shell elements. In particular, for the simulation of sheet metal forming processes, where typical locking phenomena are commonly encountered (e.g., volumetric, transverse shear and thickness locking), the availability of finite elements capable of achieving accurate simulations, while maintaining a reasonable computational cost, is desirable. In the current work, a family of solid–shell elements (SHB) is proposed for the three-dimensional analysis of thin structures. This family

consists of four solid–shell elements, namely a linear six-node prismatic element denoted SHB6 and a linear eight-node hexahedral element denoted SHB8PS, and their quadratic counterparts SHB15 and SHB20, respectively. The formulation of these elements is based on a purely three-dimensional approach, with displacements as the only degrees of freedom. Moreover, a special direction is chosen to represent the thickness, along which a user-defined number of integration points are arranged, which allows the 3D modeling of thin structures with a single layer of elements. The various locking phenomena are alleviated using the RI scheme combined with the ASM approach. The resulting SHB elements represent an interesting alternative to traditional shell and solid elements, in particular for the simulation of complex sheet metal forming processes, involving large strain, anisotropic plasticity, and double-sided contact.

The first solid–shell element, which has been developed within this SHB element family, has been originally formulated by Abed-Meraim and Combescure (2002) and consists of an eight-node hexahedral element denoted SHB8PS. Its formulation was subsequently improved in Abed-Meraim and Combescure (2009), especially in terms of locking reduction, while the hourglass modes were efficiently controlled by implementing a new stabilization procedure. The performance of the SHB8PS element was shown through a representative set of selective benchmark tests as well as through sheet metal forming processes involving large strains, anisotropic plasticity, and contact (see Abed-Meraim and Combescure, 2009; Salahouelhadj et al., 2012). Then, a six-node prismatic solid–shell element denoted SHB6 has been developed by Trinh et al. (2011), as a complement to the SHB8PS element for the modeling of complex geometries whose meshing requires the combination of hexahedral and prismatic elements. Although the performance of the SHB6 element is reasonably good in the whole, its convergence rate remains slower than that of the SHB8PS, and it requires finer meshes to obtain accurate solutions. More recently, the quadratic counterparts of the above hexahedral and prismatic solid–shell elements have been developed by Abed-Meraim et al. (2013), in order to improve the overall performance and convergence rate. These quadratic versions consist of a twenty-node hexahedral element, denoted SHB20, and a fifteen-node prismatic element, denoted SHB15. Likewise, their formulation is based on a fully three-dimensional approach with an in-plane reduced-integration rule. The performance of these quadratic elements has been evaluated by Abed-Meraim et al. (2013) within the framework of small strain and elastic benchmark problems. In the current PhD works, however, these SHB

formulations have been extended by coupling them with various advanced constitutive models within the framework of large-strain anisotropic elasto-plasticity for metallic materials, as well as orthotropic constitutive laws for multilayered composite materials. Another part of the current contribution consists of the extension of the SHB element formulations to the framework of explicit dynamic analysis. All of these resulting extended formulations for the SHB elements have been implemented into ABAQUS static/implicit and dynamic/explicit software packages, which provide an effective library of finite elements capable of modeling complex and challenging structural problems, such as sheet metal forming processes and impact/crash problems. The extended formulations of these SHB elements will be detailed in Chapter 2, while their performance will be evaluated in Chapters 3 and 4, through various nonlinear benchmark tests and complex sheet metal forming simulations (see Wang et al., 2015, 2016, 2017a, 2017b).

Conclusion

In this chapter, a literature review on the development of finite element technologies has been briefly presented. In particular, it is revealed that for the modeling of thin structural problems, the existing conventional solid and shell elements may experience various locking phenomena. In order to obtain more accurate and reliable simulation results, additional numerical techniques need to be combined with these classical formulations. Concurrently, the concept of solid–shell elements has emerged as an interesting alternative to classical solid and shell formulations. This relatively recent solid–shell concept combines the advantages of both solid and shell FE formulations. In order to alleviate the various locking phenomena, and to significantly enhance their performance, advanced numerical techniques need to be combined with the formulation of these solid–shell elements, such as the ASM approach, the EAS method or the ANS strategy. In general, the formulation of solid–shell elements is based on a purely three-dimensional approach, with displacements as the only degrees of freedom. The resulting solid–shell elements are usually computationally efficient, since only a single layer of elements with an arbitrary (user-defined) number of through-thickness integration points is required for the 3D modeling of thin structures. The detailed formulations of the proposed SHB solid–shell elements are presented in the following chapter.

Chapter 2

Formulation of the SHB solid–shell elements

Introduction

In this chapter, a family of assumed-strain based solid–shell elements (SHB elements) is presented within a unified formulation for the 3D analysis of both quasi-static and dynamic thin structural problems. This family consists of a linear eight-node hexahedral element (SHB8PS) and a linear six-node prismatic element (SHB6), and their quadratic counterparts (SHB20) and (SHB15), respectively. These SHB elements are based on a fully three-dimensional (3D) formulation with only displacements as degrees of freedom. The reduced-integration scheme together with the assumed-strain method are adopted in the formulation of the SHB elements in order to prevent most locking phenomena, which makes them very attractive and competitive for the 3D analysis of thin structures.

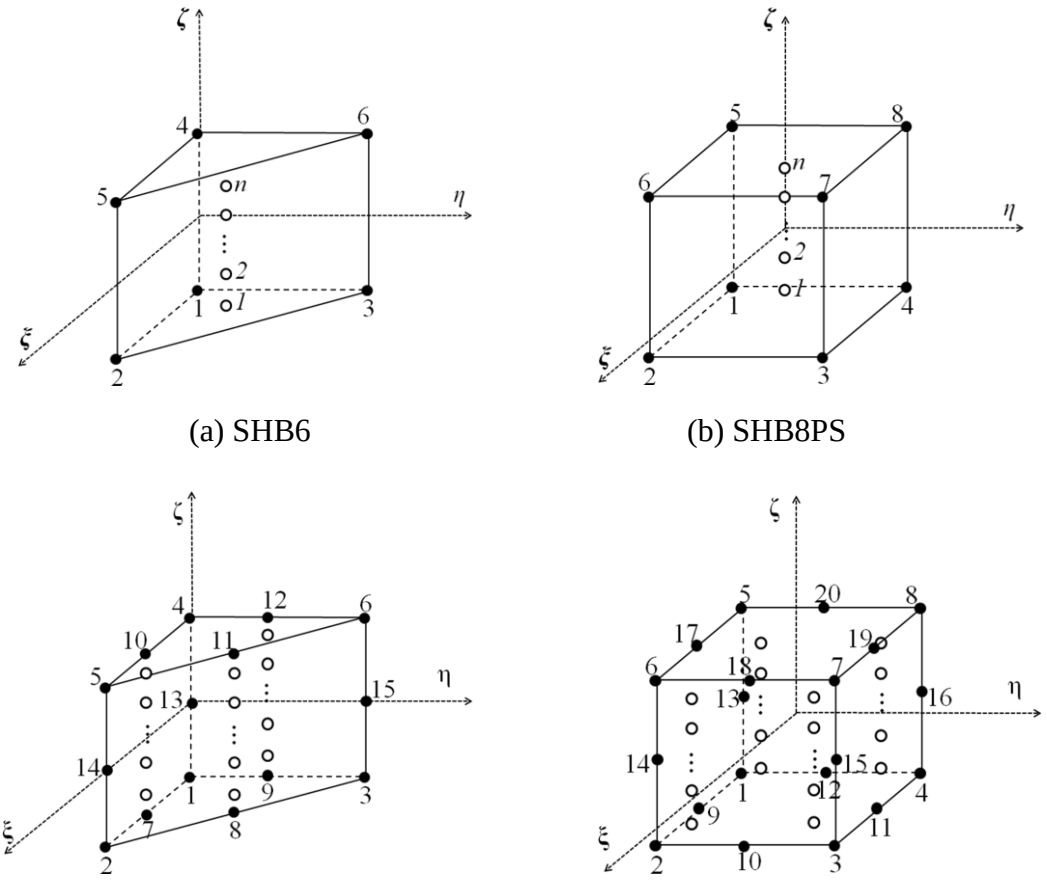
In the formulation of the SHB elements, several local frames are defined and used in their numerical implementation. Taking advantage of the unified formulation intended for this family of solid–shell elements as well as the modularity in their finite element implementation, various constitutive models can be coupled with these SHB elements, in a straightforward and systematic way, which include isotropic behavior, orthotropic elastic behavior for laminated composite materials, and anisotropic plastic behavior for metallic materials. All of the SHB elements have been implemented into the ABAQUS dynamic/explicit and static/implicit software packages for the 3D modeling of thin structural problems.

2.1 General formulation for quasi-static/implicit analysis

2.1.1 Geometry and integration points

Figure 2.1 illustrates the reference geometry as well as the location of integration points for the SHB solid–shell elements. As shown in this figure, all the SHB elements are based on the

classical 3D approach; however, a special direction ζ is chosen as the thickness direction. Along this direction, a user-defined number of integration points are arranged. The coordinates and associated weights for the integration points are obtained using the classical Gauss distribution method (see, e.g., Zienkiewicz et al., 2006).



(a) SHB6 (b) SHB8PS

(c) SHB15 (d) SHB20

Figure 2.1. Reference geometry and location of integration points for the SHB solid–shell elements: a) linear prismatic SHB6 element; b) linear hexahedral SHB8PS element; c) quadratic prismatic SHB15 element; and d) quadratic hexahedral SHB20 element.

2.1.2 Interpolation of the SHB elements

Using the classical isoparametric approach, the SHB solid–shell elements adopt the conventional shape functions N_I for the standard prismatic and hexahedral elements, which are described in details in Appendix A. The spatial coordinates x_i and displacement u_i within the element are expressed as functions of the nodal coordinates x_{iI} and the nodal displacements d_{iI}, respectively

$$x_i = x_{iI} N_I(\xi,\eta,\zeta) = \sum_{I=1}^{n} x_{iI} N_I(\xi,\eta,\zeta), \tag{2.1}$$

$$u_i = d_{iI} N_I(\xi,\eta,\zeta), \tag{2.2}$$

where the lowercase subscript i varies from 1 to 3, and represents the spatial coordinate directions, while the uppercase subscript I varies from 1 to n, with n being the number of element nodes (i.e., $n=6$ for the SHB6 element, $n=8$ for the SHB8PS element, $n=15$ for the SHB15 element, and $n=20$ for the SHB20 element). Note that in Eq. (2.2), the convention of implied summation over repeated indices has been used, which will be also adopted in the sequel.

2.1.3 Strain-displacement relationship and discrete gradient operator

Based on the interpolation of the displacement field (see Eq. (2.2)), the linear part $\boldsymbol{\varepsilon}$ of the strain tensor is defined by the following relationship:

$$\varepsilon_{ij} = \frac{1}{2}\left(u_{i,j} + u_{j,i}\right) = \frac{1}{2}\left(d_{iI} N_{I,j} + d_{jI} N_{I,i}\right). \tag{2.3}$$

The combination of Eqs. (2.1) and (2.2), along with the expression of the shape functions $N_I(\xi,\eta,\zeta)$, allows us to expand the displacement field in the following form:

$$u_i = a_{0i} + a_{1i}x_1 + a_{2i}x_2 + a_{3i}x_3 + c_{1i}h_1 + c_{2i}h_2 + \cdots + + c_{\alpha i}h_\alpha, \tag{2.4}$$

where h_α are functions of the coordinates ξ, η, ζ, in the reference coordinate system, and α varies from 1 to 2 for the SHB6 element, from 1 to 4 for the SHB8PS element, from 1 to 11 for the SHB15 element, and from 1 to 16 for the SHB20 element (the detailed expressions of functions h_α are given in Appendix B).

By evaluating Eq. (2.4) at all nodes for each SHB element, one obtains the following equation system:

$$\mathbf{d}_i = a_{0i}\mathbf{s} + a_{1i}\mathbf{x}_1 + a_{2i}\mathbf{x}_2 + a_{3i}\mathbf{x}_3 + c_{1i}\mathbf{h}_1 + c_{2i}\mathbf{h}_2 + \cdots + c_{\alpha i}\mathbf{h}_\alpha, \tag{2.5}$$

where $\mathbf{d}_i^T = \left(d_{i1}, d_{i2}, d_{i3}, \cdots, d_{in}\right)$ represent the nodal displacement vectors, and $\mathbf{x}_i^T = \left(x_{i1}, x_{i2}, x_{i3}, \cdots, x_{in}\right)$ are the nodal coordinate vectors. The constant vector $\mathbf{s}^T = \left(1, 1, \cdots, 1\right)$ is a n-component constant vector, where n represents the number of element

nodes (as defined in Subsection 2.1.2). As to vectors $\mathbf{h}_\alpha$, these are constant vectors whose expressions can be easily obtained by evaluating the h_α functions at the element nodes in the reference coordinate system (ξ,η,ζ).

By introducing the Hallquist vectors $\mathbf{b}_i = \dfrac{\partial \mathbf{N}}{\partial x_i}_{|\xi=\eta=\zeta=0}$ (Hallquist, 1983), with $\mathbf{N}$ the vector whose components are the shape functions N_I, and by applying some preliminarily established orthogonality conditions (see details in Appendix C for all SHB elements), the expression of the unknown constants a_{ji} and $c_{\alpha i}$ in Eqs. (2.4) and (2.5) can be obtained as follows:

$$a_{ji} = \mathbf{b}_j^T \cdot \mathbf{d}_i, \qquad c_{\alpha i} = \boldsymbol{\gamma}_\alpha^T \cdot \mathbf{d}_i, \tag{2.6}$$

where $\boldsymbol{\gamma}_\alpha = \dfrac{1}{k}\left[\mathbf{h}_\alpha - \sum_{j=1}^{3}\left(\mathbf{h}_\alpha^T \cdot \mathbf{x}_j\right)\mathbf{b}_j\right]$ for the linear prismatic and hexahedral SHB elements (with $k=2$ for the SHB6 element, and $k=8$ for the SHB8PS element), while the expressions of vectors $\boldsymbol{\gamma}_\alpha$ for the quadratic prismatic and hexahedral SHB elements (i.e., SHB15 and SHB20) are a little more complex and are given in Appendix C.

Substituting Eq. (2.6) into Eq. (2.4), one obtains the following convenient expression for the displacement field:

$$u_i = a_{0i} + \left(x_1\mathbf{b}_1^T + x_2\mathbf{b}_2^T + x_3\mathbf{b}_3^T + h_1\boldsymbol{\gamma}_1^T + \cdots + h_\alpha\boldsymbol{\gamma}_\alpha^T\right)\cdot \mathbf{d}_i. \tag{2.7}$$

By differentiating the above equation with respect to x_j, the displacement gradient is obtained as follows:

$$u_{i,j} = \left(\mathbf{b}_j^T + \sum_\alpha h_{\alpha,j}\boldsymbol{\gamma}_\alpha^T\right)\cdot \mathbf{d}_i = \left(\mathbf{b}_j^T + h_{\alpha,j}\boldsymbol{\gamma}_\alpha^T\right)\cdot \mathbf{d}_i. \tag{2.8}$$

Finally, the expression of the strain field, which is related to the nodal displacements by the discrete gradient operator $\mathbf{B}$, is given by

$$\nabla_s(\mathbf{u}) = \begin{bmatrix} u_{x,x} \\ u_{y,y} \\ u_{z,z} \\ u_{x,y}+u_{y,x} \\ u_{y,z}+u_{z,y} \\ u_{x,z}+u_{z,x} \end{bmatrix} = \mathbf{B}\cdot\mathbf{d} = \mathbf{B}\cdot\begin{bmatrix}\mathbf{d}_x \\ \mathbf{d}_y \\ \mathbf{d}_z\end{bmatrix}, \tag{2.9}$$

where the discrete gradient operator $\mathbf{B}$ takes the following matrix form:

$$\mathbf{B}=\begin{bmatrix} \mathbf{b}_x^T+h_{\alpha,x}\boldsymbol{\gamma}_\alpha^T & \mathbf{0} & \mathbf{0} \\ \mathbf{0} & \mathbf{b}_y^T+h_{\alpha,y}\boldsymbol{\gamma}_\alpha^T & \mathbf{0} \\ \mathbf{0} & \mathbf{0} & \mathbf{b}_z^T+h_{\alpha,z}\boldsymbol{\gamma}_\alpha^T \\ \mathbf{b}_y^T+h_{\alpha,y}\boldsymbol{\gamma}_\alpha^T & \mathbf{b}_x^T+h_{\alpha,x}\boldsymbol{\gamma}_\alpha^T & \mathbf{0} \\ \mathbf{0} & \mathbf{b}_z^T+h_{\alpha,z}\boldsymbol{\gamma}_\alpha^T & \mathbf{b}_y^T+h_{\alpha,y}\boldsymbol{\gamma}_\alpha^T \\ \mathbf{b}_z^T+h_{\alpha,z}\boldsymbol{\gamma}_\alpha^T & \mathbf{0} & \mathbf{b}_x^T+h_{\alpha,x}\boldsymbol{\gamma}_\alpha^T \end{bmatrix}. \tag{2.10}$$

2.1.4 Variational principle

The extension of the weak form of the Hu–Washizu variational principle to nonlinear solid mechanics was introduced by Fish and Belytschko (1988). For a single finite element, this three-field variational principle is given by:

$$\delta\pi(\mathbf{v},\dot{\bar{\boldsymbol{\varepsilon}}},\bar{\boldsymbol{\sigma}})=\int_{\Omega_e}\delta\dot{\bar{\boldsymbol{\varepsilon}}}^T\cdot\boldsymbol{\sigma}\,d\Omega+\delta\int_{\Omega_e}\bar{\boldsymbol{\sigma}}^T\cdot\left(\nabla_s(\mathbf{v})-\dot{\bar{\boldsymbol{\varepsilon}}}\right)d\Omega-\delta\dot{\mathbf{d}}^T\cdot\mathbf{f}^{\text{ext}}=0\,, \tag{2.11}$$

where δ denotes a variation, $\mathbf{v}$ the velocity field, $\dot{\bar{\boldsymbol{\varepsilon}}}$ the assumed-strain rate, $\bar{\boldsymbol{\sigma}}$ the interpolated stress, $\boldsymbol{\sigma}$ the Cauchy stress tensor evaluated by the constitutive law, $\dot{\mathbf{d}}$ the nodal velocities, $\mathbf{f}^{\text{ext}}$ the external nodal forces and $\nabla_s(\mathbf{v})$ the symmetric part of the velocity gradient.

The assumed-strain formulation of the SHB solid–shell elements is based on the simplified form of the Hu–Washizu mixed variational principle, as suggested by Simo and Hughes (1986), which writes at the element level

$$\delta\pi(\dot{\bar{\boldsymbol{\varepsilon}}})=\int_{\Omega_e}\delta\dot{\bar{\boldsymbol{\varepsilon}}}^T\cdot\boldsymbol{\sigma}\,d\Omega-\delta\dot{\mathbf{d}}^T\cdot\mathbf{f}^{\text{ext}}=0. \tag{2.12}$$

It is worth noting that in the formulation of the linear prismatic and hexahedral solid–shell elements (i.e., SHB6 and SHB8PS, respectively), the assumed-strain rate $\dot{\bar{\boldsymbol{\varepsilon}}}$ is expressed in terms of a projected matrix $\bar{\mathbf{B}}$, which is derived from the classical $\mathbf{B}$ operator (see Abed-Meraim and Combescure, 2009; Trinh et al., 2011), in order to eliminate most locking phenomena. For the quadratic solid–shell elements (i.e., SHB15 and SHB20), however, no significant locking has been revealed when evaluating their performance on a selective and representative set of benchmark problems (see Abed-Meraim et al., 2013; Wang et al., 2017a; Wang et al., 2017b). Consequently, no projection is applied to the discrete gradient operator $\mathbf{B}$ for the quadratic SHB15 and SHB20 solid–shell elements.

For the sake of simplicity, we denote by a unified symbol $\bar{\mathbf{B}}$ the discrete gradient operator that is obtained by projection of the classical $\mathbf{B}$ operator onto an appropriate sub-space for the

linear SHB elements, which simply reduces to the classical $\mathbf{B}$ operator for the quadratic SHB elements. Accordingly, the expression of the assumed-strain rate can be expressed as

$$\dot{\bar{\boldsymbol{\varepsilon}}}(x,t) = \bar{\mathbf{B}} \cdot \dot{\mathbf{d}}. \tag{2.13}$$

Substituting the above equation into the simplified form of the Hu–Washizu variational principle, the expressions of the element stiffness matrix $\mathbf{K}_e$ and internal force vector $\mathbf{f}^{\text{int}}$ are obtained as follows:

$$\begin{cases} \mathbf{K}_e = \int_{\Omega_e} \bar{\mathbf{B}}^T \cdot \mathbf{C}^{\text{ep}} \cdot \bar{\mathbf{B}} \, d\Omega + \mathbf{K}_{\text{geom}} \\ \mathbf{f}^{\text{int}} = \int_{\Omega_e} \bar{\mathbf{B}}^T \cdot \boldsymbol{\sigma}(\dot{\boldsymbol{\varepsilon}}) \, d\Omega \end{cases}, \tag{2.14}$$

where $\mathbf{C}^{\text{ep}}$ is the fourth-order elasto-plastic tangent modulus, whose expression will be detailed in the Subsection devoted to the constitutive modeling, while $\mathbf{K}_{\text{geom}}$ is the geometric stiffness matrix, which is derived from the linearization of the virtual work principle and which is due to the nonlinear (quadratic) part of the strain tensor. Adopting the vector form for both the stress tensor $\boldsymbol{\sigma}$ and the quadratic part of the strain tensor $\boldsymbol{\varepsilon}^Q(\delta\mathbf{d}, \Delta\mathbf{d})$, the geometric stiffness matrix can be expressed as:

$$\mathbf{K}_{\text{geom}} = \int_{\Omega_e} \boldsymbol{\sigma}^T \cdot \boldsymbol{\varepsilon}^Q(\delta\mathbf{d}, \Delta\mathbf{d}) \, d\Omega, \tag{2.15}$$

where the components of $\boldsymbol{\varepsilon}^Q(\delta\mathbf{d}, \Delta\mathbf{d})$ are computed by $\varepsilon_{ij}^Q(\delta\mathbf{d}, \Delta\mathbf{d}) = \delta\mathbf{d}^T \cdot \mathbf{B}_{ij}^Q \cdot \Delta\mathbf{d}$, in which $\mathbf{B}_{ij}^Q$ represents the quadratic discrete gradient operator given by:

$$\mathbf{B}_{ij}^Q = \begin{bmatrix} \left(\mathbf{b}_i + h_{\alpha,i}\boldsymbol{\gamma}_\alpha\right)\left(\mathbf{b}_j^T + h_{\alpha,j}\boldsymbol{\gamma}_\alpha^T\right) & \mathbf{0} & \mathbf{0} \\ \mathbf{0} & \left(\mathbf{b}_i + h_{\alpha,i}\boldsymbol{\gamma}_\alpha\right)\left(\mathbf{b}_j^T + h_{\alpha,j}\boldsymbol{\gamma}_\alpha^T\right) & \mathbf{0} \\ \mathbf{0} & \mathbf{0} & \left(\mathbf{b}_i + h_{\alpha,i}\boldsymbol{\gamma}_\alpha\right)\left(\mathbf{b}_j^T + h_{\alpha,j}\boldsymbol{\gamma}_\alpha^T\right) \end{bmatrix}. \tag{2.16}$$

Then, the contribution $\mathbf{k}_{\boldsymbol{\sigma}}(P_I)$, at the integration point P_I, to the overall geometric stiffness matrix can be expressed as:

$$\begin{aligned} \mathbf{k}_{\boldsymbol{\sigma}}(P_I) = {} & \sigma_{xx}(P_I)\mathbf{B}_{xx}^Q(P_I) + \sigma_{yy}(P_I)\mathbf{B}_{yy}^Q(P_I) + \sigma_{zz}(P_I)\mathbf{B}_{zz}^Q(P_I) + \sigma_{xy}(P_I)\left(\mathbf{B}_{xy}^Q(P_I) + \mathbf{B}_{yx}^Q(P_I)\right) \\ & + \sigma_{yz}(P_I)\left(\mathbf{B}_{yz}^Q(P_I) + \mathbf{B}_{zy}^Q(P_I)\right) + \sigma_{xz}(P_I)\left(\mathbf{B}_{xz}^Q(P_I) + \mathbf{B}_{zx}^Q(P_I)\right) \end{aligned}. \tag{2.17}$$

Finally, the geometric stiffness matrix $\mathbf{K}_{geom}$ can be obtained using the contribution of all integration points as:

$$\mathbf{K}_{\text{geom}} = \sum_{I=1}^{n_{\text{int}}} \omega(P_I) J(P_I) \mathbf{k}_{\boldsymbol{\sigma}}(P_I) . \tag{2.18}$$

It is worth noting that, due to the particular location of the integration points (i.e., along the thickness direction), six hourglass modes are revealed in the linear hexahedral SHB8PS element (see Abed-Meraim and Combescure, 2009). To avoid hourglass-type instabilities, an extra stabilization procedure is required in the formulation of the SHB8PS element in order to control these spurious zero-energy modes. This leads to an additional stabilization stiffness matrix $\mathbf{K}_{\text{STAB}}$, and additional stabilization internal forces $\mathbf{f}_{\text{STAB}}$. The detailed formulation regarding this stabilization procedure will be given in Subsection 2.3.

2.2 Definition of local frames

The SHB solid–shell elements are formulated within the framework of large displacements and rotations. They can also be combined with various types of behavior laws, including advanced large-strain anisotropic constitutive equations for metallic materials. To this end, several local frames need to be introduced with respect to the global coordinate system, as illustrated in Fig. 2.2. The first type of local frame, which is denoted as the "element frame", is attached to the element mid-plane associated with each integration point. In these local physical coordinate systems, where the ζ-coordinate represents the thickness direction, the fourth-order elasticity tensor is specified. The second type of local physical coordinate system is the so-called "material frame", which is introduced to define the anisotropic plastic behavior in the case of metallic materials. The time integration of the large-strain anisotropic elasto-plastic constitutive equations, which is achieved at each integration point, also uses this local material frame in order to satisfy the objectivity (material invariance) requirements. Additionally, a third local coordinate system, designated as "co-rotational frame", is defined at the element level in order to simplify the calculation of the stabilization terms involved in the expression of both the stiffness matrix and the internal forces, in the particular case of the SHB8PS element.

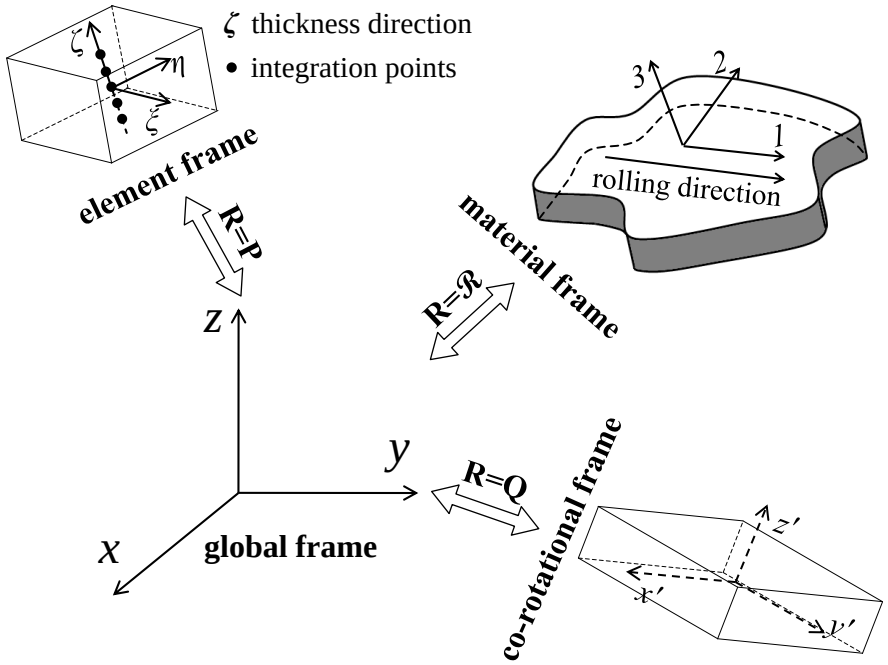


Figure 2.2. Illustration of the local frames used in the formulation of the SHB solid–shell elements.

For a given rotation matrix $\mathbf{R}$, corresponding to one of the three local coordinate systems described above, the tensor variables can be transformed from the global coordinate system into the local coordinate frame by using the following classical formulas:

$$\begin{cases} \mathbf{a}^{\text{loc}} = \mathbf{R}^T \cdot \mathbf{a}^{\text{glo}} \cdot \mathbf{R} \\ \mathbf{A}^{\text{loc}} = \mathbf{R}^T \cdot \mathbf{R}^T \cdot \mathbf{A}^{\text{glo}} \cdot \mathbf{R} \cdot \mathbf{R}^{'} \end{cases} \tag{2.19}$$

where $\mathbf{a}^{\text{loc}}$ and $\mathbf{A}^{\text{loc}}$ represent second-order, respectively, fourth-order tensors expressed in the local coordinate system, while $\mathbf{a}^{\text{glo}}$ and $\mathbf{A}^{\text{glo}}$ are their expressions in the global coordinate frame.

2.3 Special treatments for the linear SHB elements

In the two previous sections, the formulations of the SHB elements for quasi-static/implicit analysis have been introduced in a general form. It has also been mentioned above that some special numerical treatments are needed in the formulation of the low-order SHB elements (i.e., SHB6 and SHB8PS elements) in order to further improve their performances. In the following Subsections, the projection technique for the SHB6 and SHB8PS elements and the stabilization procedure for the SHB8PS element will be described.

2.3.1 Assumed-strain projection for the SHB6 element

In order to eliminate different locking phenomena and hence to further improve the performance of the linear prismatic SHB6 element, the classical discrete gradient operator $\mathbf{B}$ is projected onto an appropriate subspace, which leads to a modified discrete gradient operator $\overline{\mathbf{B}}$.

It has been shown in Trinh et al. (2011) that the main locking phenomenon in the SHB6 element is due to the transverse shear strain. To eliminate this transverse shear locking, the original discrete gradient operator $\mathbf{B}$ is first decomposed into two parts as follows:

$$\mathbf{B} = \mathbf{B}_1 + \mathbf{B}_2, \tag{2.20}$$

where the operator $\mathbf{B}_1$ contains the gradients associated with the membrane strains as well as the normal strain, while the remaining gradients associated with the transverse shear strains are included in the operator $\mathbf{B}_2$. Their expressions are given by:

$$\mathbf{B}_1 = \begin{bmatrix} \mathbf{b}_x^T + h_{\alpha,x}\boldsymbol{\gamma}_\alpha^T & \mathbf{0} & \mathbf{0} \\ \mathbf{0} & \mathbf{b}_y^T + h_{\alpha,y}\boldsymbol{\gamma}_\alpha^T & \mathbf{0} \\ \mathbf{0} & \mathbf{0} & \mathbf{b}_z^T + h_{\alpha,z}\boldsymbol{\gamma}_\alpha^T \\ \mathbf{b}_y^T + h_{\alpha,y}\boldsymbol{\gamma}_\alpha^T & \mathbf{b}_x^T + h_{\alpha,x}\boldsymbol{\gamma}_\alpha^T & \mathbf{0} \\ \mathbf{0} & \mathbf{0} & \mathbf{0} \\ \mathbf{0} & \mathbf{0} & \mathbf{0} \end{bmatrix}, \tag{2.21}$$

$$\mathbf{B}_2 = \begin{bmatrix} \mathbf{0} & \mathbf{0} & \mathbf{0} \\ \mathbf{0} & \mathbf{0} & \mathbf{0} \\ \mathbf{0} & \mathbf{0} & \mathbf{0} \\ \mathbf{0} & \mathbf{0} & \mathbf{0} \\ \mathbf{0} & \mathbf{b}_z^T + h_{\alpha,z}\boldsymbol{\gamma}_\alpha^T & \mathbf{b}_y^T + h_{\alpha,y}\boldsymbol{\gamma}_\alpha^T \\ \mathbf{b}_z^T + h_{\alpha,z}\boldsymbol{\gamma}_\alpha^T & \mathbf{0} & \mathbf{b}_x^T + h_{\alpha,x}\boldsymbol{\gamma}_\alpha^T \end{bmatrix}. \tag{2.22}$$

Then, the second part $\mathbf{B}_2$ of the discrete gradient operator is projected as follows, introducing a shear scaling factor ω:

$$\overline{\mathbf{B}}_2 = \omega \mathbf{B}_2, \tag{2.23}$$

where ω is a shear scaling factor, whose value is chosen so that the shear locking is attenuated.

Using the above decomposition and projection for the discrete gradient operator, the element stiffness matrix $\mathbf{K}_e$ can be computed as:

$$\mathbf{K}_e = \mathbf{K}_1 + \mathbf{K}_2 , \tag{2.24}$$

where

$$\mathbf{K}_1 = \int_{\Omega_e} \mathbf{B}_1^T \cdot \mathbf{C}^{\text{ep}} \cdot \mathbf{B}_1 \, d\Omega , \tag{2.25}$$

and

$$\mathbf{K}_2 = \int_{\Omega_e} \mathbf{B}_1^T \cdot \mathbf{C}^{\text{ep}} \cdot \bar{\mathbf{B}}_2 \, d\Omega + \int_{\Omega_e} \bar{\mathbf{B}}_2^T \cdot \mathbf{C}^{\text{ep}} \cdot \mathbf{B}_1 \, d\Omega + \int_{\Omega_e} \bar{\mathbf{B}}_2^T \cdot \mathbf{C}^{\text{ep}} \cdot \bar{\mathbf{B}}_2 \, d\Omega . \tag{2.26}$$

The particular decomposition of the discrete gradient operator **B** (see Eqs. (2.20), (2.21) and (2.22)), together with the projection defined by Eq. (2.23), yields a simplified form for the projected stiffness matrix $\mathbf{K}_2$, in which the cross-terms vanish. The final element stiffness matrix $\mathbf{K}_e$ becomes:

$$\mathbf{K}_e = \mathbf{K}_1 + \mathbf{K}_2 = \int_{\Omega_e} \mathbf{B}_1^T \cdot \mathbf{C}^{\text{ep}} \cdot \mathbf{B}_1 \, d\Omega + \int_{\Omega_e} \bar{\mathbf{B}}_2^T \cdot \mathbf{C}^{\text{ep}} \cdot \bar{\mathbf{B}}_2 \, d\Omega . \tag{2.27}$$

To this SHB6 stiffness matrix given by Eq. (2.27), one should add the associated geometric stiffness matrix, whose formulation has already been given in Subsection 2.1.4. In practice, the value of the shear scaling factor ω in Eq. (2.23) is identified through numerical experiments. In the current implementation of the SHB6 element, the value of such a factor is taken equal to one half, which results in reasonably good performance for the element over the variety of popular benchmark problems that have been tested.

Note also that, due to the in-plane reduced-integration scheme adopted for the SHB6 element, zero-energy hourglass modes are likely to appear. Fortunately, no such spurious modes have been revealed through the benchmark tests. Therefore, no stabilization procedure is required for the SHB6 element, which has also been shown in Trinh et al. (2011) through an element rank deficiency analysis.

2.3.2 Stabilization procedure and assumed-strain projection for the SHB8PS element

The in-plane reduced-integration (RI) scheme used in the formulation of the SHB8PS element aims to enhance the computational efficiency and to avoid some locking phenomena. However, it is well known that the use of RI techniques may result in spurious zero-energy

(hourglass) modes, due to rank deficiency of the resulting stiffness matrix. In Abed-Meraim and Combescure (2009), six hourglass modes have been identified for the SHB8PS element. Following the approach proposed by Belytschko and Bindeman (1993), a stabilization stiffness matrix has been formulated and added to the SHB8PS element stiffness matrix $\mathbf{K}_e$ in order to control the associated hourglass modes.

Similar to the above-mentioned projection technique for the SHB6 element, the starting point of the stabilization approach for the SHB8PS element is also the decomposition of the classical discrete gradient operator $\mathbf{B}$ (see its expression in Eq. (2.10)) into two parts, as follows:

$$\mathbf{B} = \mathbf{B}_{12} + \mathbf{B}_{34}, \tag{2.28}$$

where the operators $\mathbf{B}_{12}$ and $\mathbf{B}_{34}$ take the following form:

$$\mathbf{B}_{12} = \begin{bmatrix} \mathbf{b}_x^T + \sum_{\alpha=1}^{2} h_{\alpha,x}\boldsymbol{\gamma}_\alpha^T & \mathbf{0} & \mathbf{0} \\ \mathbf{0} & \mathbf{b}_y^T + \sum_{\alpha=1}^{2} h_{\alpha,y}\boldsymbol{\gamma}_\alpha^T & \mathbf{0} \\ \mathbf{0} & \mathbf{0} & \mathbf{b}_z^T + \sum_{\alpha=1}^{2} h_{\alpha,z}\boldsymbol{\gamma}_\alpha^T \\ \mathbf{b}_y^T + \sum_{\alpha=1}^{2} h_{\alpha,y}\boldsymbol{\gamma}_\alpha^T & \mathbf{b}_x^T + \sum_{\alpha=1}^{2} h_{\alpha,x}\boldsymbol{\gamma}_\alpha^T & \mathbf{0} \\ \mathbf{0} & \mathbf{b}_z^T + \sum_{\alpha=1}^{2} h_{\alpha,z}\boldsymbol{\gamma}_\alpha^T & \mathbf{b}_y^T + \sum_{\alpha=1}^{2} h_{\alpha,y}\boldsymbol{\gamma}_\alpha^T \\ \mathbf{b}_z^T + \sum_{\alpha=1}^{2} h_{\alpha,z}\boldsymbol{\gamma}_\alpha^T & \mathbf{0} & \mathbf{b}_x^T + \sum_{\alpha=1}^{2} h_{\alpha,x}\boldsymbol{\gamma}_\alpha^T \end{bmatrix}, \tag{2.29}$$

$$\mathbf{B}_{34} = \begin{bmatrix} \sum_{\alpha=3}^{4} h_{\alpha,x}\boldsymbol{\gamma}_\alpha^T & \mathbf{0} & \mathbf{0} \\ \mathbf{0} & \sum_{\alpha=3}^{4} h_{\alpha,y}\boldsymbol{\gamma}_\alpha^T & \mathbf{0} \\ \mathbf{0} & \mathbf{0} & \sum_{\alpha=3}^{4} h_{\alpha,z}\boldsymbol{\gamma}_\alpha^T \\ \sum_{\alpha=3}^{4} h_{\alpha,y}\boldsymbol{\gamma}_\alpha^T & \sum_{\alpha=3}^{4} h_{\alpha,x}\boldsymbol{\gamma}_\alpha^T & \mathbf{0} \\ \mathbf{0} & \sum_{\alpha=3}^{4} h_{\alpha,z}\boldsymbol{\gamma}_\alpha^T & \sum_{\alpha=3}^{4} h_{\alpha,y}\boldsymbol{\gamma}_\alpha^T \\ \sum_{\alpha=3}^{4} h_{\alpha,z}\boldsymbol{\gamma}_\alpha^T & \mathbf{0} & \sum_{\alpha=3}^{4} h_{\alpha,x}\boldsymbol{\gamma}_\alpha^T \end{bmatrix}. \tag{2.30}$$

Based on the above decomposition, the element stiffness matrix $\mathbf{K}_e$ can be rewritten in the following form:

$$\mathbf{K}_e = \mathbf{K}_{12} + \mathbf{K}_{34}, \tag{2.31}$$

where

$$\mathbf{K}_{12} = \int_{\Omega_e} \mathbf{B}_{12}^T \cdot \mathbf{C}^{\text{ep}} \cdot \mathbf{B}_{12} \, d\Omega, \tag{2.32}$$

and

$$\mathbf{K}_{34} = \int_{\Omega_e} \mathbf{B}_{12}^T \cdot \mathbf{C}^{\text{ep}} \cdot \mathbf{B}_{34} \, d\Omega + \int_{\Omega_e} \mathbf{B}_{34}^T \cdot \mathbf{C}^{\text{ep}} \cdot \mathbf{B}_{12} \, d\Omega + \int_{\Omega_e} \mathbf{B}_{34}^T \cdot \mathbf{C}^{\text{ep}} \cdot \mathbf{B}_{34} \, d\Omega. \tag{2.33}$$

The first part $\mathbf{K}_{12}$ is the only term of the stiffness matrix that does not vanish when evaluated at the integration points of the SHB8PS element. The second part $\mathbf{K}_{34}$ corresponds to the stabilization stiffness matrix for the SHB8PS element, as the latter vanishes when evaluated at the integration points. The vanishing of matrix $\mathbf{K}_{34}$ reduces the stiffness matrix to only its first part $\mathbf{K}_{12}$, which induce zero-energy hourglass modes for the SHB8PS element, as discussed by Abed-Meraim and Combescure (2009). In the latter contribution, it has been proposed to compute the stabilization stiffness matrix and internal load vector in a local co-rotational frame, which leads to simplified expressions (see also Belytschko and Bindeman, 1993).

It is worth noting that, for the SHB8PS element, the stabilization procedure is applied in conjunction with the assumed-strain method, whose principle is similar to that applied for the SHB6 element. But before defining the corresponding projection, we start by replacing the previous Hallquist vectors $\mathbf{b}_i$ by the mean form $\hat{\mathbf{b}}_i$ introduced by Flanagan and Belytschko (1981):

$$\hat{\mathbf{b}}_i = \frac{1}{\Omega_e} \int_{\Omega_e} \mathbf{N}_{,i}\left(\xi, \eta, \zeta\right) d\Omega. \tag{2.34}$$

It is noteworthy that both forms $\mathbf{b}_{\text{i}}$ and $\hat{\mathbf{b}}_i$ have been tested on a large number of benchmark tests, and the latter Flanagan–Belytschko mean form always showed better performance. Based on such a mean form, the original vectors $\boldsymbol{\gamma}_\alpha$ are replaced by new vectors $\hat{\boldsymbol{\gamma}}_\alpha$ given by:

$$\hat{\boldsymbol{\gamma}}_\alpha = \frac{1}{8}\left[\mathbf{h}_\alpha - \sum_{j=1}^{3}\left(\mathbf{h}_\alpha^T \cdot \mathbf{x}_j\right)\hat{\mathbf{b}}_j\right]. \tag{2.35}$$

Then, using the above new vectors $\hat{\mathbf{b}}_i$ and $\hat{\boldsymbol{\gamma}}_\alpha$, the discrete gradient operator becomes:

$$\hat{\mathbf{B}} = \hat{\mathbf{B}}_{12} + \hat{\mathbf{B}}_{34}, \tag{2.36}$$

where

$$\hat{\mathbf{B}}_{12} = \begin{bmatrix} \hat{\mathbf{b}}_x^T + \sum_{\alpha=1}^{2} h_{\alpha,x}\hat{\boldsymbol{\gamma}}_\alpha^T & \mathbf{0} & \mathbf{0} \\ \mathbf{0} & \hat{\mathbf{b}}_y^T + \sum_{\alpha=1}^{2} h_{\alpha,y}\hat{\boldsymbol{\gamma}}_\alpha^T & \mathbf{0} \\ \mathbf{0} & \mathbf{0} & \hat{\mathbf{b}}_z^T + \sum_{\alpha=1}^{2} h_{\alpha,z}\hat{\boldsymbol{\gamma}}_\alpha^T \\ \hat{\mathbf{b}}_y^T + \sum_{\alpha=1}^{2} h_{\alpha,y}\hat{\boldsymbol{\gamma}}_\alpha^T & \hat{\mathbf{b}}_x^T + \sum_{\alpha=1}^{2} h_{\alpha,x}\hat{\boldsymbol{\gamma}}_\alpha^T & \mathbf{0} \\ \mathbf{0} & \hat{\mathbf{b}}_z^T + \sum_{\alpha=1}^{2} h_{\alpha,z}\hat{\boldsymbol{\gamma}}_\alpha^T & \hat{\mathbf{b}}_y^T + \sum_{\alpha=1}^{2} h_{\alpha,y}\hat{\boldsymbol{\gamma}}_\alpha^T \\ \hat{\mathbf{b}}_z^T + \sum_{\alpha=1}^{2} h_{\alpha,z}\hat{\boldsymbol{\gamma}}_\alpha^T & \mathbf{0} & \hat{\mathbf{b}}_x^T + \sum_{\alpha=1}^{2} h_{\alpha,x}\hat{\boldsymbol{\gamma}}_\alpha^T \end{bmatrix}, \tag{2.37}$$

and

$$\hat{\mathbf{B}}_{34} = \begin{bmatrix} \sum_{\alpha=3}^{4} h_{\alpha,x}\hat{\boldsymbol{\gamma}}_\alpha^T & \mathbf{0} & \mathbf{0} \\ \mathbf{0} & \sum_{\alpha=3}^{4} h_{\alpha,y}\hat{\boldsymbol{\gamma}}_\alpha^T & \mathbf{0} \\ \mathbf{0} & \mathbf{0} & \sum_{\alpha=3}^{4} h_{\alpha,z}\hat{\boldsymbol{\gamma}}_\alpha^T \\ \sum_{\alpha=3}^{4} h_{\alpha,y}\hat{\boldsymbol{\gamma}}_\alpha^T & \sum_{\alpha=3}^{4} h_{\alpha,x}\hat{\boldsymbol{\gamma}}_\alpha^T & \mathbf{0} \\ \mathbf{0} & \sum_{\alpha=3}^{4} h_{\alpha,z}\hat{\boldsymbol{\gamma}}_\alpha^T & \sum_{\alpha=3}^{4} h_{\alpha,y}\hat{\boldsymbol{\gamma}}_\alpha^T \\ \sum_{\alpha=3}^{4} h_{\alpha,z}\hat{\boldsymbol{\gamma}}_\alpha^T & \mathbf{0} & \sum_{\alpha=3}^{4} h_{\alpha,x}\hat{\boldsymbol{\gamma}}_\alpha^T \end{bmatrix}. \tag{2.38}$$

At this stage, the second term $\hat{\mathbf{B}}_{34}$ is projected onto $\overline{\hat{\mathbf{B}}}_{34}$, which writes:

$$\overline{\hat{\mathbf{B}}}_{34} = \begin{bmatrix} \sum_{\alpha=3}^{4} h_{\alpha,x}\hat{\boldsymbol{\gamma}}_\alpha^T & \mathbf{0} & \mathbf{0} \\ \mathbf{0} & \sum_{\alpha=3}^{4} h_{\alpha,y}\hat{\boldsymbol{\gamma}}_\alpha^T & \mathbf{0} \\ \mathbf{0} & \mathbf{0} & h_{3,z}\hat{\boldsymbol{\gamma}}_3^T \\ \mathbf{0} & \mathbf{0} & \mathbf{0} \\ \mathbf{0} & \mathbf{0} & \mathbf{0} \\ \mathbf{0} & \mathbf{0} & h_{4,x}\hat{\boldsymbol{\gamma}}_4^T \end{bmatrix}. \tag{2.39}$$

The element stiffness matrix given in Eq. (2.31) is then expressed as the sum of the following two contributions:

$$\mathbf{K}_{12} = \int_{\Omega_e} \hat{\mathbf{B}}_{12}^T \cdot \mathbf{C}^{\text{ep}} \cdot \hat{\mathbf{B}}_{12} \, d\Omega \,, \tag{2.40}$$

$$\mathbf{K}_{\text{STAB}} = \int_{\Omega_e} \hat{\mathbf{B}}_{12}^T \cdot \mathbf{C}^{\text{ep}} \cdot \bar{\hat{\mathbf{B}}}_{34} \, d\Omega + \int_{\Omega_e} \bar{\hat{\mathbf{B}}}_{34}^T \cdot \mathbf{C}^{\text{ep}} \cdot \hat{\mathbf{B}}_{12} \, d\Omega + \int_{\Omega_e} \bar{\hat{\mathbf{B}}}_{34}^T \cdot \mathbf{C}^{\text{ep}} \cdot \bar{\hat{\mathbf{B}}}_{34} \, d\Omega \,. \tag{2.41}$$

Following the approach proposed by Belytschko and Bindeman (1993), the stabilization stiffness, Eq. (2.41), is calculated in the co-rotational coordinate system defined in Section 2.2. Within this local frame, the first two terms of the stabilization stiffness matrix vanish, and the treatment of shear locking becomes more efficient. The main derivations within this co-rotational coordinate system are given hereafter.

The components of the column vectors, which define the rotation matrix, are computed as:

$$a_{1i} = \mathbf{\Lambda}_1^T \cdot \mathbf{x}_i \,, \quad a_{2i} = \mathbf{\Lambda}_2^T \cdot \mathbf{x}_i \,, \quad i = 1, 2, 3 \,, \tag{2.42}$$

with

$$\begin{cases} \mathbf{\Lambda}_1^T = \left(-1, 1, 1, -1, -1, 1, 1, -1\right) \\ \mathbf{\Lambda}_2^T = \left(-1, -1, 1, 1, -1, -1, 1, 1\right) \\ \mathbf{\Lambda}_3^T = \left(-1, -1, -1, -1, 1, 1, 1, 1\right) \end{cases}. \tag{2.43}$$

The second vector $\mathbf{a}_2$ is then modified by adding a correction term $\mathbf{a}_c$ to satisfy the orthogonality condition $\mathbf{a}_1^T \cdot \left(\mathbf{a}_2 + \mathbf{a}_c\right) = 0$, which leads to

$$\mathbf{a}_c = -\frac{\mathbf{a}_1^T \cdot \mathbf{a}_2}{\mathbf{a}_1^T \cdot \mathbf{a}_1} \mathbf{a}_1 \,. \tag{2.44}$$

Finally, the third vector $\mathbf{a}_3$ is simply obtained by classical cross-product:

$$\mathbf{a}_3 = \mathbf{a}_1 \times \left(\mathbf{a}_2 + \mathbf{a}_c\right). \tag{2.45}$$

The rotation matrix **Q** (see Fig. 2.2), which maps any tensor variable from the global coordinate system to the local co-rotational system, is given by:

$$Q_{1i} = \frac{a_{1i}}{\left\|\mathbf{a}_1\right\|}, \quad Q_{2i} = \frac{a_{2i} + a_{ci}}{\left\|\mathbf{a}_2 + \mathbf{a}_c\right\|}, \quad Q_{3i} = \frac{a_{3i}}{\left\|\mathbf{a}_3\right\|}. \tag{2.46}$$

It is important to note that this co-rotational coordinate system is designed so that it coincides with the element reference frame. Hence, the relationships between the two coordinate systems can be approximated as:

$$\frac{\partial \tilde{x}_i}{\partial \xi_i} = \frac{1}{\partial \xi_i / \partial \tilde{x}_i} = \frac{1}{8} \mathbf{\Lambda}_i^{\mathrm{T}} \cdot \tilde{\mathbf{x}}_i, \quad \frac{\partial \tilde{x}_i}{\partial \xi_j} = \frac{\partial \xi_j}{\partial \tilde{x}_i} = 0 \text{ if } i \neq j, \tag{2.47}$$

where vector $\tilde{\mathbf{x}}_i$ represents the nodal coordinates expressed in the local co-rotational frame.

Thanks to the above relationships (see Eq. (2.47)), the following simplifications can be made:

$$h_{i,i} = \frac{\partial h_i}{\partial \tilde{x}_i} = 0, \quad h_{j,i} = \frac{8\xi_k}{\mathbf{\Lambda}_i^T \cdot \tilde{\mathbf{x}}_i}, \quad h_{4,i} = \frac{8\xi_j \xi_k}{\mathbf{\Lambda}_i^T \cdot \tilde{\mathbf{x}}_i}, \quad \tilde{J} = \frac{\mathbf{\Lambda}_1^T \cdot \tilde{\mathbf{x}}_1}{8} \frac{\mathbf{\Lambda}_2^T \cdot \tilde{\mathbf{x}}_2}{8} \frac{\mathbf{\Lambda}_3^T \cdot \tilde{\mathbf{x}}_3}{8}, \tag{2.48}$$

where $\tilde{J}$ denotes the determinant of the Jacobian matrix. Note that in the above formulas as well as in the following equations, there is no summation on repeated subscripts. These involved subscripts i, j and k are two by two distinct and take all possible permutations given in the following Table 2.1.

Table 2.1. Possible permutations for subscripts i, j and k.

i	j	k
1	2	3
1	3	2
2	1	3
2	3	1
3	1	2
3	2	1

Then, Eq. (2.48) leads to:

$$\begin{cases} \int_{\Omega_e} h_{i,j} \, d\Omega = 0 \\ H_{ii} = \int_{\Omega_e} \left(h_{j,i}\right)^2 \, d\Omega = \int_{\Omega_e} \left(h_{k,i}\right)^2 \, d\Omega = 3 \int_{\Omega_e} \left(h_{4,i}\right)^2 \, d\Omega = \dfrac{1}{3} \dfrac{\left(\mathbf{\Lambda}_j^T \cdot \tilde{\mathbf{x}}_j\right)\left(\mathbf{\Lambda}_k^T \cdot \tilde{\mathbf{x}}_k\right)}{\mathbf{\Lambda}_i^T \cdot \tilde{\mathbf{x}}_i}. \\ H_{ij} = \int_{\Omega_e} h_{j,i} h_{i,j} \, d\Omega = \dfrac{1}{3} \mathbf{\Lambda}_k^T \cdot \tilde{\mathbf{x}}_k \end{cases} \tag{2.49}$$

Using the above expressions, the stabilization stiffness matrix defined in Eq. (2.41) can be computed directly in the local co-rotational system as:

$$\mathbf{K}_{\text{STAB}} = \begin{bmatrix} \mathbf{k}_{11} & \mathbf{k}_{12} & \mathbf{k}_{13} \\ \mathbf{k}_{21} & \mathbf{k}_{22} & \mathbf{k}_{23} \\ \mathbf{k}_{31} & \mathbf{k}_{32} & \mathbf{k}_{33} \end{bmatrix}, \tag{2.50}$$

in which, the 8×8 sub-matrices $\mathbf{k}_{ij}$ are given by:

$$\begin{cases} \mathbf{k}_{11} = \left(\bar{\lambda} + 2\mu\right) H_{11} \left[\hat{\gamma}_3 \hat{\gamma}_3^T + \dfrac{1}{3} \hat{\gamma}_4 \hat{\gamma}_4^T \right] \\ \mathbf{k}_{22} = \left(\bar{\lambda} + 2\mu\right) H_{22} \left[\hat{\gamma}_3 \hat{\gamma}_3^T + \dfrac{1}{3} \hat{\gamma}_4 \hat{\gamma}_4^T \right], \\ \mathbf{k}_{33} = \mu H_{11} \dfrac{1}{3} \hat{\gamma}_4 \hat{\gamma}_4^T \\ \mathbf{k}_{ij} = \mathbf{0}, \quad i \neq j \end{cases} \tag{2.51}$$

where $\bar{\lambda} = \dfrac{E\nu}{1-\nu^2}$ and $\mu = \dfrac{E}{2(1+\nu)}$. The latter elasticity constants are derived from a modified (improved) plane-stress-type constitutive law, which will be discussed subsequently in the Section devoted to the constitutive modeling.

In the same way as for the stiffness matrix, the internal forces of the element are decomposed into two parts as follows:

$$\mathbf{f}^{\text{int}} = \mathbf{f}_{12}^{\text{int}} + \mathbf{f}^{\text{STAB}}, \tag{2.52}$$

where the stabilization forces $\mathbf{f}^{\text{STAB}}$ are given by

$$\mathbf{f}^{\text{STAB}} = \begin{Bmatrix} \mathbf{f}_1^{\text{STAB}} \\ \mathbf{f}_2^{\text{STAB}} \\ \mathbf{f}_3^{\text{STAB}} \end{Bmatrix}, \tag{2.53}$$

with $\mathbf{f}_i^{\text{STAB}} = \sum_{\alpha=3}^{4} Q_{i\alpha} \hat{\boldsymbol{\gamma}}_\alpha$. The generalized stresses $Q_{i\alpha}$ are related to the so-called generalized strain rates $\dot{q}_{i\alpha} = \hat{\boldsymbol{\gamma}}_\alpha^T \cdot \dot{\mathbf{d}}_i$ using the following expressions:

$$\begin{cases} \dot{Q}_{13} = \left(\bar{\lambda} + 2\mu\right) H_{11} \dot{q}_{13} \\ \dot{Q}_{14} = \dfrac{1}{3}\left(\bar{\lambda} + 2\mu\right) H_{11} \dot{q}_{14} \\ \dot{Q}_{23} = \left(\bar{\lambda} + 2\mu\right) H_{22} \dot{q}_{23} \\ \dot{Q}_{24} = \dfrac{1}{3}\left(\bar{\lambda} + 2\mu\right) H_{22} \dot{q}_{24} \\ \dot{Q}_{33} = 0 \\ \dot{Q}_{34} = \dfrac{1}{3}\mu H_{11} \dot{q}_{34} \end{cases}. \tag{2.54}$$

Once the stabilization stiffness matrix and internal force vector are thus computed in the local co-rotational coordinate system, they are transformed back to the global coordinate system for the assembly process. The above formulas, which provide the expressions of the stabilization stiffness matrix and internal force vector, are valid for elastic behavior. In the case of elastic–plastic behavior, the involved Young modulus E should be replaced by the averaged tangent modulus over the integration points across the thickness.

2.4 General formulation for dynamic/explicit analysis

In the present PhD work, the above quasi-static versions of the SHB solid–shell elements are extended to the explicit dynamic framework for the simulation of impact problems and complex processes that are difficult to perform using quasi-static solvers. Several aspects of the dynamic versions of the SHB elements (and the associated numerical subroutines) are common to the quasi-static/implicit versions described in the previous section. Therefore, only the key points relating to the dynamic formulations are presented in what follows.

2.4.1 Velocity field interpolation

Unlike the quasi-static formulation, the dynamic/explicit formulation is based on the interpolation of the velocity field. The coordinates x_i and velocities v_i inside the element are interpolated using the following expressions:

$$x_i = x_{iI} N_I(\xi,\eta,\zeta) = \sum_{I=1}^{n} N_I(\xi,\eta,\zeta) x_{iI}, \tag{2.55}$$

$$v_i = \dot{d}_{iI} N_I(\xi,\eta,\zeta) = \sum_{I=1}^{n} \dot{d}_{iI} N_I(\xi,\eta,\zeta), \tag{2.56}$$

where x_{iI} and $\dot{d}_{iI}$ are the nodal coordinates and nodal velocities, respectively.

Using the above interpolation and following the same derivation lines presented in the previous section, one can easily obtain the new (equivalent) expressions for the velocity field and the velocity gradient as follows:

$$\begin{cases} v_i = a_{0i} + \left(x_1 \mathbf{b}_1^T + x_2 \mathbf{b}_2^T + x_3 \mathbf{b}_3^T + h_1 \boldsymbol{\gamma}_1^T + \cdots + h_\alpha \boldsymbol{\gamma}_\alpha^T \right) \cdot \dot{\mathbf{d}}_i \\ v_{i,j} = \left(\mathbf{b}_j^T + \sum_\alpha h_{\alpha,j} \boldsymbol{\gamma}_\alpha^T \right) \cdot \dot{\mathbf{d}}_i = \left(\mathbf{b}_j^T + h_{\alpha,j} \boldsymbol{\gamma}_\alpha^T \right) \cdot \dot{\mathbf{d}}_i \end{cases} . \tag{2.57}$$

Following the same steps as for the quasi-static formulation, the discrete gradient operator $\mathbf{B}$ can be easily obtained, whose expression is similar to that given by Eq. (2.10).

Based on the simplified form of the Hu–Washizu variational principle, the internal forces associated with the SHB elements are given by:

$$\mathbf{f}^{\text{int}} = \int_{\Omega_e} \bar{\mathbf{B}}^T \cdot \boldsymbol{\sigma}(\dot{\bar{\boldsymbol{\varepsilon}}}) \, d\Omega, \tag{2.58}$$

where the $\bar{\mathbf{B}}$ operator is the projection of the classical discrete gradient operator $\mathbf{B}$, in order to eliminate most locking phenomena (see Section 2.1.4).

2.4.2 Modeling of the mass matrix

For dynamic analysis, the stiffness matrix $\mathbf{K}_e$ is not required in the calculations, while the element mass matrix $\mathbf{M}^e$ is involved and its components need to be defined first. As illustrated in Fig. 2.3, several methods have been proposed in the literature for the computation of the mass matrix of standard finite elements (see, e.g., Zienkiewicz et al, 2006), some of which are described hereafter.

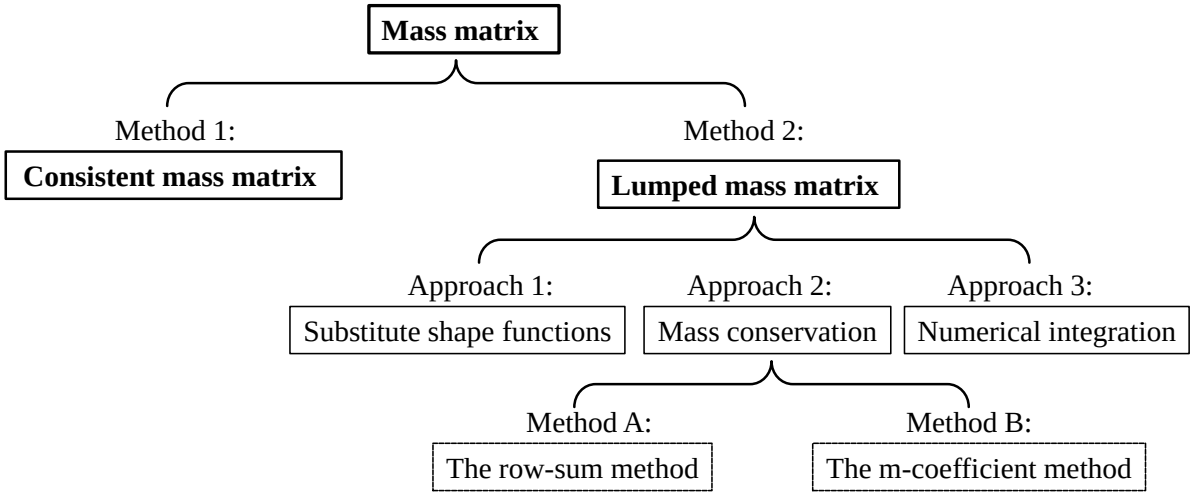


Figure 2.3. Several approaches for computing the element mass matrix.

2.4.2.1 Consistent mass matrix

The first classical method is known as the "consistent mass matrix", in which the mass matrix has a full rank, and is consistently computed using the usual shape functions. The consistent mass matrix $\mathbf{M}^e$ (with a size of $3n \times 3n$) is built from the following block of components:

$$M_{IJ} = \int_{\Omega_e} \rho N_I N_J d\Omega, \tag{2.59}$$

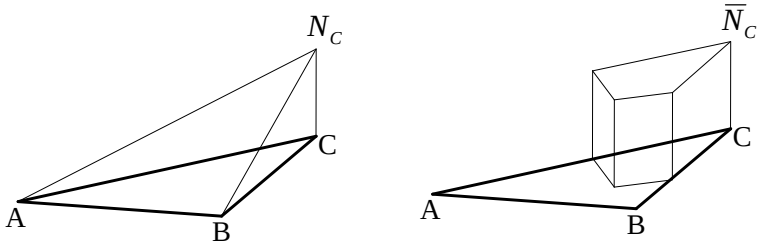
where I, J represent the node numbers, N_I and N_J are the shape functions and ρ is the material density.

2.4.2.2 Lumped mass matrix

Although the "consistent mass matrix" method is the most classical and accurate approach for computing the mass matrix, its cumbersome computational cost greatly restricts its implementation into FE codes. For the sake of convenience and efficiency, the "lumped mass matrix" method is adopted nowadays in many FE codes for its computational and storage advantages. In this subsection, several popular approaches for computing the lumped mass matrix are presented.

Approach 1: Substitute shape functions

In this approach, new substitute shape functions denoted $\overline{N}_i$ are used, instead of the traditional shape functions N_i, to compute the lumped mass matrix. For illustration purposes, a triangular shell element is considered here. As depicted in Fig. 2.4 (a), classical linear shape functions are usually adopted for the interpolation of the coordinates and displacements in triangular elements, while for the definition of the lumped mass matrix, new substitute piecewise shape functions are used. The latter are constant within some pieces of their domain of definition, while they are equal to zero elsewhere, as illustrated in Fig. 2.4 (b).



(a) linear shape function (b) piecewise constant shape function

Figure 2.4. Traditional linear and substitute piecewise shape functions for a triangular shell element.

Accordingly, the lumped mass matrix is built from the following block of components:

$$M_{IJ} = \begin{cases} \int_{\Omega_e} \rho \bar{N}_I \bar{N}_J d\Omega & I = J \\ 0 & I \neq J \end{cases}, \quad \text{with} \quad \sum_{\mathrm{I}} \bar{N}_I = 1. \tag{2.60}$$

Approach 2: Mass conservation

The second approach for the calculation of the lumped mass matrix is based on the mass conservation condition over the whole element. So far, a number of alternatives for the mass matrix calculation based on the mass conservation principle have been proposed in the literature (see, e.g., Zienkiewicz et al, 2006). In this subsection, two well-known methods, denoted as "the row-sum method" and "the m-coefficient method", are presented through an example of 8-node linear hexahedral element (see Fig. 2.5).

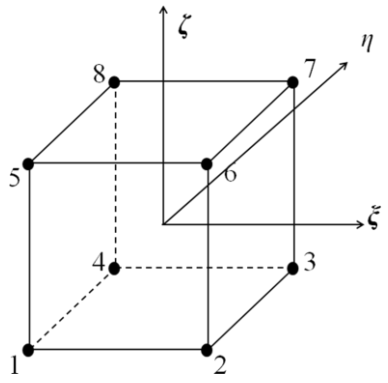


Figure 2.5. 8-node linear hexahedral element.

The traditional shape functions for a standard linear hexahedral element are expressed as:

$$\begin{cases} N_1 = \frac{1}{8}(1-\xi)(1-\eta)(1-\zeta), & N_5 = \frac{1}{8}(1-\xi)(1-\eta)(1+\zeta) \\ N_2 = \frac{1}{8}(1+\xi)(1-\eta)(1-\zeta), & N_6 = \frac{1}{8}(1+\xi)(1-\eta)(1+\zeta) \\ N_3 = \frac{1}{8}(1+\xi)(1+\eta)(1-\zeta), & N_7 = \frac{1}{8}(1+\xi)(1+\eta)(1+\zeta) \\ N_4 = \frac{1}{8}(1-\xi)(1+\eta)(1-\zeta), & N_8 = \frac{1}{8}(1-\xi)(1+\eta)(1+\zeta) \end{cases}. \tag{2.61}$$

1) The row-sum method

In this method, a transition matrix $\mathbf{T}$ is first defined, whereby the relationship between the shape functions and the lumped matrix can be established in what follows:

$$
\begin{aligned}
\mathbf{T} &= \int_{\Omega_e} \mathbf{N}\cdot\mathbf{N}^{\mathrm{T}}\, d\Omega \\
&= \int_{\Omega_e} \begin{bmatrix} N_1 \\ N_2 \\ N_3 \\ N_4 \\ N_5 \\ N_6 \\ N_7 \\ N_8 \end{bmatrix} \cdot \begin{bmatrix} N_1 & N_2 & N_3 & N_4 & N_5 & N_6 & N_7 & N_8 \end{bmatrix} d\Omega \\
&= \int_{\Omega_e} \begin{bmatrix} N_1N_1 & N_1N_2 & N_1N_3 & \cdots & N_1N_6 & N_1N_7 & N_1N_8 \\ N_2N_1 & N_2N_2 & N_2N_3 & \cdots & N_2N_1 & N_2N_7 & N_2N_8 \\ N_3N_1 & N_3N_2 & N_3N_3 & \cdots & N_3N_1 & N_3N_7 & N_3N_8 \\ \vdots & \vdots & \vdots & \ddots & \vdots & \vdots & \vdots \\ N_6N_1 & N_6N_2 & N_6N_3 & \cdots & N_6N_6 & N_6N_7 & N_6N_8 \\ N_7N_1 & N_7N_2 & N_7N_3 & \cdots & N_7N_6 & N_7N_7 & N_7N_8 \\ N_8N_1 & N_8N_2 & N_8N_3 & \cdots & N_8N_6 & N_8N_7 & N_8N_8 \end{bmatrix} d\Omega .
\end{aligned}
\tag{2.62}
$$

Combining Eqs. (2.61) and (2.62), one can easily calculate all components of the transition matrix $\mathbf{T}$ by:

$$
T_{IJ} = \int_{\xi=-1}^{+1}\int_{\eta=-1}^{+1}\int_{\zeta=-1}^{+1} N_I N_J \, d\xi\, d\eta\, d\zeta = \frac{1}{216}\left(3+\xi_I\xi_J\right)\left(3+\eta_I\eta_J\right)\left(3+\zeta_I\zeta_J\right), \tag{2.63}
$$

where ξ_I, η_I, ζ_I, ξ_J, η_J and ζ_J $(I, J = 1, \cdots, 8)$ are the node coordinates of the element in the reference frame.

Then, a diagonal matrix $\mathbf{S}$ is defined, whose components are the row sum of the $\mathbf{T}$ matrix.

$$\mathbf{S}=\begin{bmatrix}\sum_{1}^{8}T_{1i} & & & & & & & \\ & \sum_{1}^{8}T_{2i} & & & & & & \\ & & \sum_{1}^{8}T_{3i} & & & & & \\ & & & \sum_{1}^{8}T_{4i} & & & & \\ & & & & \sum_{1}^{8}T_{5i} & & & \\ & & & & & \sum_{1}^{8}T_{6i} & & \\ & & & & & & \sum_{1}^{8}T_{7i} & \\ & & & & & & & \sum_{1}^{8}T_{8i}\end{bmatrix}. \tag{2.64}$$

Note that both matrices $\mathbf{T}$ and $\mathbf{S}$ are calculated above in the local element reference frame, while the mass matrix should be computed in the global coordinate system. To achieve this, the determinant of the Jacobian matrix $\mathbf{J}$, denoted as $|\mathbf{J}|$, is computed, which allows transferring the **S** matrix from the local element reference frame to the global coordinate system. The resulting lumped mass matrix (with a size of 24×24 for a linear hexahedral element) is given by:

$$\mathbf{M}^{e}=\begin{bmatrix}\rho|\mathbf{J}|S_{11} & & & & & & & \\ & \ddots & & & & & & \\ & & \rho|\mathbf{J}|S_{88} & & & & & \\ & & & \rho|\mathbf{J}|S_{11} & & & & \\ & & & & \ddots & & & \\ & & & & & \rho|\mathbf{J}|S_{88} & & \\ & & & & & & \rho|\mathbf{J}|S_{11} & \\ & & & & & & & \ddots \\ & & & & & & & & \rho|\mathbf{J}|S_{88}\end{bmatrix}. \tag{2.65}$$

2) The m-coefficient method

Unlike the previous row-sum method, the “m-coefficient” method is easier to implement. In this method, the final lumped mass matrix can be derived from the following block of components:

$$M_{IJ} = \begin{cases} m\int_{\Omega_e} \rho N_I N_J d\Omega & I = J \\ 0 & I \neq J \end{cases}, \quad \text{with} \quad m = \int_{\Omega_e} \rho d\Omega \Big/ \sum_{I=1}^{n} \int_{\Omega_e} \rho N_I N_I d\Omega \,. \tag{2.66}$$

As expressed in the above equation, all shape functions are involved in the calculation of the mass matrix, but without cross-multiplication. The transition matrix $\mathbf{T}$ has only diagonal constant components in this case, with the non-zero components given by:

$$T_{II} = \int_{\xi=-1}^{+1} \int_{\eta=-1}^{+1} \int_{\zeta=-1}^{+1} N_I N_I \, d\xi \, d\eta \, d\zeta = \frac{1}{64}\left(2+\frac{2}{3}\xi_I\xi_I\right)\left(2+\frac{2}{3}\eta_I\eta_I\right)\left(2+\frac{2}{3}\zeta_I\zeta_I\right) = \frac{8}{27}. \tag{2.67}$$

Then, according to the expression given in Eq. (2.66), one can easily calculate the coefficient *m* by:

$$m = \int_{\Omega_e} \rho d\Omega \Big/ \sum_{I=1}^{8} \int_{\Omega_e} \rho N_I N_I d\Omega = \frac{27}{8}. \tag{2.68}$$

Finally, the diagonal matrix $\mathbf{S}$ is given by

$$\mathbf{S} = \begin{bmatrix} mT_{11} & & & & & & & \\ & mT_{22} & & & & & & \\ & & mT_{33} & & & & & \\ & & & mT_{44} & & & & \\ & & & & mT_{55} & & & \\ & & & & & mT_{66} & & \\ & & & & & & mT_{77} & \\ & & & & & & & mT_{88} \end{bmatrix}. \tag{2.69}$$

Once matrix $\mathbf{S}$ is obtained, the remaining steps for calculating the final mass matrix $\mathbf{M}^e$ are the same as for the row-sum method (see Eq. (2.65)).

Approach 3: Numerical integration

The last approach for the determination of the lumped mass matrix is the so-called numerical integration approach. The main steps of this method are similar to those of the row-sum method; however, the full integration is achieved using the integration points of the element:

$$M_{IJ} = \int_{\Omega_e} \rho N_I N_J d\Omega = \sum_{ip=1}^{NIP} w\left(\xi_{ip}, \eta_{ip}, \zeta_{ip}\right) \rho\left(N_I N_J\right)\Big|_{\left(\xi_{ip}, \eta_{ip}, \zeta_{ip}\right)}, \tag{2.70}$$

where *NIP* represents the total number of integration points, while ξ_{ip}, η_{ip} and ζ_{ip} are the local coordinates of a given integration point, and $w\left(\xi_{ip}, \eta_{ip}, \zeta_{ip}\right)$ is the associated weight coefficient.

Then, the transition matrix $\mathbf{T}$ is given by:

$$\mathbf{T} = \begin{bmatrix} \sum_{ip=1}^{NIP} N_1 N_1 w_{ip} & \cdots & \cdots & \cdots & \cdots & \cdots & \sum_{ip=1}^{NIP} N_1 N_8 w_{ip} \\ \vdots & & \vdots & \vdots & \cdots & \vdots & \vdots & \vdots \\ \vdots & & \vdots & \vdots & \cdots & \vdots & \vdots & \vdots \\ \vdots & & \vdots & \vdots & \ddots & \vdots & \vdots & \vdots \\ \vdots & & \vdots & \vdots & \cdots & \vdots & \vdots & \vdots \\ \vdots & & \vdots & \vdots & \cdots & \vdots & \vdots & \vdots \\ \sum_{ip=1}^{NIP} N_8 N_1 w_{ip} & \cdots & \cdots & \cdots & \cdots & \cdots & \sum_{ip=1}^{NIP} N_8 N_8 w_{ip} \end{bmatrix}. \tag{2.71}$$

Considering the shape functions given by Eq. (2.61), all components of matrix $\mathbf{T}$ can be calculated as

$$\begin{aligned} T_{IJ} &= \sum_{ip=1}^{NIP} N_I N_J w_{ip} \\ &= \sum_{ip=1}^{NIP} \left[\frac{1}{8}\left(1+\xi_I \xi_{ip}\right)\left(1+\eta_I \eta_{ip}\right)\left(1+\zeta_I \zeta_{ip}\right) \right] \left[\frac{1}{8}\left(1+\xi_J \xi_{ip}\right)\left(1+\eta_J \eta_{ip}\right)\left(1+\zeta_J \zeta_{ip}\right) \right] w_{ip}. \end{aligned} \tag{2.72}$$

Finally, the calculation of the diagonal matrix $\mathbf{S}$ and, therefore, the lumped mass matrix $\mathbf{M}^e$ follows the same procedure as that of the row-sum method.

In summary, several methods can be used to compute the element mass matrix for explicit dynamic analysis. Compared to the other methods discussed above, the "m-coefficient" method shows a number of advantages in terms of simplicity, ease of implementation and storage aspects (diagonal matrix). For these reasons, the "m-coefficient" method is adopted in the current work for the formulation of the explicit dynamic versions of the SHB elements.

2.5 Constitutive equations

As mentioned before, all formulations (implicit/quasi-static and explicit/dynamic) of the SHB solid–shell elements are coupled in the current work with various types of constitutive equations, which allows for a broad range of applications. In this section, some classical

material behavior models are presented. The corresponding constitutive equations are combined with the SHB elements within the framework of large displacements and rotations.

2.5.1 Isotropic and anisotropic elastic material behavior

In the formulation of the SHB solid–shell elements, the elasticity law is defined in the so-called "element frame", which corresponds to the element mid-plane associated with the ζ-coordinate of each integration point (see Fig. 2.2). In this local physical coordinate system, which is attached to the integration points of the element, the fourth-order elasticity tensor $\mathbf{C}^{\text{ele}}$ is specified.

2.5.1.1 Isotropic elasticity

In order to model the classical isotropic elastic behavior, an improved plane-stress type elasticity law is adopted in the formulations of the linear SHB elements (i.e., SHB6 and SHB8PS), which allows enhancing their performances with regard to thickness locking (see, e.g., Abed-Meraim and Combescure, 2009; Trinh et al., 2011). Such a modified elasticity matrix $\mathbf{C}^{\text{ele}}$ is defined in the local "element frame" as follows:

$$\mathbf{C}^{\text{ele}} = \begin{bmatrix} \bar{\lambda}+2\mu & \bar{\lambda} & 0 & 0 & 0 & 0 \\ \bar{\lambda} & \bar{\lambda}+2\mu & 0 & 0 & 0 & 0 \\ 0 & 0 & E & 0 & 0 & 0 \\ 0 & 0 & 0 & \mu & 0 & 0 \\ 0 & 0 & 0 & 0 & \mu & 0 \\ 0 & 0 & 0 & 0 & 0 & \mu \end{bmatrix} \text{ with } \mu = \frac{E}{2(1+\nu)} \text{ and } \bar{\lambda} = \frac{E\nu}{1-\nu^2}, \tag{2.73}$$

where E and ν are Young's modulus and Poisson's ratio, respectively.

It is worth noting that, although the above modified elasticity law is used to enhance the SHB element immunity with regard to thickness locking, it still allows considering the stress/strain variations through the thickness, in contrast to conventional shell element formulations, in which plane-stress-type restrictions are commonly adopted.

For the quadratic SHB elements (i.e., SHB15 and SHB20), however, such a modification in the elasticity matrix is not required, since their performance has been assessed with both the enhanced plane-stress-type elasticity matrix and the classical fully three-dimensional one, showing quite equivalent results (see, e.g., Trinh et al., 2011; Wang et al., 2017b). Therefore,

the following classical fully three-dimensional elasticity matrix is implemented with the proposed quadratic versions of the SHB elements:

$$\mathbf{C}^{\text{ele}} = \begin{bmatrix} \lambda+2\mu & \lambda & \lambda & 0 & 0 & 0 \\ \lambda & \lambda+2\mu & \lambda & 0 & 0 & 0 \\ \lambda & \lambda & \lambda+2\mu & 0 & 0 & 0 \\ 0 & 0 & 0 & \mu & 0 & 0 \\ 0 & 0 & 0 & 0 & \mu & 0 \\ 0 & 0 & 0 & 0 & 0 & \mu \end{bmatrix} \text{ with } \lambda = \frac{E\nu}{(1+\nu)(1-2\nu)}, \quad \mu = \frac{E}{2(1+\nu)}. \tag{2.74}$$

2.5.1.2 Orthotropic elasticity

In order to extend the application range of the SHB solid–shell elements to the 3D nonlinear analysis of composite laminates, their formulations are coupled with orthotropic elastic behavior (see, e.g., Wang et al., 2017c). According to the fully 3D orthotropic elasticity approach, the associated orthotropic elasticity tensor $\mathbf{C}^{\text{orth}}$ is defined in the local "element frame" as:

$$\left(\mathbf{C}^{\text{orth}}\right)^{-1} = \begin{bmatrix} \frac{1}{E_1} & -\frac{\nu_{21}}{E_2} & -\frac{\nu_{31}}{E_3} & 0 & 0 & 0 \\ -\frac{\nu_{12}}{E_1} & \frac{1}{E_2} & -\frac{\nu_{32}}{E_3} & 0 & 0 & 0 \\ -\frac{\nu_{13}}{E_1} & -\frac{\nu_{23}}{E_2} & \frac{1}{E_3} & 0 & 0 & 0 \\ 0 & 0 & 0 & \frac{1}{G_{12}} & 0 & 0 \\ 0 & 0 & 0 & 0 & \frac{1}{G_{23}} & 0 \\ 0 & 0 & 0 & 0 & 0 & \frac{1}{G_{13}} \end{bmatrix}, \tag{2.75}$$

where E_i represents the Young modulus in the *i*-th direction, ν_{ij} is the Poisson ratio associated with the *i*-th and *j*-th directions, and G_{12}, G_{13}, and G_{23} are the shear moduli. Furthermore, the thermodynamic constraint on the elastic constants for orthotropic materials, which is expressed by the relation $\nu_{ij}E_j = \nu_{ji}E_i$, should always be satisfied.

In order to model angle-ply laminates using the SHB elements, a local coordinate system attached to the fiber axes, which consist of the fiber direction, the transverse direction and the

normal direction (i.e., normal to the mid-plane), has to be defined for each laminate ply. For conciseness, only the quadratic SHB20 element is chosen for illustration. Figure 2.6 gives a schematic representation of the fiber orientations in the local element frame, in the case of the quadratic hexahedral SHB20 element.

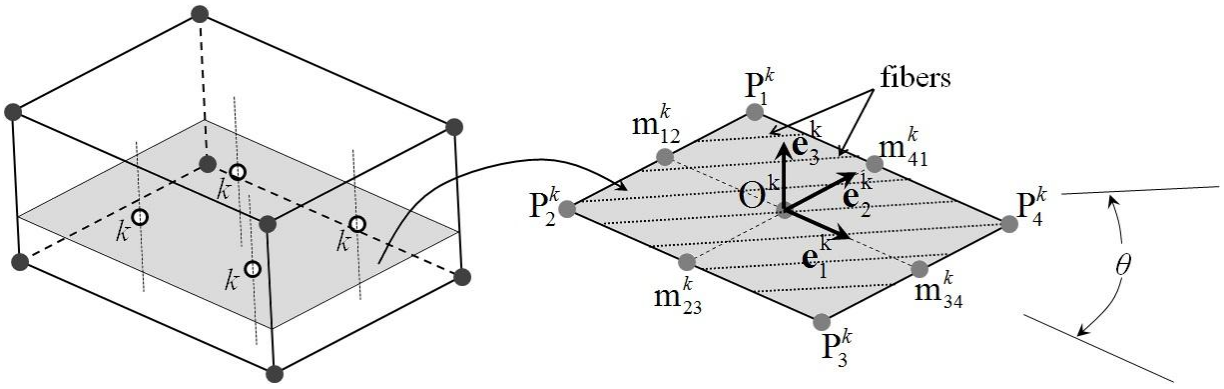


Figure 2.6. Schematic representation of the fiber orientations with respect to the local element frame for the SHB20 element.

Several techniques can be adopted for the modeling of multilayered composite structures using solid–shell elements. The simplest one consists in discretizing the entire thickness with one element layer per ply, which leads in the end to as many element layers as plies. However, this technique leads to a large number of degrees of freedom for the composite structure in the case of refined in-plane meshes, which in turn significantly increases the computational time. Another technique can be used, which is based on stacking the different composite plies within a single solid–shell element. In this latter case, each ply is modeled using one integration point and, therefore, the stiffness matrix associated with the entire thickness is calculated using the classical Gauss integration scheme over all integration points. This alternative technique, which is adopted for the SHB elements, allows for 3D modeling of multilayered composite structures using only a single solid–shell element through the thickness.

As depicted in Fig. 2.6, the *k*-th ply of the laminate is represented by a mid-plane, which is associated with the in-plane integration points. In the resulting mid-plane, the orthogonal system $\mathbf{e}_1^k$, $\mathbf{e}_2^k$ and $\mathbf{e}_3^k$ associated with the *k*-th ply of the laminate is defined with respect to the element frame as follows. First, four points P_1^k, P_2^k, P_3^k and P_4^k are determined using the physical nodal coordinates. These latter points allow us, in turn, to define four mid-points m_{12}^k,

m_{23}^k, m_{34}^k and m_{41}^k, which are the barycenters of (P_1^k P_2^k), (P_2^k P_3^k), (P_3^k P_4^k) and (P_4^k P_1^k), respectively. Then, the first base vector, $\mathbf{e}_1^k$, of the local coordinate system is defined as being parallel to $\left(\mathrm{m}_{12}^k\ \mathrm{m}_{34}^k\right)$, while the second vector $\mathbf{e}_2^k$ is defined parallel to $\left(\mathrm{m}_{23}^k\ \mathrm{m}_{41}^k\right)$. Vector $\mathbf{e}_2^k$ is modified by adding a correction term $\mathbf{e}_c^k$, so that vectors $\mathbf{e}_1^k$ and $\left(\mathbf{e}_2^k+\mathbf{e}_c^k\right)$ are orthogonal, which gives

$$\mathbf{e}_c^k=-\frac{\left(\mathbf{e}_1^k\right)^T\cdot\mathbf{e}_2^k}{\left(\mathbf{e}_1^k\right)^T\cdot\mathbf{e}_1^k}\mathbf{e}_1^k. \tag{2.76}$$

Finally, the third base vector $\mathbf{e}_3^k$, which is along the thickness direction, is simply obtained by the following cross-product (see Fig. 2.6):

$$\mathbf{e}_3^k=\mathbf{e}_1^k\times\left(\mathbf{e}_2^k+\mathbf{e}_c^k\right). \tag{2.77}$$

Using the above unit vectors, one can derive the rotation matrix $\mathbf{R}=\mathbf{P}$ (see Fig. 2.2), which maps any tensor variable between the local element frame and the global coordinate system, as follows:

$$P_{1i}=\frac{e_{1i}^k}{\left\|\mathbf{e}_1^k\right\|},\quad P_{2i}=\frac{e_{2i}^k+e_{ci}^k}{\left\|\mathbf{e}_2^k+\mathbf{e}_c^k\right\|},\quad P_{3i}=\frac{e_{3i}^k}{\left\|\mathbf{e}_3^k\right\|}. \tag{2.78}$$

Once the above orthogonal system is obtained, the elasticity matrix associated with the current *k*-th ply of the laminate $\mathbf{C}(\theta)^k$ which is expressed in the local element frame, is given by the following relationship:

$$\mathbf{C}(\theta)^k=\mathbf{T}(\theta)^k\cdot\mathbf{C}^{\mathrm{orth}}\cdot\left(\mathbf{T}(\theta)^k\right)^T, \tag{2.79}$$

where θ is the fiber orientation angle with respect to the orthotropy directions, and $\mathbf{T}(\theta)^k$ the rotation matrix, which allows mapping the orthotropic elasticity tensor from the fiber reference axes to the local element frame. Its expression has the following form:

$$\mathbf{T}(\theta)^k = \begin{bmatrix} c^2 & s^2 & 0 & 2cs & 0 & 0 \\ s^2 & c^2 & 0 & -2cs & 0 & 0 \\ 0 & 0 & 1 & 0 & 0 & 0 \\ -cs & cs & 0 & c^2-s^2 & 0 & 0 \\ 0 & 0 & 0 & 0 & -s & s \\ 0 & 0 & 0 & 0 & -s & c \end{bmatrix} \text{ with } c=\cos(\theta) \text{ and } s=\sin(\theta). \tag{2.80}$$

The operation described above is repeated for all plies of the composite laminate, as illustrated in Fig. 2.7, which allows considering several stacking sequences of plies within a single element layer.

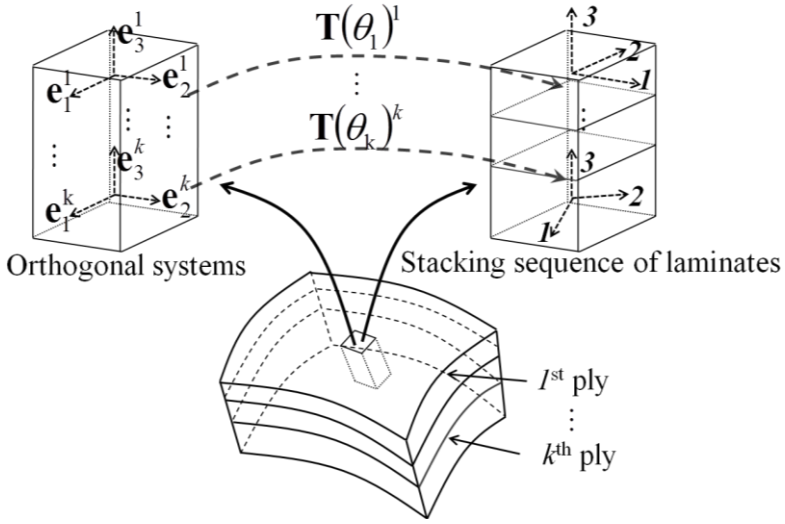


Figure 2.7. Illustration of stacking sequence for multilayered composite materials.

2.5.2 Anisotropic constitutive equations for metallic materials

The formulations of the SHB elements are also coupled with advanced large-strain anisotropic elasto-plastic constitutive models for metallic materials. For this purpose, the anisotropic plastic behavior of the material is defined in the local so-called "material frame" (see Fig. 2.2). The time integration of the large-strain anisotropic elasto-plastic constitutive equations, which is achieved at each integration point, also uses this local material frame in order to satisfy the objectivity (material invariance) requirements.

2.5.2.1 Anisotropic yield function

The anisotropic plastic behavior of the material is taken into account by considering the quadratic Hill'48 yield criterion (Hill, 1948). The corresponding plastic yield function f is written in the following form:

$$f = \bar{\sigma}_{eq} - Y \le 0, \tag{2.81}$$

where $\bar{\sigma}_{eq} = \sqrt{(\boldsymbol{\sigma}' - \boldsymbol{\alpha}) : \mathbf{H} : (\boldsymbol{\sigma}' - \boldsymbol{\alpha})}$ is the equivalent stress, and $\boldsymbol{\sigma}'$ is the deviatoric part of the Cauchy stress tensor $\boldsymbol{\sigma}$. The fourth-order tensor $\mathbf{H}$ contains the six Hill anisotropy coefficients (F, G, H, L, M and N). The isotropic hardening of the material is described by the scalar variable Y, which characterizes the size of the yield surface, while the kinematic hardening is represented by the back-stress tensor $\boldsymbol{\alpha}$.

2.5.2.2 Plastic flow rule

In the local material frame, the rate form of the stress–strain relationship can be expressed using the following hypoelastic law:

$$\dot{\boldsymbol{\sigma}} = \mathbf{C} : \left(\mathbf{D} - \mathbf{D}^p \right), \tag{2.82}$$

where $\mathbf{C}$ is the fourth-order elasticity tensor, which is obtained by rotating the elasticity tensor $\mathbf{C}^{\text{ele}}$ (see Eqs. (2.73) and (2.74)) from the element frame to the material frame. The strain rate tensor $\mathbf{D}$ is additively decomposed into an elastic part $\mathbf{D}^e$ and a plastic part $\mathbf{D}^p$. The latter is defined by an associative plastic flow rule

$$\mathbf{D}^p = \dot{\lambda} \frac{\partial f}{\partial \boldsymbol{\sigma}} = \dot{\lambda} \mathbf{V}, \tag{2.83}$$

where $\mathbf{V}$ is the flow direction normal to the yield surface f. The plastic multiplier $\dot{\lambda}$ in Eq. (2.83) is determined by the consistency condition.

2.5.2.3 Elasto-plastic tangent modulus

The plastic multiplier $\dot{\lambda}$ in Eq. (2.83) is determined by using the consistency condition $\dot{f} = 0$, which leads to

$$\dot{\lambda} = \frac{\mathbf{V} : \mathbf{C} : \mathbf{D}}{\mathbf{V} : \mathbf{C} : \mathbf{V} + \mathbf{V} : \mathbf{H}_{\boldsymbol{\alpha}} + H_Y}, \tag{2.84}$$

where the hardening moduli H_Y and $\mathbf{H}_{\boldsymbol{\alpha}}$ are scalar and tensor components involved in the evolution laws describing the isotropic and kinematic hardening, respectively. The latter can be expressed in the following generic form:

$$\begin{cases} \dot{Y} = H_Y \dot{\lambda} \\ \dot{\boldsymbol{\alpha}} = \mathbf{H}_{\boldsymbol{\alpha}} \dot{\lambda} \end{cases}. \tag{2.85}$$

The most commonly used isotropic hardening laws are adopted in the formulations of the SHB elements. These isotropic hardening models are summarized in Table 2.2. In the latter, σ_0 and $\bar{\varepsilon}$ are the initial yield stress and the equivalent plastic strain, respectively, while K, ε_0, and N are the corresponding hardening parameters of the material.

Table 2.2. Definition of the commonly used isotropic hardening models and their evolution laws.

Hardening	Perfectly plastic	Linear	Swift	Voce	Ludwig
Y	σ_0	$\sigma_0 + K\bar{\varepsilon}$	$K\left(\varepsilon_0 + \bar{\varepsilon}\right)^N$	$\sigma_0 + K\left(1 - e^{-N\bar{\varepsilon}}\right)$	$\sigma_0 + K\bar{\varepsilon}^N$
$H_Y = dY/d\bar{\varepsilon}$	0	K	$NK^{\frac{1}{N}} Y^{\frac{N-1}{N}}$	$N\left(\sigma_0 + K - Y\right)$	$NK^{\frac{1}{N}}\left(Y - \sigma_0\right)^{\frac{N-1}{N}}$

Also, several laws have been proposed in the literature to describe the kinematic hardening contribution to the material behavior. In the formulations of the SHB elements, the nonlinear kinematic hardening model proposed by Armstrong and Frederick (1966) is adopted. According to this model, the evolution of the back-stress variable $\boldsymbol{\alpha}$ is given by the following rate expression:

$$\dot{\boldsymbol{\alpha}} = C_X\left(\alpha_{sat}\mathbf{n} - \boldsymbol{\alpha}\right)\dot{\lambda} = \mathbf{H}_{\boldsymbol{\alpha}}\dot{\lambda}, \tag{2.86}$$

where C_X and α_{sat} are the kinematic hardening parameters, while $\mathbf{n} = \left(\boldsymbol{\sigma}' - \boldsymbol{\alpha}\right)/\bar{\sigma}_{eq}$ represents the kinematic hardening saturation direction.

Finally, by substituting the expression of the plastic multiplier $\dot{\lambda}$ into the hypoelastic law (Eq. (2.82)), the elasto-plastic tangent modulus is derived as

$$\mathbf{C}^{\text{ep}} = \mathbf{C} - \gamma \frac{\left(\mathbf{C}:\mathbf{V}\right)\otimes\left(\mathbf{V}:\mathbf{C}\right)}{\mathbf{V}:\mathbf{C}:\mathbf{V} + \mathbf{V}:\mathbf{H}_{\boldsymbol{\alpha}} + H_Y}, \tag{2.87}$$

where $\gamma = 0$ for elastic loading/unloading, and $\gamma = 1$ for strict plastic loading.

2.5.2.4 Time integration scheme

For all individual elements, at any time increment $\Delta t = t_{n+1} - t_n$, the required input variables include: the nodal coordinates $\mathbf{x}$ and the displacement increment $\Delta\mathbf{u}$.

Hughes and Winget (1980) proposed the use of the gradient of the displacement increment evaluated at the middle of the time step to calculate the spin tensor and strain increments $\Delta\mathbf{W}^{\text{glo}}$ and $\Delta\boldsymbol{\varepsilon}^{\text{glo}}$, respectively. The latter are evaluated in the global frame using the following expressions:

$$\Delta\mathbf{W}^{\text{glo}} = \left(\frac{\partial \Delta\mathbf{u}}{\partial \mathbf{x}_{t_n + \Delta t/2}} \right)^{asym}, \tag{2.88}$$

$$\Delta\boldsymbol{\varepsilon}^{\text{glo}} = \left(\frac{\partial \Delta\mathbf{u}}{\partial \mathbf{x}_{t_n + \Delta t/2}} \right)^{sym}, \tag{2.89}$$

where $\mathbf{x}_{t_n+\Delta t/2} = \frac{1}{2}\left(\mathbf{x}_{t_n} + \mathbf{x}_{t_{n+1}}\right)$.

Correspondingly, the rotation matrix $\boldsymbol{\mathcal{R}}$, which maps any vector or tensor from the global frame to the local material frame (see Fig. 2.2), is updated between the increments n and $n+1$ as follows:

$$\boldsymbol{\mathcal{R}}_{\text{n+1}} = \mathbf{r} \cdot \boldsymbol{\mathcal{R}}_{\text{n}}, \tag{2.90}$$

where the rotation increment $\mathbf{r}$ is defined as:

$$\mathbf{r} = \left(\mathbf{I} - \frac{1}{2}\Delta\mathbf{W} \right)^{-1} \cdot \left(\mathbf{I} + \frac{1}{2}\Delta\mathbf{W} \right), \tag{2.91}$$

where $\mathbf{I}$ is the second-order identity tensor.

Then, the elasticity tensor $\mathbf{C}^{\text{ele}}$, the Cauchy stress tensor $\boldsymbol{\sigma}^{\text{glo}}$ and the strain increment tensor $\Delta\boldsymbol{\varepsilon}^{\text{glo}}$ can be transferred to the material frame by:

$$\begin{cases} \mathbf{C}^{\text{glo}} = \mathbf{P}_n \cdot \mathbf{P}_n \cdot \mathbf{C}^{\text{ele}} \cdot \mathbf{P}_n^T \cdot \mathbf{P}_n^T \\ \mathbf{C}^{\text{mat}} = \boldsymbol{\mathcal{R}}_{n+1}^T \cdot \boldsymbol{\mathcal{R}}_{n+1}^T \cdot \mathbf{C}^{\text{glo}} \cdot \boldsymbol{\mathcal{R}}_{n+1} \cdot \boldsymbol{\mathcal{R}}_{n+1} \\ \boldsymbol{\sigma}^{\text{mat}} = \boldsymbol{\mathcal{R}}_n^T \cdot \boldsymbol{\sigma}^{\text{glo}} \cdot \boldsymbol{\mathcal{R}}_n \\ \Delta\boldsymbol{\varepsilon}^{\text{mat}} = \boldsymbol{\mathcal{R}}_n^T \cdot \Delta\boldsymbol{\varepsilon}^{\text{glo}} \cdot \boldsymbol{\mathcal{R}}_n \end{cases}. \tag{2.92}$$

With the above required input data thus computed in the local material frame, the integration of the elastic–plastic constitutive equations can be performed at each integration point of the element (using a User Material (UMAT) subroutine that is developed for each specific material behavior). In this developed UMAT subroutine, the final Cauchy stress state $\boldsymbol{\sigma}_{n+1}^{\text{mat}}$ and the final elasto-plastic tangent modulus $\mathbf{C}_{ep}^{\text{mat}}$ are updated at time t_{n+1} using the forward fourth-order Runge–Kutta integration scheme. Then, the resulting updated tensors are transferred back into the global frame using the rotation matrix in order to update the final element stiffness matrix $\mathbf{K}_e$ and the associated internal forces $\mathbf{f}^{\text{int}}$ (see Section 2.1 for details).

$$\begin{cases} \boldsymbol{\sigma}_{n+1}^{\text{glo}} = \boldsymbol{\mathcal{R}}_{n+1} \cdot \boldsymbol{\sigma}_{n+1}^{\text{mat}} \cdot \boldsymbol{\mathcal{R}}_{n+1}^{T} \\ \mathbf{C}_{\text{ep}}^{\text{glo}} = \boldsymbol{\mathcal{R}}_{n+1} \cdot \boldsymbol{\mathcal{R}}_{n+1} \cdot \mathbf{C}_{\text{ep}}^{\text{mat}} \cdot \boldsymbol{\mathcal{R}}_{n+1}^{T} \cdot \boldsymbol{\mathcal{R}}_{n+1}^{T} \end{cases}. \tag{2.93}$$

Conclusion

In this chapter, the formulation of four assumed-strain based solid–shell elements has been presented. With respect to the earlier developments, the formulation of these elements has been extended here to the framework of large strains and advanced constitutive equations, including isotropic behavior, orthotropic elastic behavior for laminated composite materials and anisotropic plastic behavior for metallic materials. In addition, the quasi-static versions of the SHB solid–shell elements have been extended to the explicit dynamic framework for the simulation of impact problems and complex processes that are difficult to perform using quasi-static solvers. Based on a convenient fully three-dimensional framework, with only translational degrees of freedom and few through-thickness integration points, these elements appear to be very attractive, as they are able to accurately reproduce shell-like behavior using only a single element layer. The resulting SHB elements have been implemented into ABAQUS static/implicit and dynamic/explicit software packages in order to extend their application range to nonlinear quasi-static and dynamic analyses as well as the simulation of complex and challenging sheet metal forming processes.

Chapter 3

Validation of the SHB family elements

Introduction

In this chapter, a variety of popular benchmark tests, including linear and nonlinear problems, is selected to evaluate the performance of the proposed SHB elements, both in static and dynamic analyses. As stated in the previous chapter, all SHB elements have been implemented into ABAQUS using both standard/quasi-static and explicit/dynamic solvers. For comparison purposes, the results obtained with the SHB elements are consistently compared with analytical and reference solutions as well as with the numerical results yielded by ABAQUS solid and shell elements.

First, the performance of the proposed SHB elements is validated through classical linear benchmark problems, in the framework of small strain and isotropic elastic behavior. Then, a series of selective and representative nonlinear benchmark tests (involving large rotations, large strain, material nonlinearity …) is conducted to assess the performance of the SHB elements in quasi-static and dynamic analyses. In the subsequent benchmark tests, all geometries are discretized using the following nomenclature. For hexahedral elements, meshes of $N_1 \times N_2 \times N_3$ elements are adopted, where N_1 denotes the number of elements in the length direction, N_2 is the number of elements in the width direction, and N_3 is the number of elements in the thickness direction. For meshes with prismatic elements, the nomenclature adopted is $(N_1 \times N_2 \times 2) \times N_3$, which corresponds to twice the total number of elements involved in hexahedron-based meshes, due to the subdivision of each hexahedron into two prisms. For ABAQUS shell elements, the nomenclature adopted for quadrilateral shell elements is $N_1 \times N_2$, while the nomenclature for triangular shell elements is $N_1 \times N_2 \times 2$. It is also worth noting that an arbitrary number of integration points can be arranged through the thickness for the SHB elements. In this chapter, only two integration points are sufficient to model linear and nonlinear elastic benchmark tests, while three integration points are used in the case of elasto-plastic benchmark problems. Tables 3.1 and 3.2 summarize the description of all finite elements used for comparison purposes.

Table 3.1. Prismatic, hexahedral and shell finite elements used in the quasi-static analysis.

Linear elements	Prismatic elements / Triangular shell element	SHB6	6-node prismatic solid–shell element with a user-defined number of through-thickness integration points
		C3D6	6-node prismatic solid element with two integration points through the thickness
		S3	3-node triangular shell element with a user-defined number of through-thickness integration points
	Hexahedral elements / Quadrilateral shell element	SHB8PS	8-node hexahedral solid–shell element with a user-defined number of through-thickness integration points
		C3D8R	8-node reduced-integration hexahedral solid element with one integration point through the thickness
		S4R	4-node quadrilateral shell element with a user-defined number of through-thickness integration points
Quadratic elements	Prismatic elements / Triangular shell element	SHB15	15-node prismatic solid–shell element with a user-defined number of through-thickness integration points
		C3D15	15-node prismatic solid element with three integration points through the thickness
		STRI65	6-node triangular shell element with a user-defined number of through-thickness integration points
	Hexahedral elements / Quadrilateral shell element	SHB20	20-node hexahedral solid–shell element with a user-defined number of through-thickness integration points
		C3D20	20-node hexahedral solid element with three integration points through the thickness
		S8R	8-node quadrilateral shell element with a user-defined number of through-thickness integration points

Table 3.2. Prismatic, hexahedral and shell finite elements used in the dynamic analysis.

Linear elements	Prismatic elements / Triangular shell element	SHB6	6-node prismatic solid–shell element with a user-defined number of through-thickness integration points
		C3D6	6-node prismatic solid element with one integration point through the thickness
		S3R	3-node triangular shell element with a user-defined number of through-thickness integration points
	Hexahedral elements / Quadrilateral shell element	SHB8PS	8-node hexahedral solid–shell element with a user-defined number of through-thickness integration points
		C3D8R	8-node reduced-integration hexahedral solid element with one integration point through the thickness
		S4R	4-node quadrilateral shell element with a user-defined number of through-thickness integration points
Quadratic elements	Prismatic element	SHB15	15-node prismatic solid–shell element with a user-defined number of through-thickness integration points
	Hexahedral element	SHB20	20-node hexahedral solid–shell element with a user-defined number of through-thickness integration points

3.1 Linear benchmark problems

The following first four linear tests are performed to examine the convergence rate of the SHB elements. Then, the SHB elements are evaluated in the framework of vibration analysis (i.e., for the calculation of eigenfrequencies of thin plate structures). For comparison purposes, the results obtained with the SHB elements are consistently compared with reference solutions as well as with the results given by ABAQUS solid elements.

3.1.1 Linear static beam problems

3.1.1.1 Elastic cantilever beam subjected to out-of-plane bending forces

The first linear static test is an elastic cantilever beam with four concentrated loads at its free end. The geometric dimensions and material parameters for this test are given in Fig. 3.1. This simple test aims to analyze the behavior of the SHB elements in the case of bending-dominated conditions. The analytical solution for the deflection at the load point is U_{ref} = 7.326×10^{-3} m. The convergence results are given in Tables 3.3 and 3.4, in terms of normalized

deflection with respect to the analytical solution, with comparison to ABAQUS solid elements. These simulation results show that all of the SHB elements provide an excellent convergence rate, with nevertheless a slower convergence rate for the linear prismatic element SHB6. For the latter element, this is quite expectable, since its triangular geometry and the associated linear interpolation functions lead to constant strain fields in the element, which requires finer meshes to obtain accurate solutions (see, e.g., Trinh et al., 2011).

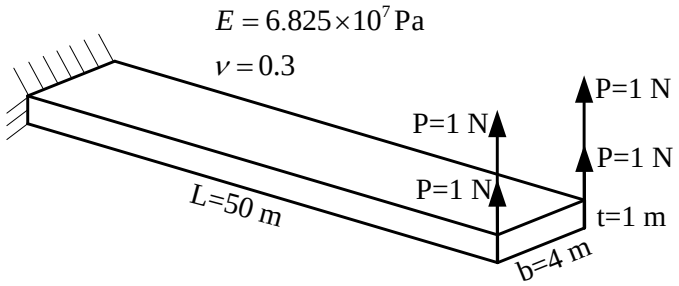


Figure 3.1. Elastic cantilever beam subjected to out-of-plane bending forces.

Table 3.3. Normalized deflection results for the cantilever beam under out-of-plane bending using linear elements.

Mesh	SHB6	Mesh	C3D6	Mesh	SHB8PS	Mesh	C3D8R
	U/U_{ref}		U/U_{ref}		U/U_{ref}		U/U_{ref}
12×2×2×1	0.7062	12×2×2×1	0.3632	5×1×1	0.9750	5×1×2	1.3117
24×2×2×1	0.9019	24×2×2×1	0.6466	10×1×1	0.9898	10×1×2	1.3224
48×2×2×1	0.9669	48×2×2×1	0.7869	12×4×1	0.9898	12×4×2	1.3142
100×4×2×1	0.9807	100×4×2×1	0.8595	24×4×1	0.9933	24×4×2	1.3187

Table 3.4. Normalized deflection results for the cantilever beam under out-of-plane bending using quadratic elements.

Mesh	SHB15	Mesh	C3D15	Mesh	SHB20	Mesh	C3D20
	U/U_{ref}		U/U_{ref}		U/U_{ref}		U/U_{ref}
12×2×2×1	0.9896	12×2×2×1	0.9806	2×1×1	0.9672	2×1×1	0.8401
24×2×2×1	0.9925	24×2×2×1	0.9874	5×1×1	0.9865	5×1×1	0.9459
				10×1×1	0.9929	10×1×1	0.9738

3.1.1.2 Elastic cantilever beam subjected to in-plane bending forces

The second linear static test is selected to evaluate the behavior of the proposed SHB elements in the case of in-plane transverse shearing and bending forces. Fig. 3.2 provides the geometric and material parameters for this test. Considering the in-plane loading condition, this benchmark test allows, in particular, the assessment of the membrane behavior of the investigated elements. The reference deflection at the loading point, which is given analytically using Airy's function solution for plane-stress problems, is equal to $U_{ref} = 0.3573$. The convergence results of all SHB elements are reported in Tables 3.5 and 3.6, with comparison to ABAQUS solid elements. One can observe the good convergence rate of the proposed SHB elements with respect to their ABAQUS solid counterparts, which indicates that no membrane locking has been encountered in this test.

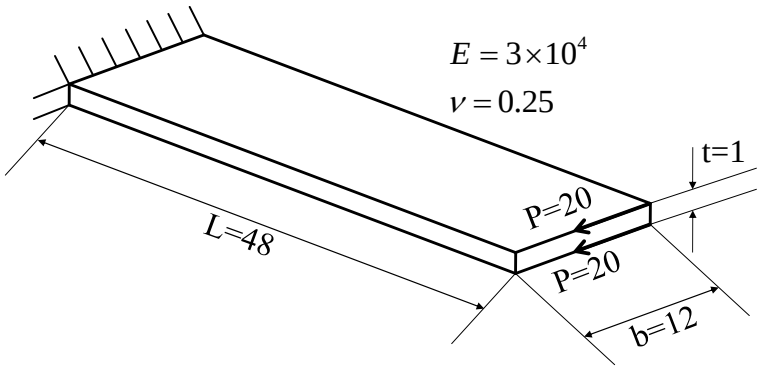


Figure 3.2. Elastic cantilever beam subjected to in-plane bending forces.

Table 3.5. Normalized deflection results for the cantilever beam under in-plane bending using linear elements.

Mesh	SHB6	Mesh	C3D6	Mesh	SHB8PS	Mesh	C3D8R
	U/U_{ref}		U/U_{ref}		U/U_{ref}		U/U_{ref}
6×(4×2)×1	0.6219	6×(4×2)×1	0.6177	2×1×1	0.8785	2×1×2	79.457
12×(4×2)×1	0.8122	12×(4×2)×1	0.8079	2×2×1	0.9034	2×2×2	1.2841
24×(4×2)×1	0.8722	24×(4×2)×1	0.8681	3×2×1	0.9430	3×2×2	1.3778
16×(16×2)×1	0.9285	16×(16×2)×1	0.9246	6×4×1	0.9852	6×4×2	1.1178
32×(16×2)×1	0.9835	32×(16×2)×1	0.9808	12×4×1	0.9974	12×4×2	1.1875

Table 3.6. Normalized deflection results for the cantilever beam under in-plane bending using quadratic elements.

Mesh	SHB15	Mesh	C3D15	Mesh	SHB20	Mesh	C3D20
	U/U_{ref}		U/U_{ref}		U/U_{ref}		U/U_{ref}
2×(1×2)×1	0.949	2×(1×2)×1	0.946	2×1×1	0.967	2×1×1	0.935
4×(2×2) ×1	0.965	4×(2×2) ×1	0.953	2×2×1	0.988	2×2×1	0.952
6×(2×2) ×1	0.987	6×(2×2) ×1	0.979	3×2×1	0.995	3×2×1	0.974
6×(4×2)×1	0.998	6×(4×2)×1	0.993	6×4×1	1.004	6×4×1	0.991
12×(4×2) ×1	1.003	12×(4×2) ×1	1.000				

3.1.1.3 Elastic cantilever beam subjected to torsion-type forces

The third linear static test is illustrated in Fig. 3.3 and consists of a cantilever beam subjected to torsion-type loading. The free end of the beam is loaded by two opposite concentrated forces causing twisting-type loading along the beam. The geometric and material parameters are given in Fig. 3.3. In the same way as before, the deflection results at one load point, normalized with respect to the reference solution $U_{ref} = 3.537\times10^{-2}$ m, are reported in Tables 3.7 and 3.8. Similar to the previous test problems, the simulation results show again that all of the SHB elements provide a good convergence rate, when compared to their ABAQUS solid counterparts, without noticeable locking phenomena, except for the linear prismatic element SHB6 that requires finer meshes for convergence.

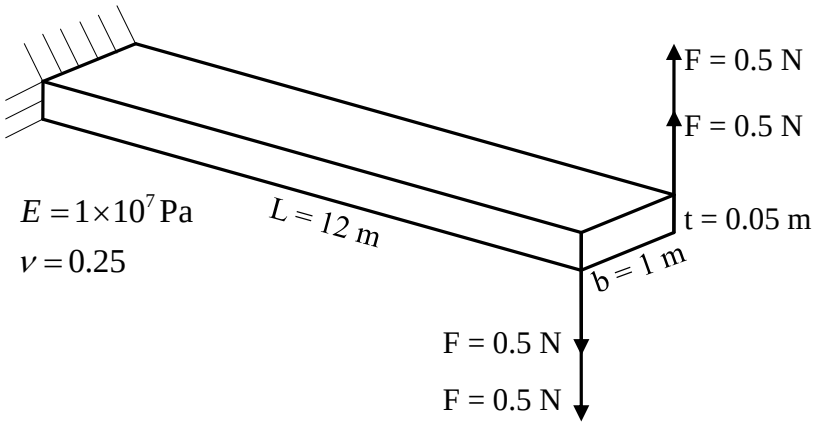


Figure 3.3. Elastic cantilever beam subjected to torsion-type loading.

Table 3.7. Normalized deflection results for the cantilever beam under torsion-type loading using linear elements.

Mesh	SHB6	Mesh	C3D6	Mesh	SHB8PS	Mesh	C3D8R
	U/U_{ref}		U/U_{ref}		U/U_{ref}		U/U_{ref}
10×5×2×1	0.0107	10×5×2×1	0.0251	10×5×1	1.0470	10×5×2	0.0039
20×5×2×1	0.0247	20×5×2×1	0.0188	20×5×1	1.0479	20×5×2	0.0153
50×5×2×1	0.0916	50×5×2×1	0.0535	50×5×1	1.0500	50×5×2	0.0900
50×10×2×1	0.3438	50×10×2×1	0.1303	50×10×1	1.0289	50×10×2	0.2983
100×20×2×1	1.0873	100×20×2×1	0.3257				

Table 3.8. Normalized deflection results for the cantilever beam under torsion-type loading using quadratic elements.

Mesh	SHB15	Mesh	C3D15	Mesh	SHB20	Mesh	C3D20
	U/U_{ref}		U/U_{ref}		U/U_{ref}		U/U_{ref}
10×5×2×1	0.9783	10×5×2×1	0.9403	10×5×1	1.0278	10×5×1	0.9883
20×5×2×1	1.0111	20×5×2×1	0.9896	20×5×1	1.0280	20×5×1	0.9987

3.1.1.4 Elastic twisted beam subjected to bending forces

The twisted beam problem, as introduced by MacNeal and Harder (1985), is another popular benchmark test for the validation of new finite elements (see, e.g., Belytschko and Bindeman, 1993; Chen and Stolarski, 1998; Fontes Valente, 2004; Cardoso et al., 2008; Schwarze and Reese, 2009). As shown in Fig. 3.4, the twisted beam is clamped at one side, while it is free at the other side. Two typical bending conditions, the in-plane bending force $P=1$ in the *y*-direction, and the out-of-plane bending force $F=1$ in the *x*-direction, are considered here to evaluate the performance of the SHB elements. The deflection at the corner point A (see Fig. 3.4) is analyzed. The reference solutions corresponding to both in-plane bending case and out-of-plane bending case are $V_{ref} = 5.42\times10^{-3}$ and $U_{ref} = 1.75\times10^{-3}$, respectively (see MacNeal and Harder, 1985).

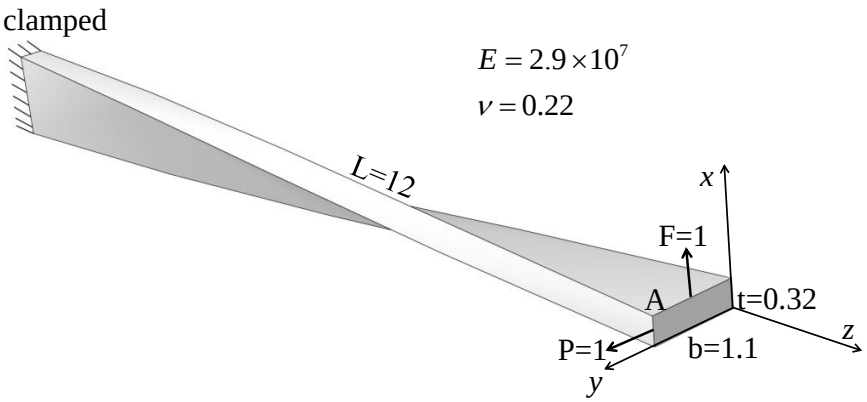


Figure 3.4. Elastic twisted beam subjected to bending forces.

The normalized deflection results for both in-plane bending and out-of-plane bending cases are summarized in Tables 3.9 to 3.12, respectively. On the whole, one can notice the very good convergence rate of the SHB elements, when compared to their ABAQUS solid counterparts; especially the quadratic SHB20 element, for which only few elements in the length direction of the twisted beam are sufficient to obtain an accurate solution.

Table 3.9. Normalized deflection results for the elastic twisted beam under in-plane bending using linear elements.

Mesh	SHB6	Mesh	C3D6	Mesh	SHB8PS	Mesh	C3D8R
	V/V_{ref}		V/V_{ref}		V/V_{ref}		V/V_{ref}
6×(2×2)×1	0.5745	6×(2×2)×1	0.2316	4×2×1	0.9954	4×2×2	1.3296
12×(4×2)×1	0.8027	12×(4×2)×1	0.4578	6×2×1	0.9958	6×2×2	1.3282
24×(4×2)×1	0.9379	24×(4×2)×1	0.7451	8×2×1	0.9968	8×2×2	1.3289
36×(8×2)×1	0.9707	36×(8×2)×1	0.8333	10×2×1	0.9976	10×2×2	1.3298

Table 3.10. Normalized deflection results for the elastic twisted beam under in-plane bending using quadratic elements.

Mesh	SHB15	Mesh	C3D15	Mesh	SHB20	Mesh	C3D20
	V/V_{ref}		V/V_{ref}		V/V_{ref}		V/V_{ref}
4×(2×2)×1	0.8118	4×(2×2)×1	0.9451	4×2×1	0.994	4×2×1	0.910
6×(2×2) ×1	0.9278	6×(2×2) ×1	0.9740	6×2×1	0.998	6×2×1	0.965
8×(2×2) ×1	0.9668	8×(2×2) ×1	0.9841	8×2×1	1.000	8×2×1	0.980
10×(2×2)×1	0.9824	10×(2×2)×1	0.9887				

Table 3.11. Normalized deflection results for the elastic twisted beam under out-of-plane bending using linear elements.

Mesh	SHB6	Mesh	C3D6	Mesh	SHB8PS	Mesh	C3D8R
	U/U_{ref}		U/U_{ref}		U/U_{ref}		U/U_{ref}
6×(2×2)×1	0.5725	6×(2×2)×1	0.2286	4×2×1	0.9080	4×2×2	1.2629
12×(4×2)×1	0.8059	12×(4×2)×1	0.4642	6×2×1	0.9564	6×2×2	1.2994
24×(4×2)×1	0.9297	24×(4×2)×1	0.7440	8×2×1	0.9737	8×2×2	1.3126
36×(8×2)×1	0.9743	36×(8×2)×1	0.8450	10×2×1	0.9819	10×2×2	1.3188

Table 3.12. Normalized deflection results for the elastic twisted beam under out-of-plane bending using quadratic elements.

Mesh	SHB15	Mesh	C3D15	Mesh	SHB20	Mesh	C3D20
	U/U_{ref}		U/U_{ref}		U/U_{ref}		U/U_{ref}
4×(2×2)×1	0.8552	4×(2×2)×1	0.9479	4×2×1	0.9985	4×2×1	0.9388
6×(2×2) ×1	0.9434	6×(2×2) ×1	0.9820	6×2×1	1.0007	6×2×1	0.9791
8×(2×2) ×1	0.9746	8×(2×2) ×1	0.9924				
10×(2×2)×1	0.9874	10×(2×2)×1	0.9964				

3.1.2 Plate vibration problems

3.1.2.1 Simple rectangular cantilever plate

The first plate vibration problem applies to a rectangular cantilever plate with constant thickness. As illustrated in Fig. 3.5, the rectangular plate, with length L, width b=L/2 and thickness t, is fully clamped at one side, while the other sides are totally free. The predicted results, in terms of non-dimensional frequency coefficient $\omega/\sqrt{D/\rho tL^4}$, associated with the first four natural frequencies ω are summarized in Tables 3.13 and 3.14 for the linear and quadratic elements, respectively, where $D = Et^3/12(1-\nu^2)$ is the flexural rigidity of the plate, E and ν are the Young modulus and Poisson ratio, respectively. All predicted results using the SHB8PS, SHB20 and SHB15 elements are in good agreement with the theoretical results as well as with the reference solutions given by Barton (1951) and Anderson et al. (1968). For the linear prismatic SHB6 element, due to its relatively poor performance, finer meshes are required to obtain relatively accurate solutions. However, one can note that, using the same

in-plane mesh, the SHB solid–shell elements provide the closest results with respect to the reference solutions, as compared to their ABAQUS solid counterparts.

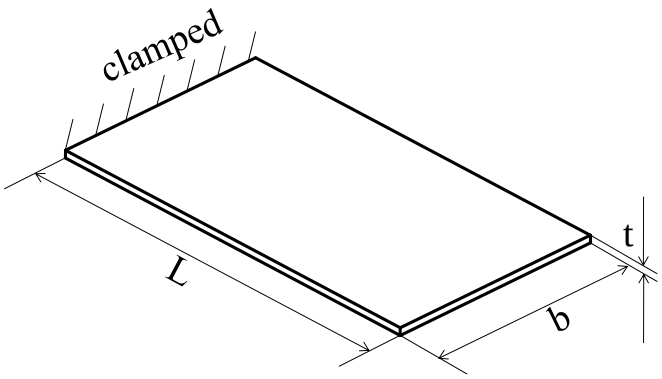


Figure 3.5. Simple rectangular cantilever plate as proposed by Anderson et al. (1968).

Table 3.13. Natural frequency coefficients for the rectangular cantilever plate using linear elements.

Mode	Theoretical results*	Experimental results*	Simulated results**	SHB6	C3D6	SHB8PS	C3D8R
				400×200×2×1	400×200×2×1	20×10×1	20×10×2
1	3.47	3.42	3.44	4.022	4.61	3.44	3.050
2	14.93	14.52	14.77	20.51	27.11	14.66	19.11
3	21.26	20.86	21.50	28.03	31.53	21.42	53.63
4	48.71	46.9	48.19	59.97	76.89	47.69	105.57

Note: results marked by * are taken from Barton (1951), while results marked by ** are available in Anderson et al. (1968).

Table 3.14. Natural frequency coefficients for the rectangular cantilever plate using quadratic elements.

Mode	Theoretical results*	Experimental results*	Simulated results**	SHB15	C3D15	SHB20	C3D20
				10×5×2×1	10×5×2×1	10×5×1	10×5×1
1	3.47	3.42	3.44	3.44	3.52	3.44	3.52
2	14.93	14.52	14.77	14.56	16.47	14.46	14.97
3	21.26	20.86	21.50	21.43	22.02	21.22	22.11
4	48.71	46.9	48.19	47.63	56.00	46.95	49.22

Note: results marked by * are taken from Barton (1951), while results marked by ** are available in Anderson et al. (1968).

3.1.2.2 Fully clamped square plate

The second plate vibration problem relates to a fully clamped square plate, as illustrated in Fig. 3.6. The length to thickness ratio for this square plate is fixed equal to 1000, and the Poisson ratio of the material is 0.3. For comparison with reference solutions from the literature, the non-dimensional frequency coefficient λ is calculated for the first six natural frequencies of the plate, which is defined as $\lambda^2 = \omega L^2 \sqrt{\rho t / D}$, where D is the flexural rigidity defined in the previous test problem. All predicted frequency coefficients obtained using the SHB elements and ABAQUS solid elements, along with reference solutions taken from Leissa (1969) and Sze and Yao (2000), are summarized in Tables 3.15 and 3.16. Similar to the previous vibration problem, the obtained results show the performance and efficiency of the SHB elements in determining the natural frequencies of plates, except for the linear prismatic SHB6 element, for which finer meshes are inherently required to obtain accurate results. Also, note that linear ABAQUS solid elements provided the farthest results with respect to the reference natural frequencies.

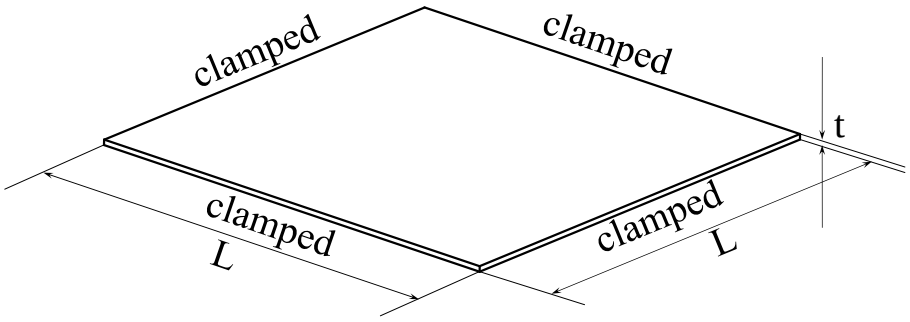


Figure 3.6. Geometry and boundary conditions for the clamped square plate.

Table 3.15. Natural frequency coefficients for the clamped square plate using linear elements.

Mode	Reference solution*	Simulated results**	SHB6	C3D6	SHB8PS	C3D8R
			400×400×2×1	400×400×2×1	16×16×1	16×16×2
1	5.999	6.024	6.659	7.376	6.004	87.583
2,3	8.567	8.671	9.079	10.104	8.599	110.65
4	10.4	10.52	11.337	12.632	10.387	120.25
5,6	11.5	11.78	12.257	13.783	11.590	120.44

Note: results marked by * are taken from Leissa (1969), while results marked by ** are taken from Sze and Yao (2000).

Table 3.16. Natural frequency coefficients for the clamped square plate using quadratic elements.

Mode	Reference solution*	Simulated results**	SHB15	C3D15	SHB20	C3D20
			16×16×2×1	16×16×2×1	16×16×1	16×16×1
1	5.999	6.024	6.027	6.303	6.012	6.093
2,3	8.567	8.671	8.632	9.082	8.605	8.776
4	10.4	10.52	10.533	11.577	10.545	10.888
5,6	11.5	11.78	11.614	12.421	11.523	11.852

Note: results marked by * are taken from Leissa (1969), while results marked by ** are taken from Sze and Yao (2000).

3.2 Nonlinear benchmark problems

3.2.1 Quasi-static analysis

3.2.1.1 Simply supported elastic square plate

Figure 3.7 illustrates a simply supported isotropic elastic square plate subjected to a central concentrated force. The detailed information about the geometric dimensions and the elastic material parameters is given in Fig. 3.7. The maximum of the concentrated load F is equal to 300. Due to symmetry, only one quarter of the plate is analyzed.

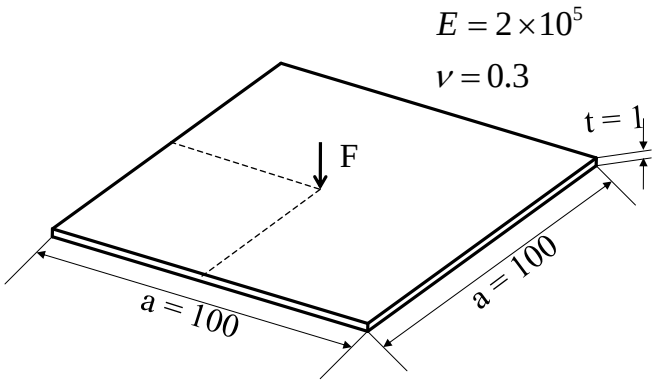
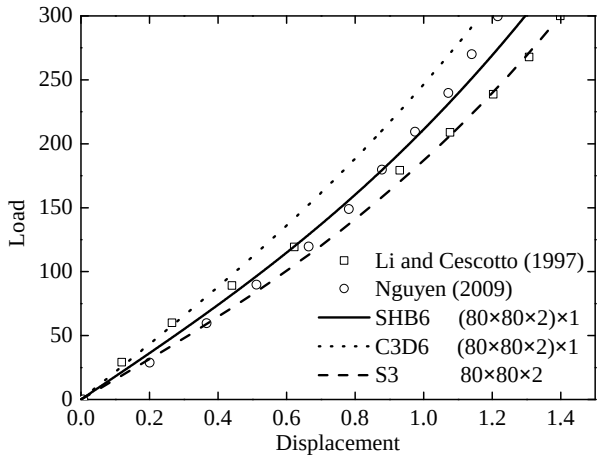
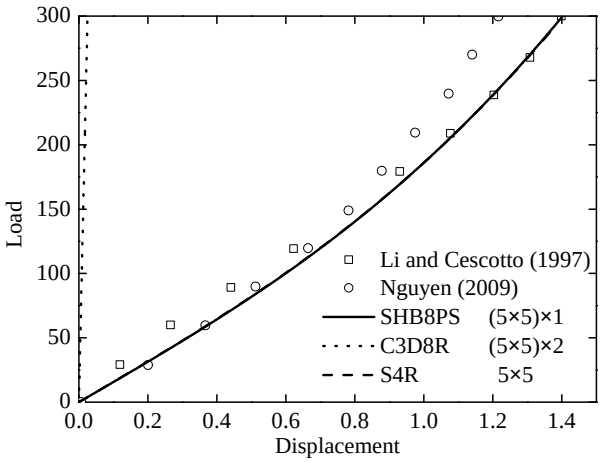


Figure 3.7. Geometric and material parameters for the simply supported square plate.

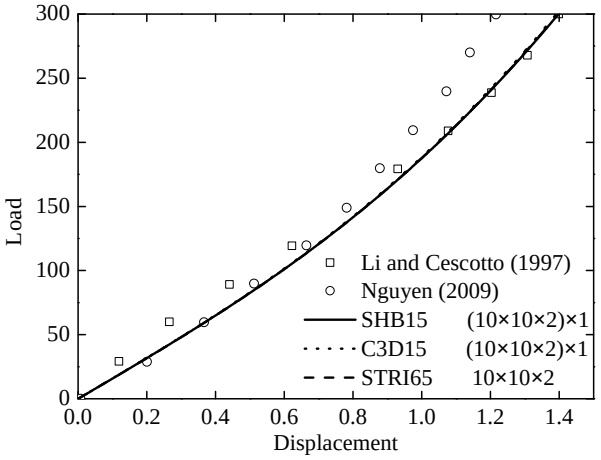
The load–displacement results at the central point of the plate given by the SHB elements are compared in Fig. 3.8 with those yielded by ABAQUS elements and also with the reference solutions taken from Li and Cescotto (1997) and Nguyen (2009).



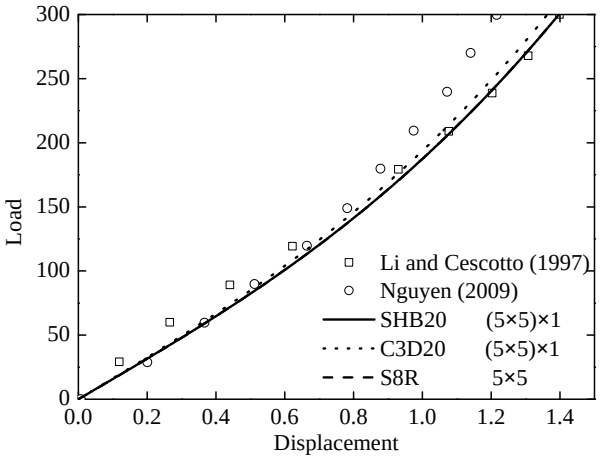
(a) linear prismatic/triangular elements



(b) linear hexahedral/quadrilateral elements



(c) quadratic prismatic/triangular elements



(d) quadratic hexahedral/quadrilateral elements

Figure 3.8. Load–displacement curves for the simply supported square plate.

In the case of triangular-based linear elements (Fig. 3.8 (a)), the results given by the SHB6 element are closer to the reference solutions than those given by the ABAQUS prismatic solid element (C3D6), while the results yielded by the ABAQUS triangular shell element (S3) are in agreement with one of the reference solutions (i.e., that taken from Li and Cescotto (1997)). For the quadrangular-based linear elements (Fig. 3.8 (b)), the load–displacement results given by the SHB8PS element are very close to those obtained with the ABAQUS quadrilateral shell element (S4R) as well as to the reference solution taken from Li and Cescotto (1997). Note that, using the same in-plane mesh as that used for the SHB8PS and S4R elements, the load–displacement curve given by the linear ABAQUS hexahedral solid element (C3D8R) lies very far from the reference solution, which suggests resorting to much finer meshes for this element. In the case of quadratic elements (Fig. 3.8 (c) and (d)), the results given by the

solid–shell elements SHB15 and SHB20 agree very well with the reference solution taken from Li and Cescotto (1997), as well as with the results obtained with the ABAQUS quadratic elements (namely, the prismatic solid element C3D15, the triangular shell element STRI65, and the quadrilateral shell element S8R), while the hexahedral solid element C3D20 is slightly stiffer.

3.2.1.2 Cantilever plate subjected to a concentrated force

An elastic cantilever plate with a concentrated force at one corner, as proposed by Hsiao (1987), is considered here. The geometric dimensions, elastic properties, and boundary conditions of the problem are all summarized in Fig. 3.9.

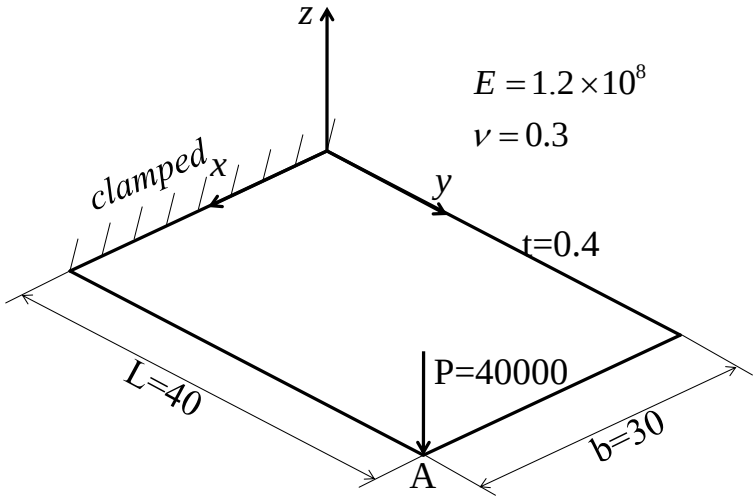
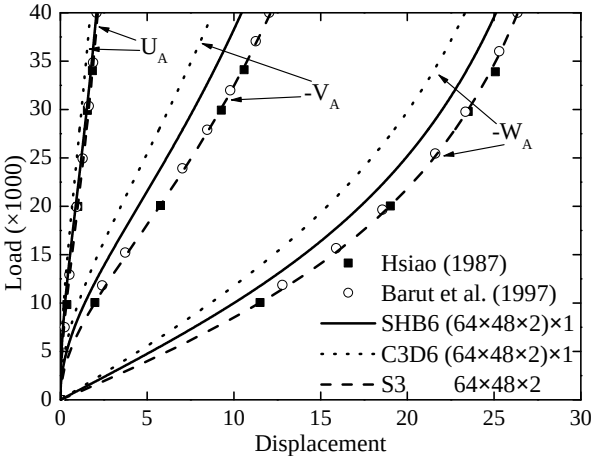
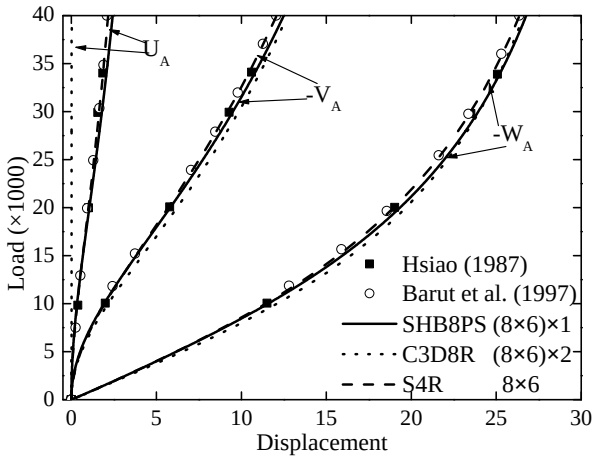


Figure 3.9. Geometric and material parameters for the cantilever plate.

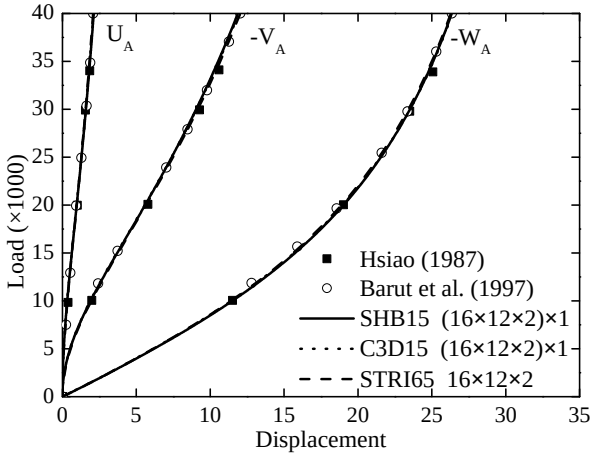
Figure 3.10 reports the load–displacement curves at the corner point A, in the *x*, *y*, and *z* directions (see Fig. 3.9). In this Fig. 3.10, the results obtained with the SHB elements are compared with those given by ABAQUS solid and shell elements, on the one hand, and with the reference solutions given by Hsiao (1987) and Barut et al. (1997), on the other hand. These comparisons reveal that, overall, the results given by the SHB elements are in very good agreement with the reference solutions, which is also the case with the ABAQUS shell elements and ABAQUS solid elements C3D8R and C3D15. However, adopting the same in-plane mesh as that used for the SHB20 and S8R elements (i.e., 4×3×1 elements), the solution given by the ABAQUS solid element C3D20 falls very far from the reference solution (see Fig. 3.10 (d)), which suggests the need for resorting to a finer mesh to achieve an accurate solution.



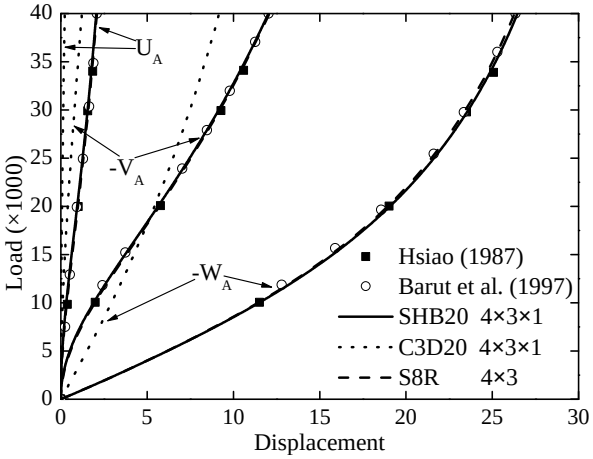
(a) linear prismatic/triangular elements



(b) linear hexahedral/quadrilateral elements



(c) quadratic prismatic/triangular elements



(d) quadratic hexahedral/quadrilateral elements

Figure 3.10. Load–displacement curves for the cantilever plate under a concentrated force.

3.2.1.3 Pinched semi-cylindrical shell

The pinched semi-cylindrical shell, as shown in Fig. 3.11, is a popular benchmark test that has been considered in several references (see, e.g., Stander et al., 1989; Klinkel et al., 1999; Sze et al., 2004), where both isotropic and laminated shells have been studied. This semi-cylindrical shell is subjected to a vertical radial force at the middle of the free circumferential edge, while the other circumferential edge is fully clamped (see Fig. 3.11 for the geometric and material parameters as well as the remaining boundary conditions). Only the case of isotropic elastic behavior is considered here. Due to the symmetry of the problem, only one half of the structure is modeled.

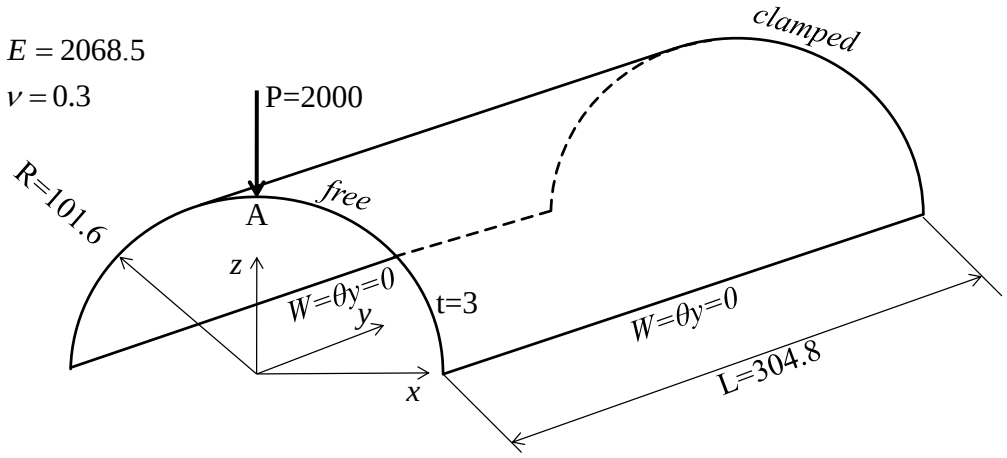
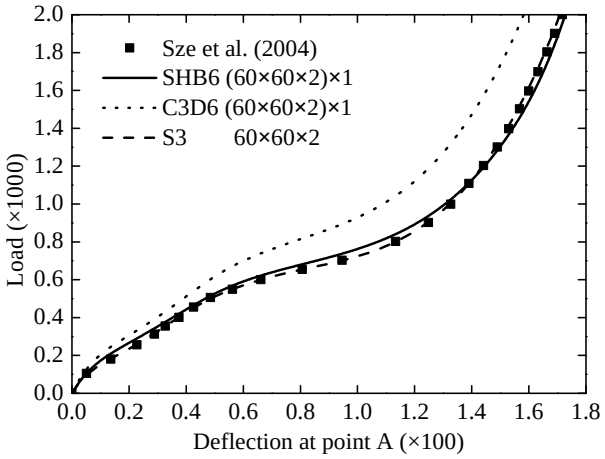


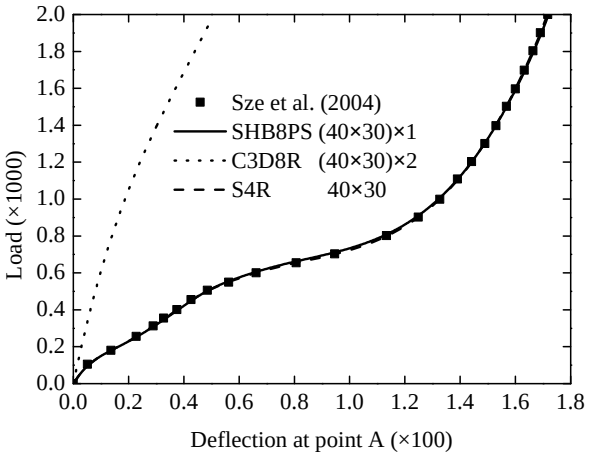
Figure 3.11. Geometric and material parameters for the pinched semi-cylindrical shell.

Figure 3.12 displays the load–deflection curves at the load point A, which are obtained using the SHB elements and ABAQUS elements, along with the reference solution available in Sze et al. (2004). The simulation results obtained by using the SHB elements show a good agreement with the reference solution given in Sze et al. (2004), the latter was obtained using (40×40×1) shell elements. Note that, using the same in-plane meshes as for the SHB elements, the load–deflection curves given by the ABAQUS C3D6, C3D8R and C3D20 solid elements lie far from the reference solution, while the ABAQUS STRI65 quadratic shell element failed to converge for this benchmark test.

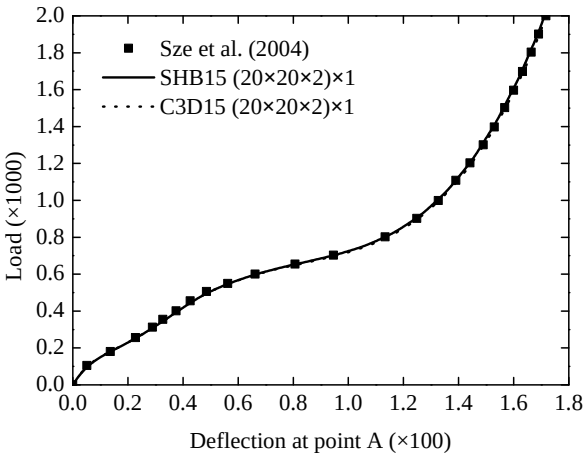
Besides the good performance shown for the proposed SHB elements, in terms of accuracy, it is important to compare their computation times with those yielded by ABAQUS elements. Such a comparison is shown here for the case of the pinched semi-cylindrical shell test. It is worth noting that ABAQUS elements are implemented by experts who are experienced in computer programming, which leads to efficient and highly optimized FE implementations, while the current FE implementation of the proposed SHB elements is far from being well optimized. Therefore, the aim of the following comparative study is not to directly compare the computation times involved by the SHB and ABAQUS elements, but only to provide the reader with an order of magnitude of the respective FE computation times required.



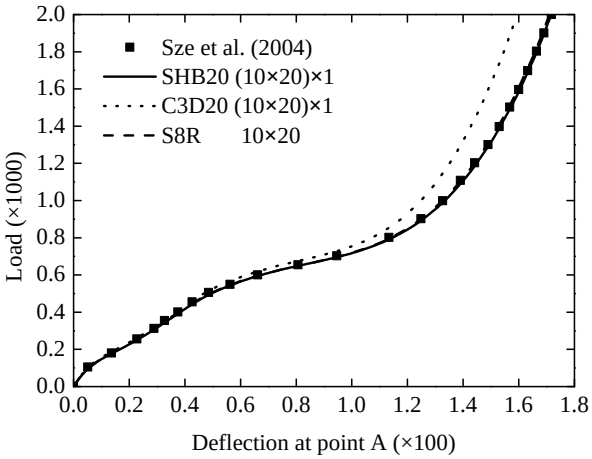
(a) linear prismatic/triangular elements



(b) linear hexahedral/quadrilateral elements



(c) quadratic prismatic/triangular elements



(d) quadratic hexahedral/quadrilateral elements

Figure 3.12. Load–deflection curves for the pinched semi-cylindrical shell.

Table 3.17 reports the respective CPU times required by the SHB elements and ABAQUS solid elements for the pinched semi-cylindrical shell problem (all simulations are based on ABAQUS 6.11 version using only one CPU). On the whole, it can be seen that the CPU times required by the ABAQUS solid elements are slightly higher than those involved by the SHB elements. However, as discussed above, in many situations, the ABAQUS solid elements require very fine in-plane meshes with several layers to achieve accurate (converged) solutions, which will result in even higher CPU times in comparison with the proposed SHB elements.

Table 3.17. Computation details for the pinched semi-cylindrical shell problem.

Element	Total number of elements	Number of layers	Number of integration points per element	Number of DOFs	CPU time (s)
SHB6	7200	1	2	7442×3	1409
C3D6	7200	1	2	7442×3	1326
SHB8PS	1200	1	2	2542×3	433
C3D8R	2400	2	1	3813×3	548
SHB15	800	1	3×2	3803×3	672
C3D15	800	1	3×3	3803×3	759
SHB20	200	1	2×2×2	1553×3	358
C3D20	200	1	3×3×3	1553×3	481

3.2.1.4 Pinched elastic–plastic hemispherical shell

A pinched hemispherical shell is considered here, which is loaded by alternating radial forces as shown in Fig. 3.13. This test is very popular since it involves both geometric and material nonlinearities. Owing to the problem symmetry, only one quarter of the structure is modeled. In addition to the mesh nomenclature previously defined, three partitions for the quarter of the hemispherical shell are created in order to achieve a relatively regular mesh (see Fig. 3.13). This leads to the following new mesh nomenclature for this test: $(3\times(N_1\times N_1))\times N_3$ for hexahedral elements, where N_1 indicates the number of elements along each edge and N_3 the number of elements in the thickness direction (see Fig. 3.14). For the prismatic elements, the total number of elements is twice that corresponding to hexahedral elements, which leads to $(3\times(N_1\times N_1\times 2))\times N_3$ elements. For the quadrilateral shell elements, the nomenclature for discretizing the quarter model is $3\times(N_1\times N_1)$, while this nomenclature is $3\times(N_1\times N_1\times 2)$ when triangular shell elements are used.

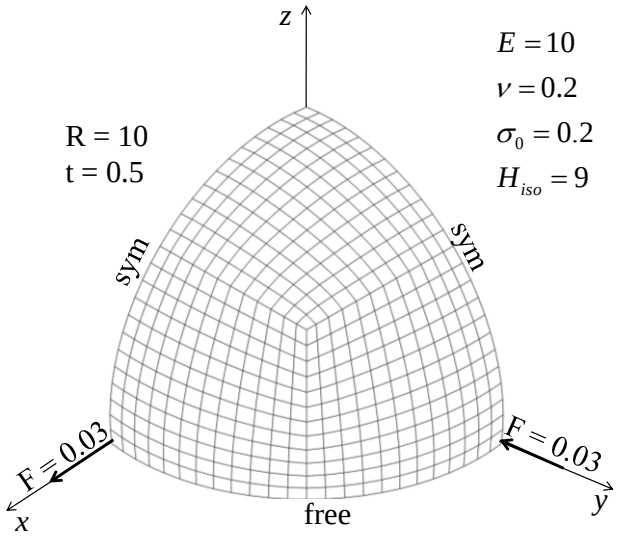


Figure 3.13. Geometric and material parameters for the pinched hemispherical shell.

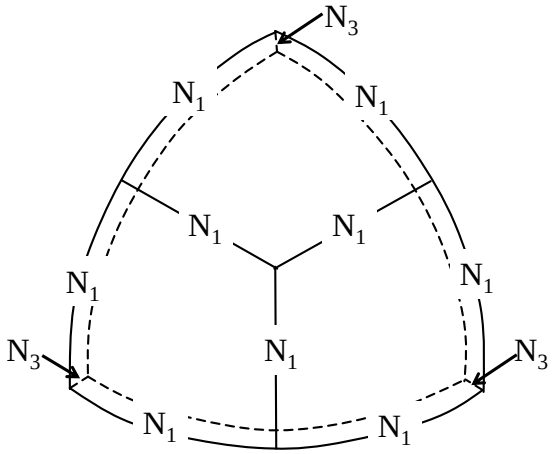
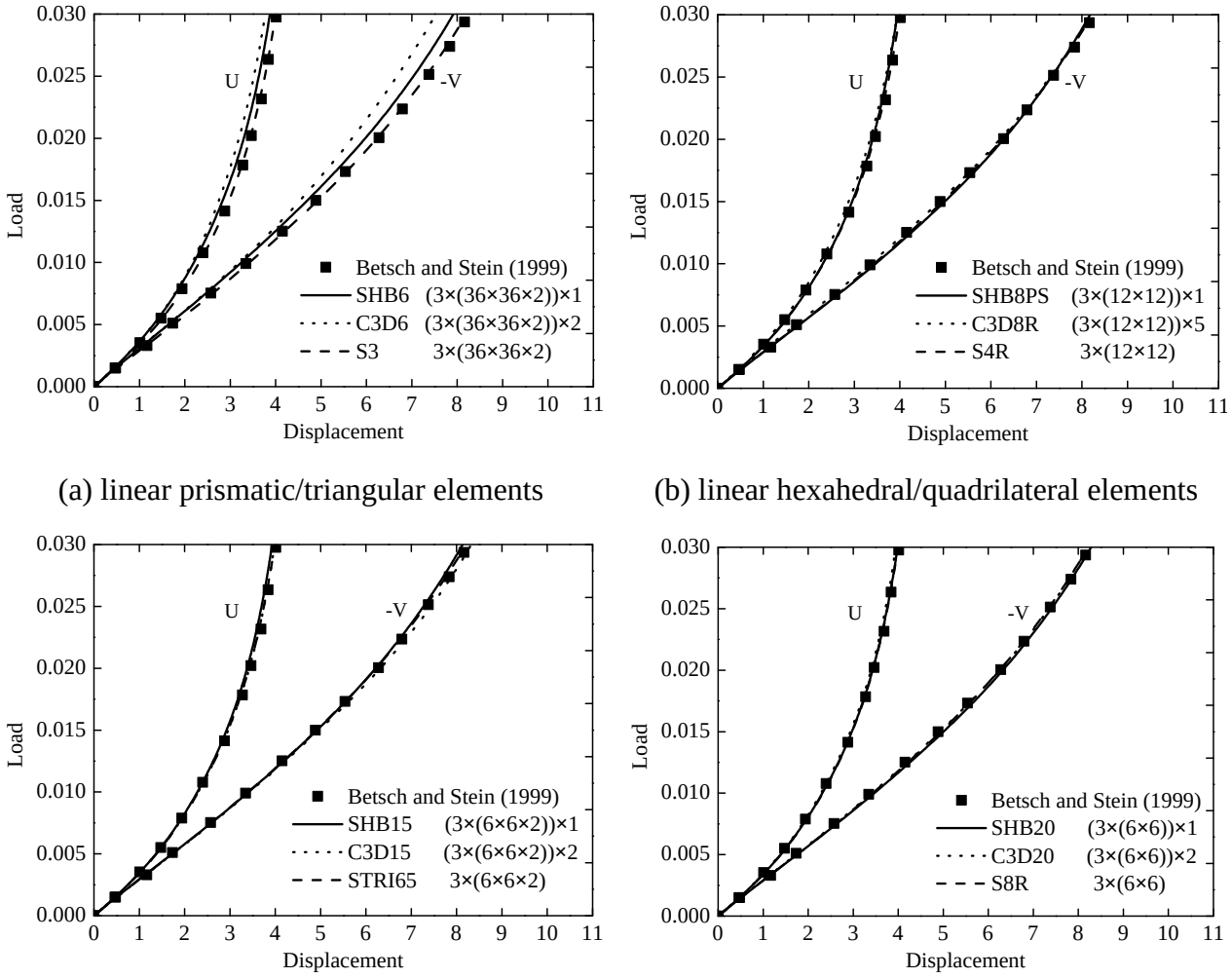


Figure 3.14. Illustration of the mesh nomenclature for the pinched hemispherical shell.

In Fig. 3.15, the displacements at the loading points in the *x* and *y* directions (namely, U and V, respectively) obtained with the SHB elements are compared with those given by ABAQUS elements as well as with the reference solution taken from Betsch and Stein (1999). Overall, all SHB and ABAQUS elements provide accurate results with respect to the reference solution, except for the SHB6 and C3D6 elements, which exhibit some relative over-stiffness (due to locking) and require finer meshes for this test problem. Note also that the proposed solid–shell elements are more efficient than their counterparts ABAQUS solid elements, since the latter require several layers of elements (up to 5 for the C3D8R) to provide comparable accuracy (see Fig. 3.15).



(a) linear prismatic/triangular elements (b) linear hexahedral/quadrilateral elements

(c) quadratic prismatic/triangular elements (d) quadratic hexahedral/quadrilateral elements

Figure 3.15. Load–displacement curves for the pinched hemispherical shell.

3.2.2 Dynamic analysis

3.2.2.1 Cantilever beam

The elastic cantilever beam bending problem studied by Olovsson et al. (2004) is considered here. The geometric dimensions, material elastic properties, applied loading, and boundary conditions are all specified in Fig. 3.16. Figure 3.17 compares the deflection history at one corner of the free end of the beam obtained with the SHB elements and ABAQUS linear elements. Note that, since no quadratic elements are available in the ABAQUS/Explicit software package, the results given by the quadratic SHB elements are only compared with the reference solution taken from Olovsson et al. (2004) (see Fig. 3.17 (c) and (d)). The numerical results show that the mesh refinement used for the linear ABAQUS solid elements (i.e., C3D6 and C3D8R) is still not sufficient to achieve accurate solutions, due to the poor

behavior of these solid elements with regard to locking and hourglassing. By contrast, all SHB elements as well as linear ABAQUS shell elements (i.e., S3R and S4R) are in good agreement with the reference solution. Note that, although adopting twice more elements (i.e., two element layers in the thickness direction), the results given by conventional linear ABAQUS solid elements are still clearly affected by locking phenomena that are involved in this typical bending-dominated problem, which is not the case for the SHB elements, thanks to the implementation of the assumed-strain method in their formulation.

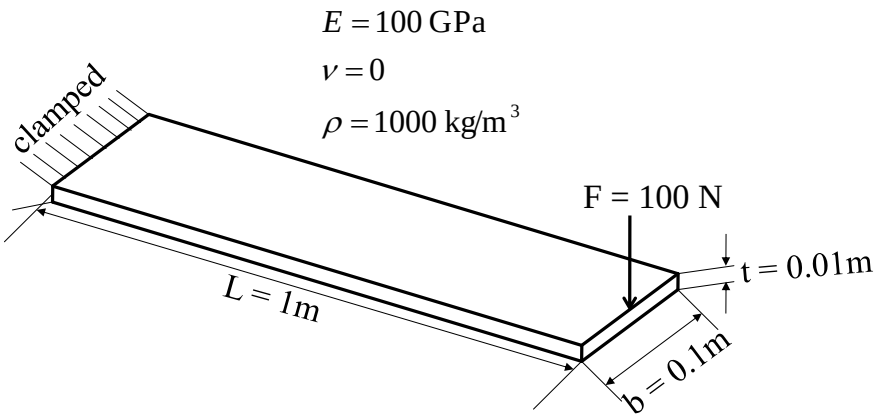
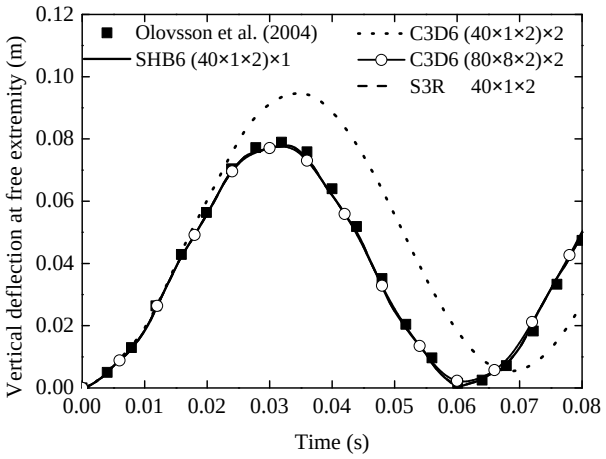
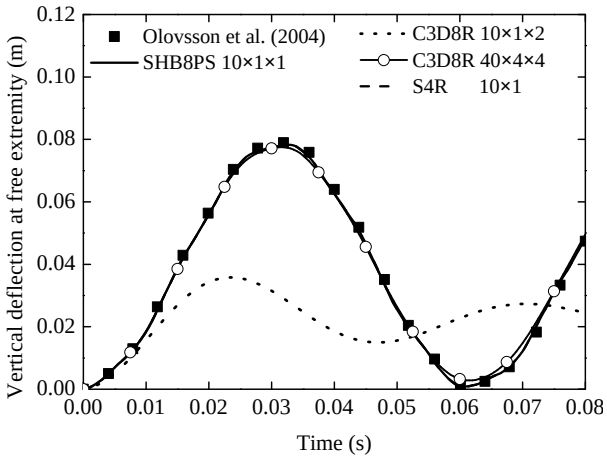


Figure 3.16. Geometric and material parameters for the cantilever beam.

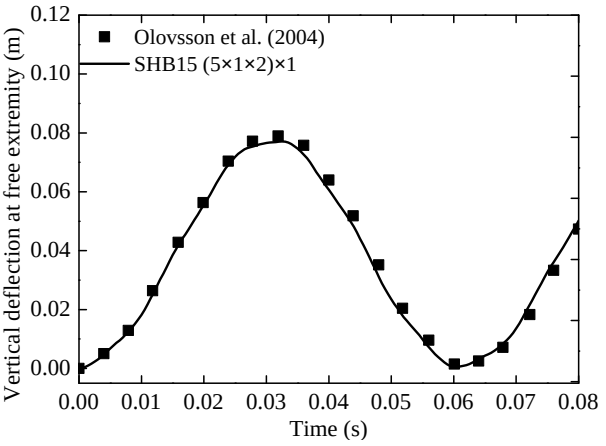
Similar to the quasi-static analysis (see subsection 3.2.1.3), the computation times required by the dynamic versions of the SHB elements are displayed for this dynamic benchmark test. Table 3.18 compares the CPU times required by the proposed SHB elements and the linear ABAQUS solid elements. It can be seen that, when using the same mesh, the proposed linear SHB elements involve CPU times that are equivalent to those of their ABAQUS solid counterparts. However, the latter require finer in-plane meshes with several layers to achieve accurate (converged) solutions (40×4×4 for the C3D8R element, and (80×8×2)×2 for the C3D6 element), which results in much higher CPU times for the ABAQUS elements in comparison with the linear SHB elements (see Table 3.18). For the quadratic SHB elements, the required CPU times are reasonably higher than those yielded by their linear counterparts, which is consistent with the number of integration points and degrees of freedom involved in quadratic formulations.



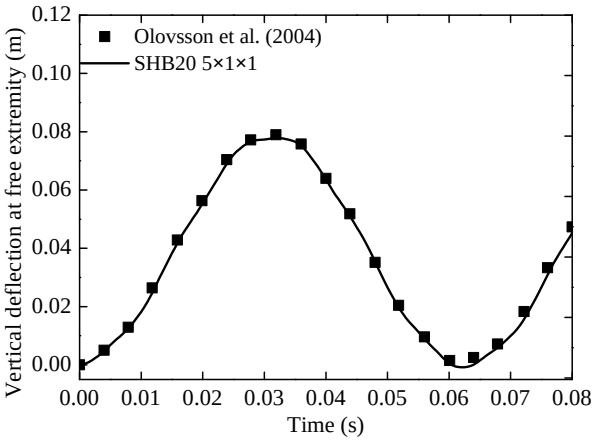
(a) linear prismatic/triangular elements



(b) linear hexahedral/quadrilateral elements



(c) quadratic prismatic element



(d) quadratic hexahedral element

Figure 3.17. Deflection history for the cantilever beam.

Table 3.18. Computation details for the cantilever beam subjected to a concentrated load.

Element	Total Number of elements	Number of layers	Number of integration points per element	Number of DOFs	CPU time (s)
SHB8PS	10×1×1	1	2	44×3	25
C3D8R	10×1×2	2	1	66×3	25
C3D8R	40×4×4	4	1	1025×3	677
SHB6	(40×1×2)×1	1	2	164×3	147
C3D6	(40×1×2)×2	2	1	246×3	112
C3D6	(80×8×2)×2	2	1	2187×3	1410
SHB15	(5×1×2)×1	1	3×2	78×3	137
SHB20	5×1×1	1	2×2×2	68×3	79

3.2.2.2 Simply supported elastic beam

The second dynamic benchmark problem consists of an elastic beam, which is simply supported at both ends. The beam is subjected to a uniform load, resulting in a maximum deflection of the order of its depth. The geometric dimensions, material properties and boundary conditions are all summarized in Fig. 3.18. Owing to the symmetry of the problem, only half of the beam is discretized. The deflection of the central point, obtained with the SHB elements, is depicted in Fig. 3.19 and compared with the linear ABAQUS solid elements, along with the reference solution taken from Flanagan and Belytschko (1981). It can be seen that the numerical results obtained with the proposed SHB elements and ABAQUS linear elements are all in good agreement with the reference solution.

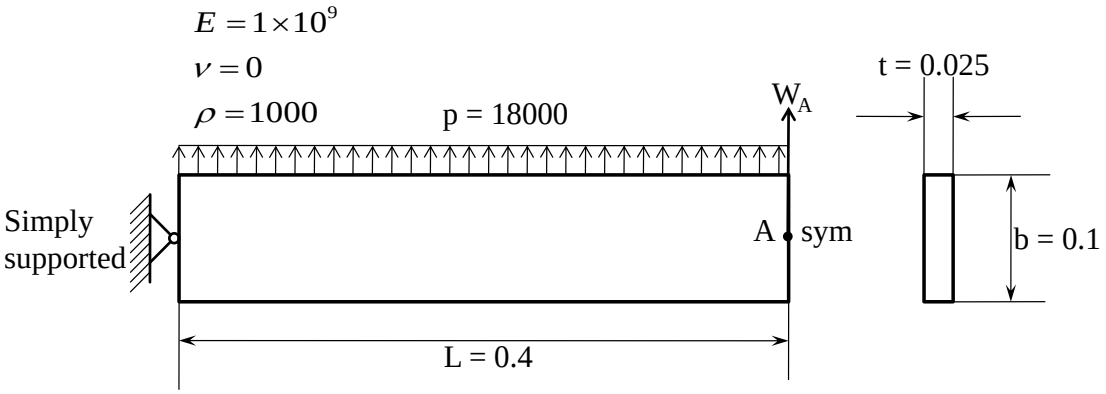
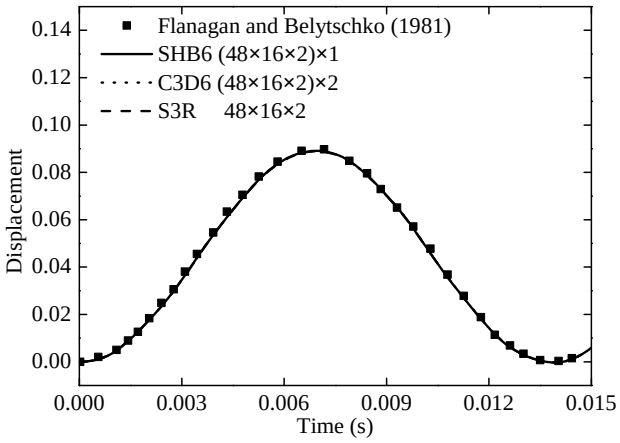
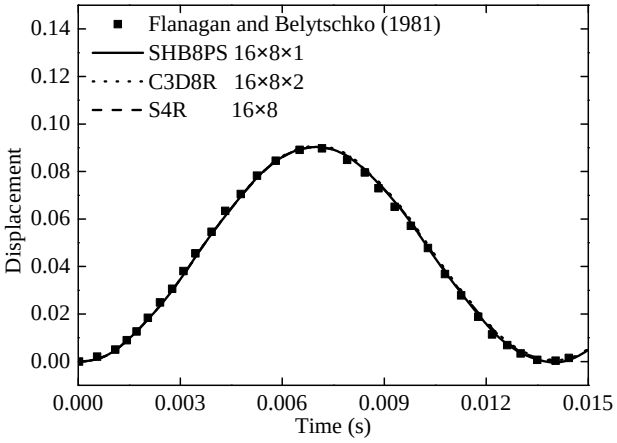


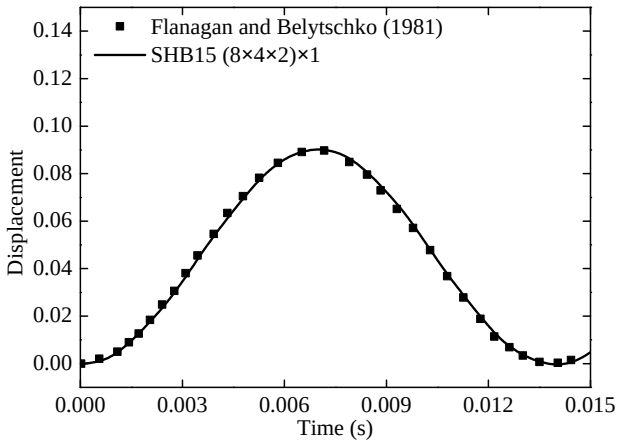
Figure 3.18. Geometric and material parameters for the simply supported elastic beam.



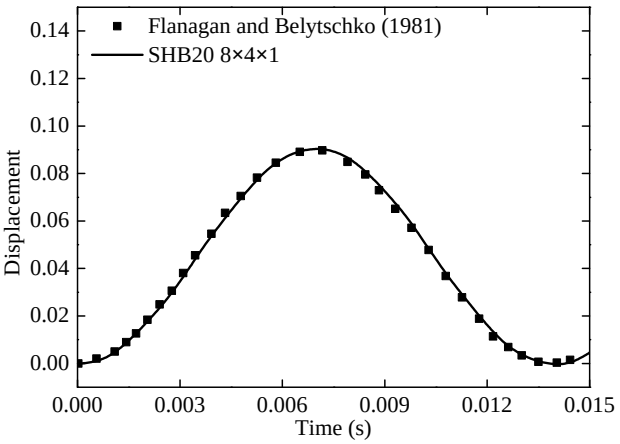
(a) linear prismatic/triangular elements



(b) linear hexahedral/quadrilateral elements



(c) quadratic prismatic element



(d) quadratic hexahedral element

Figure 3.19. Deflection history for the simply supported elastic beam.

3.2.2.3 Clamped circular annular plate under uniformly distributed pressure

Figure 3.20 illustrates a clamped circular annular plate subjected to a uniformly distributed pressure. Under such pressure, the dynamic response, in terms of deflection at the inner radius of the annular plate, is analyzed. Owing to the symmetry of the problem, only one quarter of this annulus plate is discretized. Figure 3.21 reports the deflection history obtained with the SHB elements and the ABAQUS linear solid elements, along with the reference solution provided by Saigal and Yang (1985). One can note that both the maximum deflection and the time period are well predicted using the SHB elements as well as ABAQUS linear shell elements, while the solutions yielded by the ABAQUS linear solid elements are found less accurate.

$E = 3\times10^{4}$ psi

$\nu = 0.3$

$\rho = 3\times10^{-4}$ lbs - sec.^{2} / in.^{4}

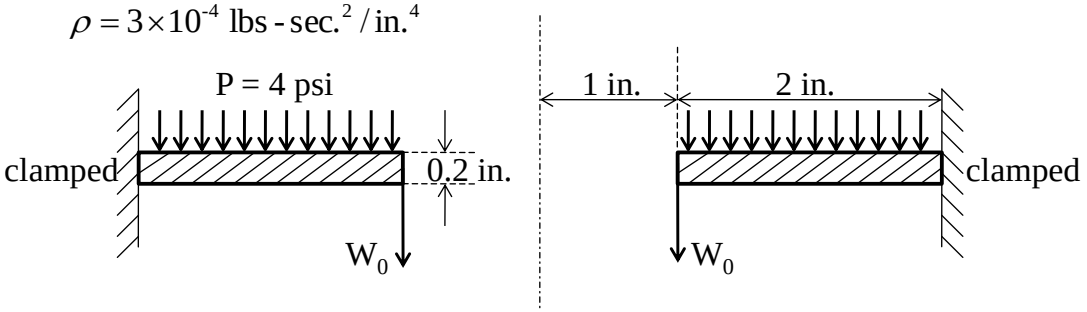
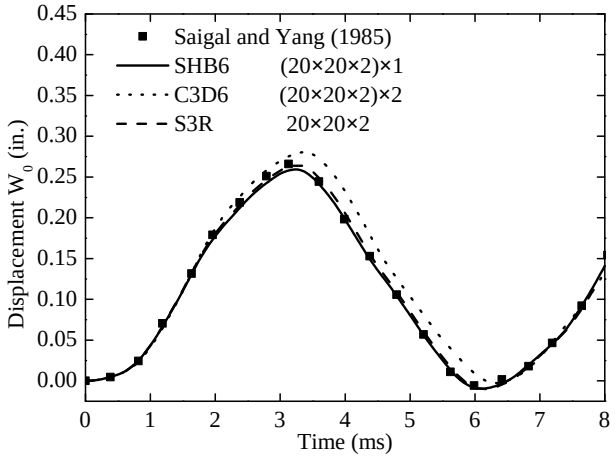
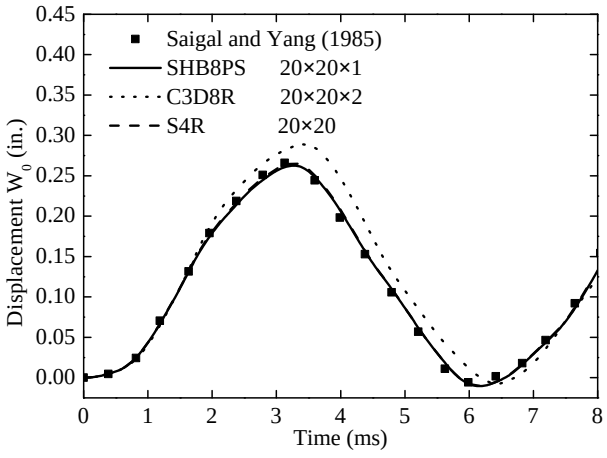


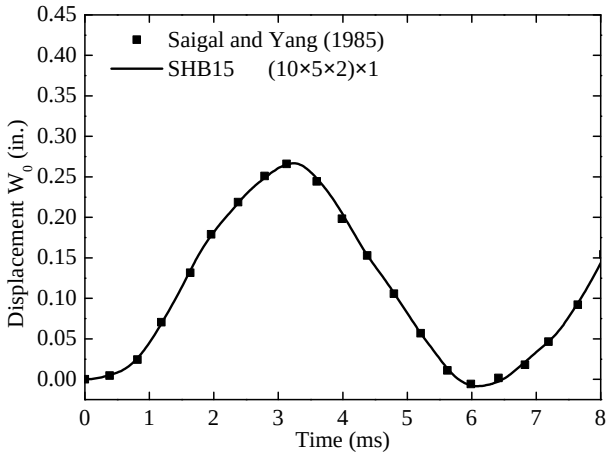
Figure 3.20. Geometric and material parameters for the clamped circular annular plate.



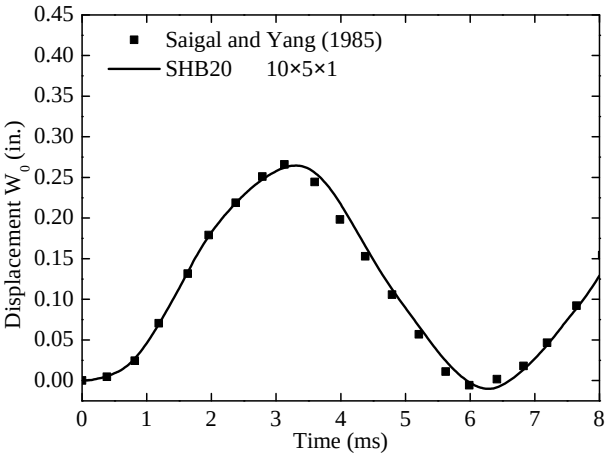
(a) linear prismatic/triangular elements



(b) linear hexahedral/quadrilateral elements



(c) quadratic prismatic element



(d) quadratic hexahedral element

Figure 3.21. Deflection history for the clamped circular annular plate.

3.2.2.4 Elastic twisted cantilever beam

A clamped twisted beam, as described in Fig. 3.22, is considered here to further evaluate the performance of the SHB elements in dynamic analysis. The geometry, material elastic properties and boundary conditions are all specified in Fig. 3.22. Figure 3.23 compares the deflection history at one corner of the free end of the beam (see point A in Fig. 3.22), as obtained with the SHB elements and ABAQUS linear elements, with the reference solution taken from Belytschko et al. (1992). It can be seen that all SHB elements perform very well with respect to the reference solution, which is also the case for ABAQUS linear shell elements. However, as pointed out in the previous benchmark tests, finer meshes are required for the ABAQUS linear solid elements (i.e., C3D6 and C3D8R) in order to achieve accurate solutions.

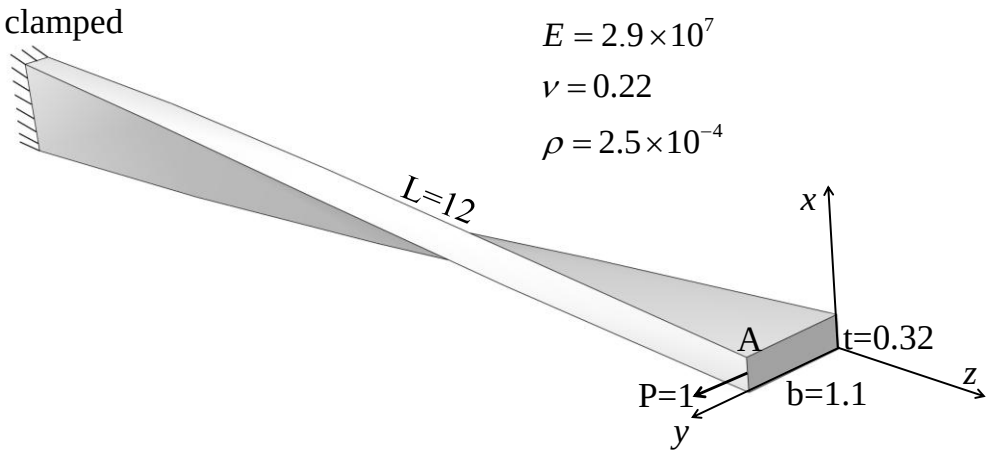
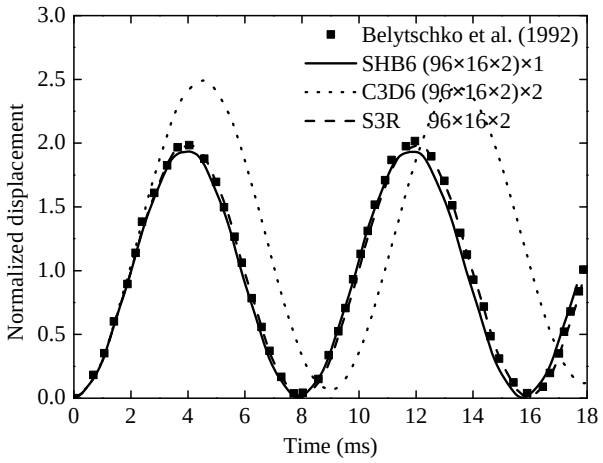
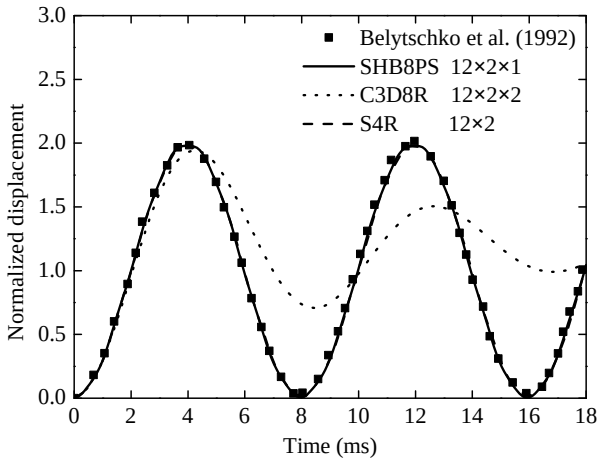


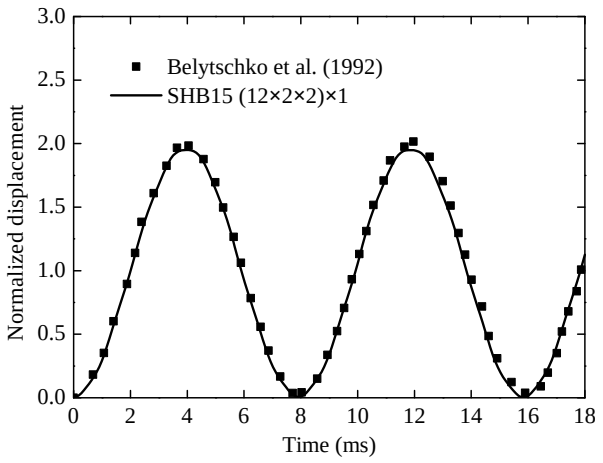
Figure 3.22. Geometric and material parameters for the elastic twisted cantilever beam.



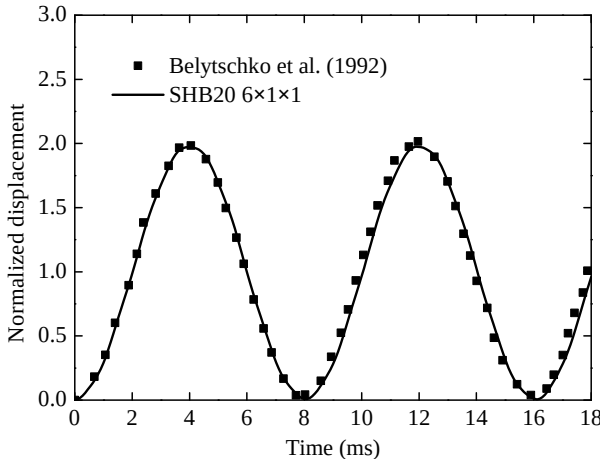
(a) linear prismatic/triangular elements



(b) linear hexahedral/quadrilateral elements



(c) quadratic prismatic element



(d) quadratic hexahedral element

Figure 3.23. Deflection history for the elastic twisted cantilever beam.

3.2.2.5 Clamped elastic spherical cap

Another explicit/dynamic problem is investigated here, as illustrated in Fig. 3.24. It consists of a fully clamped spherical cap loaded by a constant concentrated force at its apex. Owing to the symmetry, only one quarter of the cap is discretized. The dynamic response in terms of central vertical displacement is analyzed in Fig. 3.25 using the proposed SHB elements as well as ABAQUS linear elements, which are additionally compared to the reference solution taken from Mondkar and Powell (1977) and Duarte Filho and Awruch (2004). The simulation results reveal that both the peak and the period of the response are well predicted using the proposed SHB elements as well as ABAQUS linear shell elements, while the solutions yielded by the ABAQUS linear solid elements are found far from the reference solution during the second half-period.

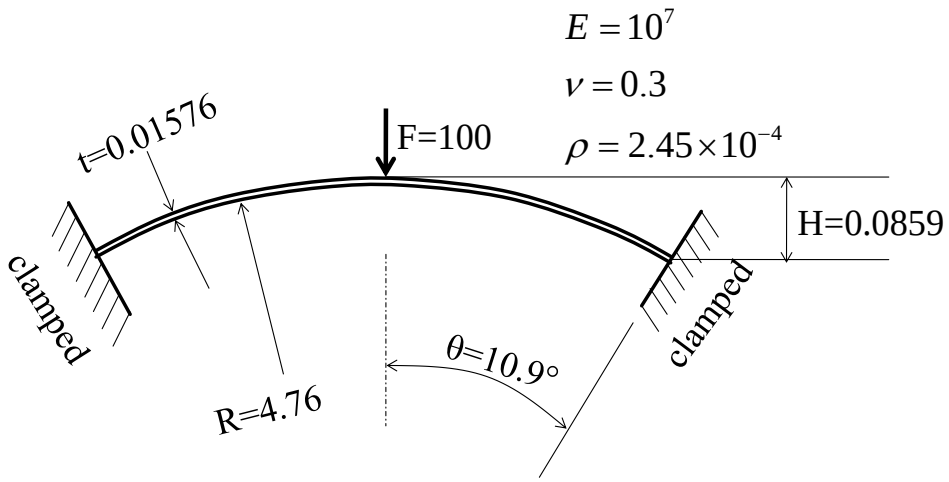
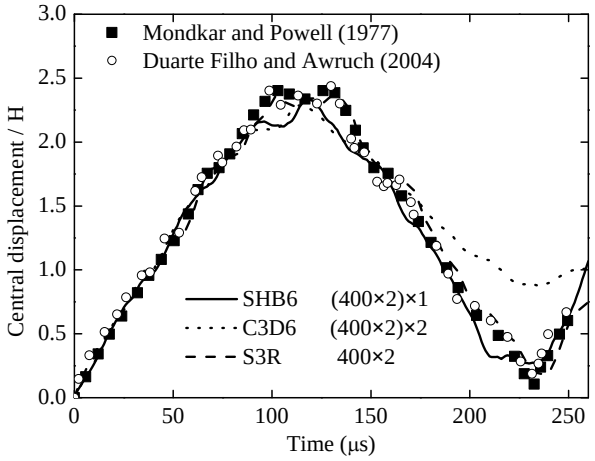
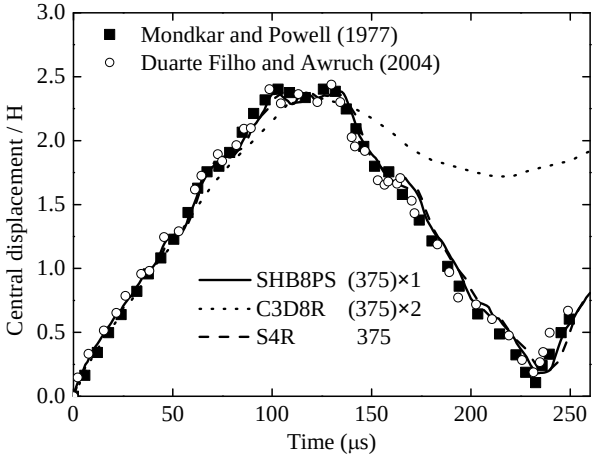


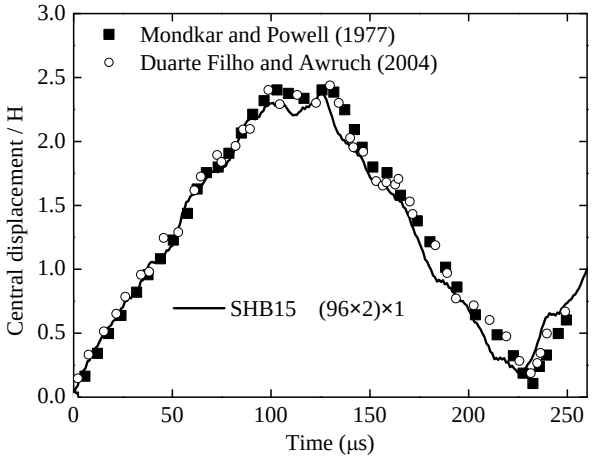
Figure 3.24. Geometric and material parameters for the clamped spherical cap.



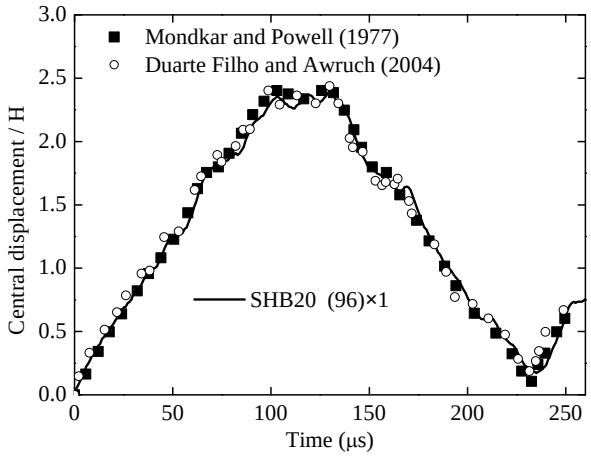
(a) linear prismatic/triangular elements



(b) linear hexahedral/quadrilateral elements



(c) quadratic prismatic element



(d) quadratic hexahedral element

Figure 3.25. Deflection history for the clamped spherical cap.

3.2.2.6 Impulsively loaded clamped plate

In this dynamic test, a long aluminum plate, clamped at both ends, is impulsively loaded with a high velocity applied over a central region of the plate surface, as illustrated in Fig. 3.26. The experiment relating to this test has been originally carried out by Balmer and Witmer (1964), and numerically studied subsequently in several literature works (see, e.g., Belytschko et al., 1984; Wu, 2013). The material of the plate is considered as elastic–perfectly-plastic. All details about the geometric dimensions, prescribed loading, and elasto-plastic material parameters are summarized in Fig. 3.26. Owing to the symmetry of the problem, only one half of the plate is modeled. Note that five integration points through the thickness are required to accurately describe the plastic behavior, which means five element layers in the case of the ABAQUS linear solid elements, and only a single element layer for the SHB elements.

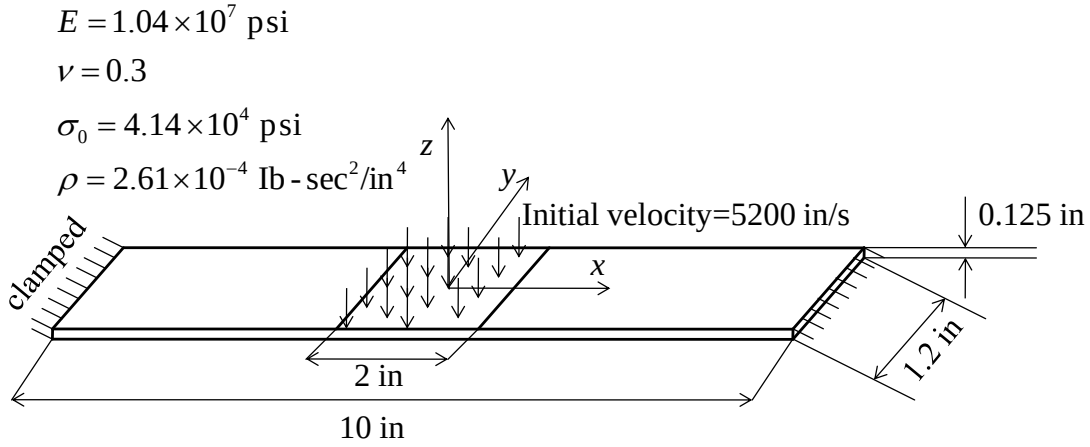
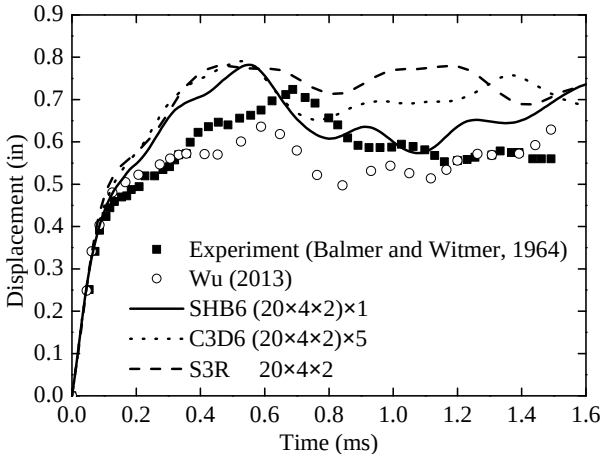
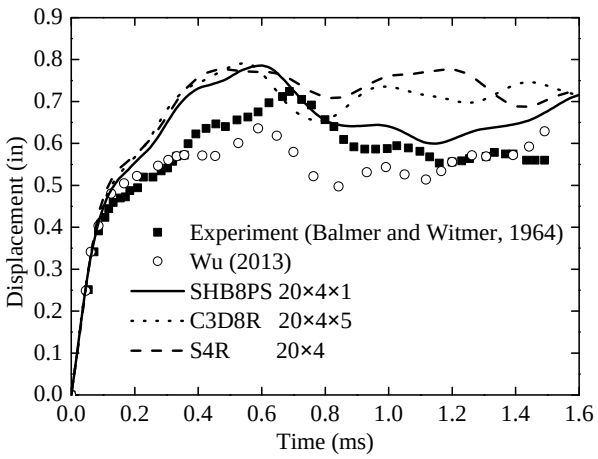


Figure 3.26. Geometric and material parameters for the explosively loaded plate.

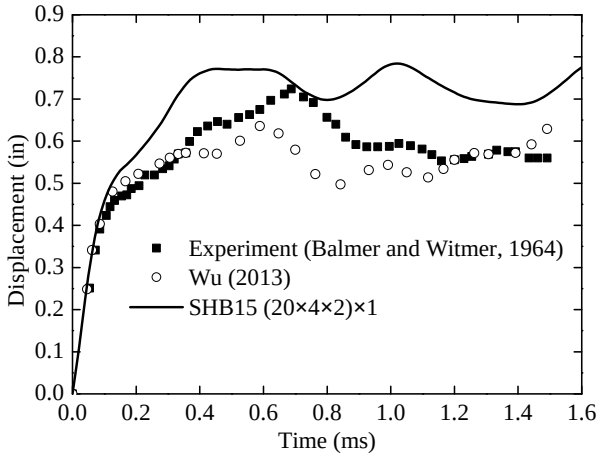
Figure 3.27 shows the predictions in terms of the vertical displacement history at the central point of the plate, along with the experimental result taken from Balmer and Witmer (1964) and the numerical reference solution obtained by Wu (2013). Compared with the simulation results given by ABAQUS linear elements, the results obtained with the linear SHB elements (i.e., SHB6 and SHB8PS) are the closest to the experimental results, while the deflection history is slightly overestimated by the quadratic SHB elements. This demonstrates the good capabilities of the proposed SHB elements in handling elastic–plastic problems with large displacements under highly nonlinear dynamic loading conditions.



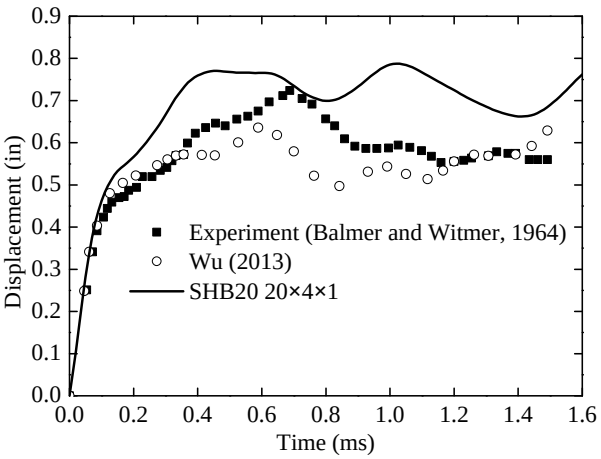
(a) linear prismatic/triangular elements



(b) linear hexahedral/quadrilateral elements



(c) quadratic prismatic element



(d) quadratic hexahedral element

Figure 3.27. Deflection history for the explosively loaded plate.

3.3 Composite multilayered structures

As discussed in Chapter 2, the quadratic SHB15 and SHB20 formulations are extended to the nonlinear analysis of orthotropic materials, which allows the three-dimensional modeling of multilayered composite structures with only a single element layer through the thickness (see, e.g., Wang et al., 2017c). Therefore, the performance of the quadratic SHB elements is assessed in this section through a variety of nonlinear benchmark problems for composite laminates.

3.3.1 Cantilever plate with ply dropoffs

It is well known that traditional shell elements are widely used in the literature for the simulation of composite structures due to their high efficiency and accuracy. However, they are not able to model composite laminates with zones having variable thickness, which is the case of the present nonlinear cantilever plate benchmark test with ply dropoffs. Therefore, only continuum finite elements, such as the proposed solid–shell and ABAQUS solid elements, are capable of modeling this type of composite structures that require a three-dimensional representation of the geometry.

Fig. 3.28 illustrates the geometry of the cantilever composite plate, with three ply dropoffs. Each of these three ply dropoffs is modeled with a single finite element layer, and contains two plies with the fiber directions oriented at [-45º/45º] from the bottom to the top with respect to the length direction. Hence, the thick end (clamped end) contains six plies, while the thinnest end (free end) contains two plies.

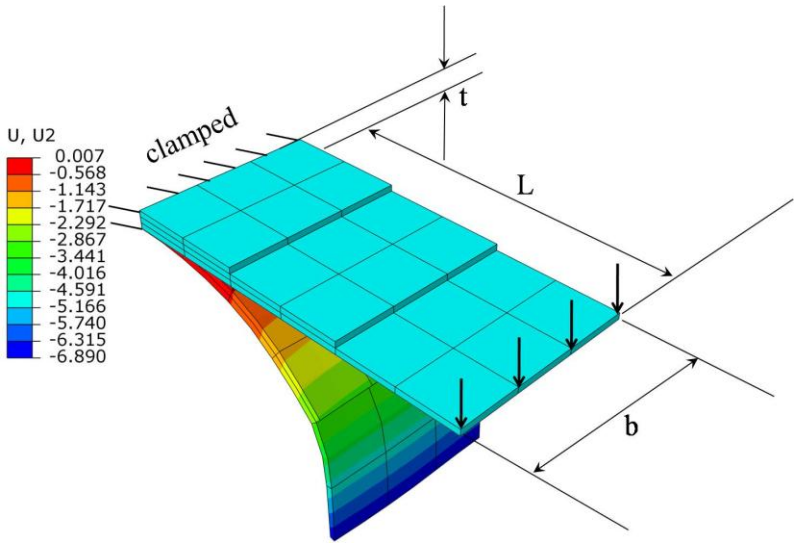


Figure 3.28. Cantilever plate with ply dropoffs.

The cantilever plate is subjected to a bending force $F = 6\times10^{9}h^{3}$, with h being the thickness of each ply (all plies have the same thickness). The engineering constants of the orthotropic material are $E_{11} = 2.5\times10^{10}$, $E_{22} = E_{33} = 10^{9}$, $\nu_{12} = \nu_{13} = \nu_{23} = 0.2$, $G_{12} = G_{13} = G_{23} = 0.5\times10^{9}$. The length of the plate is L = 12, and the width is b = 6, with the top layer removed after successive dropoffs at the coordinates x=4 and x=8 in the length direction. Three different values for the ply thickness are considered, i.e., $h = 0.1,\ 0.01$ and 0.004 .For the quadratic hexahedral elements (i.e., SHB20 and C3D20), the plate is

discretized using six elements in the length direction and three elements in the width direction. In the case of the quadratic prismatic elements (i.e., SHB15 and C3D15), 24 elements in the length direction and six elements in the width are used. The obtained final deflections, normalized with respect to the reference solutions given in Vu-Quoc and Tan (2003), are reported in Table 3.19 for the three ply thicknesses considered. One can observe that, in the case of the ply thickness $h = 0.1$, both quadratic SHB and ABAQUS elements predict well the maximum deflection of this cantilever composite plate. However, for smaller thicknesses of plies (i.e., large length to thickness aspect ratio L/h), the quadratic SHB elements provide the best predictions with very high accuracy, while the quadratic ABAQUS elements show their limitations in modeling very thin 3D structures.

Table 3.19. Normalized deflection for the cantilever plate with ply dropoffs.

Ply thickness	aspect ratio L/h	C3D15	SHB15	C3D20	SHB20
0.1	120	1.0111	0.9954	1.0003	0.9950
0.01	1200	0.9317	0.9980	0.6732	1.0061
0.004	3000	0.8338	1.0086	0.4644	1.0099

3.3.2 Cantilever bending of a laminated beam

A cantilever laminated beam, which is subjected to a bending force at its free end, is considered here. Four different stacking sequences with respect to the length direction are considered for the laminated beam, i.e., [0º/90º/0º], [30º/-60º/-60º/30º], [-45º/45º/-45º/45º] and [90º/0º/90º]. All geometric dimensions as well as orthotropic elastic parameters are given in Fig. 3.29. The load–deflection curves obtained with the quadratic SHB elements are compared in Fig. 3.30 with those given by the quadratic ABAQUS solid elements as well as with the reference solutions taken from Payette and Reddy (2014). Note that, in the case of the ABAQUS C3D15 element, it is not possible to model the different stacking sequences of the composite laminate with a single element layer, which leads to as many element layers as plies. In the case of the quadratic SHB elements as well as the ABAQUS C3D20 element, only a single element layer is used to model multilayered composite structures. The results reported in Fig. 3.30 clearly show the excellent accuracy of the SHB elements with respect to the reference solutions. For the ABAQUS quadratic elements, the simulation results are also in good agreement with the reference solutions; however, the C3D15 element requires several

element layers, which involves much more degrees of freedom in the analysis. The results of this benchmark test reveal the good performance of the proposed quadratic SHB elements for the modeling of composite laminates with orthotropic behavior.

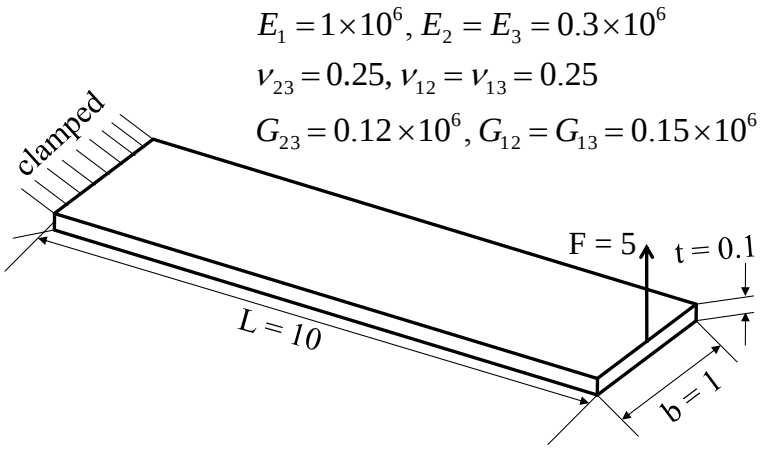
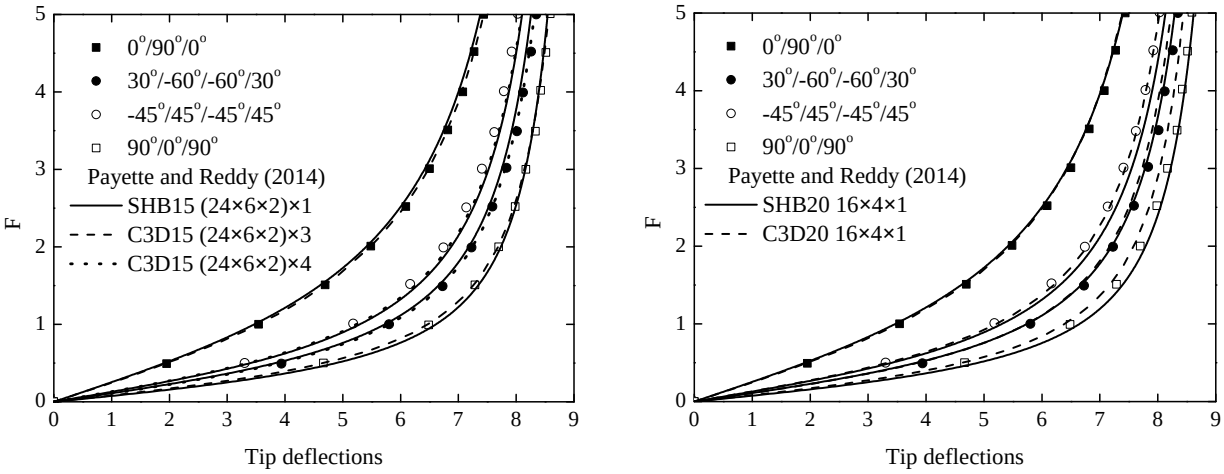


Figure 3.29. Geometric and material parameters for the cantilever laminated beam.



(a) quadratic prismatic elements (b) quadratic hexahedral elements

Figure 3.30. Load–deflection curves for the cantilever laminated beam.

3.3.3 Slit laminated annular plate

The slit annular plate problem is considered in the literature as a popular benchmark test for the performance assessment of finite elements in large displacements and rotations (see, e.g., Buechter and Ramm, 1992; Brank et al., 1995; Mohan and Kapania, 1998; Sze et al., 2004; Arciniega and Reddy, 2007; Payette and Reddy, 2014). This annular plate, as illustrated in Fig. 3.31, is clamped at one end, while the other free end is subjected to a line shear load P.

The inner and outer radii of the annular plate are given by $R_i = 6$, $R_o = 10$, respectively, while the thickness is $t = 0.03$. Two stacking sequences with respect to the radius direction are analyzed here for the composite laminate, i.e. [0º/90º/0º] and [90º/0º/90º]. The engineering constants of the orthotropic material are $E_{11} = 2 \times 10^7$, $E_{22} = E_{33} = 6 \times 10^6$, $\nu_{12} = \nu_{13} = 0.3$, $\nu_{23} = 0.25$, $G_{12} = G_{13} = 3 \times 10^6$, $G_{23} = 2.4 \times 10^6$. Figure 3.32 reports the load–out-of-plane vertical deflection curves at the corner point B of the annular plate, as obtained with the quadratic SHB and ABAQUS elements, along with the reference solutions given by Arciniega and Reddy (2007) and Payette and Reddy (2014). It can be seen that the prismatic SHB15 element shows excellent agreement with the reference solutions, which is also the case for the prismatic C3D15 ABAQUS element. For the latter, one recalls that three element layers are required to model the three plies of the laminated annular plate, while only a single layer is used for the quadratic SHB elements. As to the quadratic hexahedral elements, Fig. 3.32(b) reveals that the proposed SHB20 element provides the closest predictions, with respect to the reference solutions, along the entire loading history.

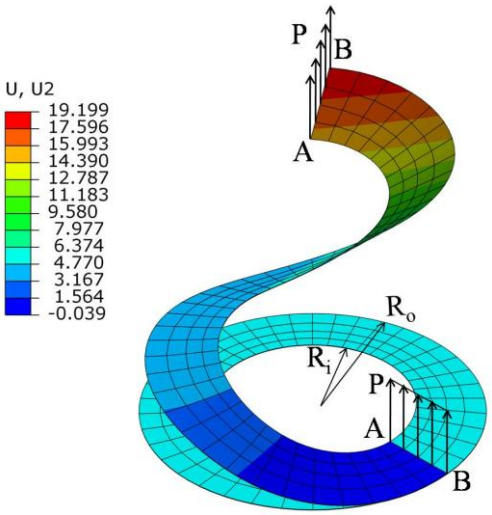
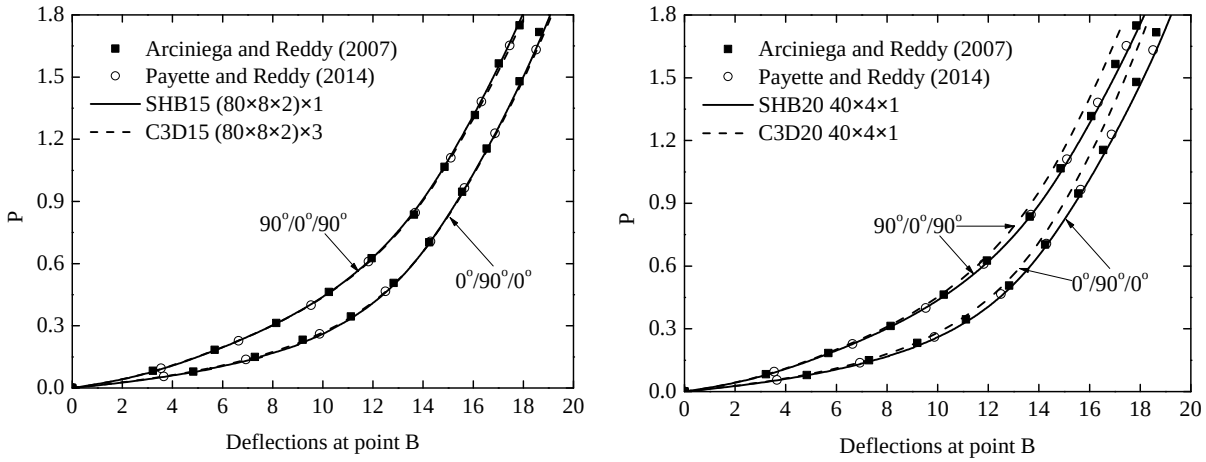


Figure 3.31. Undeformed and deformed configurations of the slit laminated annular plate.



(a) prismatic elements (b) hexahedral elements

Figure 3.32. Load–deflection curves at the corner point B for the slit laminated annular plate.

3.3.4 Pinched laminated semi-cylindrical shell

A pinched laminated semi-cylindrical shell, subjected to a concentrated force applied to its free end, is considered here to assess the performance of the proposed SHB elements in the context of curved composite structures. The geometric dimensions and the boundary conditions of the semi-cylindrical shell are given in Fig. 3.33. Two stacking sequences with respect to the axial direction of the semi-cylinder are considered here for the composite laminate, i.e. [0º/90º/0º] and [90º/0º/90º]. The engineering constants of the orthotropic material are $E_{11}=2068.5$, $E_{22}=E_{33}=517.125$, $v_{12}=v_{13}=v_{23}=0.3$, $G_{12}=G_{13}=G_{23}=795.6$. Owing to the symmetry, only one half of the model is discretized.

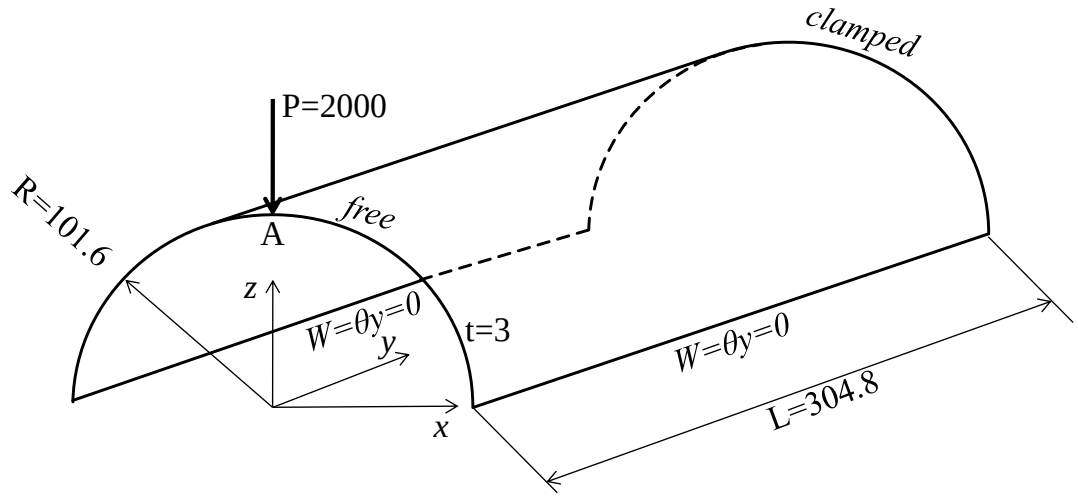
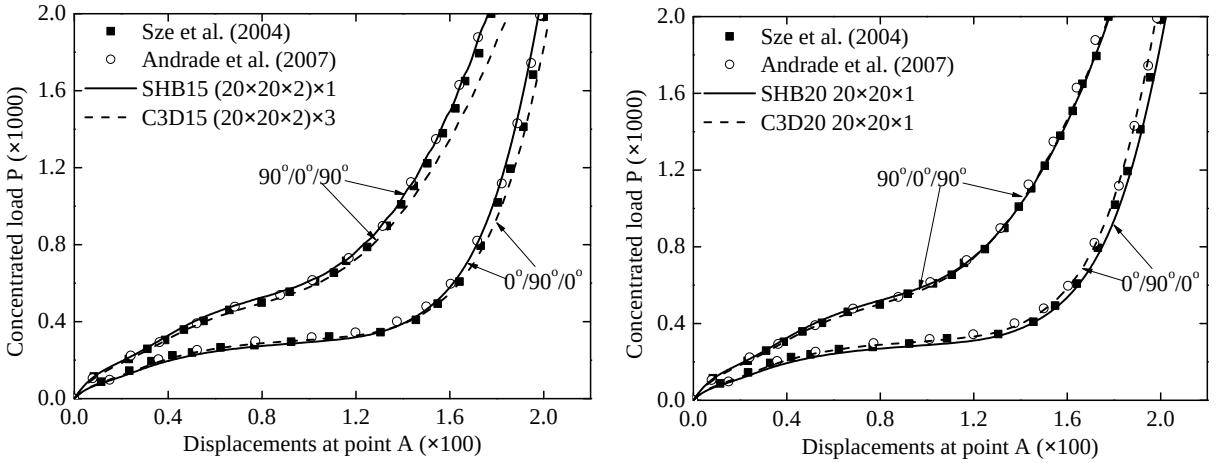


Figure 3.33. Geometric parameters for the pinched laminated semi-cylindrical shell.

Figure 3.34 depicts the load–vertical displacement curves at the loading point A, which are obtained using the quadratic SHB and ABAQUS elements, along with the reference solutions given by Sze et al. (2004) and Andrade et al. (2007). It can be seen that the results obtained with the quadratic SHB elements are in excellent agreement with the reference solutions along the entire loading history, while the results given by the prismatic C3D15 ABAQUS element show some discrepancies with respect to the reference solutions at large displacements.



(a) prismatic elements (b) hexahedral elements

Figure 3.34. Load–displacement curves for the pinched laminated semi-cylindrical shell.

3.3.5 Pinched laminated hemispherical shell

Figure 3.35 depicts a free laminated hemispherical shell with 18º circular hole at its pole. The shell is subjected to a pair of alternating forces at 90° intervals. The radius and the thickness of this thin hemispherical shell are equal to 10 and 0.08, respectively. This shell is made of a single ply of fiber-reinforced laminate, with fiber directions aligned to the circumferential direction. The engineering constants of the orthotropic material are $E_{11} = 20.46 \times 10^6$, $E_{22} = E_{33} = 4.092 \times 10^6$, $\nu_{12} = \nu_{13} = \nu_{23} = 0.313$, $G_{12} = G_{13} = 2.53704 \times 10^6$, $G_{23} = 1.26852 \times 10^6$ (see Kreja and Schmidt, 2006). Considering the problem symmetry, only one quarter of the shell is discretized.

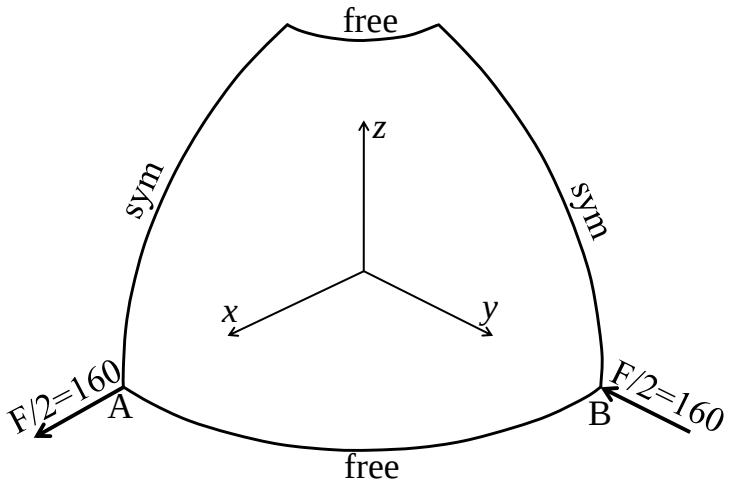
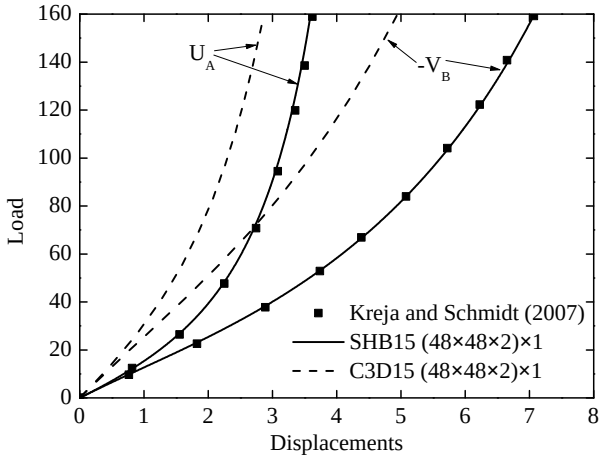
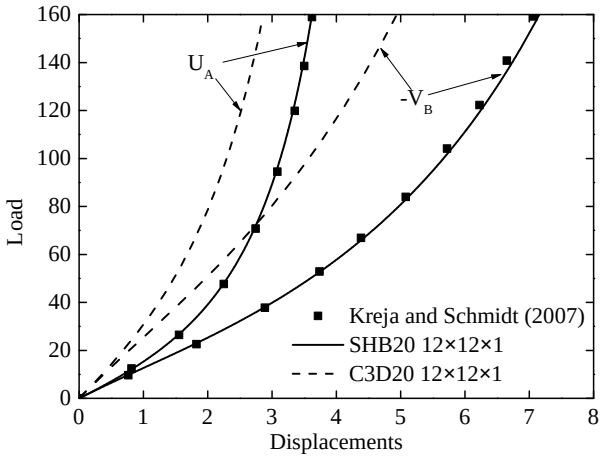


Figure 3.35. Geometry of the pinched laminated hemispherical shell.

The load–displacement curves at points A and B (see Fig. 3.35), which are obtained with the quadratic SHB and ABAQUS elements, are depicted in Fig. 3.36 along with the reference solution given by Kreja and Schmidt (2006). Note that the final displacements of points A and B, which are of the same order of magnitude as the shell radius, indicate the large displacements and rotations involved in this test (see also the final deformed shape of the hemispherical shell in Fig. 3.37). Once again, one can notice the excellent agreement between the results obtained with the quadratic SHB elements and the reference solution. However, although the adopted meshes correspond to converged results, the simulation results given by ABAQUS elements fall far from the reference solution, showing the limitations of ABAQUS quadratic elements in modeling this severe test, which involves strong geometric nonlinearities.



(a) prismatic elements



(b) hexahedral elements

Figure 3.36. Load–displacement curves at points A and B for the pinched laminated hemispherical shell.

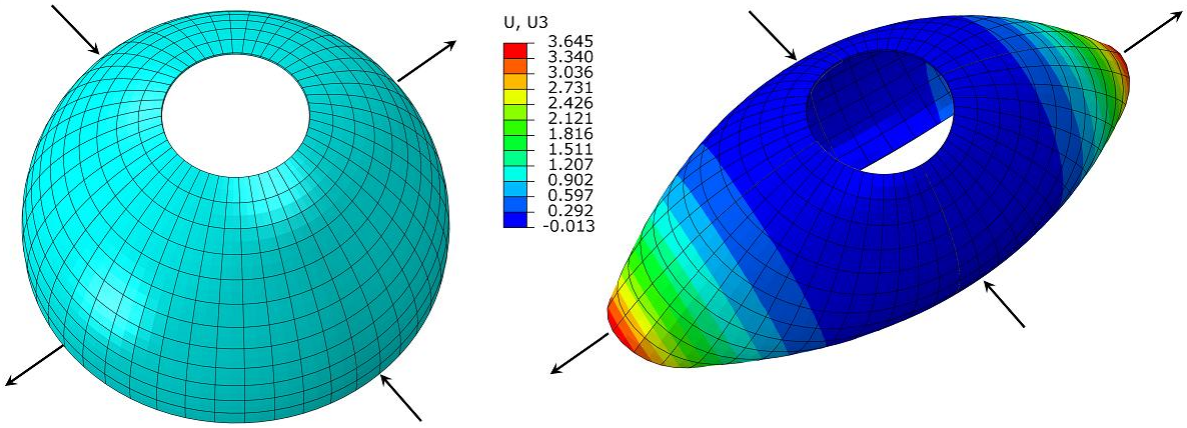


Figure 3.37. Undeformed and final deformed shapes of the pinched laminated hemispherical shell.

Conclusion

In this chapter, the proposed SHB solid–shell elements have been evaluated through a series of popular benchmark tests, including selective and representative linear benchmark problems, vibration analysis tests, and nonlinear benchmark problems, both in quasi-static and dynamic analyses. Various types of behavior models (isotropic behavior, orthotropic elastic behavior for laminated composite materials, and plastic behavior for metallic materials), have been considered in the simulations, which allowed for a broad range of nonlinear applications. Overall, the obtained results, in both types of analyses (quasi-static and dynamic), reveal the good capabilities of the proposed SHB elements and their wide prospective applications in the 3D modeling of thin structures with only a single element layer and few integration points through the thickness.

Chapter 4

Applications to the simulation of complex processes

Introduction

Through the numerical validations conducted in Chapter 3, the proposed SHB elements have been shown to be very attractive, as they are able to accurately reproduce shell-like behavior using only a single element layer. In this chapter, the performance of the SHB elements is further evaluated through complex structural problems, including impact-type problems as well as sheet metal forming processes.

The remainder of this chapter is outlined as follows. First, two dynamic/impact problems are presented in order to assess the capabilities of the SHB elements in dealing with impact–contact problems. Then, several sheet metal forming processes are selected to further examine the ability of the proposed solid–shell elements to model challenging simulation problems, involving complex nonlinear loading paths, anisotropic plasticity and double-sided contact. One recalls that these SHB elements have been implemented in both ABAQUS standard/quasi-static and explicit/dynamic software packages. Through a series of numerical simulations relating to sheet metal forming processes, it has been observed that both the implicit/quasi-static and explicit/dynamic versions of the SHB elements provide very close predictions. Consequently, for conciseness, only the numerical predictions obtained with the implicit/quasi-static versions of the SHB elements are presented in the case of sheet metal forming simulations. Also, for the sake of clarity, the simulation results will not be presented systematically for all of the four SHB elements for each of the selected structural problems. Instead, to avoid redundancy and improve readability, the simulation results will be presented selectively; i.e., either for the linear SHB elements or for the quadratic SHB elements, which allows evaluating, on the whole, the performance of the SHB elements on all the representative applications.

4.1 Simulation of impact problems

4.1.1 Low velocity impact of a circular plate

The dynamic response of a clamped circular plate subjected to impact by a projectile is investigated here to assess the capabilities of the proposed linear SHB elements in dealing with elastic–plastic impact–contact problems. Note that this dynamic benchmark test has previously been studied by Chen et al. (2007) and Mars et al. (2015). The geometric dimensions for the plate and the projectile as well as the prescribed loading and boundary conditions are all defined in Fig. 4.1. The material of the circular plate is made of 6061-T6 aluminum alloy, whose elastic–plastic properties are given in Table 4.1.

Table 4.1. Material parameters for the studied 6061-T6 aluminum alloy.

Material	E (GPa)	ν	σ_0 (MPa)	ρ (kg / m^3)
Aluminum	69	0.3	290	2600

The projectile is modeled as a rigid body with an assigned mass at its reference point. The contact between the circular plate and the projectile is assumed to be frictionless, using the hard contact approach available in the ABAQUS/Explicit code. Two typical cases, with different initial weight and velocity for the projectile, are considered:

Case 1: M = 23.5 g, V_0 = 49.1 m/s.

Case 2: M = 54.4 g, V_0 = 29.9 m/s.

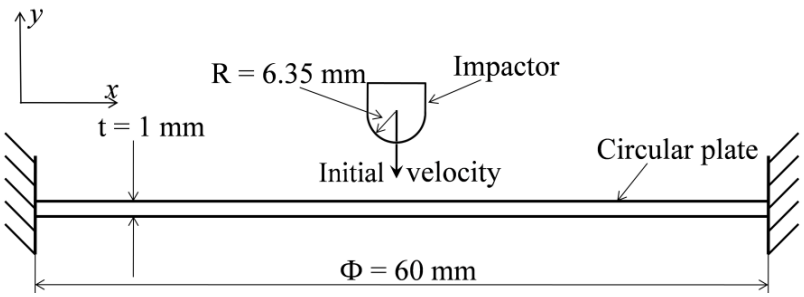
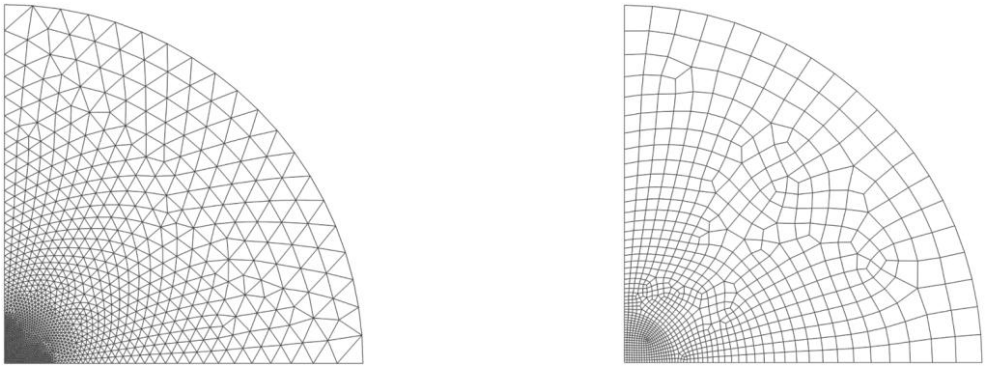


Figure 4.1. Schematic representation of a circular plate subjected to impact by a projectile.

Considering the symmetry of the problem, only one quarter of the plate is modeled using an in-plane discretization of 2708 elements in the case of prismatic elements, 2722 elements in the case of triangular shell elements, 934 elements in the case of hexahedral elements, and

951 elements in the case of quadrilateral shell elements (see Fig. 4.2 for illustration). All simulations are carried out using two integration points in the thickness direction, which means two element layers in the case of the ABAQUS C3D8R and C3D6 solid elements, and only a single element layer for all other elements used for comparison. The history of velocity and impact force for the projectile as well as the displacement response at the center of the plate are analyzed using the proposed linear SHB elements, which are then compared both with ABAQUS linear elements and with reference solutions given in Chen et al. (2007).



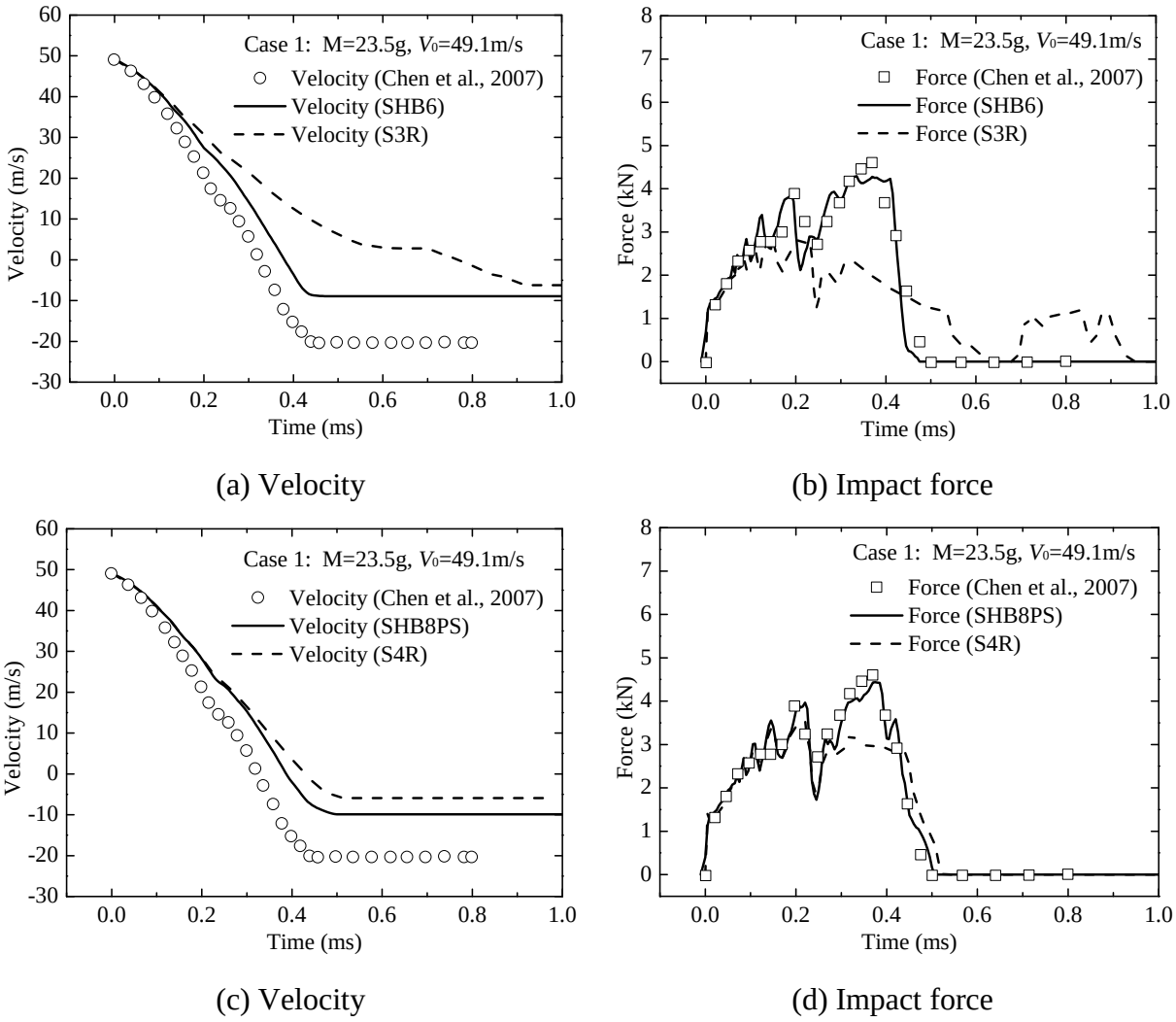
(a) Prismatic elements (b) Hexahedral elements

Figure 4.2. Initial in-plane mesh for the clamped circular plate under impact by a projectile.

The velocity and the impact force obtained with the linear SHB elements, for both cases 1 and 2, are compared in Figs. 4.3 to 4.6 with the results given by ABAQUS linear elements as well as with the numerical reference solutions given in Chen et al. (2007). For more clarity in these cross comparisons, the results given by the linear SHB elements are compared in Figs. 4.3 and 4.4 with those yielded by ABAQUS shell elements, and in Figs. 4.5 and 4.6 with ABAQUS solid elements. It can be seen that the double impact force peak, which is typically observed in such impact problems, is well reproduced by the linear SHB elements for both studied cases. More specifically, the maximum impact force peak, corresponding to the end of the indentation stage, is reached for the linear SHB elements when the velocity of the projectile decreases to zero, which is consistent with the numerical reference solutions given by Chen et al. (2007) in both studied cases.

In terms of comparison with ABAQUS, the results obtained with the linear SHB elements show good agreement with solid ABAQUS elements (see Figs. 4.5 and 4.6), while ABAQUS shell elements provide the farthest results with respect to the reference solution. It should be recalled that a finer mesh is required for the ABAQUS linear solid elements, with two

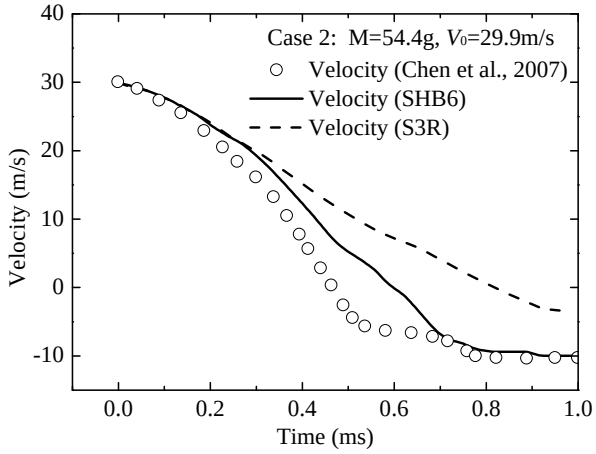
element layers in the thickness direction, which involves twice more elements than their linear SHB counterparts.



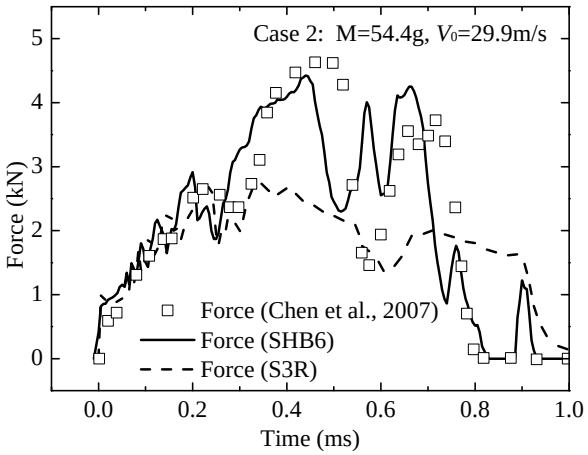
(a) Velocity (b) Impact force

(c) Velocity (d) Impact force

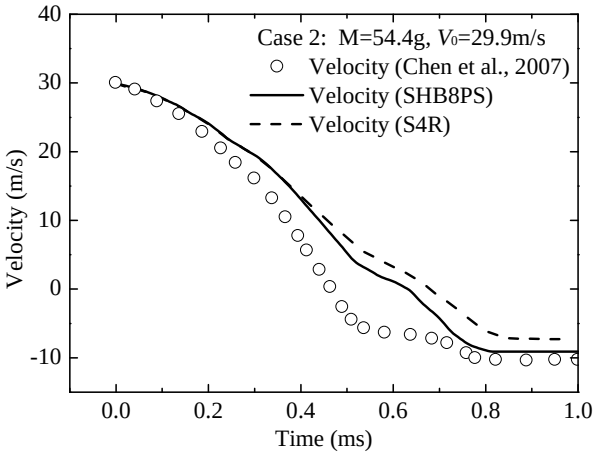
Figure 4.3. History of velocity (left) and impact force (right) for the projectile, obtained with the linear SHB elements and ABAQUS shell elements along with the reference solutions for case 1.



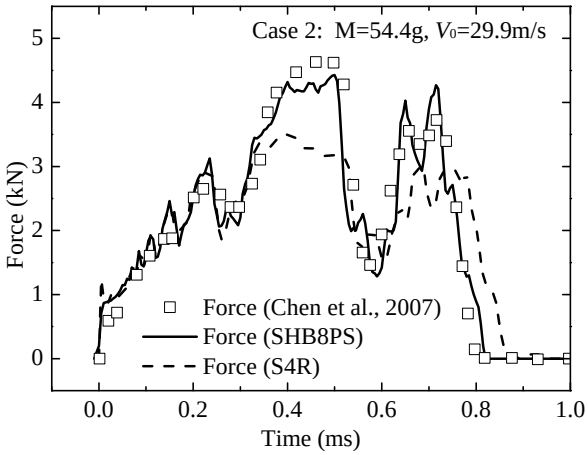
(a) Velocity



(b) Impact force

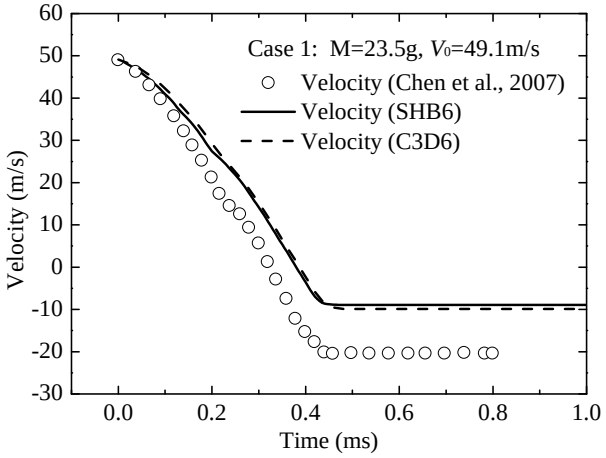


(c) Velocity

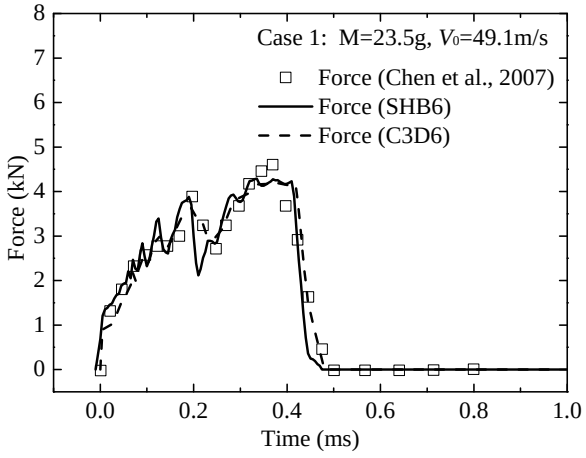


(d) Impact force

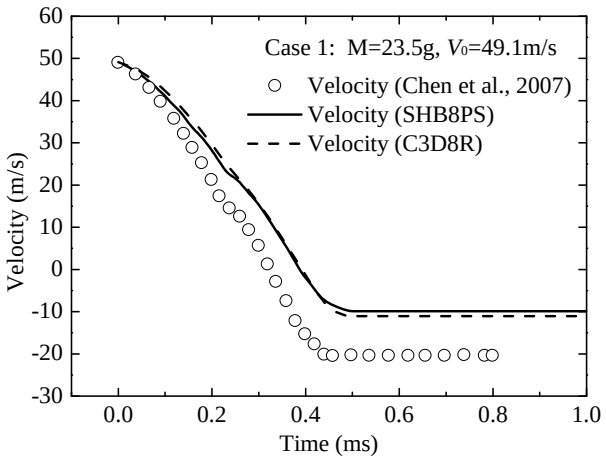
Figure 4.4. History of velocity (left) and impact force (right) for the projectile, obtained with the linear SHB elements and ABAQUS shell elements along with the reference solutions for case 2.



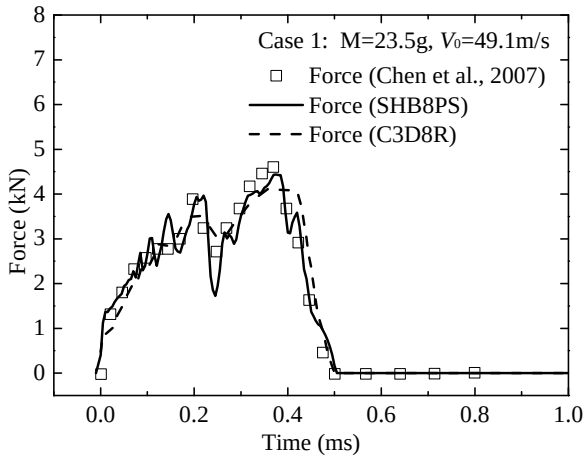
(a) Velocity



(b) Impact force

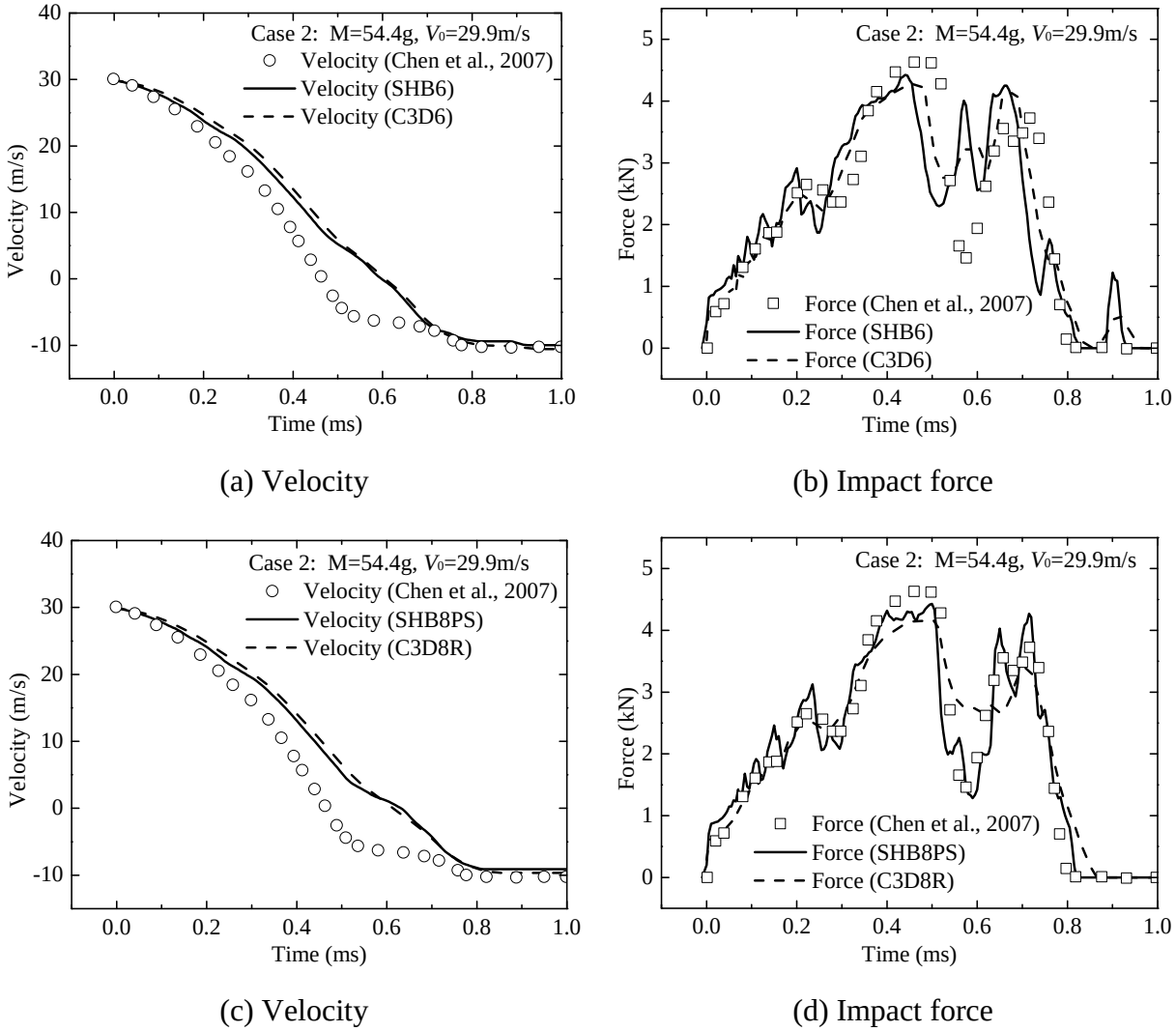


(c) Velocity



(d) Impact force

Figure 4.5. History of velocity (left) and impact force (right) for the projectile, obtained with the linear SHB elements and ABAQUS solid elements along with the reference solutions for case 1.



(a) Velocity (b) Impact force

(c) Velocity (d) Impact force

Figure 4.6. History of velocity (left) and impact force (right) for the projectile, obtained with the linear SHB elements and ABAQUS solid elements along with the reference solutions for case 2.

4.1.2 Impact of a boxbeam

In this example, a steel boxbeam, fixed at one end as illustrated in Fig. 4.7, is impacted by an infinite mass with a constant velocity of 1.27 m/s. As shown by the top-view section A-A' in Fig. 4.7, this boxbeam has an empty rectangular cross-section. The material of the boxbeam is considered as elastic–plastic with the Ludwig isotropic hardening law (see the detailed expression in Chapter 2, Table 2.2). The associated material parameters are summarized in Table 4.2. The contact between the impactor and the boxbeam as well as self-contacts in the boxbeam are assumed to be frictionless.

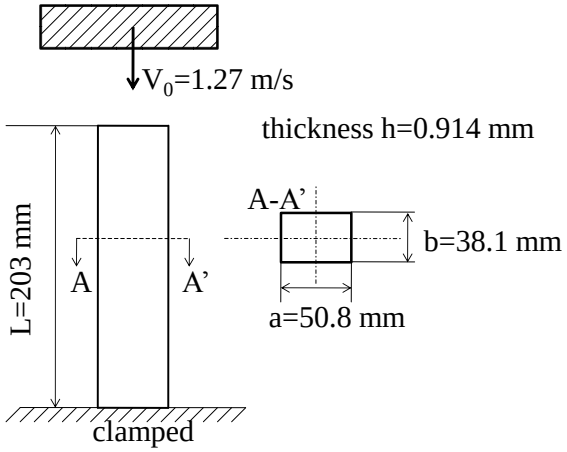


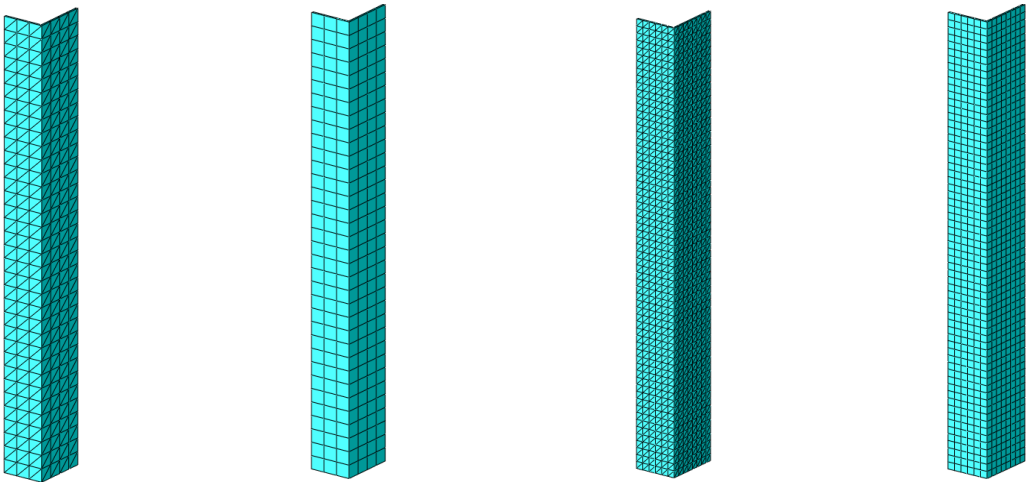
Figure 4.7. Schematic representation of a boxbeam impacted by an infinite mass.

Table 4.2. Material parameters for the boxbeam.

Material	E (GPa)	ν	σ_0 (MPa)	K (MPa)	N	ρ (kg / m^3)
Boxbeam	210	0.3	206	450	0.5	7800

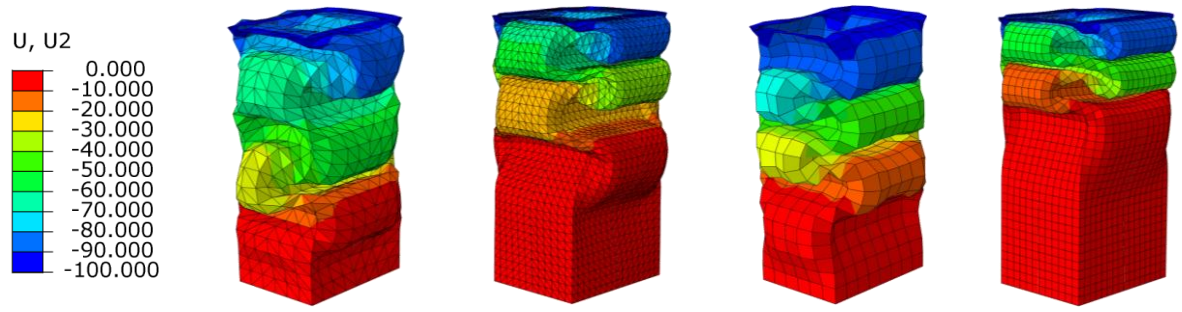
The impactor is considered as a rigid body, while the boxbeam is modeled by the quadratic SHB elements (i.e., SHB15 and SHB20) due to their good performance in dynamic analysis. Owing to the problem symmetry, only one quarter of the boxbeam is discretized using the following new mesh nomenclature. For hexahedral elements, meshes of $N_1 \times (N_2 \times N_3) \times N_4$ elements are adopted, where N_1 indicates the number of elements in the length of the boxbeam, N_2 is the number of elements in the largest width direction (i.e., width of a=50.8 mm), N_3 is the number of elements in the smallest width direction (i.e., width of b=38.1 mm), and N_4 is the number of elements in the thickness direction. For meshes with prismatic elements, the nomenclature adopted is $N_1 \times (N_2 \times N_3 \times 2) \times N_4$, which corresponds to twice the total number of elements involved in hexahedron-based meshes. For ABAQUS shell elements, the nomenclature adopted for quadrilateral shell elements is $N_1 \times (N_2 \times N_3)$, while the nomenclature for triangular shell elements is $N_1 \times (N_2 \times N_3 \times 2)$. For comparison purposes, coarse and fine meshes are considered in the simulations, as shown in Fig. 4.8 for the quadratic SHB elements. One recalls that, since no quadratic elements are available in the ABAQUS/Explicit software package, the results given by the quadratic SHB elements are compared with those yielded by the linear ABAQUS solid and shell elements along with the experimental results provided in Zeng and Combescure (1998). Similar to the previous test problem, only two integration points through the thickness are adopted for this dynamic problem, which requires

two element layers for the linear ABAQUS solid elements (i.e., C3D6 and C3D8R). Figures 4.9–4.11 display the deformed shape of the boxbeam, obtained with the ABAQUS and SHB elements for both coarse and fine meshes, at time 0.08 s, which corresponds to a displacement of 100 mm for the impactor. These figures reveal the effect of the mesh size and the element type on the number and location of periodic buckling patterns that are typical in such crash/impact problems. Indeed, the number of buckling patterns obtained with the quadratic SHB elements agrees qualitatively with that yielded by the linear ABAQUS shell elements, while the corresponding locations occur near the top of the boxbeam for the linear ABAQUS shell elements, and occur in the middle of the boxbeam for the quadratic SHB elements using the fine mesh. For the linear ABAQUS solid elements, both the number and location of the periodic buckling patterns differ from those predicted by the linear ABAQUS shell and quadratic SHB elements. Figures 4.12 and 4.13 show the predicted reaction force–displacement curves for the impactor obtained using the coarse and fine meshes, respectively. These predictions are compared to the experimental results given in Zeng and Combescure (1998). These simulation results confirm the above discussion regarding the effect of the mesh size and the element type on the numerical predictions. More specifically, the three impact force peaks, corresponding to the occurrence of the periodic buckling patterns, are well reproduced by the quadratic SHB elements when a fine mesh is adopted. By contrast, the linear ABAQUS solid and shell elements provide the farthest results with respect to the experimental curve, and appear to be less suitable for this type of crashworthiness analysis.



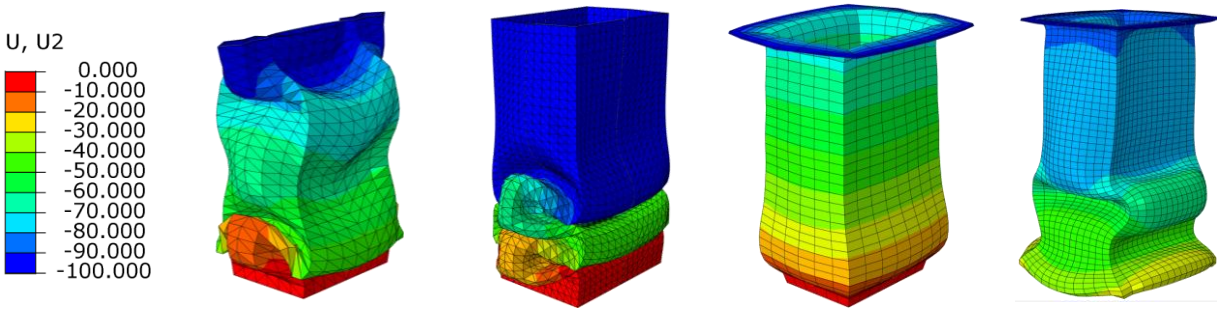
(a) 34×(4×3×2)×1 SHB15 elements | (b) 34×(4×3)×1 SHB20 elements | (c) 64×(8×6×2)×1 SHB15 elements | (d) 64×(8×6)×1 SHB20 elements

Figure 4.8. Coarse and fine undeformed meshes for the boxbeam using the quadratic SHB elements.



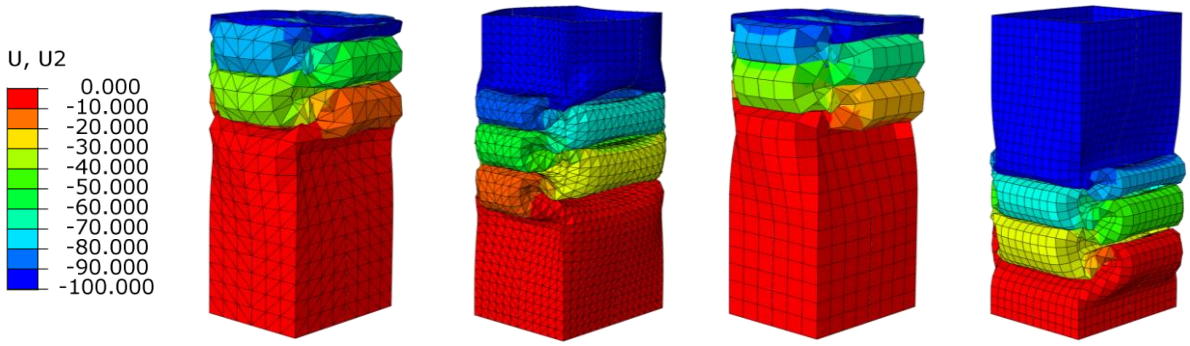
(a) 34×(4×3×2) S3R elements | (b) 64×(8×6×2) S3R elements | (c) 34×(4×3) S4R elements | (d) 64×(8×6) S4R elements

Figure 4.9. Deformed shape for the boxbeam, at time 0.08s, using the linear ABAQUS shell elements.



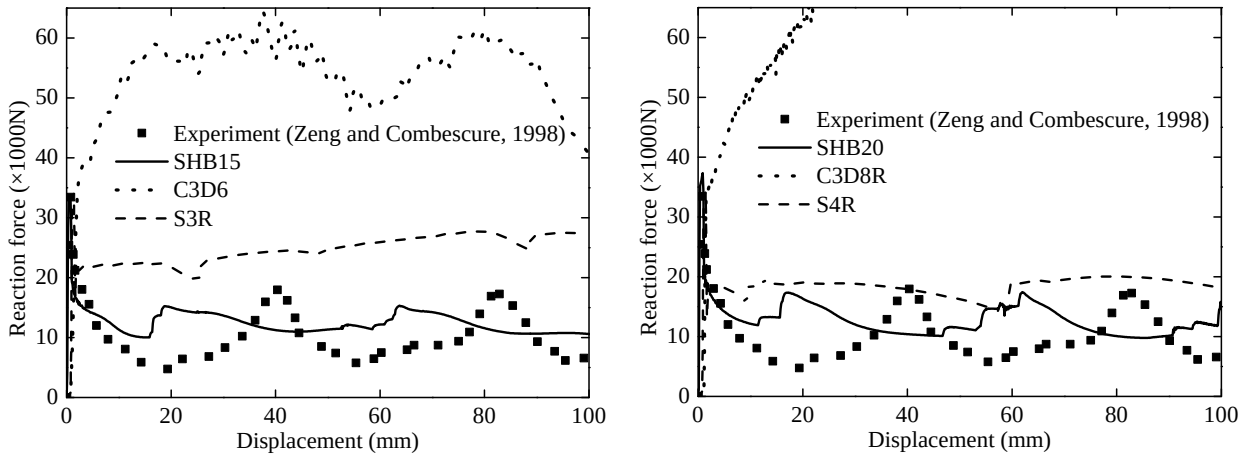
(a) 34×(4×3×2)×2 C3D6 elements | (b) 64×(8×6×2)×2 C3D6 elements | (c) 34×(4×3)×2 C3D8R elements | (d) 64×(8×6)×2 C3D8R elements

Figure 4.10. Deformed shape for the boxbeam, at time 0.08s, using the linear ABAQUS solid elements.



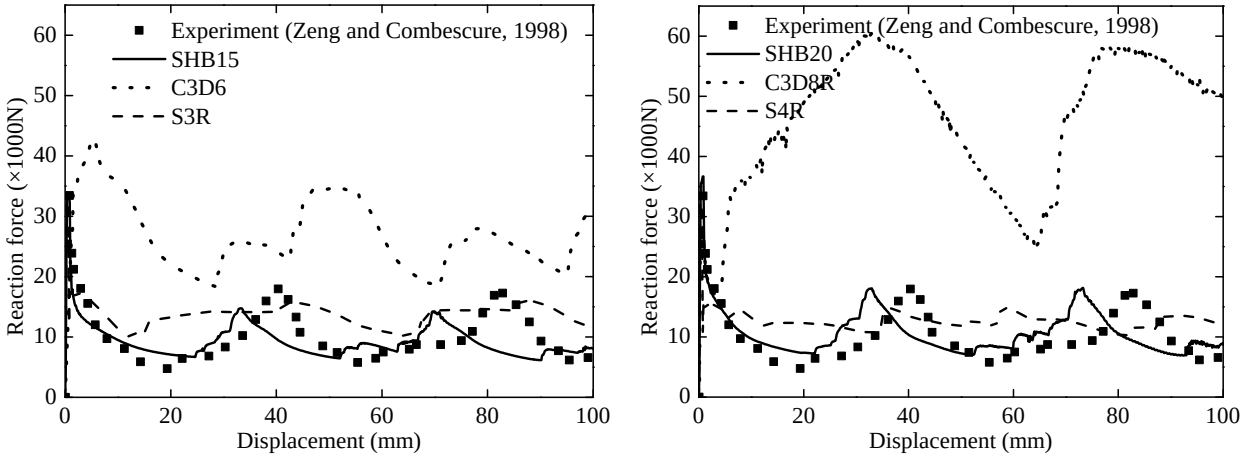
(a) 34×(4×3×2)×1 SHB15 elements | (b) 64×(8×6×2)×1 SHB15 elements | (c) 34×(4×3)×1 SHB20 elements | (d) 64×(8×6)×1 SHB20 elements

Figure 4.11. Deformed shape for the boxbeam, at time 0.08s, using the quadratic SHB elements.



(a) Prismatic/triangular elements (b) Hexahedral/quadrilateral elements

Figure 4.12. Reaction force–displacement curves for the impactor using the coarse mesh.



(a) Prismatic/triangular elements (b) Hexahedral/quadrilateral elements

Figure 4.13. Reaction force–displacement curves for the impactor using the fine mesh.

4.2 Simulation of sheet metal forming processes

This section is dedicated to the validation of the proposed SHB elements in the context of sheet metal forming. To achieve this, a set of selective benchmark problems are simulated using the SHB elements, which consist of well-known deep drawing processes, a springback problem as well as an incremental forming process. These challenging applications involve complex simulations with strong and coupled nonlinearities (i.e., geometric and material nonlinearities as well as contact). Only a single element layer, with few integration points, is consistently considered throughout this section, for all meshes consisting of SHB elements.

The simulation results are compared both with those given by ABAQUS elements and with experimental measurements taken from the literature. It should be noted that, in order to obtain accurate and reliable predictions in the following simulations, five integration points are arranged through the thickness for the linear elements, while only three through-thickness integration points are used for more advanced quadratic elements. The detailed analysis regarding the effect of the number of through-thickness integration points on the predicted results can be found in previous studies (see, e.g., Abed-Meraim and Combescure 2009; Wang et al., 2015; Wang et al., 2016, 2017a, 2017b).

4.2.1 Deep drawing of a hemispherical cup

The deep drawing of a hemispherical cup using the linear SHB elements is considered here. The forming setup and the dimensions of the tools are shown in Fig. 4.14. A circular steel sheet, with initial blank radius R = 126.4 mm and thickness t = 0.7 mm, is considered in the simulations. The material properties of the sheet, which is made of an AA2090-T3 aluminum alloy, are given in Table 4.3. The stress–strain curve is described by the Swift isotropic hardening law, while kinematic hardening is not taken into account (see Laurent, 1996). The Hill'48 plastic yield surface is considered here to model the plastic anisotropy of the studied material. The associated three values of Lankford's coefficients r_0, r_{45} and r_{90}, required to identify Hill's coefficients, are summarized in Table 4.3. Since no blank-holder is used in this test, the blank is clamped all around its circumferential edge during the forming process. The friction coefficient associated with the contact between the tools and the blank is set to 0.15.

Table 4.3. Material parameters for the hemispherical cup.

Material	E (GPa)	ν	K (MPa)	ε_0	N	r_0	r_{45}	r_{90}
Steel	210	0.3	545	0.003	0.209	1.8011	1.5279	2.2404

Owing to the axial symmetry of the problem, only one quarter of the circular sheet is modeled, with an in-plane mesh discretization of 5250 elements in the case of prismatic elements, 2625 elements for hexahedral SHB8PS element case, and a finer in-plane mesh, 3083 elements, in the case of C3D8R element. The initial meshes of the circular sheet and the final deformed shapes of the hemispherical cup using the linear SHB elements are shown in Figs. 4.15 and 4.16, respectively.

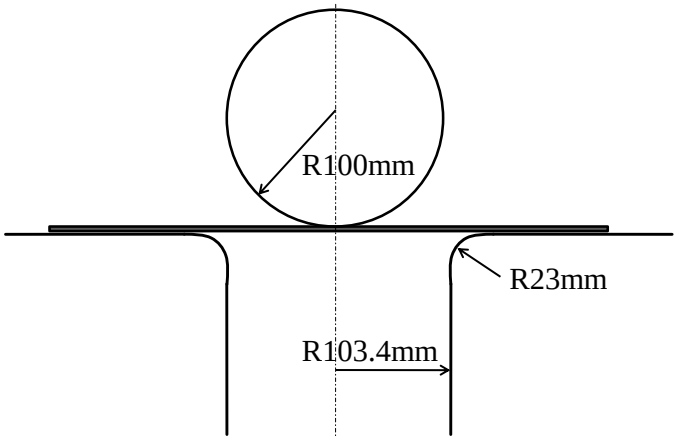
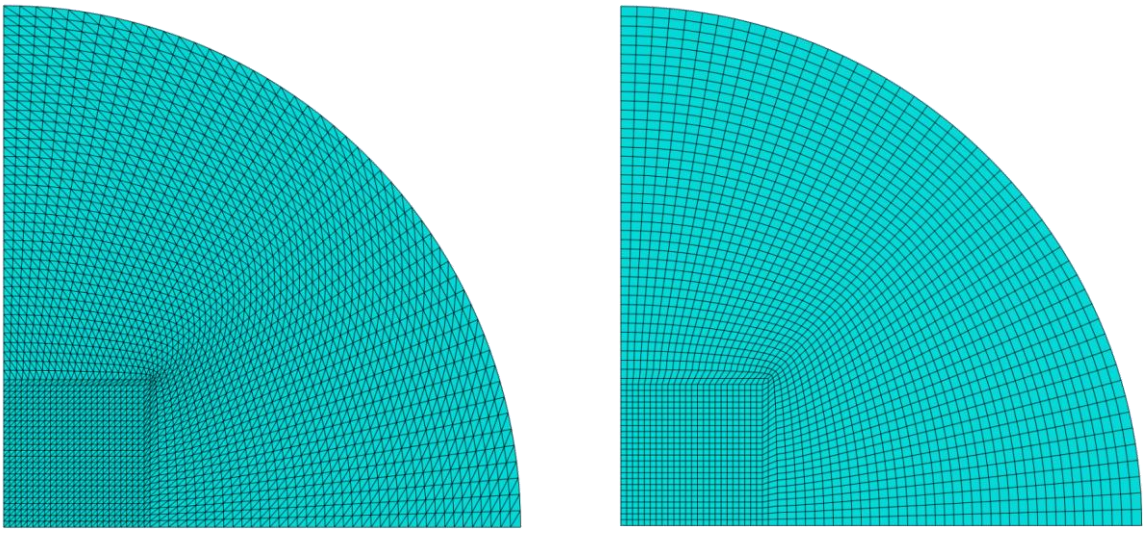
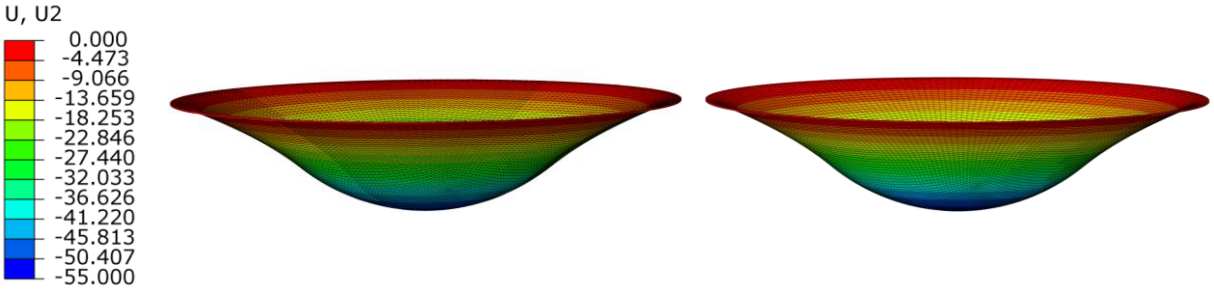


Figure 4.14. Hemispherical deep drawing setup.



(a) SHB6 elements (b) SHB8PS elements

Figure 4.15. Initial meshes for one quarter of the circular sheet using the linear SHB elements.



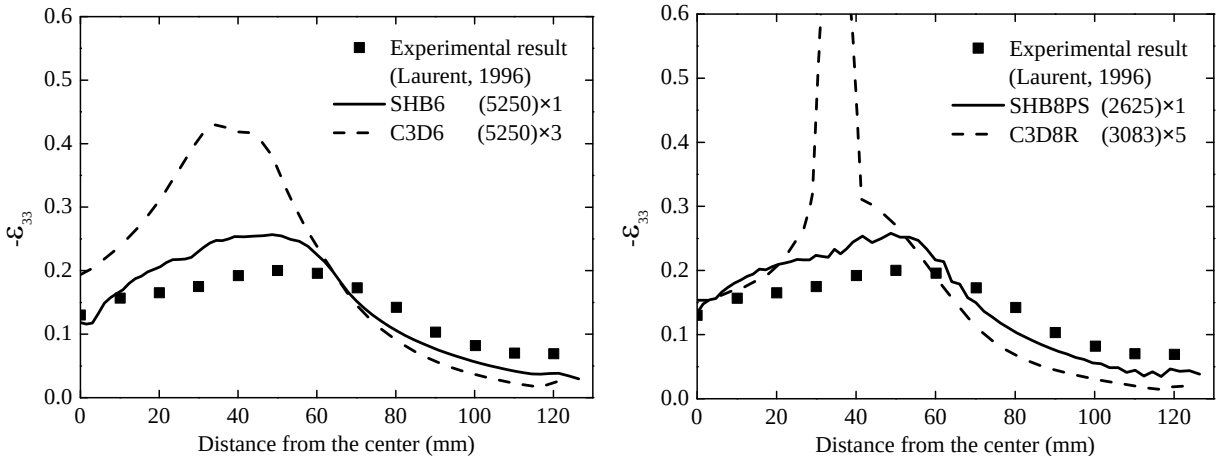
(a) SHB6 elements (b) SHB8PS elements

Figure 4.16. Final deformed shape for the hemispherical cup using the linear SHB elements.

The profile of the thickness strain of the blank along the rolling direction and the reaction force of the punch are reported in Fig. 4.17 and Fig. 4.19, respectively. These simulation results, which are obtained by using the linear SHB elements and only ABAQUS solid elements, are compared to the experimental results provided by Laurent (1996). Indeed, traditional shell elements do not allow displaying thickness strain variations due to their two-dimensional formulation.

From the predictions of the thickness strain profile in Fig. 4.17, the SHB elements provide the closest results to the experimental one in terms of overall evolution and order of magnitude, while the results obtained with the linear ABAQUS solid elements are inaccurate, especially in the zone located about 40 mm from the center of the blank. These contrasted results reveal that linear ABAQUS solid elements are not able to correctly handle the severe contact conditions between the blank and the punch in this zone, which leads to highly distorted meshes (see Figure 4.18).

Figure 4.19 shows the punch force evolution, as predicted by ABAQUS solid and SHB elements, together with the experimental results. Compared to ABAQUS solid elements, the results obtained with the linear SHB elements are in much better agreement with the experiments, which confirms once again the ability of the proposed SHB elements to model complex sheet metal forming processes using only a single layer of elements.



(a) linear prismatic elements (b) linear hexahedral elements

Figure 4.17. Simulation results in terms of thickness strain.

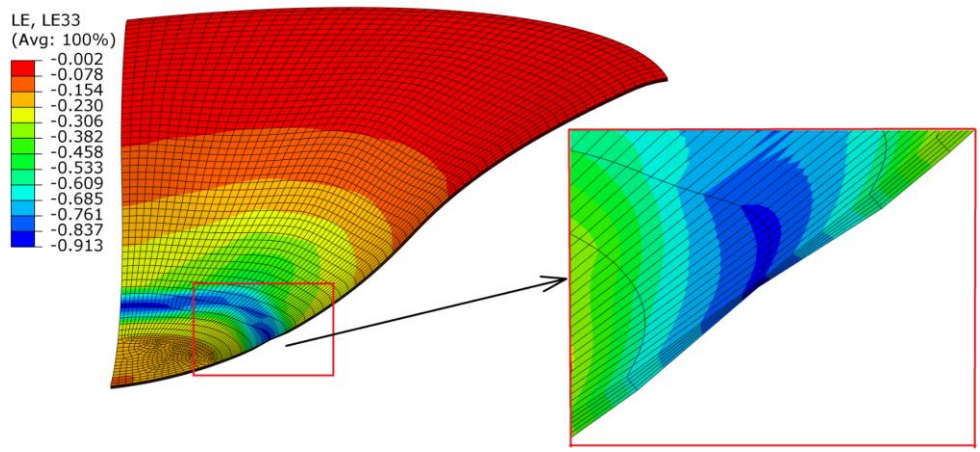
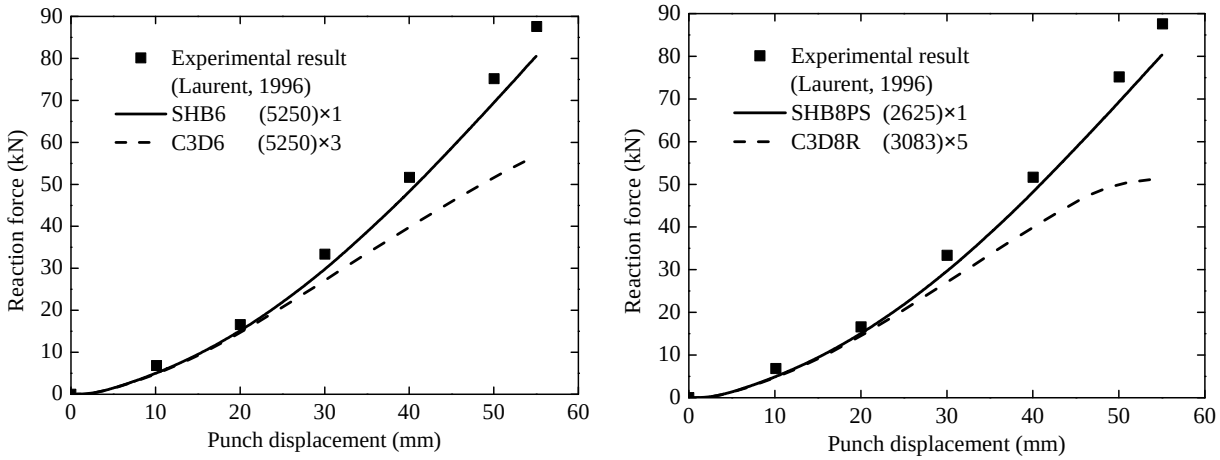


Figure 4.18. Final deformed mesh for the hemispherical cup using the ABAQUS C3D8R solid element: illustration of the distorted mesh zone.



(a) linear prismatic elements (b) linear hexahedral elements

Figure 4.19. Punch force evolution during the deep drawing of the hemispherical cup.

4.2.2 Deep drawing of a cylindrical cup

The deep drawing of a cylindrical cup is considered as one of the most popular benchmark problems in the context of sheet metal forming processes. In particular, this test has been often adopted for the analysis of the earing evolution of the cup when anisotropic plastic behavior of metal sheets is considered (see, e.g., Barlat et al., 2003; Yoon et al., 2006; Schwarze et al., 2010). The initially circular sheet is made of an AA2090-T3 aluminum alloy with an initial thickness of 1.6 mm. The plastic behavior of the sheet is described by the Swift isotropic hardening law (see Chapter 2, Table 2.2) together with the Hill'48 anisotropic yield

surface. The associated material parameters are summarized in Table 4.4. The schematic view of the drawing setup and the dimensions of the forming tools are shown in Fig. 4.20.

Table 4.4. Material parameters for the AA2090-T3 aluminum alloy.

Material	E (MPa)	ν	K (MPa)	ε_0	N	r_0	r_{45}	r_{90}
AA2090-T3	70,500	0.34	646	0.025	0.227	0.2115	1.5769	0.6923

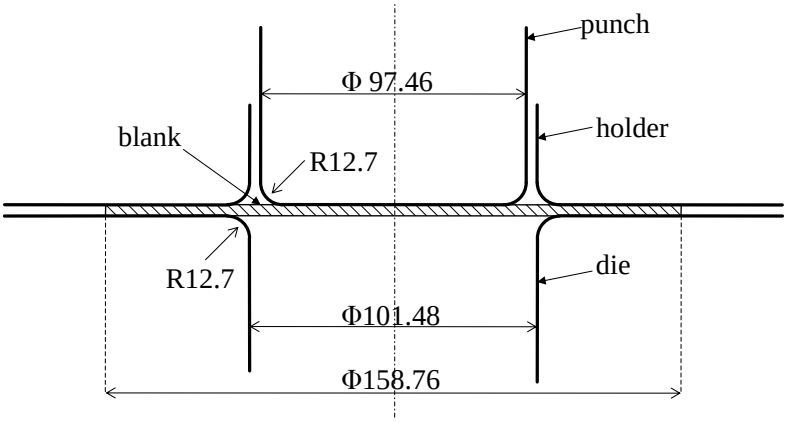
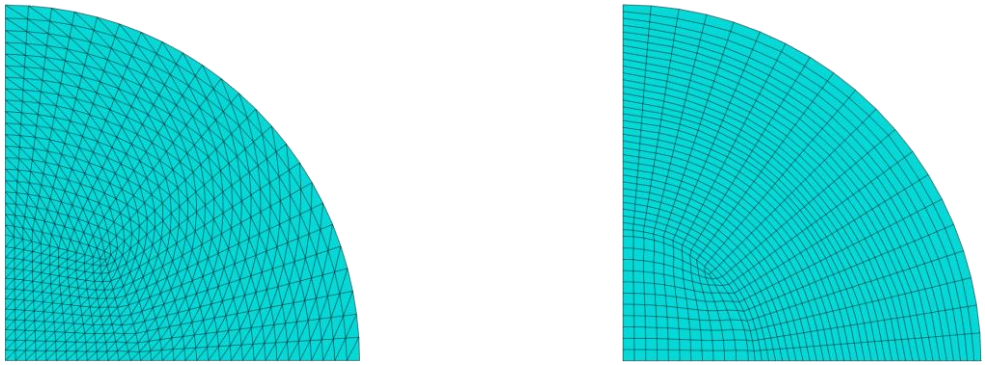


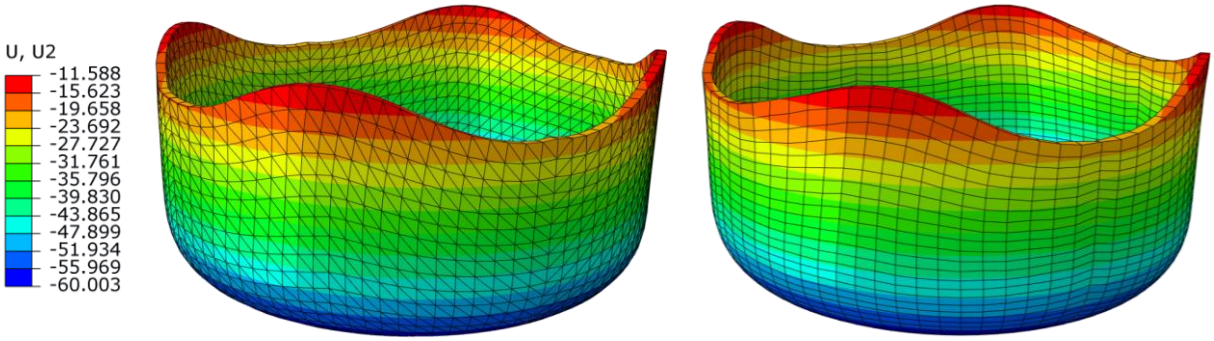
Figure 4.20. Schematic view for the cylindrical cup drawing process.

Due to symmetry considerations, only one quarter of the circular sheet is modeled, with an in-plane discretization of 1248 elements, in the case of triangular shell or prismatic elements, 800 elements in the case of quadrilateral shell or SHB8PS elements, and 1181 elements in the case of ABAQUS C3D8R solid element. The initial meshes with the linear SHB elements are depicted in Fig. 4.21. In the simulations, a constant holder force of 22.2 kN is applied during the forming process, and the friction coefficient associated with the contact between the sheet and the forming tools is taken equal to 0.1. Figure 4.22 shows the geometric shape of the formed ears for a completely drawn cup, as obtained with the linear SHB elements. It can be seen that the linear SHB elements predict four ears for the cylindrical cup, which is consistent with the use of the quadratic Hill'48 yield surface for the description of the material planar anisotropy.



(a) SHB6 elements (b) SHB8PS elements

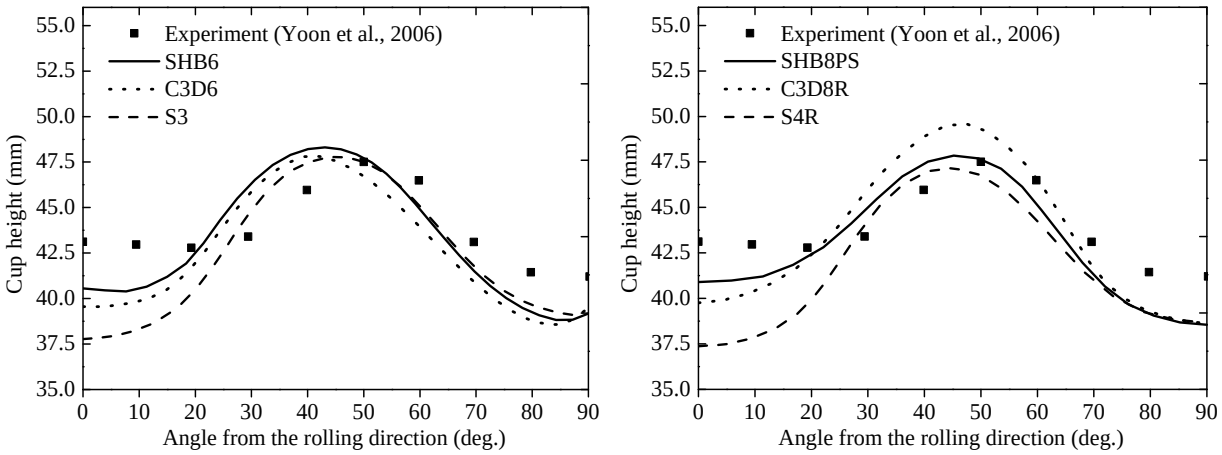
Figure 4.21. Initial meshes for one quarter of the circular sheet.



(a) SHB6 elements (b) SHB8PS elements

Figure 4.22. Final deformed shape for a completely drawn cylindrical cup.

The cup height profile predictions obtained with the linear SHB elements and ABAQUS elements are reported in Fig. 4.23, for the quarter of the cylindrical cup, and compared with the experimental measurements given by Yoon et al. (2006). On the whole, it can be observed that both the shape and the height of the earing profiles predicted with the linear SHB elements are in good agreement with the experiments. More specifically, in the range around the experimental peak value, the results given by the linear SHB elements are the closest to the experimental heights, in comparison with ABAQUS predictions. However, the predicted cup heights are underestimated at 0° and 90° from the rolling direction, both with the SHB elements and with ABAQUS elements. Nevertheless, these predictions could be improved in future work by adopting more appropriate anisotropic yield criteria for aluminum alloys (see, e.g., Barlat et al., 1991; Barlat et al., 2003; Yoon et al., 2006), which are able to predict more than four earing profiles for the complete circular sheet, as experimentally observed.



(a) Linear prismatic/triangular elements (b) Linear hexahedral/quadrilateral elements

Figure 4.23. Prediction of cup height profiles.

4.2.3 Deep drawing of a rectangular cup

The third sheet metal forming test investigated in this section consists in the deep drawing of a rectangular sheet with tools of rectangular shape. Because of its particular geometric characteristics, this benchmark problem is known to involve strong nonlinearities (due to large deformations, plasticity, and contact), which are more severe than those encountered in the previous deep drawing of a cylindrical cup. Note that the deep drawing of a rectangular cup has been previously studied by Choi and Huh (1999) and Huh and Choi (1999), by considering the Hill'48 quadratic yield criterion for the plastic anisotropy of the sheet and the Swift law for isotropic hardening. The initial dimensions of the rectangular sheet are 120 mm × 170 mm × 0.625 mm. The material parameters of the sheet metal, corresponding to a cold rolled steel, are summarized in Table 4.5 (see Choi and Huh, 1999), while the details on the geometry of the forming setup and its dimensions are all reported in Fig. 4.24.

Table 4.5. Material parameters associated with the anisotropic elastic–plastic model for the cold rolled steel.

Material	E (GPa)	ν	K (MPa)	ε_0	N	r_0	r_{45}	r_{90}
Steel	200	0.3	67.5	0.001	0.273	1.771	1.662	2.279

The constant blank holder force is set equal to 14.71 kN during the forming process, and the Coulomb friction coefficient relating to the contact between the forming tools and the

sheet is taken equal to 0.11. Owing to the symmetry, only one quarter of the sheet is modeled, with an in-plane discretization of 1960 elements for triangular shell or prismatic elements, and 980 elements for quadrilateral shell or hexahedral elements (see Fig. 4.25 for illustration). The final deformed shape for the rectangular cup, at punch stroke of 30 mm, is shown in Fig. 4.26 using the linear SHB elements.

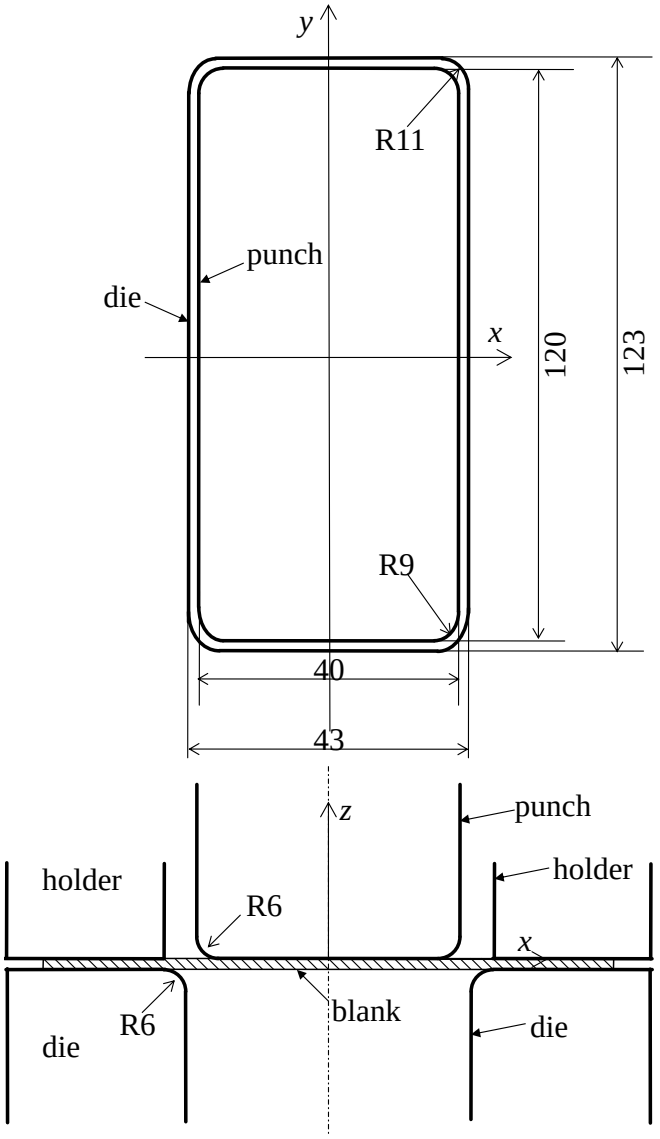
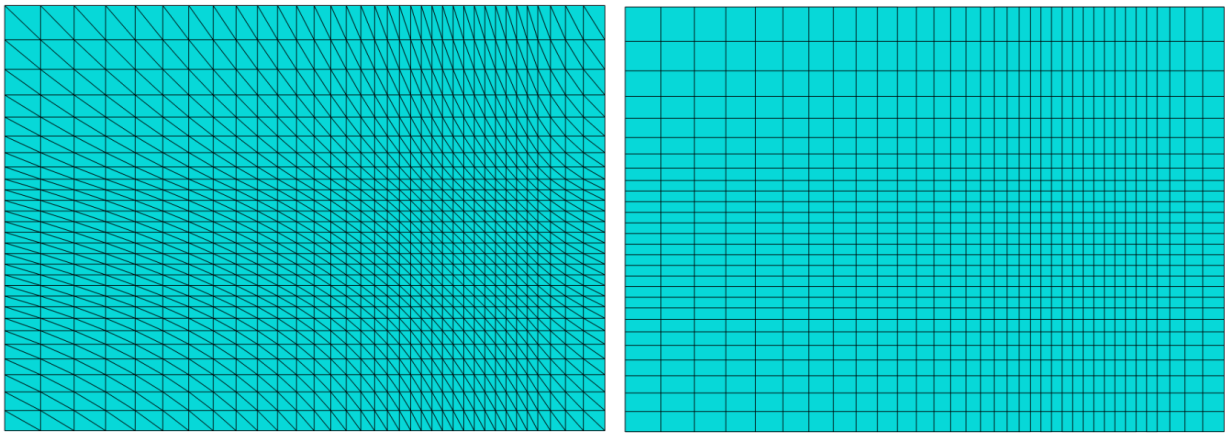
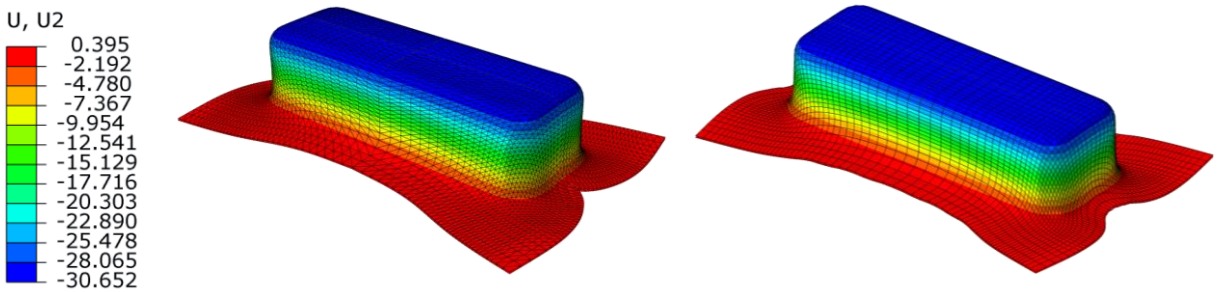


Figure 4.24. Schematic view for the rectangular cup drawing setup.



(a) 1960 SHB6 elements (b) 980 SHB8PS elements

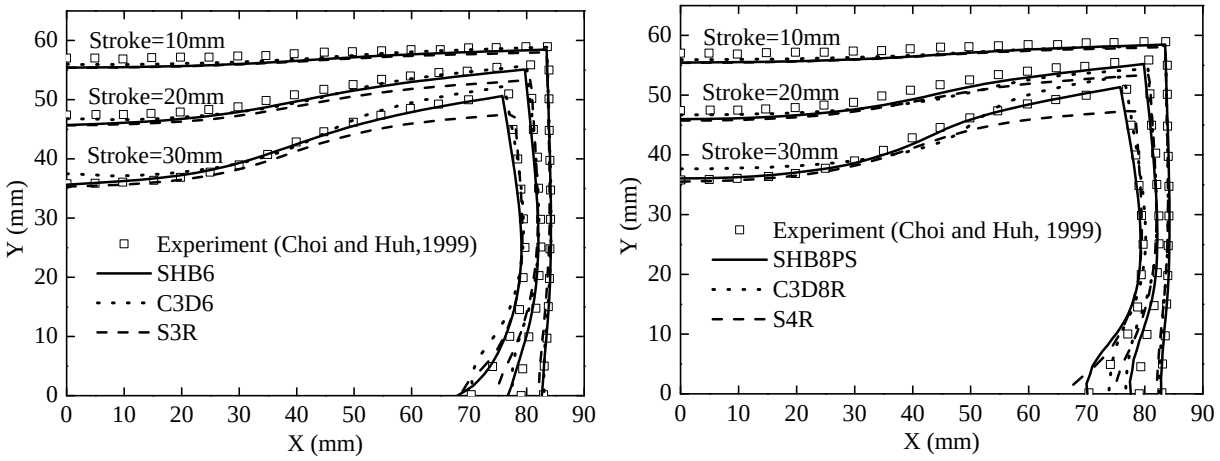
Figure 4.25. Initial in-plane meshes for a quarter of the rectangular sheet.



(a) SHB6 elements (b) SHB8PS elements

Figure 4.26. Final deformed shape for the rectangular cup at a punch stroke of 30 mm.

Figure 4.27 shows the predictions of flange contour of the sheet at different punch stroke (10, 20, and 30 mm), as obtained with the linear SHB elements and ABAQUS elements. These numerical predictions are also compared with the experimental flange contours given by Choi and Huh (1999). Overall, the flange contours predicted by both of the SHB6 and SHB8PS elements are in good agreement with those experimentally measured for the three forming stages (i.e., 10, 20, and 30 mm punch stroke). More specifically, in the case of small punch stroke (i.e., punch stroke of 10 mm), the flange contours predicted with the linear SHB elements and ABAQUS elements are quite equivalent, whereas the SHB elements provide the closest results to the experiments in the case of deep forming (i.e., punch stroke of 30 mm). These results clearly demonstrate the capability of the proposed SHB elements of accurately describing the various through-thickness phenomena using only a single element layer with few integration points.



(a) Linear prismatic/triangular elements (b) Linear hexahedral/quadrilateral elements

Figure 4.27. Prediction of flange contours at different punch strokes for the deep drawing of a rectangular cup.

4.2.4 Springback simulation of U-shape deep drawing

The springback simulation of the U-shape deep drawing process has been proposed as a benchmark test by the sheet metal forming community in the NUMISHEET'93 conference (Makinouchi et al., 1993). The schematic view of the setup and its geometric dimensions are described in Fig. 4.28. All details regarding the simulation process can be found in the related literature (see, e.g., Dvorkin and Bathe, 1984; Ponthot et al., 2000; Park and Oh, 2004; Zhang et al., 2007; Flores, 2013b). This deep drawing process is divided into two steps: the forming step, followed by the springback step. During the first step, the U-shape is formed until the maximum punch stroke of 70 mm is reached under a holding force of 2.45 kN (see Fig. 4.29 (a)). Then, the springback stage of the sheet takes place by removing the holding force and all contact between the sheet and the tools (see Fig. 4.29 (b)).

Both an aluminum-alloy sheet and a steel sheet are considered in this study. The initial dimensions of the aluminum sheet are 350 mm × 35 mm × 0.81 mm, with a friction coefficient relating to the contact between the tools and the blank equal to 0.162, while the initial dimensions of the steel sheet are 350 mm × 35 mm × 0.78 mm, with a friction coefficient equal to 0.144. The material parameters associated with both materials are summarized in Table 4.6, in which the Swift law has been considered to describe isotropic hardening, while the Hill'48 quadratic yield criterion is adopted to model the plastic anisotropy.

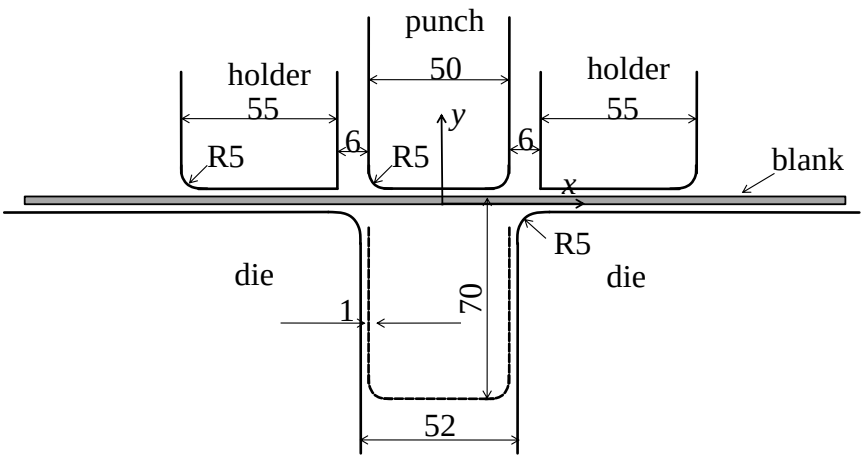
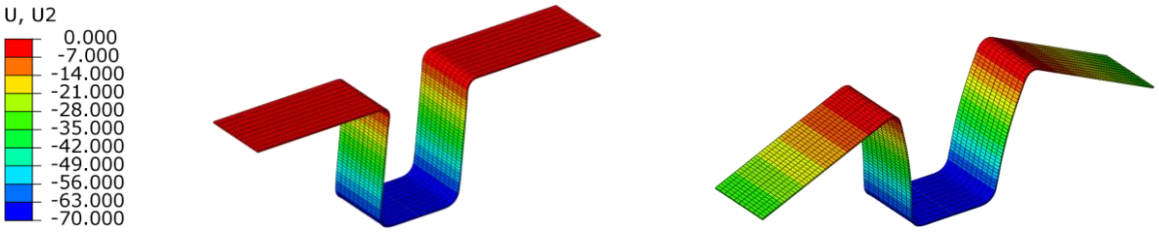


Figure 4.28. Setup of the U-bending tools.



(a) End of forming step (b) After springback

Figure 4.29. Illustration of the deformed sheet in the U-shape deep drawing test using SHB20 elements.

Table 4.6. Material parameters for the aluminum and steel sheets.

Material	E (MPa)	ν	K (MPa)	ε_0	N	r_0	r_{45}	r_{90}
Aluminum	71,000	0.33	576.79	0.01658	0.3593	0.71	0.58	0.70
Steel	206,000	0.3	565.32	0.007117	0.2589	1.79	1.51	2.27

Considering the symmetry of the problem, only one quarter of the blank is analyzed. The latter is discretized by (100×5×2)×1 triangular shell or prismatic elements and 100×5×1 hexahedral elements, respectively (the mesh nomenclature is the same as that used in Chapter 3). As stated before, only three integration points through the thickness are considered in the simulations using the quadratic SHB and ABAQUS elements. Note that the simulations with the ABAQUS quadratic shell element (i.e., S8R) failed to converge for both studied materials, which clearly emphasizes the limitations of this shell element in handling double-sided contact in sheet metal forming processes.

To quantify the amount of springback for the blank after the forming stage, the angles around the punch radius and the die radius (θ_1 and θ_2 , respectively, in Fig. 4.30) are investigated. The simulation results obtained with the quadratic SHB elements are compared in Tables 4.7 and 4.8 with those given by ABAQUS quadratic elements as well as with experimental measurements and numerical solutions available in the literature. On the whole, the angles after springback predicted with the quadratic SHB elements are in good agreement with those given by ABAQUS quadratic elements, and lie in the intervals defined by the reference results. These results demonstrate the good capabilities of the SHB elements in modeling sheet metal forming processes, where various nonlinearities (geometric, material, and double-sided contact) enter into play, while using only a single element layer with few through-thickness integration points.

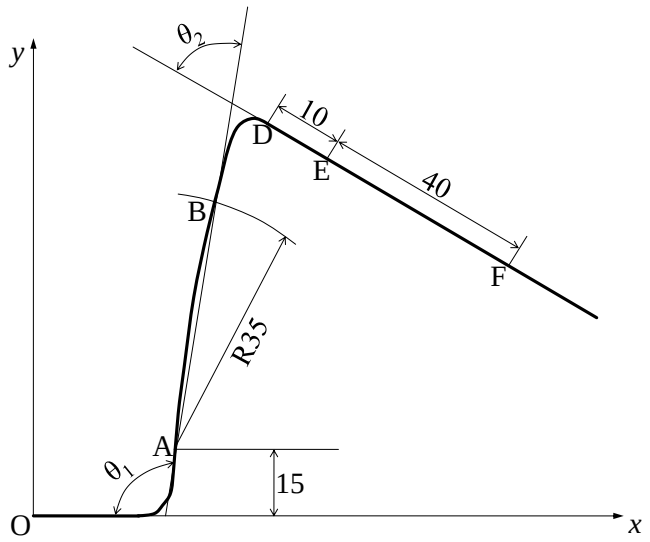


Figure 4.30. Definition of springback angles θ_1 and θ_2.

Table 4.7. Springback angles θ_1 and θ_2 for the aluminum material.

Material	Angle (°)	Experiment*	Simulation*	STRI65	C3D15	SHB15	C3D20	SHB20
Aluminum	θ_1	101.5º~116.0º	62.0º~134.0º	107.28º	108.87º	102.72º	106.03º	104.13º
	θ_2	68.5º~77.5º	63.0º~91.0º	69.85º	69.67º	70.74º	70.74º	74.53º

* Note: The experimental and simulated intervals are given in Flores (2013b).

Table 4.8. Springback angles θ_1 and θ_2 for the steel material.

Material	Angle (°)	Reference 2*	Reference 3*	STRI65	C3D15	SHB15	C3D20	SHB20
Steel	θ_1	101.06º	100.82º	97.94º	99.67º	99.37º	97.03º	98.32º
	θ_2	79.99º	80.45º	80.10º	80.27º	81.05º	82.33º	82.52º

* Note: Reference 2 corresponds to Dvorkin and Bathe (1984), while reference 3 refers to Park and Oh (2004).

4.2.5 Deep drawing of a square cup

The benchmark test of deep drawing of a square cup, as proposed in the Numisheet'93 conference (Makinouchi et al., 1993) and subsequently by several other authors (see, e.g., Kaiping et al., 1995; Choi and Huh, 1999; Schwarze et al., 2011; Xu et al., 2012; Pagani et al., 2014), is considered here to assess the ability of the proposed quadratic solid–shell elements to model challenging industrial forming applications. The geometric dimensions of the forming tools are specified in Fig. 4.31. Two square sheets, with initial dimensions of 150 mm × 150 mm ×0.81 mm and 150 mm × 150 mm × 0.78 mm, corresponding to aluminum sheet and steel sheet, respectively, are considered for the simulations. The associated elasto-plastic material parameters, according to the Swift isotropic hardening law and the von Mises yield surface, are the same as those reported in Table 4.6.

All along the forming process, a constant blank holding force of 16.6 kN is applied. The friction coefficient relating to the contact between the blank and the forming tools is taken equal to 0.162 for the aluminum sheet, and 0.144 for the steel sheet. Owing to the symmetry, only one quarter of the sheets is discretized with a mesh of (32×32×2)×1 quadratic elements, in the case of prismatic elements, and 32×32×1 quadratic elements, in the case of hexahedral elements (the mesh nomenclature is the same as that used in Chapter 3). Also, only a single element layer is used in the simulations with three integration points through the thickness. The final deformed shapes of the sheets, which correspond to a maximum punch stroke of 15 mm for the aluminum square cup and 40 mm for the steel square cup, are shown in Figs. 4.32 and 4.33, respectively.

Three draw-in distances D_x, D_y, and D_d, corresponding to the final formed cups, as illustrated in Fig. 4.34, are investigated here for both studied materials. The predicted results

for the aluminum cup and the steel cup are reported in Tables 4.9 and 4.10, respectively. Note that, for the same reasons discussed in previous sheet metal forming processes, the simulations using the ABAQUS quadratic shell elements STRI65 and S8R failed to converge and, accordingly, no results are reported for these elements.

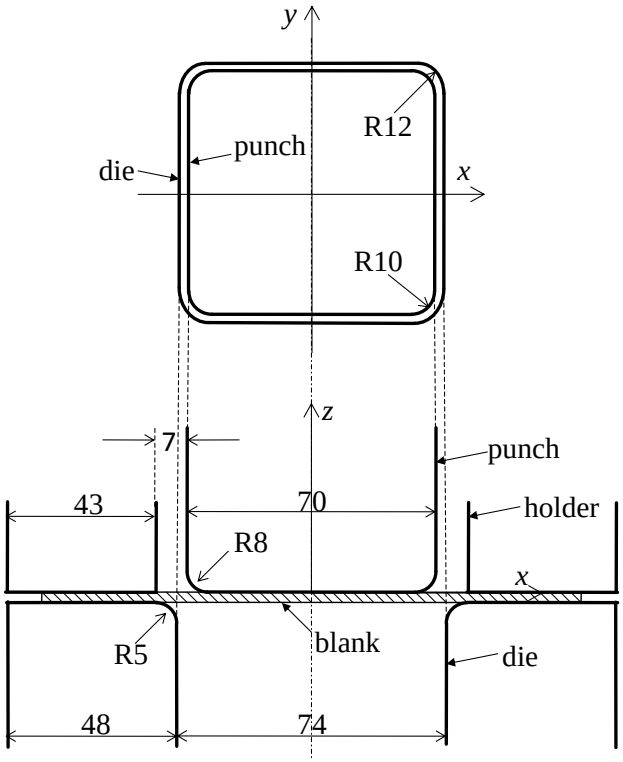
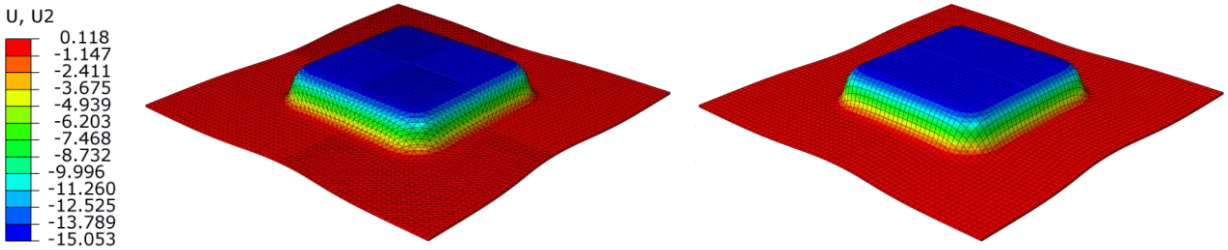
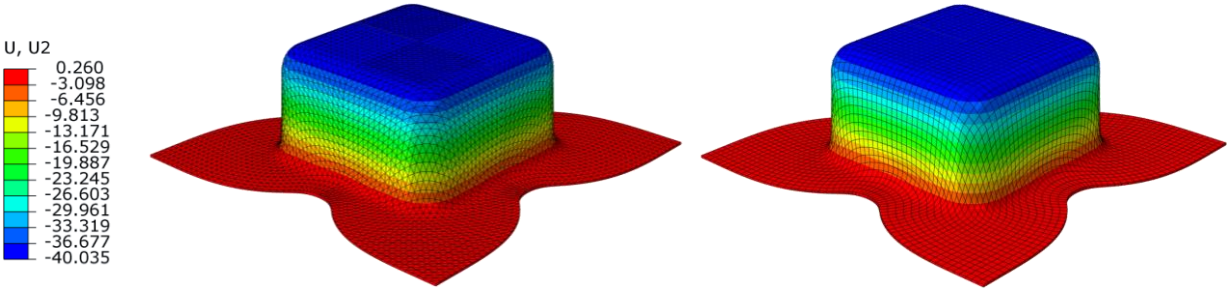


Figure 4.31. Schematic view for the square cup drawing process.



(a) SHB15 elements (b) SHB20 elements

Figure 4.32. Final deformed shape for the aluminum square cup at 15 mm punch stroke.



(a) SHB15 elements (b) SHB20 elements

Figure 4.33. Final deformed shape for the steel square cup at 40 mm punch stroke.

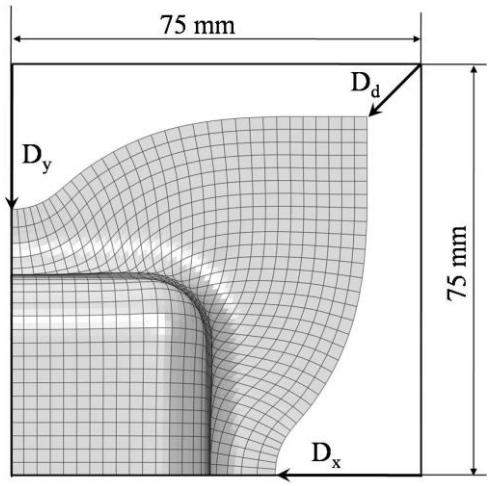


Figure 4.34. Definition of the draw-in distances for the final formed square cup.

For the aluminum cup, all draw-in distances predicted with the quadratic SHB elements lie in the range delimited by the maximum and minimum experimental measurements, which is also the case for the predictions using ABAQUS quadratic solid elements. Note also that the predicted draw-in distances D_x and D_y are identical for all simulations, which is consistent with the assumed isotropic plastic behavior of the sheets.

Table 4.9. Draw-in distances for the aluminum cup at 15 mm punch stroke.

	Mesh	Number of integration points per element	D_x (mm)	D_y (mm)	D_d (mm)
Min. experiment	—	—	3.80	3.90	2.30
Max. experiment	—	—	6.45	6.49	3.79
C3D15	(32×32×2)×1	18	5.52	5.52	2.59
SHB15	(32×32×2)×1	9	5.87	5.87	3.00
C3D20	32×32×1	27	5.31	5.31	2.39
SHB20	32×32×1	12	5.61	5.61	2.32

Table 4.10. Draw-in distances for the steel cup at 40 mm punch stroke.

	Mesh	Number of integration points per element	D_x (mm)	D_y (mm)	D_d (mm)
Min. experiment	—	—	26.75	26.75	14.06
Max. experiment	—	—	29.60	29.58	16.31
C3D15	(32×32×2)×1	18	26.57	26.57	13.64
SHB15	(32×32×2)×1	9	29.64	29.64	15.89
C3D20	32×32×1	27	26.57	26.57	13.73
SHB20	32×32×1	12	29.81	29.81	15.63

With respect to the experimental range for the steel cup, the predicted draw-in distances D_x and D_y are very slightly overestimated with the quadratic SHB elements, while they are very slightly underestimated with the quadratic ABAQUS solid elements. Nevertheless, the diagonal draw-in distance D_d predicted with the quadratic SHB elements is in good agreement with the experimental measurements, whereas it is somewhat underestimated with the quadratic ABAQUS solid elements. On the whole, the proposed quadratic solid–shell elements perform better than their ABAQUS counterparts, considering the above-discussed results and the fact that the latter require more integration points (IPs) per element (18 IPs for the C3D15 element and 27 IPs for the C3D20 element, compared to only 9 IPs for the SHB15 element and 12 IPs for the SHB20 element).

4.2.6 Single point incremental sheet metal forming

For the past two decades, the incremental forming technology has attracted much attention due to its advantages in terms of economical operability. Single Point Incremental Forming (SPIF) has become a typical test in the context of incremental forming process (see, e.g., Bouffioux et al., 2008; Sena et al., 2010; Henrard et al., 2011; Sena et al., 2016). As illustrated in Fig. 4.35, a clamped square sheet is gradually deformed in its central area by applying a spherical punch with a radius of 5 mm following a preset path. The punch is

initially set to be tangent to the sheet surface, and located 41 mm away from one side of the sheet. The whole forming process consists in the following five steps:

1) The punch indents the sheet with 5 mm depth along the *y*-direction;
2) The punch moves at the same depth following a line of 100 mm along the *x*-direction;
3) The punch indents a second time the sheet up to a depth of 10 mm;
4) The punch moves back, at the same new depth, following a line of 100 mm along the *x*-direction;
5) Finally, an unloading step takes place, with the punch returning back to its initial position.

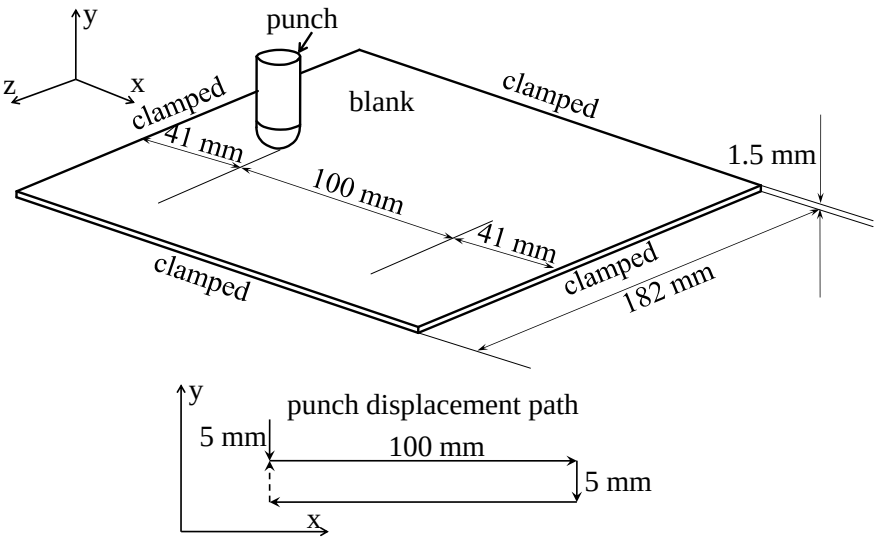


Figure 4.35. Description of the single point incremental forming test.

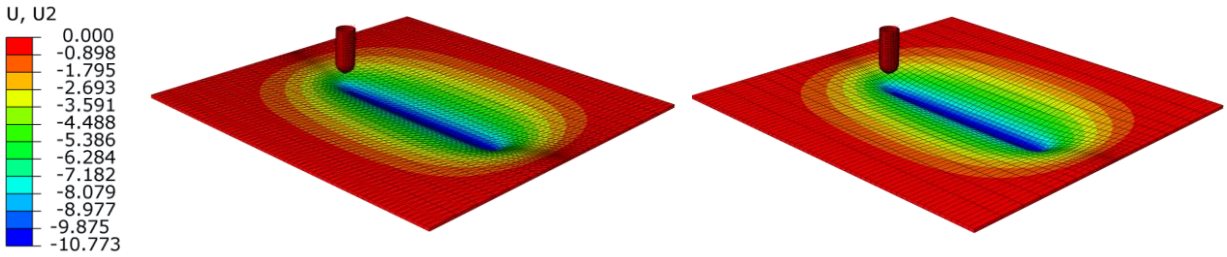
The material used for the simulations is an aluminum alloy AA3103-O (see Bouffioux et al., 2008). The associated elasto-plastic material parameters are summarized in Table 4.11, according to the Swift isotropic hardening law.

Table 4.11. Material parameters for the AA3103-O aluminum alloy.

Material	E (MPa)	ν	K (MPa)	ε_0	N
AA3103-O	72,600	0.36	180	0.00057	0.229

The contact conditions between the punch and the sheet are assumed frictionless. Because the sheet is deformed mainly in the central area, only one half of the model is meshed with

(60×15×2)×1 quadratic elements, in the case of prismatic elements, and 60×15×1 quadratic elements, in the case of hexahedral elements (again, the mesh nomenclature is the same as that used in Chapter 3). The obtained results in terms of punch force–punch displacement correspond to converged solutions using only a single element layer with three through-thickness integration points. Figure 4.36 shows the final deformed mesh for this SPIF test, as obtained with the proposed quadratic SHB elements.

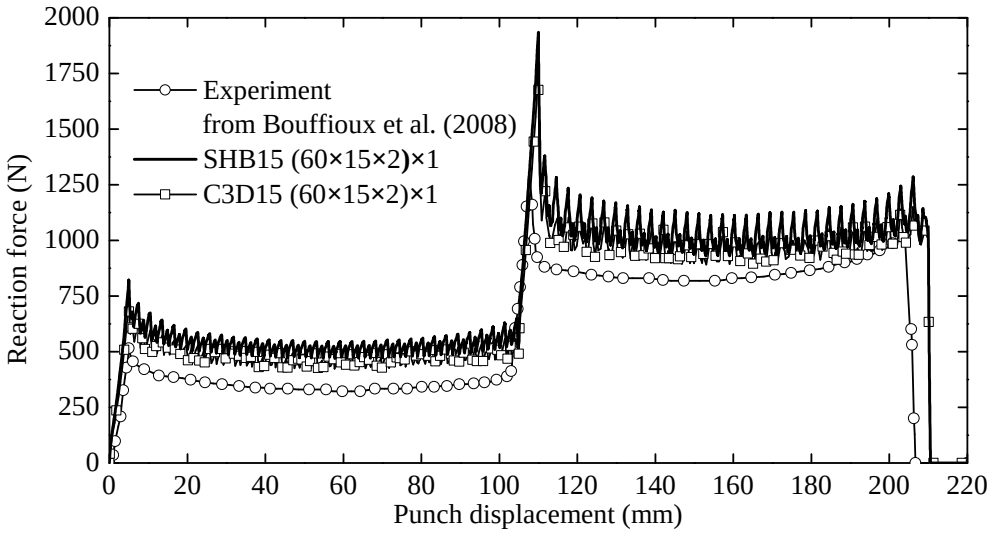


(a) (60×15×2)×1 SHB15 elements (b) 60×15×1 SHB20 elements

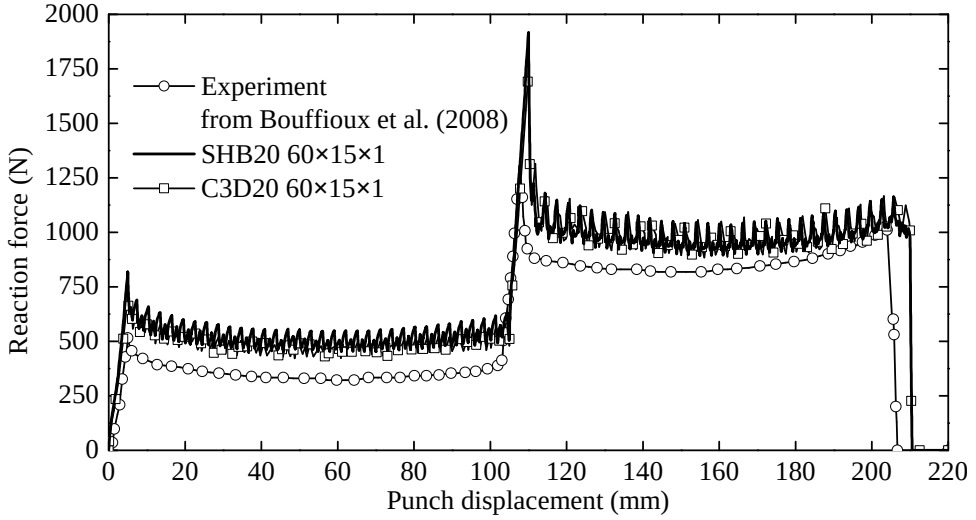
Figure. 4.36. Final deformed shape for the SPIF sheet.

The punch force–punch displacement responses simulated with the proposed quadratic SHB elements are compared in Fig. 4.37 with those given by ABAQUS elements as well as with the experimental results provided by Bouffioux et al. (2008). It should be noted that the simulations using ABAQUS shell elements (i.e., STRI65 and S8R) failed to converge, due to contact-type nonlinearities. This suggests, once again, that finite element formulations based on fully 3D approaches are more appropriate to model sheet metal forming processes in which double-sided contact enters into play. As shown in Fig. 4.37, the punch force–punch displacement responses obtained with the quadratic SHB elements are in good agreement with those given by quadratic ABAQUS elements, although both lying higher than the experimental results. Note that oscillations in the simulated curves are observed both for the SHB elements and for ABAQUS elements. Indeed, when the punch slides during the forming process, the contact between the punch and the sheet within a confined zone is lost and recovered several times, until another new zone comes into the same situation. This phenomenon causes oscillations in the punch force–punch displacement curve, whose amplitudes and number depend on the mesh size of the punch and the sheet (see, e.g., Wriggers, 2006). In order to reduce these numerical oscillations, a refined mesh for the sheet is used in the simulations, which consists of (100×30×2)×1 quadratic elements, in the case of prismatic elements, and 100×30×1 quadratic elements, in the case of hexahedral elements.

Figure 4.38 reports the results obtained by using refined meshes, where it is clearly shown that the simulated punch force–punch displacement curves are much smoother than those obtained with coarse meshes.

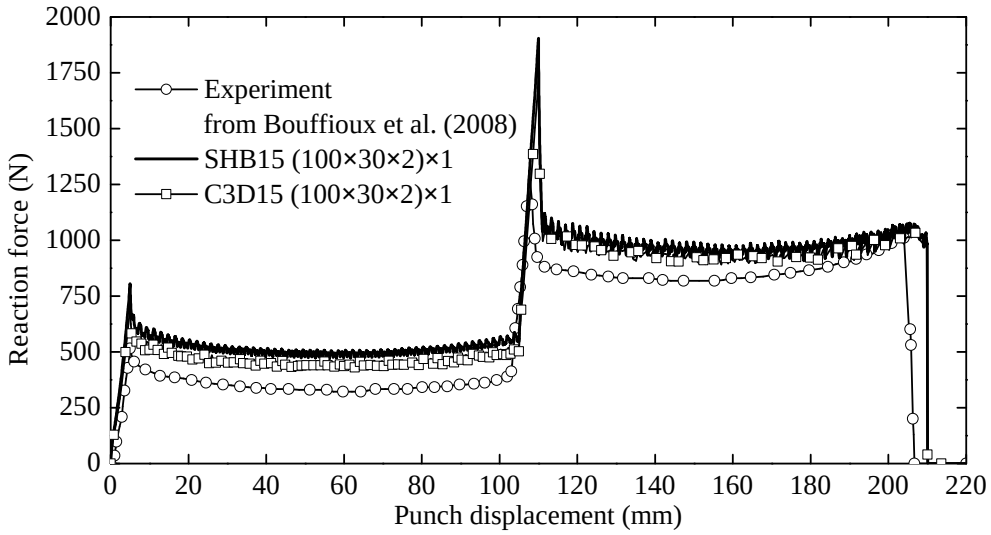


(a) (60×15×2)×1 prismatic elements

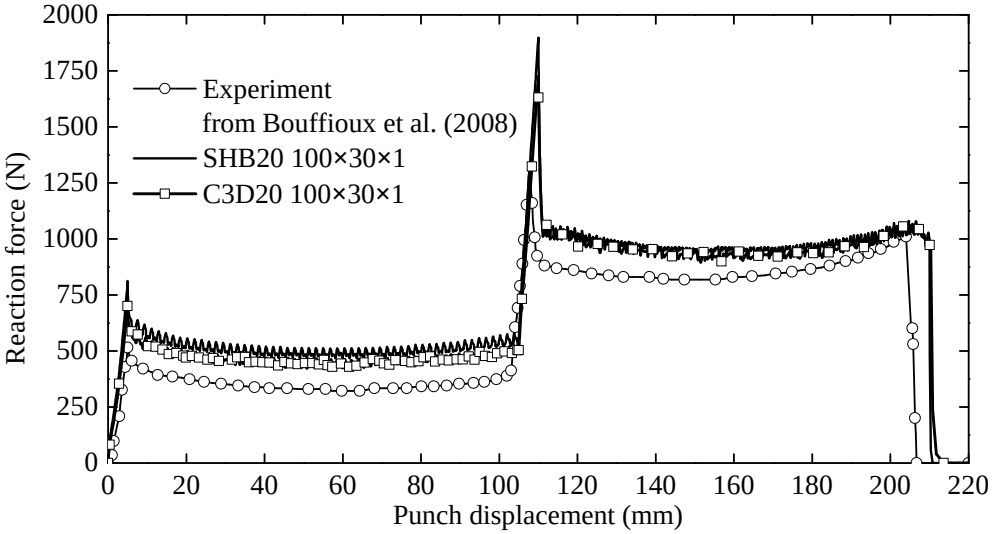


(b) 60×15×1 hexahedral elements

Figure 4.37. Simulation results using coarse meshes, in terms of punch force evolution for the SPIF test, along with experiments taken from Bouffioux et al. (2008).



(a) (100×30×2)×1 prismatic elements



(b) 100×30×1 hexahedral elements

Figure 4.38. Simulation results using fine meshes, in terms of punch force evolution for the SPIF test, along with experiments taken from Bouffioux et al. (2008).

Conclusion

In this chapter, the proposed SHB solid–shell elements have been applied to the simulation of complex and challenging problems, including impact/crash problems and sheet metal forming processes, in order to assess their capabilities in handling various types of nonlinearities (geometric, material, and due to contact). Various comparisons between the numerical results provided by the proposed SHB elements and reference or experimental measurements revealed that the proposed solid–shell elements are able to successfully model

such complex processes, using only a single element layer with few through-thickness integration points. Furthermore, the proposed SHB elements provided the closest results to the experimental data, when compared to existing state-of-the-art ABAQUS solid and shell elements. It is worth noting that, in the simulations of sheet metal forming processes, ABAQUS shell elements failed to converge, which reveals that these conventional shell elements are not appropriate for handling double-sided contact in such complex forming processes. The SHB elements represent an interesting alternative to traditional shell elements, especially for the simulation of complex problems involving double-sided contact, which are very common in sheet metal forming processes.

Conclusions and future works

Conclusions

In this work, a family of prismatic and hexahedral solid–shell (SHB) elements with their linear and quadratic versions has been proposed for the three-dimensional modeling of thin structures. Several numerical treatments, such as the assumed strain method (ASM), the reduced integration rule and the stabilization technique, have been adopted in the formulation of the SHB elements to eliminate the main locking phenomena. A common characteristic feature for these elements is that they are based on a fully three-dimensional approach, with only translational degrees of freedom. In addition, they are designed to be used with only a single element layer, while attributing an arbitrary user-defined number of integration points in the thickness direction. This makes them very attractive, due to their computational efficiency in both quasi-static and dynamic analyses.

With regard to earlier developments, the formulation of the proposed solid–shell elements has been extended in this work to the framework of large displacements and rotations as well as explicit/dynamic analysis. Moreover, the resulting formulations have been combined with advanced constitutive models, including orthotropic elastic behavior for composite materials and anisotropic plastic behavior for metallic materials, which allows for a broad range of applications. All of the SHB elements have been implemented into ABAQUS implicit/static and explicit/dynamic software packages, with the help of UEL and VUEL subroutines, respectively, in order to model various quasi-static and dynamic problems.

The performance of the proposed SHB elements has been first evaluated on a series of selective linear and nonlinear benchmark tests. For each benchmark problem, the results given by the SHB elements have been compared with those yielded by their ABAQUS counterparts as well as with reference solutions taken from the literature. For all benchmark tests, the numerical results obtained with the SHB elements showed very good agreement with the available reference solutions. Compared to state-of-the-art ABAQUS shell elements, the performance of the SHB elements is often comparable; however, in most numerical tests, ABAQUS solid elements require finer meshes (in the plane and through the thickness) to provide accurate solutions.

Then, the SHB elements have been applied to the simulation of more challenging numerical tests, including impact/crash problems and sheet metal forming processes. Various comparisons between the simulation results given by the SHB elements and the experimental measurements revealed that the proposed solid–shell elements are able to successfully model such complex processes, using only a single element layer with few through-thickness integration points. Furthermore, the SHB elements provided the closest results to the experimental data, when compared to their ABAQUS counterparts. It is worth noting that the simulations of the investigated sheet metal forming processes using ABAQUS quadratic shell elements failed to converge, which reveals that these shell elements are not appropriate for handling double-sided contact in such complex forming processes.

Overall, the proposed SHB elements, and especially the quadratic versions, showed good capabilities in modeling various types of structural problems, with relatively coarse meshes and few integration points through the thickness, whereas conventional solid elements required finer meshes to achieve accurate solutions. Also, the SHB elements represent an interesting alternative to traditional shell elements, especially for the simulation of complex problems involving double-sided contact, which are very common in the simulation of sheet metal forming processes.

Future works

As revealed in Chapters 3 and 4 of the manuscript, the proposed SHB solid–shell elements have provided good predictions for a series of popular benchmark tests as well as a variety of complex problems. However, some numerical aspects still need to be improved in order to make the SHB elements more efficient with respect to the current versions. In future works, the following aspects should be pursued:

1) Combining different elements within a single simulation: the proposed family of SHB elements, which consists of two prismatic elements and two hexahedral elements, has been implemented into ABAQUS standard/quasi-static and explicit/dynamic software packages. It has been shown, on the whole, that the performance of the hexahedral SHB elements (i.e., SHB8PS and SHB20) is better than that of the prismatic SHB elements (i.e., SHB6 and SHB15). However, these hexahedral and prismatic solid–shell elements complement each other very well, as combination of these may prove necessary for the simulation of

complex shaped geometries, which cannot be meshed using only hexahedral elements. Similar situations may also be encountered when using free mesh-generation tools, which results in meshes comprising both hexahedral and prismatic elements.

2) Improvement of the computational efficiency: in the current contribution, attention has mainly been focused on the accuracy of the SHB solid–shell elements. It is worth noting that, for all of the SHB elements, the simulations have been performed using only a single element layer and few through-thickness integration points. Consequently, the resulting finite element (FE) models are inherently less expensive, in terms of number of degrees of freedom (DOF) and integration points, than those using conventional solid finite elements. However, the FE implementation of the proposed SHB elements is achieved via several open-source subroutines, which allow interfacing with ABAQUS software. These subroutines are far from being well optimized in terms of computer programming. In future works, the current FE implementation of the SHB elements could be better optimized, e.g. by employing the same programming techniques as those used in commercial FE software packages.

3) Application of the SHB elements to more complex problems: although various numerical tests have been investigated in this work in order to evaluate the performance of the SHB elements, it will also be very interesting to further extend their application range to more complex and challenging problems, involving severe combined geometric and material nonlinearities. In this process, more advanced material behavior models, such as constitutive equations based on non-quadratic anisotropic yield functions that are more suitable to aluminum alloys, should be implemented in the future in order to allow a broad range of industrial applications.

Part II: Résumé Français

Résumé en français de la thèse

Introduction

Motivation de la thèse

Les structures minces sont largement utilisées dans de nombreuses industries afin de réduire le poids de produits et d'améliorer leurs performances mécaniques. La simulation par éléments finis (EF) de ces structures minces est devenue un outil indispensable dans la conception de produits et l'optimisation des processus de fabrication. Malgré le développement croissant des ressources de calcul, la fiabilité et l'efficacité des simulations numériques par EF restent encore à améliorer. Traditionnellement, pour la simulation de structures minces, les éléments finis coques classiques sont très utilisés, ou alternativement les éléments finis solides sont employés pour prendre en compte les effets tridimensionnels (3D). Cependant, dans certaines situations, les éléments finis coques et les éléments finis solides traditionnels souffrent de divers phénomènes de verrouillage, tels que le verrouillage en cisaillement, le verrouillage en membrane, le verrouillage volumétrique, etc. En outre, les éléments finis coques ne sont souvent pas adaptés pour la modélisation de problèmes complexes impliquant un contact sur les deux faces. Afin de lever ces verrous scientifiques, des efforts considérables ont été menés dans la littérature ces dernières décennies pour le développement d'éléments finis performants.

Les éléments finis membrane ont été largement utilisés en raison de leur efficacité de calcul dans la simulation de problèmes de flexion. Afin d'obtenir des résultats plus précis, une attention particulière a été accordée dans la littérature au développement d'éléments finis coques pour la modélisation de structures minces. Par rapport aux éléments finis membrane, les éléments finis coques offrent une meilleure précision pour la modélisation de structures minces. Cependant, la formulation d'éléments finis coques est typiquement basée sur l'hypothèse des contraintes planes, ce qui limite leurs applications pour la simulation de procédés de mise en forme des tôles minces. En outre, ils ne peuvent pas tenir compte des variations d'épaisseur, puisque seul le plan médian de la tôle mince est modélisé, ce qui rend difficile la gestion du contact sur les deux faces.

Parallèlement, les éléments finis solides permettent une modélisation plus réaliste d'un certain nombre de problèmes structurels grâce à leur formulation tridimensionnelle, évitant ainsi les hypothèses géométriques et cinématiques d'une part, et les hypothèses de comportement (contraintes planes) d'autre part. Cependant, dans la simulation de structures minces, l'utilisation d'éléments finis solides implique l'utilisation d'un nombre important d'éléments finis, ce qui est en partie attribuable aux limitations du rapport d'aspect de l'élément fini solide, ainsi qu'aux effets de verrouillage inhérents aux fonctions d'interpolation de bas degrés. De plus, plusieurs couches d'éléments solides dans la direction de l'épaisseur sont nécessaires pour décrire avec précision les différents phénomènes non linéaires, ce qui augmente considérablement les temps de calcul.

Plus récemment, le concept d'éléments finis solide–coque a émergé, ce qui représente aujourd'hui une alternative intéressante aux éléments finis solides et coques conventionnels, en particulier pour les simulations des procédés de mise en forme des tôles minces. En effet, les éléments finis solide–coque combinent les avantages des formulations des éléments solides et des éléments coques. Leurs principales caractéristiques, qui les rendent très attrayants, peuvent être résumées comme suit : l'utilisation de lois constitutives tridimensionnelles sans l'hypothèse des contraintes planes; connexion facile avec des éléments solides conventionnels puisque les déplacements sont les seuls degrés de liberté considérés; calcul direct des variations d'épaisseur; considération naturelle du contact sur les deux faces de l'élément; aptitude à modéliser avec précision des structures minces avec une seule couche d'élément fini et peu de points d'intégration dans la direction de l'épaisseur.

Ce travail contribue au développement d'une famille d'éléments finis solide–coque (SHB) pour la modélisation tridimensionnelle de structures minces. Le champ d'application de ces éléments finis solide–coque est élargi aux problèmes complexes, impliquant plusieurs phénomènes non-linéaires (grands déplacements, grandes rotations, non-linéarité matérielle et contact).

Objectifs de la thèse

Dans ce travail, une famille d'éléments finis solide–coque SHB, composée d'éléments linéaires, prismatique SHB6 et hexaédrique SHB8PS, et leurs homologues quadratiques SHB15 et SHB20, est développée pour la modélisation tridimensionnelle de structures minces. Considérant les contributions antérieurs d'Abed-Meraim et ses collègues dans le

développement de cette famille d'éléments finis SHB, nous résumons ci-après les principaux objectifs de ce travail :

- Les éléments finis SHB proposés dans cette contribution représentent des extensions des versions quasi-statiques précédentes. Ils sont formulés ici avec une nouvelle matrice de masse diagonalisée, afin de simuler des problèmes explicites/dynamiques, ainsi que des procédés de mise en forme de tôle minces ;
- Dans la présente contribution, la formulation des éléments SHB est combinée avec plusieurs lois de comportement, incluant le comportement élastique orthotrope pour les matériaux composites et le comportement plastique anisotrope pour les matériaux métalliques ;
- L'ensemble des éléments finis SHB a été implémenté dans les logiciels d'EF statique/implicite et dynamique/explicite d'ABAQUS, afin d'étendre leur champ d'application à des analyses quasi-statiques et dynamiques non linéaires.
- Contrairement aux contributions antérieures, qui se limitaient à la simulation de problèmes d'académiques, le champ d'application des éléments SHB est élargi dans ce travail pour inclure des problèmes de type dynamique et d'impact, ainsi que des procédés de mise en forme complexes.

Organisation de la thèse

Le manuscrit de thèse est structuré en quatre chapitres principaux, qui sont décrits comme suit. Le premier chapitre présente une revue de la littérature sur l'état de l'art des technologies d'éléments finis utilisées pour la modélisation de structures minces. Le chapitre 2 présente la formulation détaillée des quatre éléments solide−coque proposés. Dans le chapitre 3, nous proposons une série de tests numériques afin d'évaluer la performance des éléments SHB dans le cas d'analyses quasi-statique et dynamique. Les éléments SHB sont ensuite appliqués dans le chapitre 4 à la simulation de problèmes dynamique de type impact, ainsi que la simulation procédés complexes de mise en forme des tôles minces. Enfin, les principales conclusions et perspectives concernant ce travail sont présentées dans la partie conclusion de ce manuscrit.

Chapitre 1. Étude bibliographique sur la technologie d'élément finis solide–coque

Afin d'économiser les matières premières des matériaux, de réduire le poids et d'améliorer les performances mécaniques, les structures minces sont de plus en plus utilisées de nos jours dans l'industrie modernes. Le développement rapide des ressources de calcul a rendu la simulation numérique de ces structures minces par éléments finis (EF) possible dans les processus de conception et de fabrication des produits. Cependant, la fiabilité et la précision des ces simulations restent encore à améliorer.

Il est bien connu que la théorie des coques permet de développer des éléments fins très efficaces, en particulier, grâce à leurs formulations dégénérées. A cet égard, les éléments finis coques conventionnels ont été le plus souvent adoptés pour l'analyse EF des structures minces. Bien que les éléments coques impliquent des coûts de calcul relativement faibles, leurs formulations dégénérées conduisent à plusieurs limitations. Par exemple, la formulation d'éléments finis coques conventionnels est typiquement basée sur l'hypothèse des contraintes planes, ce qui limite leur application dans la simulation de procédés de mise en forme des tôles minces. En outre, les éléments finis coques ne peuvent pas tenir compte des variations d'épaisseur, puisque seul le plan médian de la structure mince est modélisé, ce qui rend la gestion du contact sur les deux faces très difficile, voire impossible dans certaines situations. De plus, les éléments coques souffrent de divers phénomènes de verrouillage, notamment dans la simulation de problèmes de flexion. Parallèlement, les éléments solides ont été développés sur la base de formulations entièrement tridimensionnelles, qui permettent la modélisation physique des variations d'épaisseur. Cependant, des phénomènes de verrouillage sont également présents dans ces éléments solides conventionnels, en particulier pour les formulations à bas degrés, qui ne peuvent être évitées en raffinement seulement le maillage.

Pour remédier à ces inconvénients, des efforts considérables ont été consacrés dans la littérature au développement d'éléments solide–coque au cours des dernières décennies. L'idée principale de ce concept original d'éléments finis solide–coque est de combiner en un seul élément les avantages des formulations des éléments finis solide et coque. Les principaux avantages du concept d'élément fini solide–coque peuvent être résumés comme suit : basée sur une approche purement tridimensionnelle, la formulation peut être aisément implémentée puisque les déplacements sont les seuls degrés de liberté; considération de lois de

comportement entièrement tridimensionnelles sans l'hypothèse des contraintes planes; le contact sur les deux faces peut être établi naturellement grâce à la disponibilité des surfaces réelles supérieures et inférieures; modélisation tridimensionnelle des structures minces avec seulement une seule couche élément fini et peu de points d'intégration à travers l'épaisseur.

Eléments finis solides tridimensionnelles

État de l'art

Les éléments finis solide sont généralement utilisés pour la modélisation tridimensionnelle de structures massives sans aucune simplification géométrique. La géométrie des éléments finis solides est complètement définie par les coordonnées des nœuds, et les déplacements nodaux permettent l'interpolation des déplacements à l'intérieur de l'élément dans toutes les directions. De plus, des équations constitutives entièrement tridimensionnelle sont adoptées pour ces éléments finis solides, ce qui permet une description réaliste des différents phénomènes sans l'utilisation d'hypothèses restrictives (par exemple, l'hypothèse des contraintes planes).

Grâce à leurs formulations entièrement 3D, les éléments finis solide possèdent de nombreux avantages, et sont conçus pour être des éléments finis à usage général. Dans la majorité des situations non linéaires, les éléments finis solides de bas degrés (à interpolation linéaire) sont préférés en raison de leur coût faible de calcul. Cependant, ils présentent souvent de mauvaises performances et souffrent de plusieurs phénomènes de verrouillage dans la simulations de structures minces, en particulier, pour des problèmes de flexion (voir, par exemple, Adam et al., 2014, 2015a). Ces phénomènes de verrouillage, qui compromettent considérablement la performance des éléments solides, sont brièvement présentés dans ce qui suit.

Traitement des phénomènes de verrouillage

1) Verrouillage en cisaillement

Le verrouillage en cisaillement se produit habituellement lorsque les éléments sont soumis à des sollicitations de type flexion. Ce verrouillage en cisaillement est dû au fait que l'élément fini n'est pas capable de modéliser des situations de flexion pure sans introduire des déformations indésirables (parasites) de cisaillement transversale, ce qui entraîne une rigidité excessive des éléments en cisaillement (voir, par exemple, Prathap, 1985; Huang, 1987; Tessler et Spiridigliozzi, 1988). Ce phénomène apparaît surtout dans le cas d'éléments finis de

bas degrés, en raison de leur cinématique particulièrement simple, qui n'est pas assez riche pour représenter la solution correcte. Le phénomène de verrouillage en cisaillement peut être évité en utilisant des traitements numériques spécifiques, tels que la technique d'intégration réduite (voir, par exemple, Zienkiewicz et al., 1971), la méthode de la déformation postulée «*Assumed Strain*» (voir, par exemple, Belytschko et Bindeman, 1993), ou aussi la considération d'éléments finis de degrés élevé.

2) Verrouillage en pincement

Le verrouillage en pincement (dans le sens de l'épaisseur) peut également se produire dans le cas d'éléments finis hexaédriques de bas degrés. Pour illustrer ce phénomène, considérons le problème de flexion pure décrit par la Fig. 1.2. À partir des équations (1.6) et (1.7), on peut remarquer qu'une approximation constante de la déformation dans l'épaisseur ε_y est obtenue, alors que la contrainte correspondante σ_y a une distribution linéaire le long de la direction $\vec{y}$ (si $\nu \neq 0$). Une telle incohérence entre la distribution de la contrainte et la déformation dans le sens de l'épaisseur conduit à l'effet de verrouillage indésirable, désigné par le verrouillage en pincement (voir, par exemple, Petchsasithon et Gosling, 2005).

3) Verrouillage volumétrique

Lorsqu'on considère un comportement matériel incompressible ou presque incompressible, les éléments finis standard souffrent généralement du phénomène de verrouillage volumétrique. Ce dernier ne peut être évité par le raffinement du maillage et, par conséquent, certains éléments finis montrent des performances médiocres lorsque le coefficient de Poisson du matériau approche la valeur limite de 0.5, ce qui fait tendre le module de compressibilité K (voir équation (1.8)) vers l'infini. Par conséquent, l'élément fini devient trop rigide par rapport à celui des matériaux incompressibles réels si $\varepsilon_{ii} = tr(\boldsymbol{\varepsilon}) \neq 0$ (voir Nguyen, 2009). Généralement, la technique d'intégration réduite sélective, la formulation mixte de Galerkin et la technique de stabilisation peuvent être utilisées pour traiter ce type de verrouillage (voir, par exemple, Elguedj et al., 2008; Davim, 2012). Dans certains cas, le verrouillage volumétrique peut également être évité en définissant des volumes nodaux et en évaluant les pressions nodales moyennes en termes de ces volumes locaux au lieu d'utiliser le volume entier de l'élément fini.

Eléments coques conventionnels

L'état de l'art

Les éléments coques conventionnels ont été développés spécifiquement pour l'analyse de structures minces (i.e., lorsque la dimension de l'épaisseur est sensiblement plus petite que les autres dimensions). Selon les bases théoriques sur lesquelles reposent leurs formulations, les éléments coques peuvent être classés en deux familles principales : les coques plates conventionnelles et les coques dégénérées. Pour les éléments coques plats conventionnels, la géométrie de la coque est approximée par un élément fini plat. Certaines théories classiques, telles que la théorie de Kirchhoff pour les plaques minces et la théorie de Reissner–Mindlin pour les plaques épaisses, sont généralement adoptées comme modèles théoriques de base pour la formulation d'éléments finis coques plats, qui sont bien détaillées dans plusieurs livres d'éléments finis (voir, par exemple, Bathe, 1996; Zienkiewicz et Taylor, 2000). Pour la seconde famille d'éléments finis coques, ces éléments sont dégénérés à partir de formulations d'éléments finis tridimensionnels, et sont communément utilisés pour représenter la surface médiane de structures minces, comme illustré à la Figure 1.4 pour un élément coque à 4 nœuds. Dans la plupart des théories coques, certaines hypothèses de base sont considérées à des fins d'implémentation numérique. En général, les hypothèses suivantes sont largement utilisées dans les formulations d'éléments finis coques :

- La représentation physique de l'épaisseur de la structure est négligée.
- La normale à la surface médiane reste droite après déformation.
- La contrainte normale transversale est supposée négligeable.

En négligeant l'épaisseur physique de la structure, l'hypothèse des contraintes planes est adoptée dans la formulation des éléments finis coques, ce qui permet d'améliorer l'efficacité de calcul. Par conséquent, les éléments finis coques sont généralement plus performant que les éléments finis solides. Au cours des dernières décennies, les éléments finis coques conventionnels ont été largement développés dans la littérature pour la simulation de structures minces. Cependant, un certain nombre de phénomènes de verrouillage existent également dans ces éléments coques conventionnels, qui sont particulièrement révélés dans la simulation de structures minces. Dans cette sous-section, deux phénomènes de verrouillage typiques sont brièvement présentés, i.e., le verrouillage en cisaillement et le verrouillage de type membrane.

Phénomènes de verrouillage

1) Verrouillage en cisaillement transversal

Similaire aux éléments solides discutés précédemment, le verrouillage en cisaillement transversal est l'un des phénomènes de verrouillage les plus fréquemment rencontrés dans les éléments finis coques. Ce verrouillage est dû au fait que l'hypothèse de Kirchhoff–Love n'est pas prise en compte dans les interpolations de déplacement, ce qui ne permet pas de reproduire l'état de cisaillement transversal nul dans les problèmes de flexion pure (voir, par exemple, Zienkiewicz et al., 1971; Kui et al., 1985; César de Sá et al., 2002).

2) Verrouillage en membrane

Le verrouillage en membrane est caractérisé par l'apparition de déformation de membrane parasite dans le cas de sollicitations en flexion de poutres courbes et de structures minces. Afin d'expliquer clairement l'origine du verrouillage en membrane, nous présentons le cas d'une poutre courbe, comme illustré par la Figure 1.7. Basé sur la théorie des poutres (voir, par exemple, Timoshenko, 1995), on peut obtenir les expressions du déplacement circonférentiel u, le déplacement radial w, la déformation membrane ε et la déformation flexion χ (voir équations (1.15) et (1.16), respectivement). Considérant la réponse physique de la flexion inextensible, ce qui est habituellement le cas pour les poutres courbes et coques, il est nécessaire que la déformation membrane tende vers zéro. La première expression dans l'équation (1.17) représente la condition réelle et elle reflète la déformation réelle des poutres courbes. Cependant, les trois autres conditions restantes induisent une rigidité de flexion excessive de l'élément, et provoquent le verrouillage en membrane.

Méthodes numériques pour atténuer les problèmes de verrouillage

Les phénomènes de verrouillage se produisent généralement lorsque des éléments finis de bas degrés sont considérés dans les simulations de structures minces. Par conséquent, la rigidité de l'élément fini utilisé est surestimée en raison de déformations parasites. Un certain nombre de méthodes et techniques numériques ont été développées dans la littérature pour traiter ces phénomènes de verrouillage pour les éléments finis solides et coques. La technique d'intégration réduite « *reduced integration* » (RI) a été la première méthode numérique pour atténuer certains phénomènes de verrouillage (voir, par exemple, Hughes et al., 1978; Stolarski et Belytschko, 1982, 1983; Briassoulis, 1989; Belytschko et al., 1992; Zhu et Cescotto, 1996; Hauptmann et al., 2000; Geyer et Groenwold, 2003; Parente et al., 2006;

Schwarze et Reese, 2009; Winkler, 2010; Schwarze et al., 2011; Bouclier et al., 2012; Edem et Gosling, 2013; Pagani et al., 2014). Cependant, tous les phénomènes de verrouillage ne peuvent pas être traités par la technique RI, ce qui nécessite des traitements supplémentaires pour améliorer les performances des éléments finis coques (voir, par exemple, Zienkiewicz et al., 1971; Hughes et al., 1978).

La solution la plus efficace pour éviter l'apparition de problèmes de verrouillage est l'utilisation de formulations mixtes, dans lesquelles des interpolations séparées (indépendantes) sont adoptées pour les déplacements et les contraintes, ou par la projection des déplacements nodaux de manière à minimiser le plus possible les déformations parasites (voir, par exemple, Rhiu et Lee, 1987; Chang et al., 1989; Polit and Touratier, 2000; Brischetto et al., 2012). Dans ce contexte, la méthode de la déformation postulée « *assumed strain method* » (ASM) a été introduite dans les éléments finis coques par Bathe et Dvorkin (1986). Elle a été ensuite largement étendue aux éléments finis solide (voir, par exemple, Belytschko et Bindeman, 1993; Zhu et Cescotto, 1996; Flores, 2013a). En combinant la méthode ASM avec la technique RI, les éléments résultants ont montré de bonnes performances par rapport aux phénomènes de verrouillages en cisaillement et volumétrique. La méthode améliorée de la déformation postulée « *enhanced assumed strain* » (EAS) est également largement utilisée dans la formulation d'éléments finis de bas degrés. Elle est basée sur l'introduction de modes de déformation supplémentaires pour éliminer les problèmes de verrouillage (voir, par exemple, Simo et Rifai, 1990; Simo et Armero, 1992). La méthode EAS est souvent associée à la méthode de déformation naturelle postulée « *assumed natural strain* » (ANS) pour éviter la plupart des phénomènes de verrouillage (voir, par exemple, Wagner et al., 2002). Les méthodes numériques discutées ci-dessus ont été largement utilisées dans la littérature dans les formulations d'éléments finis solide et coque bidimensionnels et tridimensionnels, ce qui a finalement motivé les chercheurs à développer le nouveau concept d'éléments finis solide–coque pour la modélisation tridimensionnelle de structures minces.

Eléments finis solide–coque

L'état de l'art

Au cours de dernières décennies, le concept d'éléments finis solide–coque a attiré une attention considérable de chercheurs et de développeurs d'EF. L'objectif principal du développement des éléments finis solide–coque est de permettre une modélisation

tridimensionnelle de structures minces sans l'occurrence de problèmes de verrouillage, tout en ayant une description précise des phénomènes non linéaires à travers l'épaisseur. En d'autres termes, les éléments finis solide–coque consiste à combiner les avantages des formulations d'éléments finis solides et coques conventionnels. Les principaux avantages de ces éléments solide–coque peuvent être résumés comme suit : le calcul direct des variations d'épaisseur grâce à une formulation tridimensionnelle, avec les déplacements comme étant les seuls degrés de liberté; la considération de lois de comportement tridimensionnelle sans l'introduction d'hypothèses simplificatrices (par exemple l'hypothèse des contraintes planes); traitement naturel du contact sur les deux faces de l'éléments, ce qui les rend plus adaptés à des applications industrielles; modélisation tridimensionnelle de structures minces avec une seule couche d'élément et peu de points d'intégration, tout en décrivant avec précision les phénomènes non-linéaires dans la direction de l'épaisseur.

Plusieurs techniques numériques ont été développées pour les éléments finis solide–coque afin d'atténuer la plupart des pathologies de verrouillage. Parmi elles, la technique RI (voir Zienkiewicz et al, 1971) ou la technique d'intégration réduite sélective « *selective reduced integration* » (SRI) (voir Hughes, 1980), qui permettent de rende les éléments finis solide–coque très attrayants en termes de coût de calcul. Toutefois, en raison du schéma d'intégration réduit, certains éléments finis peuvent présenter des modes sabliers indésirables «*hourglass modes*» (à énergie nulle), qui nécessitent des procédures spécifiques pour leur stabilisation (voir, par exemple, Abed-Meraim et Combesure, 2009). En outre, plusieurs stratégies supplémentaires ont été combinées avec les techniques ci-dessus afin d'améliorer la performance des éléments finis solide–coque par rapport aux problèmes de verrouillage. Les méthodes les plus couramment utilisées sont la méthode ASM, la méthode EAS et la méthode ANS (voir, par exemple, Cho et al., 1998; Hauptmann et Schweizerhof, 1998; Puso, 2000; Sze et Yao, 2000; Abed-Meraim et Combescure, 2002; Alves de Sousa et al., 2005; Parente et al., 2006; Reese, 2007; Cardoso et al., 2008; Abed-Meraim et Combescure, 2009; Schwarze et Reese, 2009; Moreira et al., 2010; Li et al., 2011; Edem et Gosling, 2012; Bouclier et al., 2013a, 2013b; Flores, 2013a, 2013b; Naceur et al., 2013; Pagani et al., 2014; Bouclier et al., 2015; Caseiro et al., 2015; Ben Bettaieb et al., 2015; Kpeky et al., 2015; Flores, 2016).

Traitement des phénomènes de verrouillage

Afin d'éliminer les phénomènes de verrouillage et d'améliorer les performances globales, plusieurs traitements numériques sont adoptés dans la formulation des éléments finis solide−coque. Dans cette sous-section, nous présentons brièvement les quatre méthodes les plus couramment utilisées pour les éléments finis solide−coque, qui sont la méthode ASM, la méthode EAS, la méthode ANS et la méthode dite « mixte ».

1) Méthode de déformation postulée (ASM)

Basé sur un cadre variationnel, la méthode ASM est souvent adoptée dans la formulation d'éléments solide−coque. Dans les travaux pionniers de Hughes (1980), l'approche « **B** -bar » a été introduite afin de résoudre spécifiquement les problèmes de verrouillage volumétrique. Cette approche consiste en la projection de l'opérateur gradient discrétisé classique **B** en un opérateur projeté $\overline{\mathbf{B}}$, dans lequel la contribution de la partie volumétrique est réduite (voir, par exemple, Simo et Hughes, 1986). Plus tard, un certain nombre de contributions ont prouvé que la méthode ASM est capable d'améliorer significativement la performance des éléments finis conventionnels, et en particulier les éléments finis solide−coque (voir, par exemple, Belytschko et Bindeman, 1991, 1993; Stolarski et Chen, 1995; Li et Cescotto, 1997; Cho et al., 1998; Abed-Meraim et Combescure, 2002; Hong et Kim, 2002; Lee et al., 2002; Flores et Oñate, 2005; Kulikov et Plotnikova, 2006; Abed-Meraim et Combescure, 2009; Wisniewski et al., 2010).

La méthode ASM est généralement basée sur le principe variationnel de Hu−Washizu (voir, par exemple, Simo et al., 1985; Simo et Hughes, 1986; Belytschko et Bindeman, 1991, 1993). À partir de la forme faible du principe variationnel de Hu−Washzu (voir l'équation (1.18)), la contrainte interpolée est supposée orthogonale à la différence entre la partie symétrique du gradient de vitesse et le taux de déformation postulée, ce qui conduit à la forme simplifiée du principe de Hu−Washizu (voir équation (1.19)). La déformation postulée est définie en termes de la matrice modifiée $\overline{\mathbf{B}}$ (voir l'équation (1.21)). Cette dernière est obtenue en projetant l'opérateur gradient discrétisé **B** sur un sous espace approprié afin d'éliminer la plupart des phénomènes de verrouillage.

2) Méthode améliorée de la déformation postulée (EAS)

La méthode EAS proposée par Simo et Rifai (1990) a également suscité beaucoup d'intérêt durant les deux dernières décennies pour surmonter les problèmes de verrouillage (voir, par exemple, Simo et Rifai, 1990; Puso, 2000; César de Sá et al., 2002; Areias et al., 2003; Bui et al., 2004; Pimpinelli, 2004; Valente et al., 2004; Cardoso et al., 2008; Nguyen, 2009; Li et al., 2011; Sena et al., 2011; Flores, 2013b, Ben Bettaieb et al., 2015). Le principe fondamental de la méthode EAS consiste en l'introduction d'un champ de déformation supplémentaire renforcée $\widetilde{\mathbf{E}}^{\alpha}$ au champ de déformation compatible $\mathbf{E}^{\text{com}}$. En remplaçant le champ de déformation modifié dans le principe variationnel de Hu–Washizu, et en utilisant la condition d'orthogonalité définie par l'équation (1.27), on peut obtenir les équations d'équilibre finales pour l'élément fini étudié.

3) Méthode de la déformation naturelle assumée (ANS)

La méthode ANS consiste à interpoler les déformations de cisaillements à des positions spécifiques au lieu d'utiliser le champ de déformation standard, ce qui permet de réduire significativement les verrouillages de cisaillement et volumétrique. Cette interpolation, également connue sous le nom de méthode d'interpolation mixte, a été proposée dans les travaux de Hughes et Tezduyar (1981) pour les plaques de Mindlin, puis étendue aux éléments finis coques par Dvorkin et Bathe (1984). La méthode ANS a été largement appliquée pour l'amélioration de divers éléments finis (voir, par exemple, Bathe et Dvorkin, 1986; Militello et Felippa, 1990a, 1990b; Hauptmann et Schweizerhof, 1998; Sze et Zhu, 1999; Sze et Yao, 2000; Sze et Chan, 2001; Kim et Kim, 2002; Vu-Quoc et Tan, 2003; Lee, 2004; Kim et al., 2005; Klinkel et al., 2006; Cardoso et al., 2008; Schwarze et Reese, 2009; Nguyen, 2009; Norachan et al., 2012; Edem et Gosling, 2012, 2013; Flores, 2013b; Caseiro et al., 2014, 2015).

Pour décrire le concept de base de la méthode ANS, on considère ici un élément solide–coque hexaédrique isoparamétrique à 8 nœuds, comme illustré par la Fig. 1.8. Dans cette Fig. 1.8, un plan médian est défini par quatre points E, F, G et H par rapport au système de coordonnées local naturel. Afin d'éviter le verrouillage en cisaillement, deux déformations transversales de cisaillement postulées sont interpolées comme l'indique l'équation (1.33). En remplaçant les champs de déformation de cisaillement standard par les nouveaux champs de

déformation naturelle postulée, un nouvel opérateur gradient discrétisé $\widetilde{\mathbf{B}}$ est obtenue. Ce dernier permet d'éliminer le verrouillage en cisaillement.

Cependant, pour les structures minces courbes, certains effets de verrouillage particuliers, tels que le verrouillage trapézoïdale, pourraient être causés par la déformation transversale normale. Similaire au traitement du verrouillage en cisaillement, la méthode ANS peut également être appliquée à la déformation transversale normale afin d'éliminer ce type de verrouillage. Par conséquent, comme exprimé dans l'équation (1.34), la déformation postulée est interpolée à travers les déformations naturelles aux quatre points E, F, G et H (plus de détails peuvent être trouvés dans les travaux de Vu-Quoc et Tan, 2003; Kim et al., 2005; Nguyen, 2009).

4) Formulations mixtes (ou combinées)

Bien que les approches ci-dessus aient été introduites et discutées séparément (i.e., la technique RI ou SRI, la méthode ASM, EAS ou ANS), elles sont parfois combinées dans la même formulation d'un élément fini solide–coque, ce qui permet d'améliorer encore plus la performance. Cette stratégie de combinaison de plusieurs approches dans la même formulation est souvent appelée formulation mixte. Tel que discuté ci-dessus, la technique d'intégration réduite (RI) permet d'améliorer l'efficacité des éléments finis solide–coque en terme de temps de calcul de calcul (et peut également contribuer à atténuer certains effets de verrouillage), alors que les méthodes ASM, EAS et ANS introduisent des champs de déformation améliorée pour le traitement des phénomènes de verrouillage. Un effort considérable a été consacré dans la littérature pour le développement de ce type de formulation combinée. Par exemple, dans le travail de Li et Cescotto (1997), la technique RI a été combinée avec la méthode ASM pour le développement d'un élément hexaédrique à 8 nœuds. De plus, l'approche combinée, qui couple les méthodes EAS et ANS dans une formulation unique, a été appliquée pour développer plusieurs éléments solide–coque sans verrouillage (voir, par exemple, Vu-Quoc et Tan, 2003; Cardoso et al., 2008; Nguyen, 2009; Ben Bettaieb et al., 2015). Il a été démontré que ces formulations combinées permettent d'améliorer significativement les performances des éléments solide–coque dans le cas de maillages grossiers, ce qui les rend très attrayants pour la modélisation tridimensionnelle de structures minces.

5) Formulation EF basée sur l'approximation NURBS

Plus récemment, les éléments finis à base d'approximation NURBS (« *Non-Uniform Rational B-Splines* »), proposés par Hughes et al. (2005), ont été développés pour l'analyse isogéométrique des structures. Au lieu d'utiliser les polynômes de Lagrange classique pour l'interpolation, Hughes et collaborateurs ont introduit les fonctions NURBS dans les éléments finis pour maintenir une géométrie exacte (voir, par exemple, Hughes et al., 2005, 2008; Elguedj et al., 2008). Ces fonctions NURBS ont a été utilisées pour le développement de nouveau élément finis sans problème de verrouillage. La revue de la littérature révèle que la technologie d'éléments finis basés sur les fonctions NURBS peut améliorer considérablement les performances des éléments finis et présente des perspectives prometteuses pour les progrès futurs dans les formulations d'éléments finis solide−coque.

Famille d'éléments finis solide−coque SHB

Dans le cadre de simulations prédictives et fiables de structures tridimensionnelles minces, notre groupe de recherche s'est intéressé au développement d'éléments finis solide−coque performants. En particulier, pour les simulations de processus de mise en forme des tôles minces, dans lesquelles les phénomènes typiques de verrouillage peuvent être fréquemment rencontrés (par exemple, verrouillage en cisaillement, verrouillage volumétrique et verrouillage en pincement), la disponibilité d'éléments finis capables de réaliser des simulations précises est nécessaire, tout en ayant des temps de calcul raisonnables. Dans ce travail, une famille d'éléments finis solide−coque (SHB) est proposée pour l'analyse tridimensionnelle de structures minces. Cette famille se compose de quatre éléments solide−coque, à savoir un élément prismatique linéaire à six nœuds dénoté SHB6 et un élément hexaédrique linéaire à huit nœuds dénoté SHB8PS, et leurs contreparties quadratiques SHB15 et SHB20, respectivement. La formulation de ces éléments repose sur une approche purement tridimensionnelle, avec les déplacements comme les seuls degrés de liberté. De plus, une direction spéciale est choisie pour représenter l'épaisseur, le long de laquelle un nombre arbitraire de points d'intégration est réparti, ce qui permet la modélisation tridimensionnelle de structures minces avec une seule couche d'éléments finis. Les divers phénomènes de verrouillage sont atténués en utilisant le schéma RI associé à l'approche ASM. Les éléments finis SHB représentent une alternative intéressante aux éléments finis solides et coques traditionnels, en particulier pour la simulation de processus complexes de mise en

forme des tôles minces, impliquant plusieurs sources de non linéarité (grandes déformations, plasticité anisotrope et contact sur les deux faces de la tôle).

Le premier élément fini solide–coque, qui a été développé au sein de cette famille d'éléments SHB, a été initialement formulé par Abed-Meraim et Combescure (2002) et consiste en un élément fini hexaédrique à huit nœuds dénoté SHB8PS. Sa formulation a ensuite été améliorée dans Abed-Meraim et Combescure (2009), notamment en termes de réduction de verrouillage, tandis que les modes de sablier « *hourglass* modes» ont été efficacement contrôlés par une nouvelle procédure de stabilisation. La performance de l'élément SHB8PS a été démontrée à travers de cas tests de référence ainsi que par la simulation de procédés de mise en forme des tôles minces (voir Abed-Meraim et Combescure, 2009; Salahouelhadj et al., 2012). Par la suite, un élément prismatique à six nœuds dénoté SHB6 a été développé par Trinh et al. (2012), en complément de l'élément SHB8PS pour la modélisation de géométries complexes. Bien que la performance de l'élément SHB6 soit raisonnablement bonne en général, sa rapidité de convergence reste moins bonne que celle du SHB8PS, et il nécessite des maillages plus fins pour obtenir des solutions précises. Plus récemment, les homologues quadratiques des éléments solide–coque SHB ont été développés par Abed-Meraim et al. (2013), afin d'améliorer la performance globale et la rapidité de convergence. Ces versions quadratiques consiste en un élément hexaédrique à vingt nœuds, dénoté SHB20, et un élément prismatique à quinze nœuds, dénoté SHB15. De même, leur formulation est basée sur une approche entièrement tridimensionnelle avec une intégration réduite dans le plan. La performance de ces éléments quadratiques a été évaluée par Abed-Meraim et al. (2013) dans le cadre de cas tests élastiques en petites déformations.

Dans ce travail, les formulations des éléments finis SHB ont été étendues en les combinant à plusieurs modèles de comportement avancé dans le cadre des grandes déformations élasto-plasticité anisotrope pour les matériaux métalliques, ainsi que des lois constitutives orthotropes spécifiques aux matériaux composites multicouches. Une autre partie de la contribution actuelle consiste à étendre les formulations d'éléments finis SHB au cadre d'une analyse dynamique explicite. L'ensemble de ces formulations étendues a été implémenté dans les logiciels statique/implicite et dynamique/explicite d'ABAQUS, ce qui permet de fournir une bibliothèque d'éléments finis solide–coque capable de modéliser des problèmes structurels complexes, tels que des processus de mise en forme des tôles minces et des problèmes de dynamique rapide (impact / crash). Les formulations étendues de ces éléments

SHB sont détaillées dans le chapitre 2, tandis que leurs performances sont évaluées dans les chapitres 3 et 4 (voir aussi dans Wang et al., 2015, 2016, 2017a, 2017b).

Conclusion

Dans ce chapitre, une revue de la littérature sur le développement de technologies d'éléments finis a été brièvement présentée. En particulier, il a été révélé que pour la modélisation de problèmes structurels minces, les éléments solides et coques conventionnels peuvent présenter plusieurs phénomènes de verrouillage. Afin d'obtenir des prédictions précises et fiables, des techniques numériques supplémentaires doivent être associées aux formulations de base des éléments finis. Parallèlement, le concept d'éléments finis solide–coque est apparu comme une alternative intéressante aux éléments finis solide et coque. Ce type d'éléments finis solide–coque combine les avantages des formulations d'éléments solides et coques. Afin d'atténuer les phénomènes de verrouillage dans les éléments finis solide–coque et d'améliorer leurs performances, des techniques numériques avancées sont associées à leurs formulations, telles que la méthode ASM, EAS ou ANS. En générale, la formulation des éléments finis solide–coque est basée sur une approche purement tridimensionnelle, avec les déplacements comme étant les seuls degrés de liberté. Les éléments finis solide–coque sont généralement efficaces, puisqu'une seule couche d'éléments et un nombre arbitraire de points d'intégration à travers l'épaisseur sont nécessaires pour la modélisation tridimensionnelle de structures minces.

Chapitre 2. Formulation des éléments finis solide–coque SHB

Dans ce chapitre, une famille d'éléments finis solide–coque (SHB) est présentée dans une formulation unifiée pour l'analyse tridimensionnelle de structures minces. Ces éléments SHB sont basés sur une formulation entièrement tridimensionnelle avec les déplacements comme étant les seuls degrés de liberté. La technique d'intégration réduite est combinée avec la méthode de la déformation postulée (ASM) dans la formulation des éléments SHB afin d'éviter les différents phénomènes de verrouillage, ce qui les rend très attrayants et compétitifs pour l'analyse tridimensionnelle de structures minces.

En utilisant une formulation unifiée, et grâce à une implémentation numérique modulaire, plusieurs lois constitutives peuvent être couplées avec les éléments SHB, incluant une loi de comportement élastique isotrope, un comportement élastique orthotrope pour des matériaux

composites et un comportement plastique anisotrope pour des matériaux métalliques. L'ensemble des éléments SHB a été implémenté dans les logiciels statique/implicite et dynamique/explicite d'ABAQUS pour la modélisation tridimensionnelle de structures minces.

Formulation des éléments SHB unifiée pour l'analyse quasi-statique/implicite

La Fig. 2.1 illustre la géométrie ainsi que la position des points d'intégration pour les éléments SHB. Comme le montre cette figure, tous les éléments SHB sont basés sur une approche tridimensionnelle classique; cependant, une direction spéciale ζ est choisie comme la direction de l'épaisseur. Dans cette direction, un nombre de points d'intégration défini par l'utilisateur est réparti. Les coordonnées des points d'intégration et leurs poids associés sont obtenus en suivant la méthode classique de distribution de Gauss (voir, par exemple, Zienkiewicz et al., 2006).

En utilisant l'approche isoparamétrique classique, les éléments SHB adoptent les mêmes fonctions de forme classique N_I que pour les éléments prismatiques et hexaédriques standards. À partir de ces fonctions de forme, les coordonnées spatiales x_i et les déplacements u_i dans l'élément sont exprimés en fonction des coordonnées nodales x_{iI} et les déplacements nodaux d_{iI}, respectivement, par

$$x_i = x_{iI} N_I(\xi,\eta,\zeta) = \sum_{I=1}^{n} x_{iI} N_I(\xi,\eta,\zeta), \tag{R.1}$$

$$u_i = d_{iI} N_I(\xi,\eta,\zeta), \tag{R.2}$$

où l'indice en minuscule i représente les directions des coordonnées spatiales, alors que l'indice en majuscule I indique le nombre de nœuds de l'élément courant.

Sur la base de l'interpolation ci-dessus du champ de déplacement, on peut obtenir l'opérateur gradient discrétisé $\mathbf{B}$, qui contient les dérivées des fonctions de forme et définit la relation entre le champ de déformation $\nabla_s(\mathbf{u})$ et le champ de déplacement nodal $\mathbf{d}$, par l'équation suivante

$$\nabla_s(\mathbf{u}) = \mathbf{B}\cdot\mathbf{d}. \tag{R.3}$$

Comme mentionné précédemment, la méthode ASM est adoptée dans la formulation des éléments solide–coque SHB. Elle est basée sur la forme simplifiée du principe Hu–Washizu introduit par Simo et Hughes (1986) :

$$\pi(\dot{\boldsymbol{\varepsilon}}) = \int_{\Omega_e} \delta\dot{\boldsymbol{\varepsilon}}^T \cdot \boldsymbol{\sigma}\, d\Omega - \delta\dot{\mathbf{d}}^T \cdot \mathbf{f}^{\text{ext}} = 0\,, \tag{R.4}$$

où δ représente une variation, $\dot{\boldsymbol{\varepsilon}}$ la vitesse de déformation postulée, $\boldsymbol{\sigma}$ le champ de contrainte, $\dot{\mathbf{d}}$ les vitesses nodales et $\mathbf{f}^{\text{ext}}$ les forces nodales externes.

La vitesse de déformation postulée $\dot{\boldsymbol{\varepsilon}}$ est exprimée en termes de la nouvelle matrice $\overline{\mathbf{B}}$, qui est obtenue en projetant l'opérateur gradient discrétisé $\mathbf{B}$ sur un sous espace approprié afin d'éviter les différents phénomènes de verrouillage. La vitesse de déformation postulée $\dot{\boldsymbol{\varepsilon}}$ est définie par :

$$\dot{\boldsymbol{\varepsilon}}(x,t) = \overline{\mathbf{B}}(x) \cdot \dot{\mathbf{d}}(t)\,. \tag{R.5}$$

En remplaçant l'équation ci-dessus dans le principe variationnel (équation (R.4)), la matrice de rigidité $\mathbf{K}_e$ de l'élément et le vecteur de forces internes $\mathbf{f}^{\text{int}}$ sont obtenus comme suit :

$$\mathbf{K}_e = \int_{\Omega_e} \overline{\mathbf{B}}^T \cdot \mathbf{C}^{\text{ep}} \cdot \overline{\mathbf{B}}\, d\Omega + \mathbf{K}_{\text{geom}}, \qquad \mathbf{f}^{\text{int}} = \int_{\Omega_e} \overline{\mathbf{B}}^T \cdot \boldsymbol{\sigma}(\dot{\boldsymbol{\varepsilon}})\, d\Omega\,, \tag{R.6}$$

où $\mathbf{C}^{\text{ep}}$ est un tenseur d'ordre de quatre et représente le module tangent élasto-plastique, dont l'expression sera détaillée dans la sous-section consacrée à la modélisation du comportement, tandis que $\mathbf{K}_{\text{geom}}$ est la matrice de rigidité géométrique, qui provient de la linéarisation du principe des travaux virtuels et est due au termes non-linéaire (quadratique) du tenseur de déformation.

Définition des repères locaux

Afin d'implémenter numériquement les éléments SHB, plusieurs repères locaux sont introduits par rapport au système de coordonnées globales, comme illustré par la Fig. 2.2. Le premier repère local, désigné par le « repère de l'élément », est attaché au plan médian associé à chaque point d'intégration. Dans le système de coordonnées physiques locales, où la coordonnée ζ représente la direction de l'épaisseur, le tenseur d'élasticité est défini. Le deuxième repère local est le « repère du matériau », qui est utilisé pour définir le comportement plastique anisotrope dans le cas de matériaux métalliques. De plus, un

troisième repère local, désigné comme le « repère co-rotationnel », est défini au niveau de l'élément afin de simplifier le calcul des termes de stabilisation dans le cas particulier de l'élément SHB8PS.

Procédures spécifiques pour les éléments SHB linéaires

Projection de type « déformation postulée » pour l'élément SHB6

Afin d'éliminer les différents phénomènes de verrouillage et améliorer davantage les performances de l'élément SHB6 prismatique linéaire, l'opérateur gradient discrétisé classique $\mathbf{B}$ est projeté sur un sous-espace approprié, ce qui conduit à un opérateur modifié $\overline{\mathbf{B}}$. Il a été montré dans Trinh et al. (2011) que le principal phénomène de verrouillage dans l'élément SHB6 vient du cisaillement transversal. Pour éliminer ce blocage en cisaillement transversal, l'opérateur gradient discrétisé $\mathbf{B}$ est d'abord décomposé en deux parties comme suit :

$$\mathbf{B} = \mathbf{B}_1 + \mathbf{B}_2, \tag{R.7}$$

où l'opérateur $\mathbf{B}_1$ contient les gradients associés aux déformations membranes ainsi que la déformation normale, tandis que les gradients restants sont inclus dans l'opérateur $\mathbf{B}_2$.

Ensuite, la deuxième partie $\mathbf{B}_2$ est projetée comme suit :

$$\overline{\mathbf{B}}_2 = \omega \mathbf{B}_2, \tag{R.8}$$

où ω est un coefficient de correction cisaillement transverse.

Une telle décomposition de l'opérateur gradient discrétisé permet d'obtenir la matrice de rigidité simplifiée suivante pour l'élément SHB6 :

$$\mathbf{K}_e = \mathbf{K}_1 + \mathbf{K}_2 = \int_{\Omega_e} \mathbf{B}_1^T \cdot \mathbf{C}^{\text{ep}} \cdot \mathbf{B}_1 \, d\Omega + \int_{\Omega_e} \overline{\mathbf{B}}_2^T \cdot \mathbf{C}^{\text{ep}} \cdot \overline{\mathbf{B}}_2 \, d\Omega. \tag{R.9}$$

Projection de type « déformation postulée » et stabilisation pour l'élément SHB8PS

Le schéma d'intégration réduit dans le plan utilisé dans la formulation de l'élément SHB8PS permet de réduire considérablement les temps de calcul et améliore la performance de cet élément vis-à-vis des phénomènes de verrouillage. Cependant, il est bien connu que l'utilisation d'une telle technique peut conduire à l'apparition des modes de sablier « hourglass modes ». Dans Abed-Meraim et Combescure (2009), six modes de sablier ont été identifiés dans l'élément SHB8PS. Suivant l'approche proposée par Belytschko et Bindeman

(1993), une matrice de rigidité de stabilisation a été formulée et ajoutée à la matrice de rigidité de l'élément SHB8PS afin de contrôler les modes de sablier associés.

Similaire à la technique de projection mentionnée ci-dessus pour l'élément SHB6, le point de départ de l'approche de stabilisation pour l'élément SHB8PS est également la décomposition de l'opérateur gradient discrétisé $\mathbf{B}$ en deux parties. Il convient de noter que les termes de stabilisation (matrice de rigidité et vecteur des forces internes) sont exprimés dans le repère co-rotationnel, ce qui simplifie leurs calculs. Avant de définir la projection correspondante, les vecteurs de Hallquist $\mathbf{b}_i$ sont remplacés par la forme moyenne $\hat{\mathbf{b}}_i$ introduite par Flanagan et Belytschko (1981), ce qui permet d'obtenir le nouvel opérateur $\hat{\mathbf{B}}$. Ce dernier peut être également décomposé en deux parties comme suit :

$$\hat{\mathbf{B}} = \hat{\mathbf{B}}_{12} + \hat{\mathbf{B}}_{34}, \tag{R.10}$$

où les expressions de $\hat{\mathbf{B}}_{12}$ et $\hat{\mathbf{B}}_{34}$ sont données dans par équations (2.37) et (2.38).

Sur la base de la décomposition ci-dessus, le deuxième terme $\hat{\mathbf{B}}_{34}$ est projeté en un opérateur sur $\overline{\hat{\mathbf{B}}}_{34}$, qui s'écrit comme :

$$\overline{\hat{\mathbf{B}}}_{34} = \begin{bmatrix} \sum_{\alpha=3}^{4} h_{\alpha,x}\hat{\boldsymbol{\gamma}}_{\alpha}^{T} & \mathbf{0} & \mathbf{0} \\ \mathbf{0} & \sum_{\alpha=3}^{4} h_{\alpha,y}\hat{\boldsymbol{\gamma}}_{\alpha}^{T} & \mathbf{0} \\ \mathbf{0} & \mathbf{0} & h_{3,z}\hat{\boldsymbol{\gamma}}_{3}^{T} \\ \mathbf{0} & \mathbf{0} & \mathbf{0} \\ \mathbf{0} & \mathbf{0} & \mathbf{0} \\ \mathbf{0} & \mathbf{0} & h_{4,x}\hat{\boldsymbol{\gamma}}_{4}^{T} \end{bmatrix}. \tag{R.11}$$

Enfin, La matrice de rigidité finale de l'élément SHB8PS, qui comprend les termes originaux et les termes stabilisées, peut être réécrite sous la forme suivante :

$$\mathbf{K}_e = \mathbf{K}_{12} + \mathbf{K}_{\text{STAB}} = \int_{\Omega_e} \hat{\mathbf{B}}_{12}^{T} \cdot \mathbf{C}^{\text{ep}} \cdot \hat{\mathbf{B}}_{12}\, d\Omega + \int_{\Omega_e} \overline{\hat{\mathbf{B}}}_{34}^{T} \cdot \mathbf{C}^{\text{ep}} \cdot \overline{\hat{\mathbf{B}}}_{34}\, d\Omega. \tag{R.12}$$

De la même manière que pour la matrice de rigidité, les forces internes de l'élément sont décomposées en deux parties comme suit :

$$\mathbf{f}^{\text{int}} = \mathbf{f}_{12}^{\text{int}} + \mathbf{f}^{\text{STAB}} = \mathbf{f}_{12}^{\text{int}} + \begin{Bmatrix} \mathbf{f}_1^{\text{STAB}} \\ \mathbf{f}_2^{\text{STAB}} \\ \mathbf{f}_3^{\text{STAB}} \end{Bmatrix}, \tag{R.13}$$

où $\mathbf{f}_i^{\text{STAB}} = \sum_{\alpha=3}^{4} Q_{i\alpha}\hat{\boldsymbol{\gamma}}_\alpha$ (les détails de calcul peuvent être trouvés dans la sous-section 2.3.2).

Formulation générale pour l'analyse dynamique/explicite

Dans le présent travail, les versions quasi-statique des éléments SHB, présentées ci-dessus, sont étendues au cadre dynamique/explicite pour la simulation de problèmes d'impact et de procédés complexes qui sont difficiles à réaliser en utilisant des solveurs quasi-statiques. Plusieurs aspects des versions dynamiques des éléments SHB sont communs à ceux des versions décrites dans la section précédente. Par conséquent, seuls les principaux points relatifs aux formulations dynamiques sont présentés dans ce qui suit.

Interpolation du champ de vitesse

Contrairement à la formulation quasi-statique, la formulation dynamique/explicite est basée sur l'interpolation du champ de vitesse. En suivant les mêmes règles de dérivation présentées dans la section précédente, on peut facilement obtenir les nouvelles expressions pour le champ de vitesse et le gradient de vitesse comme suit :

$$\begin{cases} v_i = a_{0i} + \left(x_1\mathbf{b}_1^T + x_2\mathbf{b}_2^T + x_3\mathbf{b}_3^T + h_1\boldsymbol{\gamma}_1^T + \cdots + h_\alpha\boldsymbol{\gamma}_\alpha^T \right) \cdot \dot{\mathbf{d}}_i \\ v_{i,j} = \left(\mathbf{b}_j^T + \sum_\alpha h_{\alpha,j}\boldsymbol{\gamma}_\alpha^T \right) \cdot \dot{\mathbf{d}}_i = \left(\mathbf{b}_j^T + h_{\alpha,j}\boldsymbol{\gamma}_\alpha^T \right) \cdot \dot{\mathbf{d}}_i \end{cases}. \tag{R.14}$$

À partir de la forme simplifiée du principe variationnel de Hu−Washizu, on peut obtenir l'opérateur gradient discrétisé $\mathbf{B}$ et les forces internes $\mathbf{f}^{\text{int}}$ associées aux éléments SHB.

Modélisation de la matrice masse

Pour l'analyse dynamique, la matrice de rigidité $\mathbf{K}_e$ n'est pas nécessaire dans les calculs, tandis que la matrice masse $\mathbf{M}^e$ de l'élément doit être définie. Comme illustré par la Figure 2.3, plusieurs méthodes ont été proposées dans la littérature pour le calcul de la matrice masse d'éléments finis standards (voir, par exemple, Zienkiewicz et al., 2006).

Dans la présente contribution, nous proposons une méthode simple, dénommée la méthode du m-coefficient, pour calculer les matrices masse pour les éléments SHB. Les composantes de la matrice masse sont données par la relation suivante :

$$M_{IJ} = \begin{cases} m\int_{\Omega_e} \rho N_I N_J d\Omega & I = J \\ 0 & I \neq J \end{cases}, \quad \text{with} \quad m = \int_{\Omega_e} \rho d\Omega \Big/ \sum_{I=1}^{n} \int_{\Omega_e} \rho N_I N_I d\Omega . \tag{R.15}$$

Modélisation du comportement : lois constitutives

Comme indiqué précédemment, les formulations des éléments finis solide–coque SHB sont couplées dans ce travail à différents types de lois constitutives, ce qui permet d'étendre les champs d'application des éléments SHB. Dans cette section, quelques modèles de comportement de matériaux classiques sont présentés.

Comportement élastique linéaire

1) Elasticité isotrope

Afin de modéliser le comportement classique élastique isotrope, une loi d'élasticité modifiée est adoptée dans les formulations des éléments linéaires SHB (i.e., SHB6 et SHB8PS), ce qui permet d'améliorer leurs performances en matière de verrouillage en pincement (voir, par exemple, Abed-Meraim et Combescure, 2009, Trinh et al., 2011). Une telle matrice d'élasticité modifiée est définie dans le repère local d'élément comme suit :

$$\mathbf{C}^{\text{ele}} = \begin{bmatrix} \bar{\lambda}+2\mu & \bar{\lambda} & 0 & 0 & 0 & 0 \\ \bar{\lambda} & \bar{\lambda}+2\mu & 0 & 0 & 0 & 0 \\ 0 & 0 & E & 0 & 0 & 0 \\ 0 & 0 & 0 & \mu & 0 & 0 \\ 0 & 0 & 0 & 0 & \mu & 0 \\ 0 & 0 & 0 & 0 & 0 & \mu \end{bmatrix} \text{ with } \mu = \frac{E}{2(1+\nu)} \text{ and } \bar{\lambda} = \frac{E\nu}{1-\nu^2}, \tag{R.16}$$

où E est le module d'Young et ν est le coefficient de Poisson.

Cependant, pour les éléments SHB quadratiques (i.e., SHB15 et SHB20), il a été démontré dans Trinh et al. (2011) et Wang et al. (2016e) qu'une telle modification de la matrice d'élasticité n'est pas nécessaire, et qu'une loi tridimensionnelle élastique classique permet d'obtenir des résultats précis. Par conséquent, une loi élastique classique est adoptée pour les éléments quadratiques SHB, dont la matrice d'élasticité s'écrit comme :

$$\mathbf{C}^{\text{ele}} = \begin{bmatrix} \lambda+2\mu & \lambda & \lambda & 0 & 0 & 0 \\ \lambda & \lambda+2\mu & \lambda & 0 & 0 & 0 \\ \lambda & \lambda & \lambda+2\mu & 0 & 0 & 0 \\ 0 & 0 & 0 & \mu & 0 & 0 \\ 0 & 0 & 0 & 0 & \mu & 0 \\ 0 & 0 & 0 & 0 & 0 & \mu \end{bmatrix} \text{ avec } \lambda = \frac{E\nu}{(1+\nu)(1-2\nu)}, \quad \mu = \frac{E}{2(1+\nu)}. \text{ (R.17)}$$

2) Elasticité orthotrope

Afin d'étendre l'application des éléments solide–coque SHB à l'analyse tridimensionnelle de structures composites, leurs formulations sont couplées à un comportement élastique orthotrope. Pour cela, on définit le tenseur d'élasticité orthotrope $\mathbf{C}^{\text{orth}}$ dans le repère local d'élément par :

$$\left(\mathbf{C}^{\text{orth}}\right)^{-1} = \begin{bmatrix} \frac{1}{E_1} & -\frac{\nu_{21}}{E_2} & -\frac{\nu_{31}}{E_3} & 0 & 0 & 0 \\ -\frac{\nu_{12}}{E_1} & \frac{1}{E_2} & -\frac{\nu_{32}}{E_3} & 0 & 0 & 0 \\ -\frac{\nu_{13}}{E_1} & -\frac{\nu_{23}}{E_2} & \frac{1}{E_3} & 0 & 0 & 0 \\ 0 & 0 & 0 & \frac{1}{G_{12}} & 0 & 0 \\ 0 & 0 & 0 & 0 & \frac{1}{G_{23}} & 0 \\ 0 & 0 & 0 & 0 & 0 & \frac{1}{G_{13}} \end{bmatrix}. \quad \text{(R.18)}$$

où E_i représente le module d'Young dans la direction i ; ν_{ij} est le coefficient de Poisson associé; G_{12}, G_{13} et G_{23} sont les modules de cisaillement.

Dans ce travail, un composite stratifié est modélisée par une seule couche d'élément solide–coque SHB. Dans ce cas, chaque pli du composite stratifié est modélisé par un point d'intégration et, par conséquent, la matrice de rigidité du stratifié résultant est calculée en utilisant le schéma d'intégration de Gauss sur l'ensemble des points d'intégration. Pour cela, nous définissons un système orthogonal lié l'élément étudié, ce qui permet de définir la direction de la fibre, la direction transversale et direction normale.

Une fois que le système orthogonal ci-dessus est défini, la matrice d'élasticité associée à la k^{ième} couche courante du stratifié est exprimée dans le repère local de l'élément comme suit :

$$\mathbf{C}(\theta)^k = \mathbf{T}(\theta)^k \cdot \mathbf{C}^{\text{orth}} \cdot \left(\mathbf{T}(\theta)^k\right)^T, \tag{R.19}$$

où θ est l'angle d'orientation de la fibre par rapport aux directions d'orthotrope, et $\mathbf{T}(\theta)^k$ est la matrice de rotation.

Modélisation de l'anisotropie plastique pour les matériaux métalliques

Lorsque le comportement plastique est considéré pour les matériaux métalliques, le tenseur taux de déformation $\mathbf{D}$ est décomposé en une partie élastique $\mathbf{D}^e$ et une partie plastique $\mathbf{D}^p$. Ce dernier est défini en utilisant la règle normale d'écoulement plastique suivante :

$$\mathbf{D}^p = \dot{\lambda}\frac{\partial f}{\partial \boldsymbol{\sigma}} = \dot{\lambda}\mathbf{V}, \tag{R.20}$$

où $\mathbf{V}$ est la direction d'écoulement normale à la surface de charge f, et $\dot{\lambda}$ est le multiplicateur plastique à déterminer par la condition de cohérence.

Dans ce travail, le comportement plastique anisotrope est pris en compte en utilisant la surface de charge quadratique de Hill'48 (Hill, 1948). Le critère de plasticité peut s'exprimer sous la forme suivante :

$$f = \bar{\sigma}_{eq} - Y \le 0, \tag{R.21}$$

où $\bar{\sigma}_{eq} = \sqrt{(\boldsymbol{\sigma}' - \boldsymbol{\alpha}) : \mathbf{H} : (\boldsymbol{\sigma}' - \boldsymbol{\alpha})}$ est le contrainte équivalente; $\boldsymbol{\sigma}'$ est la partie déviatorique du tenseur de contrainte de Cauchy $\boldsymbol{\sigma}$; le tenseur du quatrième ordre $\mathbf{H}$ contient les six coefficients d'anisotropie de Hill (F, G, H, L, M et N). L'écrouissage isotrope et l'écrouissage cinématique du matériau sont décrits par la variables internes Y et $\boldsymbol{\alpha}$, respectivement.

Conclusion

Dans ce chapitre, nous avons présenté la formulation principale de quatre éléments finis solide–coque SHB. Par rapport aux développements antérieurs, la formulation de ces éléments a été étendue ici au cadre de grandes déformations, et à plusieurs type de loi de comportement, incluant le comportement élastique orthotrope pour les matériaux composites stratifiés et le comportement plastique anisotrope pour les matériaux métalliques. De plus, les

versions quasi-statiques des éléments SHB ont été étendues au cadre dynamique explicite pour l'analyse dynamique des structures minces ainsi que la simulation de processus complexes de mise en forme des tôles minces.

Chapitre 3. La validation des éléments SHB

Dans ce chapitre, une variété de tests populaires est sélectionnée pour évaluer la performance des éléments SHB proposés dans les analyses statiques et dynamiques. A titre de comparaison, les résultats obtenus avec les éléments SHB sont constamment comparés avec des solutions analytiques et de référence ainsi les résultats numériques obtenus par les éléments ABAQUS (les descriptions détaillées de tous les éléments finis impliqués dans cette thèse sont données dans les tableaux 3.1 et 3.2). Pour des raisons de simplicité, plusieurs tests numériques typiques sont sélectionnés ici pour afficher la performance des éléments SHB.

Problème statique linéaire

Poutre élastique soumise à des forces de flexion hors plan

Ce test statique linéaire consiste en une poutre élastique encastrée d'un côté et soumise à quatre forces concentrées de l'autre côté (extrémité libre). Les dimensions géométriques ainsi que et les paramètres matériau pour ce test sont donnée dans la Fig 3.1. Ce test permet d'analyser le comportement des éléments SHB dans le cas d'une flexion hors plan. La solution analytique de la deflection à l'extrémité libre est $U_{ref} = 7.326\times10^{-3}$ m. Les résultats de convergence sont donnés dans les tableaux 3.3 et 3.4 en termes de déflection normalisée par rapport à la solution analytique ainsi que les résultats simulés obtenus par les éléments solides d'ABAQUS. Ces résultats de simulation montrent que la vitesse de convergence des éléments SHB est excellente, avec néanmoins une vitesse de convergence plus lente pour l'élément prismatique linéaire SHB6. Pour cet élément SHB6, un maillage plus fin est nécessaire pour obtenir une solution précise, ce qui est cohérent avec ce type d'élément fini à base de triangle, dont les fonctions d'interpolation (linéaires) ne peuvent prédir que des champs de déformation constants dans l'élément (voir Trinh et al., 2011).

Problème de vibration

Plaque rectangulaire simple

Ce problème de vibration consiste en une plaque rectangulaire avec une épaisseur constante. Comme illustré par la Fig. 3.5, la plaque rectangulaire, de longueur L, largeur b=L/2 et épaisseur t, est encastrée d'un côté, et libre sur les autres côtés. Les résultats prédits, en termes de coefficient de fréquence adimensionnel $\omega \Big/ \sqrt{D/\rho \mathrm{tL}^4}$, associés aux quatre premières fréquences propres ω de la plaque, sont résumés dans les tableaux 3.13 et 3.14 pour les éléments linéaires et quadratiques respectivement, où $D = E\mathrm{t}^3/12\left(1-\nu^2\right)$ est la rigidité de flexion de la plaque, E et ν sont le module d'Young et le coefficient de Poisson, respectivement. Les résultats numériques obtenus par les éléments SHB8PS, SHB20 et SHB15 sont en bon accord avec les résultats théoriques ainsi qu'avec les solutions de référence données par Barton (1951) et Anderson et al. (1968). Pour l'élément prismatique SHB6, en raison de sa performance relativement faible, des maillages plus fins sont nécessaires pour obtenir des solutions plus précises.

Analyse quasi-statique non linéaire

Plaque carrée élastique simplement supportée

La Figure 3.7 illustre une plaque carrée élastique isotrope simplement appuyée, et soumise à une force centrale concentrée. Les données de géométrie et matériau sont regroupées dans la Fig. 3.7. La charge concentrée F est égal à 300. En raison de la symétrie, seul un quart de la plaque est analysé. Le déplacement du point central de la plaque, obtenu par les éléments SHB, est comparé dans la Fig. 3.8 à ceux fournis par les éléments ABAQUS ainsi qu'aux solutions de référence de Li et Cescotto (1997) et Nguyen (2009).

Dans le cas des éléments linéaires à base de triangle (Fig. 3.8 (a)), le résultat fourni par l'élément SHB6 est plus proche des solutions de référence que ceux donnés par l'élément solide prismatique d'ABAQUS (C3D6), tandis que les résultats obtenus par l'élément coque triangulaire d'ABAQUS (S3) est en accord avec l'une des deux solutions de référence (i.e., celle de Li et Cescotto (1997)). Pour les éléments linéaires à base de quadrilatéral, (Fig. 3.8 (b)), la solution obtenue par l'élément SHB8PS est très proche de celle donnée par l'élément coque quadrilatéral d'ABAQUS (S4R) ainsi que celle de référence donnée par Li et Cescotto (1997). Il est à noter que, en utilisant le même maillage dans le plan que celui pour les

éléments SHB8PS et S4R, la solution donnée par l'élément linéaire hexaédrique d'ABAQUS (C3D8R) est très éloignée des deux solutions de référence. Dans le cas des éléments quadratiques (Fig. 3.8 (c) et (d)), les résultats obtenus par les éléments SHB15 et SHB20 concordent très bien avec la solution de référence de Li et Cescotto (1997), ainsi que les résultats obtenus avec les éléments quadratiques d'ABAQUS (i.e., C3D15, STRI65 et S8R), tandis que l'élément solide hexaédrique C3D20 est légèrement plus rigide.

Analyse dynamique non linéaire

Poutre encastrée–libre

Le problème de flexion simple d'une poutre élastique encastrée–libre est étudié par est considéré ici (voir Olovsson et al. (2004)). Les dimensions géométriques, les propriétés élastiques du matériau, le chargement appliqué et les conditions aux limites sont tous spécifiées dans la Fig. 3.16. La Fig. 3.17 compare l'évolution de la déflection de l'extrémité libre de la poutre obtenue avec les éléments SHB et les éléments linéaires d'ABAQUS. Il est à noter que, étant donné qu'aucun élément quadratique n'est disponible dans le logiciel ABAQUS/Explicit, les prédictions fournies par les éléments quadratiques SHB sont comparées seulement avec la solution de référence d'Olovsson et al. (2004) (voir Figs. 3.17 (c) et (d)).

Les résultats numériques montrent que le maillage fin utilisé pour les éléments solides linéaires d'ABAQUS (C3D6 et C3D8R) n'est toujours pas suffisant pour obtenir des solutions précises, en raison du mauvais comportement de ces éléments solides en ce qui concerne le verrouillage et les modes de sablier. En revanche, tous les éléments SHB ainsi que les éléments coques linéaires d'ABAQUS (i.e., S3R et S4R) sont en bon accord avec la solution de référence. Notez aussi, bien que l'on a adopté deux fois plus d'éléments que pour les éléments SHB (i.e., deux couches d'éléments dans la direction de l'épaisseur), les résultats donnés par les éléments solides d'ABAQUS sont encore nettement affectés par les phénomènes de verrouillage qui sont impliqués dans ce problème typique de flexion, ce qui n'est pas le cas pour les éléments SHB grâce à l'implémentation de la méthode ASM dans leurs formulations.

Problème de structure composite

Comme nous l'avons vu dans le chapitre 2, les formulations quadratiques SHB15 et SHB20 sont étendues à l'analyse non linéaire de matériaux orthotropes, ce qui permet la

modélisation tridimensionnelle de structures composites stratifié avec une seule couche d'élément à travers l'épaisseur. Par conséquent, la performance des éléments quadratiques SHB est évaluée dans cette section.

Plaque stratifiée avec différents épaisseurs

Il est bien connu que les éléments coques traditionnels sont largement utilisés dans la littérature pour la simulation de structures composites en raison de leur grande efficacité et de leur précision. Cependant, ils ne sont pas capables de modéliser des stratifiés composites avec des zones d'épaisseur variable, ce qui est le cas du présent test de référence d'une plaque stratifiée ayant différentes épaisseur dans le sens de la longueur. Par conséquent, seuls les éléments finis de type solide–coque ou solide, sont capables de modéliser ce type de structures composites qui nécessitent une représentation tridimensionnelle de la géométrie.

La figure 3.28 illustre la géométrie de la plaque composite étudiée. Chaque couche du composite est modélisée avec un seul élément fini dans l'épaisseur, et contient deux plis avec les directions des fibres orientées à [-45º/45º] du bas vers le haut par rapport à la direction de la longueur de la plaque. Ainsi, l'extrémité épaisse (extrémité encastrée) contient six plis tandis que l'extrémité la plus mince (extrémité libre) contient que deux plis.

la plaque est soumise à une force de flexion $\mathrm{F} = 6\times10^{9}\mathrm{h}^{3}$, avec h l'épaisseur de chaque pli (tous les plis ont la même épaisseur). Les constantes du matériau orthotrope sont $E_{11} = 2.5\times10^{10}$, $E_{22} = E_{33} = 10^{9}$, $v_{12} = v_{13} = v_{23} = 0.2$, $G_{12} = G_{13} = G_{23} = 0.5\times10^{9}$. La longueur de la plaque est L = 12, et la largeur est b = 6, avec la couche supérieure étant enlevée aux coordonnées x=4 et x=8 dans le sens de la longueur. Trois valeurs différentes de l'épaisseur du pli sont considérées, i.e., $\mathrm{h} = 0.1$, 0.01 and 0.004. Pour les éléments hexaédriques quadratiques (SHB20 et C3D20), la plaque est discrétisée en utilisant six éléments dans la direction de la longueur et trois éléments dans la direction de la largeur. Dans le cas des éléments prismatiques quadratiques (SHB15 et C3D15), on utilise 24 éléments dans le sens de la longueur et six éléments dans la largeur. Les déflections finales obtenues, normalisées par rapport à la solution de référence donnée par Vu-Quoc et Tan (2003), sont présentées dans le tableau 3.19 pour les trois cas d'épaisseurs du pli considérées. On peut observer que, dans le cas de l'épaisseur de la couche $\mathrm{h} = 0.1$, les éléments quadratiques SHB et d'ABAQUS prédisent bien la flèche maximale de cette plaque composite. Cependant, pour les plus petites épaisseurs du pli, les éléments SHB fournissent les meilleures prédictions avec une précision

très élevée, tandis que les éléments solides quadratiques d'ABAQUS montrent leurs limites dans la modélisation tridimensionnelles de structures très minces.

Conclusion

Dans ce chapitre, les éléments SHB proposés ont été évalués à l'aide d'une série de tests de référence populaires, incluant des problèmes linéaires représentatifs, des tests d'analyses des vibrations et des problèmes non linéaires. Différents types de lois de comportement ont été considérées dans les simulations, ce qui a permis un large champ d'applications non linéaires. Dans l'ensemble, les résultats obtenus révèlent les bonnes capacités des éléments SHB proposés et leurs applications prospectives étendues dans la modélisation tridimensionnelle de structures minces avec une seule couche d'éléments et peu de points d'intégration à travers l'épaisseur.

Chapitre 4. Applications à la simulation de procédés de mise en forme complexes

Introduction

Grâce à la validation numérique effectuée dans le chapitre 3, il a été démontré que les éléments solide–coque SHB sont capables de modéliser avec précision les structures minces en utilisant une seule couche d'éléments dans l'épaisseur. Dans ce chapitre, la performance des éléments SHB est évaluée sur des problèmes structurels complexes, incluant des problèmes en dynamique rapide de type impact, ainsi que des procédés de mise en forme des tôles minces.

Problème d'impact d'une plaque circulaire

La réponse dynamique d'une plaque circulaire encastrée sur ses contours extérieurs et impactée par un projectile rigide est étudiée ici pour évaluer la performance des éléments SHB linéaires. Notons que ce test dynamique de référence a été précédemment étudié par Chen et al. (2007) et Mars et al. (2015). Les paramètres géométriques de la plaque et du projectile sont toutes définis dans la Fig. 4.1. Le matériau de la plaque est en alliage d'aluminium 6061-T6, dont les propriétés élastique et plastique sont données dans le tableau 4.1.

Le projectile est modélisé comme un corps rigide ayant une masse. Le contact entre la plaque circulaire et le projectile est supposé sans frottement (glissant). Les simulations numériques sont effectuées dans le code ABAQUS/Explicit en utilisant les version explicites des éléments SHB linéaires. Deux combinaisons masse−vitesse initiale du projectile sont considérés ici, correspondant à deux énergies cinétique différentes :

Cas 1 : M = 23.5 g, V_0 = 49.1 m/s.

Cas 2 : M = 54.4 g, V_0 = 29.9 m/s.

Considérant la symétrie du problème, seul un quart de la plaque est discrétisé à l'aide de 2708 éléments dans le cas des éléments prismatiques, 2722 éléments dans le cas des éléments coques triangulaires, 934 éléments dans le cas des éléments hexaédriques et 951 éléments dans le cas des éléments coques quadrilatéraux (voir la figure 4.2). Toutes les simulations sont effectuées en considérant deux points d'intégration dans le sens de l'épaisseur, ce qui représente deux couches d'élément dans le cas des éléments solides d'ABAQUS (i.e., C3D8R et C3D6) et une seule couche d'éléments pour tous les autres éléments utilisés pour comparaison. L'historique d'évolution de la vitesse et de la force de réaction du projectile ainsi que le relevé de déplacement du point central de la plaque sont analysés en utilisant les éléments SHB linéaires proposés. Les résultats obtenus sont comparés ensuite avec ceux fournis par les éléments linéaires d'ABAQUS et des solutions de référence données par Chen et al. (2007).

La vitesse et la force d'impact obtenues pour les deux cas étudiés sont comparées dans les Figs. 4.3 à 4.6 aux solutions numériques de référence données par Chen et al. (2007). Pour plus de clarté dans ces comparaisons, les résultats données par les éléments SHB linéaires sont comparés dans les Figs. 4.3 et 4.4 à ceux obtenus par les éléments coques d'ABAQUS, et dans les Figs. 4.5 et 4.6 à ceux donnés par les éléments solides d'ABAQUS. On peut constater que les deux pics dans la courbe d'évolution de la force d'impact, qui sont typiquement observés dans de tels problèmes d'impact, sont bien reproduits par les éléments SHB linéaires pour les deux cas étudiés. Plus précisément, le pic de la force d'impact est atteint pour les éléments SHB lorsque la vitesse du projectile diminue à zéro, ce qui est cohérent avec les solutions de référence données par Chen et al. (2007). En comparaison avec les éléments d'ABAQUS, les résultats obtenus avec les éléments SHB montrent un bon accord avec les éléments solides d'ABAQUS (voir Figs. 4.5 et 4.6), tandis que les éléments coques

d'ABAQUS fournissent des résultats plus éloignés par rapport à la solution de référence. Il convient de rappeler qu'un maillage plus fin est nécessaire pour les éléments solides linéaires d'ABAQUS, avec deux couches d'élément dans la direction de l'épaisseur, ce qui implique deux fois plus d'éléments que leurs homologues SHB.

Emboutissage profond d'un godet cylindrique

L'emboutissage profond d'un godet cylindrique est considéré dans la littérature comme un problème de référence dans le domaine des procédés de mise en forme des tôles minces. En particulier, ce procédé d'emboutissage permet d'analyser la formation de cornes d'emboutissage lorsque la tôle métallique présente une anisotropie plastique (voir, par exemple, Barlat et al., 2003; Yoon et al., 2006; Schwarze et al., 2010). La tôle mince, initialement circulaire, est constituée d'un alliage d'aluminium AA2090-T3 avec une épaisseur initiale de 1,6 mm. Le comportement plastique est décrit par la loi d'écrouissage isotrope de Swift (voir Chapitre 2, Tableau 2.2) et la surface de charge anisotrope de Hill'48. Les paramètres matériau associés sont résumés dans le Tableau 4.4. Les caractéristiques géométriques du montage d'emboutissage sont représentées par la Fig. 4.20.

En raison de la symétrie du problème, seul un quart de la tôle circulaire est modélisé avec une discrétisation dans le plan de 1248 éléments dans le cas d'éléments triangulaires ou prismatiques, 800 éléments dans le cas d'éléments coques quadrilatéraux ou hexaédriques. Les maillages initiaux avec les éléments SHB linéaires sont représentés par la Fig. 4.21. Durant le processus de formage, une force constante de serrage de 22,2 kN est appliquée. Le coefficient de frottement associé au contact entre la tôle et les outils de formage est pris égal à 0,1. La Fig. 4.22 montre godet cylindrique final obtenu en utilisant les éléments SHB linéaires. On peut y voir que les éléments SHB linéaires prédisent quatre cornes d'emboutissage pour le godet cylindrique, ce qui est cohérent avec l'utilisation de la surface de charge quadratique de Hill'48.

Les prédictions de la hauteur des cornes d'emboutissage obtenues avec l'ensemble des éléments finis sont présentées dans la figure 4.23, et sont comparées aux mesures expérimentales données par Yoon et al. (2006). Dans l'ensemble, on peut observer que la forme et le profil des cornes prédites par les éléments SHB linéaires sont en bon accord avec les mesures expérimentales. Plus précisément, dans l'intervalle autour du pic des cornes d'emboutissage, les résultats donnés par les éléments SHB linéaires sont les plus proches des

valeurs expérimentales. Cependant, les hauteurs prédites sont sous-estimées à 0° et 90° par rapport au sens de laminage pour l'ensemble de éléments finis utilisés. Cependant, ces prédictions pourraient être améliorées dans les travaux futurs en adoptant des critères de plasticité anisotropes plus approprié pour les alliages d'aluminium (voir, par exemple, Barlat et al., 1991; Barlat et al., 2003; Yoon et al., 2006), qui sont capables de prédire plus que quatre cornes d'emboutissage, comme observé expérimentalement.

Formage incrémental

Durant les deux dernières décennies, la technologie du formage incrémental a attiré l'attention de plusieurs chercheurs et industriels en raison de ses avantages en termes d'opérabilité économique. Le formage incrémental est devenu un procédé typique dans le contexte de la mise en forme des tôles minces. (voir, par exemple, Bouffioux et al., 2008; Sena et al., 2010; Henrard et al., 2011; Sena et al., 2016). Comme illustré par la Fig. 4.35, une tôle carrée, encastrée sur ses côtés, est progressivement déformée dans sa zone centrale par l'application d'un poinçon sphérique de rayon de 5 mm suivant un trajet prédéterminé. La description détaillée de ce processus est expliquée dans la section 4.2.6.

Les courbes de réponses simulées en termes de force–déplacement du poinçon en utilisant les éléments SHB quadratiques sont comparées dans la Fig. 4.37 avec ceux prédites par les éléments ABAQUS ainsi qu'avec les résultats expérimentaux fournis par Bouffioux et al. (2008). Il convient de noter que les simulations utilisant les éléments coques d'ABAQUS (i.e., STRI65 et S8R) ont présenté des problèmes de convergence dus à la présence du contact sur les deux faces des éléments coques. Cela suggère que les formulations d'éléments finis basées sur des approches purement tridimensionnelles sont plus appropriées à modéliser des procédés de mise en forme des tôles minces, dans lesquels le contact sur les deux faces de la tôle doit être considéré.

Comme le montre la Fig. 4.37, les courbes force–déplacement du poinçon obtenus avec les éléments SHB quadratiques sont en bon accord avec celles données par des éléments solides d'ABAQUS, bien que toutes les prédictions soient supérieures aux résultats expérimentaux. Il est à noter que des oscillations dans les courbes simulées sont observées pour les éléments SHB et ABAQUS. Ce phénomène d'oscillation est dû au contact entre le poinçon et la tôle, dont l'amplitude et le nombre d'oscillations dépendent de la finesse du maillage du poinçon et de la tôle (voir Wrigger, 2006). Afin de réduire ces oscillations numériques, un maillage plus

fin est utilisé, composé de (100×30×2)×1 éléments prismatiques ou 100×30×1 éléments hexaédriques. La Fig. 4.38 présente les résultats obtenus en utilisant ces maillages fins, où il est clairement montré que les courbes simulées sont beaucoup plus lisses que celles obtenus avec des maillages grossiers.

Conclusion

Dans ce chapitre, les éléments SHB proposés ont été appliqués à la simulation de problèmes complexes en dynamique rapide et en mise en forme des tôles minces. Les Différentes comparaisons entre les résultats numériques fournis par les éléments SHB et solutions de référence ont révélé que les éléments SHB sont capables de modéliser des procédés complexes en utilisant une seule couche d'éléments et peu de points d'intégration dans l'épaisseur. De plus, par rapport aux mesures expérimentales et les solutions nuémriques de référence, la performance des éléments SHB est meilleure que celle obtenue par les éléments solides et coques d'ABAQUS. En conclusion, les éléments SHB représentent une alternative intéressante aux éléments solides et coques traditionnels, en particulier pour la simulation de problèmes complexes impliquant du contact sur deux faces, ce qui est très courants dans le cas de la simulation de procédés de mise en forme des tôles minces.

Conclusions et travaux futurs

Conclusions

Dans ce travail, une famille d'éléments finis solide–coque prismatiques et hexaédriques a été proposée pour la modélisation tridimensionnelle de structures minces. Plusieurs traitements numériques, tels que la méthode de déformation postulée (ASM), la technique d'intégration réduite et la procédure de stabilisation des modes sablier, ont été adoptés dans la formulation des éléments SHB pour éliminer les principaux phénomènes de verrouillage et améliorer leurs performances. Une caractéristique commune à ces éléments est qu'ils sont basés sur une approche entièrement tridimensionnelle, avec seulement des degrés de liberté de translation. En outre, ils sont conçus pour être utilisés avec une seule couche d'éléments dans l'épaisseur, tout en attribuant un nombre arbitraire de points d'intégration dans cette direction. Cette particularité rend ces éléments SHB très attrayants en raison de leur efficacité de calcul en quasi-statique et en dynamique.

Par rapport aux développements antérieurs sur les éléments SHB, la formulation des éléments solide–coque proposés a été étendue dans ce travail au cadre de grands déplacements et rotations ainsi qu'à l'analyse dynamique/explicite. En outre, les formulations résultantes ont été combinées avec des lois constitutives avancées, incluant le comportement élastique orthotrope pour les matériaux composites et le comportement plastique anisotrope pour les matériaux métalliques, ce qui permet d'étendre leurs domaines d'applications. L'ensemble des éléments SHB a été implémenté dans les logiciels implicite/statique et explicite/dynamique d'ABAQUS à travers les routines utilisateurs UEL et VUEL, respectivement.

La performance des éléments SHB a été évaluée sur une série de cas tests linéaires et non linéaires. Pour chaque problème, les résultats des éléments SHB ont été comparés à ceux obtenus par leurs homologues d'ABAQUS ainsi qu'avec des solutions de référence extraites de la littérature. Les résultats numériques obtenus avec les éléments SHB ont montré un très bon accord avec les solutions de référence. Par rapport aux éléments coques d'ABAQUS, la performance des éléments SHB est souvent comparable; cependant, dans la plupart des cas tests numériques, les éléments solides d'ABAQUS nécessitent des maillages plus fins (dans le plan et à travers l'épaisseur) pour obtenir des solutions précises.

Ensuite, les éléments SHB ont été appliqués à la simulation de problèmes complexes, incluant des problèmes de dynamique de type impact et des procédés de mise en forme des tôles minces. Les différentes comparaisons entre les résultats de simulation donnés par les éléments SHB et les mesures expérimentales ont révélé que les éléments SHB sont capables de modéliser des processus complexes en utilisant une seul couche d'élément avec peu de points d'intégration à travers l'épaisseur. Aussi, les éléments SHB ont fourni des résultats les plus proches des données expérimentales par rapport à leurs homologues ABAQUS. Il est important de noter que les simulations des procédés de mise en forme des tôles minces avec les éléments coques quadratiques d'ABAQUS ont présenté des problèmes de convergence, ce qui révèle que ces éléments coques ne sont pas adaptés pour la simulation de problèmes impliquant le contact sur plusieurs faces comme dans le cas des procédés de mise en forme des tôles minces.

Globalement, les éléments solide–coque proposés ont montré de bonnes capacités à modéliser plusieurs types de problèmes impliquant des structures minces avec des maillages relativement grossiers et peu de points d'intégration dans l'épaisseur. Les éléments SHB

représentent également une alternative intéressante aux éléments solides et coques traditionnels, en particulier pour la simulation de problèmes complexes.

Travaux futurs

Comme révélé par les Chapitres 3 et 4 du manuscrit, les éléments SHB proposés ont fourni de bonnes prédictions. Cependant, certains aspects numériques doivent encore être améliorés afin de rendre les éléments SHB plus efficaces par rapport aux versions actuelles. Dans les travaux futurs, les aspects suivants devraient être poursuivis :

1) Combinaison de différents éléments au sein d'une même simulation. La famille d'éléments SHB proposée, constituée de deux éléments prismatiques et de deux éléments hexaédriques, a été implémentée dans le logiciel ABAQUS. Il a été montré, globalement, que la performance des éléments SHB hexaédriques (SHB8PS et SHB20) est meilleure que celle des éléments SHB prismatiques (SHB6 et SHB15). Cependant, ces éléments hexaédriques et prismatiques se complètent très bien, car la combinaison peut s'avérer nécessaire pour la simulation de géométries complexes, qui ne peuvent pas être maillées avec seulement des éléments hexaédriques.

2) Amélioration des temps de calcul des éléments SHB. Dans la contribution actuelle, nous nous sommes concentrés sur la précision des éléments SHB. Il est intéressant de noter que, pour tous les éléments SHB, les simulations ont été effectuées en utilisant une seule couche d'élément et peu de points d'intégration à traves l'épaisseur. Par conséquence, les modèles d'éléments SHB sont intrinsèquement moins coûteux, en termes de nombre de degrés de liberté (DOF) et de points d'intégration, que ceux utilisant des éléments solides classiques. Cependant, l'implémentation numérique des éléments SHB n'est pas encore optimisée en termes de programmation informatique. Dans les travaux futurs, l'implémentation numérique pourrait être mieux optimisée en s'inspirant des techniques de programmation avancées, comme celles utilisées par les codes commerciaux d'éléments finis.

3) Application des éléments SHB à des problèmes plus complexes. Bien que différents tests numériques aient été étudiés dans ce travail afin d'évaluer la performance des éléments SHB, il sera également très intéressant d'étendre encore leur champ d'application à des problèmes plus complexes et difficiles, impliquant de fortes non-linéarités géométriques et matérielles. Des modèles de comportement des matériaux plus avancés, tels que des lois constitutives basées sur des critères de plasticité anisotrope plus adaptées aux alliages

d'aluminium, devraient être implémentées afin d'élargir le champ d'application des éléments SHB.

References

Abed-Meraim F, Combescure A (2002) SHB8PS—a new adaptive, assumed-strain continuum mechanics shell element for impact analysis. *Computers & Structures* 80:791–803.

Abed-Meraim F, Combescure A (2009) An improved assumed strain solid–shell element formulation with physical stabilization for geometric non-linear applications and elastic-plastic stability analysis. *International Journal for Numerical Methods in Engineering* 80:1640–1686.

Abed-Meraim F, Trinh VD, Combescure A (2013) New quadratic solid–shell elements and their evaluation on linear benchmark problems. *Computing* 95:373–394.

Adam C, Bouabdallah S, Zarroug M, Maitournam H (2014) Improved numerical integration for locking treatment in isogeometric structural elements, Part I: Beams. *Computer Methods in Applied Mechanics and Engineering* 279:1–28.

Adam C, Bouabdallah S, Zarroug M, Maitournam H (2015a) Improved numerical integration for locking treatment in isogeometric structural elements, Part II: Plates and shells. *Computer Methods in Applied Mechanics and Engineering* 284:106–137.

Adam C, Hughes TJR, Bouabdallah S, Zarroug M, Maitournam H (2015b) Selective and reduced numerical integrations for NURBS-based isogeometric analysis. *Computer Methods in Applied Mechanics and Engineering* 284:732–761.

Ahmad S, Irons BM, Zienkiewicz OC (1970) Analysis of thick and thin shell structures by curved finite elements. *International Journal for Numerical Methods in Engineering* 2:419–451.

Alves de Sousa RJ, Cardoso RPR, Fontes Valente RA, Yoon JW, Grácio JJ, Natal Jorge RM (2005) A new one-point quadrature enhanced assumed strain (EAS) solid–shell element with multiple integration points along thickness: Part I—geometrically linear applications. *International Journal for Numerical Methods in Engineering* 62:952–977.

Ambati M, De Lorenzis L (2016) Phase-field modeling of brittle and ductile fracture in shells with isogeometric NURBS-based solid-shell elements. *Computer Methods in Applied Mechanics and Engineering* 312:351–373.

Andersen CM (1979) Evaluation of integrals for a ten-node isoparametric tetrahedral finite element. *Computers & Mathematics with Applications* 5:297–320.

Anderson RG, Irons BM, Zienkiewicz OC (1968) Vibration and stability of plates using finite elements. *International Journal of Solids and Structures* 4:1031–1055.

Andrade LG, Awruch AM, Morsch IB (2007) Geometrically nonlinear analysis of laminate composite plates and shells using the eight-node hexahedral element with one-point integration. *Composite Structures* 79:571–580.

Arciniega RA, Reddy JN (2007) Tensor-based finite element formulation for geometrically nonlinear analysis of shell structures. *Computer Methods in Applied Mechanics and Engineering* 196:1048–1073.

Areias PMA, César de Sá JMA, Conceição António CA, Fernandes AA (2003) Analysis of 3D problems using a new enhanced strain hexahedral element. *International Journal for Numerical Methods in Engineering* 58:1637–1682.

Armstrong PJ, Frederick CO (1966) A mathematical representation of the multiaxial Bauschinger effect, *Berkeley Nuclear Laboratories, CEGB Reprot, RD/B/N731*.

Balmer HA, Witmer EA (1964) Theoretical-experimental correlation of large dynamic and permanent deformations of impulsively-loaded simple structures. *Air Force Flight Dynamics Laboratory, Rept. FDP-TDR-64-108*, Wright Patterson AFB, OH.

Barlat F, Lege DJ, Brem JC (1991) A six-component yield function for anisotropic materials, *International Journal of Plasticity* 7:693–712.

Barlat F, Brem JC, Yoon JW, Chung K, Dick RE, Lege DJ, Pourboghrat F, Choi SH, Chu E (2003) Plane stress yield function for aluminum alloy sheets – part 1: theory. *International Journal of Plasticity* 19:1297–1319.

Barton MV (1951) Vibration of rectangular and skew cantilever plates. *Journal of Applied Mechanics* 18:129–134.

Barut A, Madenci E, Tesslerb A (1997) Nonlinear analysis of laminates through a Mindlin-type shear deformable shallow shell element. *Computer Methods in Applied Mechanics and Engineering* 143:155–173.

Bathe KJ, Dvorkin EN (1986) A formulation of general shell elements — The use of mixed interpolation of tensorial components. *International Journal for Numerical Methods in Engineering* 22:697–722.

Bathe KJ (1996) Finite element procedures. *Prentice-Hall, Inc.*, New Jersey, USA.

Belytschko T, Lin JI, Tsay CS (1984) Explicit algorithms for the nonlinear dynamics of shells. *Computer Methods in Applied Mechanics and Engineering* 42:225–251.

Belytschko T, Bindeman LP (1991) Assumed strain stabilization of the 4-node quadrilateral with 1-point quadrature for nonlinear problems. *Computer Methods in Applied Mechanics and Engineering* 88:311–340.

Belytschko T, Wong BL, Chiang HY (1992) Advances in one-point quadrature shell elements. *Computer Methods in Applied Mechanics and Engineering* 96:93–107.

Belytschko T, Bindeman LP (1993) Assumed strain stabilization of the eight node hexahedral element. *Computer Methods in Applied Mechanics and Engineering* 105:225–260.

Ben Bettaieb A, Duchêne L, Zhang L, Habraken AM (2011) New solid-shell finite element based on EAS and ANS concepts for sheet metal forming. *8th International Conference and Workshop on Numerical Simulation of 3D Sheet metal forming processes, NUMISHEET 2011*, 21-26th August, 2011, Seoul, South Korea.

Ben Bettaieb A, Sena JIV, Alves de Sousa RJ, Valente RAF, Habraken AM, Duchêne L (2015) On the comparison of two solid-shell formulations based on in-plane reduced and full integration schemes in linear and non-linear applications. *Finite Elements in Analysis and Design* 107:44–59.

Betsch P, Stein E (1999) Numerical implementation of multiplicative elasto-plasticity into assumed strain elements with application to shells at large strains. *Computer Methods in Applied Mechanics and Engineering* 179:215–245.

Bonet J, Burton AJ (1998) A simple average nodal pressure tetrahedral element for incompressible and nearly incompressible dynamic explicit applications. *Communications in Numerical Methods in Engineering* 14:437–449.

Bouclier R, Elguedj T, Combescure A (2012) Locking free isogeometric formulations of curved thick beams. *Computer Methods in Applied Mechanics and Engineering* 245–246:144–162.

Bouclier R, Elguedj T, Combescure A (2013a) On the development of NURBS-based isogeometric solid shell elements: 2D problems and preliminary extension to 3D. *Computational Mechanics* 52:1085–1112.

Bouclier R, Elguedj T, Combescure A (2013b) Efficient isogeometric NURBS-based solid-shell elements: Mixed formulation and $\overline{\mathrm{B}}$ -method. *Computer Methods in Applied Mechanics and Engineering* 267:86–110.

Bouclier R, Elguedj T, Combescure A (2015) An isogeometric locking-free NURBS-based solid-shell element for geometrically nonlinear analysis. *International Journal for Numerical Methods in Engineering* 101:774–808.

Bouffioux C, Eyckens P, Henrard C, Aerens R, Van Bael A, Sol H, Duflou JR, Habraken AM (2008) Identification of material parameters to predict Single Point Incremental Forming forces. *International Journal of Material Forming* 1:1147–1150.

Brank B, Peric D, Damjanic FB (1995) On implementation of a nonlinear four node shell finite element for thin multilayered elastic shells. *Computational Mechanics* 16:341–359.

Briassoulis D (1989) On the basics of the shear locking problem of C0 isoparametric plate elements. *Computers & Structures* 33(1):169–185.

Brischetto S, Polit O, Carrera E (2012) Refined shell model for the linear analysis of isotropic and composite elastic structures. *European Journal of Mechanics, A/Solids* 34:102–119.

Buechter N, Ramm E (1992) Shell theory versus degeneration-a comparison in large rotation finite element analysis. *International Journal for Numerical Methods in Engineering* 34:39–59.

Bui QV, Papeleux L, Ponthot JP (2004) Numerical simulation of springback using enhanced assumed strain elements. *Journal of Materials Processing Technology* 153–154:314–318.

Cao YP, Hu N, Lu J, Fukunaga H, Yao ZH (2002) A 3D brick element based on Hu–Washizu variational principle for mesh distortion. *International Journal for Numerical Methods in Engineering* 53: 2529–2548.

Cardoso RPR, Yoon JW, Mahardika M, Choudhry S, Alves de Sousa RJ, Valente RAF (2008) Enhanced assumed strain (EAS) and assumed natural strain (ANS) methods for one-point quadrature solid-shell elements. *International Journal for Numerical Methods in Engineering* 75:156–187.

Caseiro JF, Valente RAF, Reali A, Kiendl J, Auricchio F, Alves de Sousa RJ (2014) On the assumed natural strain method to alleviate locking in solid-shell NURBS-based finite elements. *Computational Mechanics* 53:1341–1353.

Caseiro JF, Valente RAF, Reali A, Kiendl J, Auricchio F, Alves de Sousa RJ (2015) Assumed natural strain NURBS-based solid-shell element for the analysis of large deformation elasto-plastic thin-shell structures. *Computer Methods in Applied Mechanics and Engineering* 284:861–880.

César de Sá JMA, Natal Jorge RM, Fontes Valente RA, Areias PMA (2002) Development of shear locking-free shell elements using an enhanced assumed strain formulation. *International Journal for Numerical Methods in Engineering* 53:1721–1750.

Chang TY, Saleeb AF, Graf W (1989) On the mixed formulation of A 9-node Lagrange shell element. *Computer Methods in Applied Mechanics and Engineering* 73:259–281.

Chen Y, Stolarski HK (1998) Extrapolated fields in the formulation of the assumed strain elements Part II: Three-dimensional problems. *Computer Methods in Applied Mechanics and Engineering* 154:l–29.

Chen LB, Xi F, Yang JL (2007) Elastic-plastic contact force history and response characteristics of circular plate subjected to impact by a projectile. *Acta Mechanica Sinica* 23:415–425.

Cho C, Park HC, Lee SW (1998) Stability analysis using a geometrically nonlinear assumed strain solid shell element model. *Finite Elements in Analysis and Design* 29:121–135.

Choi CK, Paik JG (1995) An effective four node degenerated shell element for geometrically nonlinear analysis. *Thin-Walled Structures* 24:261–283.

Choi TH, Huh H (1999) Sheet metal forming analysis of planar anisotropic materials by a modified membrane finite element method with bending effect. *Journal of Materials Processing Technology* 89–90:58–64.

Davim JP (2012) Statistical and computational techniques in manufacturing. *Springer*. Berlin, German.

Duarte Filho LA, Awruch AM (2004) Geometrically nonlinear static and dynamic analysis of shells and plates using the eight-node hexahedral element with one-point quadrature. *Finite Elements in Analysis and Design* 40:1297–1315.

Duchêne L, Ben Bettaieb A, Habraken AM (2011) Assessment of the enhanced assumed strain (EAS) and the assumed natural strain (ANS) techniques in the mechanical

behavior of the SSH3D solid-shell element. *11th International Conference on Computational Plasticity*, *COMPLAS XI*, 7-9th September, Barcelona, Spain.

Dvorkin EN, Bathe KJ (1984) A continuum mechanics based four-node shell element for general non-linear analysis. *Engineering Computations* 1:77–88.

Edem IB, Gosling PD (2012) One-point quadrature ANS solid–shell element based on a displacement variational formulation Part I – Geometrically linear assessment. *Computer Methods in Applied Mechanics and Engineering* 237–240:177–191

Edem IB, Gosling PD (2013) Physically stabilised displacement-based ANS solid–shell element. *Finite Elements in Analysis and Design* 74:30–40.

Elguedj T, Bazilevs Y, Calo VM, Hughes TJR (2008) B-bar an F-bar projection methods for nearly incompressible linear and non linear elasticity and plasticity using higher order NURBS element, *Computer Methods in Applied Mechanics and Engineering* 197: 5257–5296.

Fish J, Belytschko T (1988) Elements with embedded localization zones for large deformation problems. *Computers & Structures* 30:247–256.

Flanagan DP, Belytschko T (1981) A uniform strain hexahedron and quadrilateral with orthogonal hourglass control. *International Journal for Numerical Methods in Engineering* 17:679–706.

Flores FG, Oñate E (2005) Improvements in the membrane behaviour of the three node rotation-free BST shell triangle using an assumed strain approach. *Computer Methods in Applied Mechanics and Engineering* 194:907–932.

Flores FG (2013a) A ‘‘Prism’’ solid element for large strain shell analysis. *Computer Methods in Applied Mechanics and Engineering* 253:274–286.

Flores FG (2013b) Development of a non-linear triangular prism solid-shell element using ANS and EAS techniques. *Computer Methods in Applied Mechanics and Engineering* 266:81–97.

Flores FG (2016) A simple reduced integration hexahedral solid-shell element for large strains. *Computer Methods in Applied Mechanics and Engineering* 303:260–287.

Fontes Valente RA (2004) Developments on Shell and Solid-shell finite elements technology in nonlinear continuum mechanics. Ph. D. Thesis. *Universidade do Porto*, Portugal.

Geyer S, Groenwold AA (2003) On reduced integration and locking of flat shell finite elements with drilling rotations. *Communications in Numerical Methods in Engineering* 19:85–97.

Hallquist JO (1983) Theoretical manual for DYNA3D. *Report UC1D-19041*, Lawrence Livermore National Laboratory, Livermore, CA.

Hauptmann R, Schweizerhof K (1998) A systematic development of ‘solid-shell’ element formulations for linear and non-linear analysis employing only displacement degrees of freedom. *International Journal for Numerical Methods in Engineering* 42:49–69.

Hauptmann R, Schweizerhof K, Doll S (2000) Extension of the 'solid-shell' concept for application to large elastic and large elastoplastic deformations. *International Journal for Numerical Methods in Engineering* 49:1121–1141.

Hellen T K (1972) Effective quadrature rules for quadratic solid isoparametric finite elements. *International Journal for Numerical Methods in Engineering* 4:597–599.

Henrard C, Bouffioux C, Eyckens P, Sol H, Dufou JR, Van Houtte P, Van Bael A, Duchêne L, Habraken AM (2011) Forming forces in single point incremental forming: prediction by finite element simulations, validation and sensitivity. *Computational Mechanics* 47:573–590.

Hill R (1948) A theory of the yielding and plastic flow of anisotropic metals. *Proceedings of the Royal Society of London A* 193:281–297.

Hong CH, Kim YH (2002) A partial assumed strain formulation for triangular solid shell element. *Finite Elements in Analysis and Design* 38:375–390.

Hsiao KM (1987) Nonlinear analysis of general shell structures by flat triangular elements. *Computers & Structures* 25:665–675.

Huang HC (1987) Membrane locking and assumed strain shell elements. *Computers & Structures* 27:671–677.

Hughes TJR, Cohen M, Haroun M (1978) Reduced and selective integration techniques in the finite element analysis of plates. *Nuclear Engineering and Design* 46:203–222.

Hughes TJR (1980) Generalization of selective integration procedures to anisotropic and nonlinear media. *International Journal for Numerical Methods in Engineering* 15:1413–1418.

Hughes TJR, Winget J (1980) Finite rotation effects in numerical integration of rate constitutive equation arising in large deformation analysis. *International Journal for Numerical Methods in Engineering* 15:1862–1867.

Hughes TJR, Tezduyar TE (1981) Finite elements based upon Mindlin plate theory with particular reference to the four-node bilinear isoparametric element. *Journal of Applied Mechanics, Transactions of the ASME* 48:587–196.

Hughes TJR (1987) The Finite Element Method, first ed., *Prentice-Hall, Inc.*, New Jersey, USA.

Hughes TJR, Cottrell JA, Bazilevs Y (2005) Isogeometric analysis: CAD, finite elements, NURBS, exact geometry and mesh refinement. *Computer Methods in Applied Mechanics and Engineering* 194:4135–4195.

Hughes TJR, Reali A, Sangalli G (2008) Duality and unified analysis of discrete approximations in structural dynamics and wave propagation: Comparison of *p*-method finite elements with *k*-method NURBS. *Computer Methods in Applied Mechanics and Engineering* 197:4104–4124.

Huh H, Choi TH (1999) Modified membrane finite element formulation for sheet metal forming analysis of planar anisotropic materials. *International Journal of Mechanical Sciences* 42(8):1623–1643.

Kaiping L, Habraken AM, Bruneel H (1995) Simulation of square-cup deep-drawing with different finite elements. *Journal of Materials Processing Technology* 50:81–91.

Kim JH, Kim YH (2002) A three-node C0 ANS element for geometrically non-linear structural analysis. *Computer Methods in Applied Mechanics and Engineering* 191:4035–4059.

Kim KD, Liu GZ, Han SC (2005) A resultant 8-node solid-shell element for geometrically nonlinear analysis. *Computational Mechanics* 35:315–331.

Klinkel S, Gruttmann F, Wagner W (1999) A continuum based three-dimensional shell element for laminated structures. *Computers & Structures* 71:43–62.

Klinkel S, Gruttmann F, Wagner W (2006) A robust non-linear solid shell element based on a mixed variational formulation. *Computer Methods in Applied Mechanics and Engineering* 195:179–201.

Koschnick F, Bischoff M, Camprubí N, Bletzinger KU (2005) The discrete strain gap method and membrane locking. *Computer Methods in Applied Mechanics and Engineering* 194:2444–2463.

Kpeky F, Boudaoud H, Abed-Meraim F, Daya EM (2015) Modeling of viscoelastic sandwich beams using solid–shell finite elements. *Composite Structures* 133:105–116.

Kreja I, Schmidt R (2006) Large rotations in first-order shear deformation FE analysis of laminated shells. *International Journal of Non-linear Mechanics* 41:101–123.

Kui LX, Liu GQ, Zienkiewicz OC (1985) A generalized displacement method for the finite element analysis of thin shells. *International Journal for Numerical Methods in Engineering* 21:2145–2155.

Kulikov GM, Plotnikova SV (2006) Geometrically exact assumed stress–strain multilayered solid-shell elements based on the 3D analytical integration. *Computers & Structures* 84:1275–1287.

Laurent H (1996) Etude en grandes transformations d'une nouvelle famille d'éléments finis coque triangulaire à trois degrés de liberté par nœud. Application à la simulation numérique de l'emboutissage. Ph. D. Thesis, *Université du Maine*, France.

Lee S, Cho BC, Park HC, Yoon KJ, Goo NS (2002) Analysis of multi-layered actuators using an assumed strain solid element. *Materials Chemistry and Physics* 75:174–177.

Lee SJ (2004) Free vibration analysis of plates by using a four-node finite element formulated with assumed natural transverse shear strain. *Journal of Sound and Vibration* 278:657–684.

Leissa AW (1969) Vibration of Plates. Scientific and Technical Information Division, *NASA*, Washington, DC, USA.

Li KP, Cescotto S (1997) An 8-node brick element with mixed formulation for large deformation analyses. *Computer Methods in Applied Mechanics and Engineering* 141:157–204.

Li LM, Peng YH, Li DY (2011) A stabilized underintegrated enhanced assumed strain solid-shell element for geometrically nonlinear plate/shell analysis. *Finite Elements in Analysis and Design* 47:511–518.

MacNeal RH, Harder RL (1985) A proposed standard set of problems to test finite element accuracy. *Finite Elements in Analysis and Design* 1:3–20.

Makinouchi A, Nakamachi E, Oñate E, Wagoner RH (1993) NUMISHEET'93, *Proceedings of the 2nd International Conference and Workshop on Numerical Simulation of 3D Sheet Metal Forming Processes - Verification of Simulation with Experiment*, Isehara, Japan.

Mars J, Wali M, Jarraya A, Dammak F, Dhiab A (2015) Finite element implementation of an orthotropic plasticity model for sheet metal in low velocity impact simulations. *Thin-Walled Structures* 89:93–100.

Militello C, Felippa CA (1990a) A variational justification of the assumed natural strain formulation of finite elements — I. Variational principles. *Computers & Structures* 34(3):431–438.

Militello C, Felippa CA (1990b) A variational justification of the assumed natural strain formulation of finite elements — II. The C^0 four-node plate element. *Computers & Structures* 34(3):439–444.

Mohan P, Kapania RK (1998) Updated lagrangian formulation of a flat triangular element for thin laminated shells. *American Institute of Aeronautics and Astronautics Journal* 36:273–281.

Mondkar DP, Powell GH (1977) Finite element analysis of non-linear static and dynamic response. *International Journal for Numerical Methods in Engineering* 11:499–520.

Moreira RAS, Alves de Sousa RJ, Valente RAF (2010) A solid-shell layerwise finite element for non-linear geometric and material analysis. *Composite Structures* 92:1517–1523.

Naceur H, Shiri S, Coutellier D, Batoz JL (2013) On the modeling and design of composite multilayered structures using solid-shell finite element model. *Finite Elements in Analysis and Design* 70–71:1–14.

Nguyen NH, Pham VN, Hogge M, Ponthot JP (2008) An assumed natural strain technique for 2D solid-shell elements. *Fourth international conference on advanced computational methods in engineering (ACOMEN 2008)*, 26-28 May, Liège, Belgium.

Nguyen NH (2009) Development of solid-shell elements for large deformation simulation and springback prediction. Ph. D. Thesis. *Université de Liège*, Liège, Belgium.

Norachan P, Suthasupradit S, Kim KD (2012) A co-rotational 8-node degenerated thin-walled element with assumed natural strain and enhanced assumed strain. *Finite Elements in Analysis and Design* 50:70–85.

Olovsson L, Unosson M, Simonsson K (2004) Selective mass scaling for thin walled structures modeled with tri-linear solid elements. *Computational Mechanics* 34(2):134–136.

Pagani M, Reese S, Perego U (2014) Computationally efficient explicit nonlinear analyses using reduced integration-based solid-shell finite elements. *Computer Methods in Applied Mechanics and Engineering* 268:141–159.

Parente MPL, Fontes Valente RA, Natal Jorge RM, Cardoso RPR, Alves de Sousa RJ (2006) Sheet metal forming simulation using EAS solid-shell finite elements. *Finite Elements in Analysis and Design* 42:1137–1149.

Park DW, Oh SI (2004) A four-node shell element with enhanced bending performance for springback analysis. *Computer Methods in Applied Mechanics and Engineering* 193:2105–2138.

Payette GS, Reddy JN (2014) A seven-parameter spectral/hp finite element formulation for isotropic, laminated composite and functionally graded shell structures. *Computer Methods in Applied Mechanics and Engineering* 278:664–704.

Petchsasithon A, Gosling PD (2005) A locking-free hexahedral element for the geometrically non-linear analysis of arbitrary shells. *Computational Mechanics* 35:94–114.

Pimpinelli G (2004) An assumed strain quadrilateral element with drilling degrees of freedom. *Finite Elements in Analysis and Design* 41:267–283.

Polit O, Touratier M (1999) A C^0 eight node finite element based on a shell theory comparison with the degenerated approach. *Revue Européenne Des Eléments Finis* 8:111–134.

Polit O, Touratier M (2000) High-order triangular sandwich plate finite element for linear and non-linear analysis. *Computer Methods in Applied Mechanics and Engineering* 185:305-324.

Ponthot JP, Papeleux L, Gohy S, Collard X (2000) Numerical simulation of springback in sheet metal forming. *European Congress on Computational Methods in Applied Sciences and Engineering, ECCOMAS 2000*, 11-14th September, 2000, Barcelona, Spain.

Prathap G (1985) The poor bending response of the four-node plane stress quadrilateral. *International Journal for Numerical Methods in Engineering* 21:825–835.

Puso MA (2000) A highly efficient enhanced assumed strain physically stabilized hexahedral element. *International Journal for Numerical Methods in Engineering* 49:1029–1064.

Puso MA, Solberg J (2006) A stabilized nodally integrated tetrahedral. *International Journal for Numerical Methods in Engineering* 67:841–867.

Reese S (2007) A large deformation solid-shell concept based on reduced integration with hourglass stabilization. *International Journal for Numerical Methods in Engineering* 69:1671–1716.

Rhiu JJ, Lee SW (1987) A new efficient mixed formulation for thin shell finite element models. *International Journal for Numerical Methods in Engineering* 24:581–604.

Saigal S, Yang TY (1985) Nonlinear dynamic analysis with a 48 D.O.F. curved thin shell element. *International Journal for Numerical Methods in Engineering* 21:1115–1128.

Salahouelhadj A, Abed-Meraim F, Chalal H, Balan T (2012) Application of the continuum shell finite element SHB8PS to sheet forming simulation using an extended large strain anisotropic elastic–plastic formulation. *Archive of Applied Mechanics* 82:1269–1290.

Schwarze M, Reese S (2009) A reduced integration solid–shell finite element based on the EAS and the ANS concept—Geometrically linear problems. *International Journal for Numerical Methods in Engineering* 80:1322–1355.

Schwarze M, Vladimirov IN, Reese S (2010) A new continuum shell finite element for sheet metal forming applications. *International Journal of Material Forming* 3:919–922.

Schwarze M, Vladimirov IN, Reese S (2011) Sheet metal forming and springback simulation by means of a new reduced integration solid–shell finite element technology. *Computer Methods in Applied Mechanics and Engineering* 200:454–476.

Sena JIV, Alves de Sousa RJ, Valente RAF (2010) Single point incremental forming simulation with an enhanced assumed strain solid-shell finite element formulation. *International Journal of Material Forming* 3:963–966.

Sena JIV, Alves de Sousa RJ, Valente RAF (2011) On the use of EAS solid-shell formulations in the numerical simulation of incremental forming processes. *Engineering Computations* 28(3):287–313.

Sena JIV, Lequesne C, Duchêne L, Habraken AM, Valente RAF, Alves de Sousa J (2016) Single point incremental forming simulation with adaptive remeshing technique using solid-shell elements. *Engineering Computations* 33(5): 1388–1421.

Simo JC, Taylor RL, Pister KS (1985) Variational and projection methods for the volume constraint in finite deformation elasto-plasticity. *Computer Methods in Applied Mechanics and Engineering* 51:177–208.

Simo JC, Hughes TJR (1986) On the variational foundations of assumed strain methods. *Journal of Applied Mechanics, Transactions of the ASME* 53:51–54.

Simo JC, Rifai MS (1990) A class of mixed assumed strain methods and the method of incompatible modes. *International Journal for Numerical Methods in Engineering* 29:1595–1638.

Simo JC, Armero F (1992) Geometrically non-linear enhanced strain mixed methods and the method of incompatible modes. *International Journal for Numerical Methods in Engineering* 33:1413–1449.

Stander N, Matzenmiller A, Ramm E (1989) An assessment of assumed strain method in finite rotation shell analysis. *Engineering Computations* 6:58–66.

Stolarski HK, Belytschko T (1982) Membrane locking and reduced integration for curved elements. *Journal of Applied Mechanics, Transactions of the ASME* 49:172–176.

Stolarski HK, Belytschko T (1983) Shear and membrane locking in curved C^0 elements. *Computer Methods in Applied Mechanics and Engineering* 41:279–296.

Stolarski HK, Chen YI (1995) Extrapolated fields in the formulation of the assumed strain elements Part 1: Two-dimensional problems. *Computer Methods in Applied Mechanics and Engineering* 123:247–262.

Sze KY, Zhu D (1999) A quadratic assumed natural strain curved triangular shell element. *Computer Methods in Applied Mechanics and Engineering* 174:57–71.

Sze KY, Yao LQ (2000) A hybrid stress ANS solid-shell element and its generalization for smart structure modelling. Part I—solid-shell element formulation. *International Journal for Numerical Methods in Engineering* 48:545–564.

Sze KY, Chan WK (2001) A six-node pentagonal assumed natural strain solid-shell element. *Finite Elements in Analysis and Design* 37:639–655.

Sze KY, Liu XH, Lo SH (2004) Popular benchmark problems for geometric nonlinear analysis of shells. *Finite Elements in Analysis and Design* 40:1551–1569.

Tessler A, Spiridigliozzi L (1988) Resolving membrane and shear locking phenomena in curved shear-deformable axisymmetric shell elements. *International Journal for Numerical Methods in Engineering* 26:1071–1086.

Timoshenko SP (1955) Strength of materials. Part I: Elementary theory and problems. Third ed., *D. Van Nostrand Company, Inc.* Canada.

Trinh VD, Abed-Meraim F, Combescure A (2011) A new assumed strain solid–shell formulation "SHB6" for the six-node prismatic finite element. *Journal of Mechanical Science and Technology* 25:2345–2364.

Valente RAF, Alves de Sousa RJ, Jorge RMN (2004) An enhanced strain 3D element for large deformation elastoplastic thin-shell applications. *Computational Mechanics* 34:38–52.

Vlachoutsis S (1992) Shear correction factors for plates and shells. *International Journal for Numerical Methods in Engineering* 33:1537–1552.

Vu-Quoc L, Tan XG (2003) Optimal solid shells for non-linear analyses of multilayer composites. I. Statics. *Computer Methods in Applied Mechanics and Engineering* 192:975–1016.

Wagner W, Klinkel S, Gruttmann F (2002) Elastic and plastic analysis of thin-walled structures using improved hexahedral elements. *Computers & Structures* 80:857–869.

Wang P, Chalal H, Abed-Meraim F (2015) Efficient solid–shell finite elements for quasi-static and dynamic analyses and their application to sheet metal forming simulation. *Key Engineering Materials* 651–653:344–349.

Wang P, Chalal H, Abed-Meraim F (2016) Simulation of nonlinear benchmarks and sheet metal forming processes using linear and quadratic solid–shell elements combined with advanced anisotropic behavior models. *12th International Conference on Numerical Methods in Industrial Forming Processes*, 4-7th July, Troyes, France.

Wang P, Chalal H, Abed-Meraim F (2017a) Linear and quadratic solid–shell elements for quasi-static and dynamic simulations of thin 3D structures: Application to a deep drawing process. *Strojniški vestnik – Journal of Mechanical Engineering* 63:25–34.

Wang P, Chalal H, Abed-Meraim F (2017b) Quadratic solid–shell elements for nonlinear structural analysis and sheet metal forming simulation. *Computational Mechanics* 59:161–186.

Wang P, Chalal H, Abed-Meraim F (2017c) Quadratic prismatic and hexahedral solid–shell elements for geometric nonlinear analysis of laminated composite structures. *Composite Structures* 172:282–296.

Winkler R (2010) Comments on membrane locking. *Proceedings in Applied Mathematics and Mechanics* 10:229–230.

Wisniewski K, Wagner W, Turska E, Gruttmann F (2010) Four-node Hu-Washizu elements based on skew coordinates and contravariant assumed strain. *Computer & Structures* 88:1278–1284.

Wriggers P (2006) Computational contact mechanics, second ed., *Springer*, Berlin, Germany.

Wu TY (2013) Dynamic nonlinear analysis of shell structures using a vector form intrinsic finite element. *Engineering Structures* 56:2028–2040.

Xu HJ, Liu YQ, Zhong W (2012) Three-dimensional finite element simulation of medium thick plate metal forming and springback. *Finite Elements in Analysis and Design* 51:49–58.

Yoon JW, Barlat F, Dick RE, Karabin ME (2006) Prediction of six or eight ears in a drawn cup based on a new anisotropic yield function. *International Journal of Plasticity* 22:174–193.

Zeng Q, Combescure A (1998) A new one-point quadrature, general non-linear quadrilateral shell element with physical stabilization. *International Journal for Numerical Methods in Engineering* 42:1307–1338.

Zhang DJ, Cui ZS, Ruan XY, Li YQ (2007) An analytical model for predicting springback and side wall curl of sheet after U-bending. *Computational Material Science* 38:707–715.

Zhu YY, Cescotto S (1996) Unified and mixed formulation of the 8-node hexahedral elements by assumed strain method. *Computer Methods in Applied Mechanics and Engineering* 129:177–209.

Zienkiewicz OC, Taylor RL, Too JM (1971) Reduced integration technique in general analysis of plates and shells. *International Journal for Numerical Methods in Engineering* 3:275–290.

Zienkiewicz OC, Taylor RL (2000) The finite element method, Volume 2: Solid mechanics, fifth ed., *Butterworth-Heinemann*, UK.

Zienkiewicz OC, Taylor RL, Zhu JZ (2006) The finite element method, sixth ed., *Elsevier Ltd*., UK.

Appendix A

Shape functions for the SHB elements

As the SHB elements are based on a fully three-dimensional approach, they adopt the classical shape functions for standard isoparametric prismatic and hexahedral elements. In this appendix, the shape functions for all SHB elements are given in details.

A.1 Linear prismatic SHB6 element

As shown in Fig. 2.1 (a), the six nodes of the SHB6 element are numbered from 1 to 6. According to the reference coordinate system, the coordinates of all nodes are given in the following Table A.1.

Table A.1. Nodal coordinates of the SHB6 in the reference coordinate system.

No. of the node	ξ	η	ζ
1	0	0	-1
2	1	0	-1
3	0	1	-1
4	0	0	1
5	1	0	1
6	0	1	1

The shape functions associated with the linear prismatic SHB6 element are defined as:

$$\begin{cases} N_I(\xi,\eta,\zeta)=\dfrac{1}{2}(1+\zeta_I\zeta)(1-\xi-\eta), & \text{for } I=1,4 \\ N_I(\xi,\eta,\zeta)=\dfrac{1}{2}(1+\zeta_I\zeta)\xi, & \text{for } I=2,5, \\ N_I(\xi,\eta,\zeta)=\dfrac{1}{2}(1+\zeta_I\zeta)\eta, & \text{for } I=3,6 \end{cases} \tag{A.1}$$

where $\xi\in[0,1]$, $\eta\in[0,1-\xi]$, $\zeta\in[-1,1]$, while ξ_I, η_I and ζ_I are the coordinates of the I-th node.

A.2 Linear hexahedral SHB8PS element

The coordinates of the eight nodes of the SHB8PS element are given in Table A.2.

Table A.2. Nodal coordinates of the SHB8PS in the reference coordinate system.

No. of the node	ξ	η	ζ
1	-1	-1	-1
2	1	-1	-1
3	1	1	-1
4	-1	1	-1
5	-1	-1	1
6	1	-1	1
7	1	1	1
8	-1	1	1

The shape functions associated with the linear hexahedral SHB8PS element are defined as:

$$N_I(\xi,\eta,\zeta)=\frac{1}{8}\left(1+\xi_I\xi\right)\left(1+\eta_I\eta\right)\left(1+\zeta_I\zeta\right) \text{ for } I=1,\,2,\,\ldots,8\,, \tag{A.2}$$

where $(\xi,\eta,\zeta)\in[-1,1]$, while ξ_I, η_I and ζ_I are the coordinates of the I-th node.

A.3 Quadratic prismatic SHB15 element

The coordinates of the fifteen nodes of the SHB15 element are given in Table A.3.

Table A.3. Nodal coordinates of the SHB15 in the reference coordinate system.

No. of the node	ξ	η	ζ
1	0	0	-1
2	1	0	-1
3	0	1	-1
4	0	0	1
5	1	0	1
6	0	1	1
7	1/2	0	-1
8	1/2	1/2	-1
9	0	1/2	-1
10	1/2	0	1
11	1/2	1/2	1
12	0	1/2	1
13	0	0	0
14	1	0	0
15	0	1	0

The shape functions associated with the quadratic prismatic SHB15 element are defined as:

$$\begin{cases} N_I(\xi,\eta,\zeta)=\dfrac{1}{2}\left(\zeta_I\zeta+1\right)\left(1-\xi-\eta\right)\left(\zeta_I\zeta-2\xi-2\eta\right), & \text{for } I=1,4 \\ N_I(\xi,\eta,\zeta)=\dfrac{1}{2}\xi\left(\zeta_I\zeta+1\right)\left(\zeta_I\zeta+2\xi-2\right), & \text{for } I=2,5 \\ N_I(\xi,\eta,\zeta)=\dfrac{1}{2}\eta\left(\zeta_I\zeta+1\right)\left(\zeta_I\zeta+2\eta-2\right), & \text{for } I=3,6 \\ N_I(\xi,\eta,\zeta)=2\xi\left(\zeta_I\zeta+1\right)\left(1-\xi-\eta\right), & \text{for } I=7,10 \\ N_I(\xi,\eta,\zeta)=2\xi\eta\left(\zeta_I\zeta+1\right), & \text{for } I=8,11 \\ N_I(\xi,\eta,\zeta)=2\eta\left(\zeta_I\zeta+1\right)\left(1-\xi-\eta\right), & \text{for } I=9,12 \\ N_I(\xi,\eta,\zeta)=\left(1-\xi-\eta\right)\left(1-\zeta^2\right), & \text{for } I=13 \\ N_I(\xi,\eta,\zeta)=\xi\left(1-\zeta^2\right), & \text{for } I=14 \\ N_I(\xi,\eta,\zeta)=\eta\left(1-\zeta^2\right), & \text{for } I=15 \end{cases}, \tag{A.3}$$

where $\xi\in[0,1]$, $\eta\in[0,1-\xi]$, $\zeta\in[-1,1]$, while ξ_I, η_I and ζ_I are the coordinates of the I-th node.

A.4 Quadratic hexahedral SHB20 element

The coordinates of the twenty nodes of the SHB20 element are given in Table A.4.

Table A.4. Nodal coordinates of the SHB20 in the reference coordinate system.

No. of the node	ξ	η	ζ
1	-1	-1	-1
2	1	-1	-1
3	1	1	-1
4	-1	1	-1
5	-1	-1	1
6	1	-1	1
7	1	1	1
8	-1	1	1
9	0	-1	-1
10	1	0	-1
11	0	1	-1
12	-1	0	-1
13	-1	-1	0
14	1	-1	0
15	1	1	0
16	-1	1	0
17	0	-1	1
18	1	0	1
19	0	1	1
20	-1	0	1

The shape functions of the quadratic hexahedral SHB20 element are defined as:

$$\begin{cases} N_I(\xi,\eta,\zeta) = -\frac{1}{8}\left(1+\xi_I\xi\right)\left(1+\eta_I\eta\right)\left(1+\zeta_I\zeta\right)\left(\xi_I\xi+\eta_I\eta+\zeta_I\zeta+2\right), \text{for } I=1,\ 2,\ldots,8 \\ N_I(\xi,\eta,\zeta) = \frac{1}{4}\left(1-\xi^2\right)\left(1+\eta_I\eta\right)\left(1+\zeta_I\zeta\right), \qquad \text{for } I=9,\ 11,\ 17,\ 19 \\ N_I(\xi,\eta,\zeta) = \frac{1}{4}\left(1+\xi_I\xi\right)\left(1-\eta^2\right)\left(1+\zeta_I\zeta\right), \qquad \text{for } I=10,\ 12,\ 18,\ 20 \\ N_I(\xi,\eta,\zeta) = \frac{1}{4}\left(1+\xi_I\xi\right)\left(1+\eta_I\eta\right)\left(1-\zeta^2\right), \qquad \text{for } I=13,\ 14,15,\ 16 \end{cases} \quad ,(A.4)$$

where $(\xi,\eta,\zeta)\in[-1,1]$, while ξ_I, η_I and ζ_I are the coordinates of the I-th node.

Appendix B

Detailed expressions of the h_α functions

As presented in Chapter 2, the expressions of the h_α functions, which are involved in the displacement field expansion (see Eq. (2.4)), are provided in this appendix for all SHB elements.

B.1 Linear prismatic SHB6 element

The displacement field and the expression of the h_α functions for the SHB6 element are:

$$\begin{cases} u_i = a_{0i} + a_{1i}x + a_{2i}y + a_{3i}z + c_{1i}h_1 + c_{2i}h_2 & i = 1,2,3 \\ \mathbf{d}_i = a_{0i}\mathbf{s} + a_{1i}\mathbf{x}_1 + a_{2i}\mathbf{x}_2 + a_{3i}\mathbf{x}_3 + c_{1i}\mathbf{h}_1 + c_{2i}\mathbf{h}_2 & i = 1,2,3\ . \\ h_1 = \eta\zeta, \quad h_2 = \zeta\xi. \end{cases} \tag{B.1}$$

B.2 Linear hexahedral SHB8PS element

The displacement field and the expression of the h_α functions for the SHB8PS element are:

$$\begin{cases} u_i = a_{0i} + a_{1i}x + a_{2i}y + a_{3i}z + c_{1i}h_1 + c_{2i}h_2 + c_{3i}h_3 + c_{4i}h_4 & i = 1,2,3 \\ \mathbf{d}_i = a_{0i}\mathbf{s} + a_{1i}\mathbf{x}_1 + a_{2i}\mathbf{x}_2 + a_{3i}\mathbf{x}_3 + c_{1i}\mathbf{h}_1 + c_{2i}\mathbf{h}_2 + c_{3i}\mathbf{h}_3 + c_{4i}\mathbf{h}_4 & i = 1,2,3\ . \\ h_1 = \eta\zeta, \quad h_2 = \zeta\xi, \quad h_3 = \xi\eta, \quad h_4 = \xi\eta\zeta. \end{cases} \tag{B.2}$$

B.3 Quadratic prismatic SHB15 element

The displacement field and the expression of the h_α functions for the SHB15 element are:

$$\begin{cases} u_i = a_{0i} + a_{1i}x + a_{2i}y + a_{3i}z + c_{1i}h_1 + c_{2i}h_2 + c_{3i}h_3 + c_{4i}h_4 + c_{5i}h_5 + c_{6i}h_6 + c_{7i}h_7 \\ \qquad + c_{8i}h_8 + c_{9i}h_9 + c_{10i}h_{10} + c_{11i}h_{11} \qquad i = 1,2,3\ , \\ \mathbf{d}_i = a_{0i}\mathbf{s} + a_{1i}\mathbf{x}_1 + a_{2i}\mathbf{x}_2 + a_{3i}\mathbf{x}_3 + c_{1i}\mathbf{h}_1 + c_{2i}\mathbf{h}_2 + c_{3i}\mathbf{h}_3 + c_{4i}\mathbf{h}_4 + c_{5i}\mathbf{h}_5 + c_{6i}\mathbf{h}_6 \\ \qquad + c_{7i}\mathbf{h}_7 + c_{8i}\mathbf{h}_8 + c_{9i}\mathbf{h}_9 + c_{10i}\mathbf{h}_{10} + c_{11i}\mathbf{h}_{11} \qquad i = 1,2,3\ , \\ h_1 = \zeta\xi, \quad h_2 = \eta\zeta, \quad h_3 = \xi\eta, \quad h_4 = \xi\eta\zeta, \quad h_5 = \xi^2, \quad h_6 = \eta^2, \quad h_7 = \zeta^2, \\ h_8 = \xi^2\zeta, \quad h_9 = \eta^2\zeta, \quad h_{10} = \xi\zeta^2, \quad h_{11} = \eta\zeta^2. \end{cases} \tag{B.3}$$

B.4 Quadratic hexahedral SHB20 element

The displacement field and the expression of the h_α functions for the SHB20 element are:

$$\begin{cases} u_i = a_{0i} + a_{1i}x + a_{2i}y + a_{3i}z + c_{1i}h_1 + c_{2i}h_2 + c_{3i}h_3 + c_{4i}h_4 + c_{5i}h_5 + c_{6i}h_6 + c_{7i}h_7 + c_{8i}h_8 \\ \qquad + c_{9i}h_9 + c_{10i}h_{10} + c_{11i}h_{11} + c_{12i}h_{12} + c_{13i}h_{13} + c_{14i}h_{14} + c_{15i}h_{15} + c_{16i}h_{16} \qquad i = 1,2,3\ , \\ \mathbf{d}_i = a_{0i}\mathbf{s} + a_{1i}\mathbf{x}_1 + a_{2i}\mathbf{x}_2 + a_{3i}\mathbf{x}_3 + c_{1i}\mathbf{h}_1 + c_{2i}\mathbf{h}_2 + c_{3i}\mathbf{h}_3 + c_{4i}\mathbf{h}_4 + c_{5i}\mathbf{h}_5 + c_{6i}\mathbf{h}_6 + c_{7i}\mathbf{h}_7 + c_{8i}\mathbf{h}_8 \\ \qquad + c_{9i}\mathbf{h}_9 + c_{10i}\mathbf{h}_{10} + c_{11i}\mathbf{h}_{11} + c_{12i}\mathbf{h}_{12} + c_{13i}\mathbf{h}_{13} + c_{14i}\mathbf{h}_{14} + c_{15i}\mathbf{h}_{15} + c_{16i}\mathbf{h}_{16} \qquad i = 1,2,3\ , \\ h_1 = \xi\zeta\ ,\ h_2 = \zeta\eta,\ h_3 = \xi\eta,\ h_4 = \xi^2\ ,\ h_5 = \eta^2\ ,\ h_6 = \zeta^2\ ,\ h_7 = \xi\eta\zeta\ ,\ h_8 = \xi^2\eta,\ h_9 = \xi^2\zeta\ , \\ h_{10} = \eta^2\xi,\ h_{11} = \eta^2\zeta\ ,\ h_{12} = \zeta^2\xi,\ h_{13} = \zeta^2\eta,\ h_{14} = \xi^2\eta\zeta\ ,\ h_{15} = \xi\eta^2\zeta\ ,\ h_{16} = \xi\eta\zeta^2. \end{cases} \quad .(B.4)$$

Appendix C

Orthogonality conditions for the SHB elements

In order to determine the unknown constants a_{ji} and $c_{\alpha i}$ in the expressions of the displacement field (see Eqs. (2.4) and (2.5)), the Hallquist vectors $\mathbf{b}_i = \dfrac{\partial \mathbf{N}}{\partial x_i}_{|\xi=\eta=\zeta=0}$ are introduced in the formulation of the SHB elements. Such explicit derivations allow us to establish some orthogonality properties involving the Hallquist vectors $\mathbf{b}_i$, the nodal displacement vectors $\mathbf{d}_i$, the nodal coordinate vectors $\mathbf{x}_i$, the constant vector $\mathbf{s}$ and vectors $\mathbf{h}_\alpha$. Based on these orthogonality conditions, the constants a_{ji} and $c_{\alpha i}$ can be obtained through the scalar product of Eq. (2.5) by $\mathbf{b}_i^T$, $\mathbf{s}^T$ and $\mathbf{h}_\alpha^T$, successively. In this appendix, the detailed orthogonality conditions for each SHB solid–shell element are presented.

C.1 Linear prismatic SHB6 element

The orthogonality properties, which allow determining the constants a_{ji} and $c_{\alpha i}$ for the SHB6 element, are given by:

$$\begin{cases} \mathbf{b}_i^T \cdot \mathbf{h}_\alpha = 0, & \mathbf{b}_i^T \cdot \mathbf{s} = 0, & \mathbf{b}_i^T \cdot \mathbf{x}_j = \delta_{ij} \\ \mathbf{h}_\alpha^T \cdot \mathbf{s} = 0, & \mathbf{h}_\alpha^T \cdot \mathbf{h}_\beta = 2\delta_{\alpha\beta} & \\ i, j = 1, \cdots, 3 & \alpha, \beta = 1, 2 & \end{cases} . \tag{C.1}$$

C.2 Linear hexahedral SHB8PS element

The orthogonality properties, which allow determining the constants a_{ji} and $c_{\alpha i}$ for the SHB8PS element, are given by:

$$\begin{cases} \mathbf{b}_i^T \cdot \mathbf{h}_\alpha = 0, & \mathbf{b}_i^T \cdot \mathbf{s} = 0, & \mathbf{b}_i^T \cdot \mathbf{x}_j = \delta_{ij} \\ \mathbf{h}_\alpha^T \cdot \mathbf{s} = 0, & \mathbf{h}_\alpha^T \cdot \mathbf{h}_\beta = 8\delta_{\alpha\beta} & \\ i, j = 1, \cdots, 3 & \alpha, \beta = 1, \cdots, 4 & \end{cases} . \tag{C.2}$$

C.3 Quadratic prismatic SHB15 element

The orthogonality properties, which allow determining the constants a_{ji} and $c_{\alpha i}$ for the SHB15 element, are given by:

$$\begin{cases} \begin{array}{lll} \mathbf{b}_i^T \cdot \mathbf{h}_\alpha = 0, & \mathbf{b}_i^T \cdot \mathbf{s} = 0, & \mathbf{b}_i^T \cdot \mathbf{x}_j = \delta_{ij} \\ \mathbf{h}_1^T \cdot \mathbf{s} = 0, & \mathbf{h}_2^T \cdot \mathbf{s} = 0, & 2\mathbf{h}_3^T \cdot \mathbf{s} = 1, \\ \mathbf{h}_4^T \cdot \mathbf{s} = 0, & \mathbf{h}_5^T \cdot \mathbf{s} = 4, & \mathbf{h}_6^T \cdot \mathbf{s} = 4, \\ \mathbf{h}_7^T \cdot \mathbf{s} = 12, & \mathbf{h}_8^T \cdot \mathbf{s} = 0, & \mathbf{h}_9^T \cdot \mathbf{s} = 0, \\ \mathbf{h}_{10}^T \cdot \mathbf{s} = 4, & \mathbf{h}_{11}^T \cdot \mathbf{s} = 4 & \end{array} \\ i, j = 1, \cdots, 3 \end{cases}$$

$$\begin{cases} \mathbf{h}_\alpha^T \cdot \mathbf{h}_\beta = \begin{bmatrix} 3 & \frac{1}{2} & 0 & \frac{1}{4} & 0 & 0 & 0 & \frac{5}{2} & \frac{1}{4} & 0 & 0 \\ & 3 & 0 & \frac{1}{4} & 0 & 0 & 0 & \frac{1}{4} & \frac{5}{2} & 0 & 0 \\ & & \frac{1}{8} & 0 & \frac{1}{8} & \frac{1}{8} & \frac{1}{2} & 0 & 0 & \frac{1}{4} & \frac{1}{4} \\ & & & \frac{1}{8} & 0 & 0 & 0 & \frac{1}{8} & \frac{1}{8} & 0 & 0 \\ & & & & \frac{13}{4} & \frac{1}{8} & 3 & 0 & 0 & \frac{5}{2} & \frac{1}{4} \\ & & & & & \frac{13}{4} & 3 & 0 & 0 & \frac{1}{4} & \frac{5}{2} \\ & & & & & & 12 & 0 & 0 & 4 & 4 \\ & & & & & & & \frac{9}{4} & \frac{1}{8} & 0 & 0 \\ & & & & & & & & \frac{9}{4} & 0 & 0 \\ & & & & & & & & & 3 & \frac{1}{2} \\ sym & & & & & & & & & & 3 \end{bmatrix}. \\ \alpha, \beta = 1, \cdots, 11 \end{cases} \tag{C.3}$$

Based on the above conditions, the constants a_{ji} and $c_{\alpha i}$ can be determined by the scalar product of Eq. (2.5) by $\mathbf{b}_i^T$, $\mathbf{s}^T$ and $\mathbf{h}_\alpha^T$, successively, which gives:

$$a_{ji} = \mathbf{b}_j^T \cdot \mathbf{d}_i, \qquad c_{\alpha i} = \boldsymbol{\gamma}_\alpha^T \cdot \mathbf{d}_i, \tag{C.4}$$

with

$$\boldsymbol{\gamma}_\alpha^T = n_{\alpha 1}\left(\mathbf{h}_1^T - \left(\mathbf{h}_1^T \cdot \mathbf{x}_j\right)\mathbf{b}_j^T\right) + n_{\alpha 2}\left(\mathbf{h}_2^T - \left(\mathbf{h}_2^T \cdot \mathbf{x}_j\right)\mathbf{b}_j^T\right) + n_{\alpha 3}\left[\left(\mathbf{h}_3^T - \frac{1}{30}\mathbf{s}^T\right) - \left(\left(\mathbf{h}_3^T - \frac{1}{30}\mathbf{s}^T\right)\cdot \mathbf{x}_j\right)\mathbf{b}_j^T\right]$$
$$+ n_{\alpha 4}\left(\mathbf{h}_4^T - \left(\mathbf{h}_4^T \cdot \mathbf{x}_j\right)\mathbf{b}_j^T\right) + n_{\alpha 5}\left[\left(\mathbf{h}_5^T - \frac{4}{15}\mathbf{s}^T\right) - \left(\left(\mathbf{h}_5^T - \frac{4}{15}\mathbf{s}^T\right)\cdot \mathbf{x}_j\right)\mathbf{b}_j^T\right]$$
$$+ n_{\alpha 6}\left[\left(\mathbf{h}_6^T - \frac{4}{15}\mathbf{s}^T\right) - \left(\left(\mathbf{h}_6^T - \frac{4}{15}\mathbf{s}^T\right)\cdot \mathbf{x}_j\right)\mathbf{b}_j^T\right] + n_{\alpha 7}\left[\left(\mathbf{h}_7^T - \frac{4}{5}\mathbf{s}^T\right) - \left(\left(\mathbf{h}_7^T - \frac{4}{5}\mathbf{s}^T\right)\cdot \mathbf{x}_j\right)\mathbf{b}_j^T\right]$$
$$+ n_{\alpha 8}\left(\mathbf{h}_8^T - \left(\mathbf{h}_8^T \cdot \mathbf{x}_j\right)\mathbf{b}_j^T\right) + n_{\alpha 9}\left(\mathbf{h}_9^T - \left(\mathbf{h}_9^T \cdot \mathbf{x}_j\right)\mathbf{b}_j^T\right) + n_{\alpha 10}\left[\left(\mathbf{h}_{10}^T - \frac{4}{15}\mathbf{s}^T\right) - \left(\left(\mathbf{h}_{10}^T - \frac{4}{15}\mathbf{s}^T\right)\cdot \mathbf{x}_j\right)\mathbf{b}_j^T\right]$$
$$+ n_{\alpha 11}\left[\left(\mathbf{h}_{11}^T - \frac{4}{15}\mathbf{s}^T\right) - \left(\left(\mathbf{h}_{11}^T - \frac{4}{15}\mathbf{s}^T\right)\cdot \mathbf{x}_j\right)\mathbf{b}_j^T\right]$$

and

$$\left[n_{\alpha\beta}\right] = \begin{bmatrix}
\frac{17}{2} & 0 & 0 & -8 & 0 & 0 & 0 & -9 & 0 & 0 & 0 \\
 & \frac{17}{2} & 0 & -8 & 0 & 0 & 0 & 0 & -9 & 0 & 0 \\
 & & \frac{256}{17} & 0 & \frac{36}{17} & \frac{36}{17} & 2 & 0 & 0 & -\frac{58}{17} & -\frac{58}{17} \\
 & & & 24 & 0 & 0 & 0 & 8 & 8 & 0 & 0 \\
 & & & & \frac{316}{187} & \frac{146}{187} & 1 & 0 & 0 & -\frac{324}{187} & -\frac{171}{187} \\
 & & & & & \frac{316}{187} & 1 & 0 & 0 & -\frac{171}{187} & -\frac{324}{187} \\
 & & & & & & \frac{3}{2} & 0 & 0 & -\frac{3}{2} & -\frac{3}{2} \\
 & & & & & & & 10 & 0 & 0 & 0 \\
 & & & & & & & & 10 & 0 & 0 \\
 & & & & & & & & & \frac{505}{187} & \frac{585}{187} \\
\textit{sym} & & & & & & & & & & \frac{505}{187}
\end{bmatrix}, \quad \alpha, \beta = 1, \cdots, 11.$$

C.4 Quadratic hexahedral SHB20 element

The orthogonality properties, which allow determining the constants a_{ji} and $c_{\alpha i}$ for the SHB20 element, are given by:

$$\begin{cases} \begin{cases} \mathbf{b}_i^T \cdot \mathbf{h}_\alpha = 0, & \mathbf{b}_i^T \cdot \mathbf{s} = 0, & \mathbf{b}_i^T \cdot \mathbf{x}_j = \delta_{ij} \\ \mathbf{h}_1^T \cdot \mathbf{s} = 0, & \mathbf{h}_2^T \cdot \mathbf{s} = 0, & \mathbf{h}_3^T \cdot \mathbf{s} = 0, \\ \mathbf{h}_4^T \cdot \mathbf{s} = 16, & \mathbf{h}_5^T \cdot \mathbf{s} = 16, & \mathbf{h}_6^T \cdot \mathbf{s} = 16, \\ \mathbf{h}_7^T \cdot \mathbf{s} = 0, & \mathbf{h}_8^T \cdot \mathbf{s} = 0, & \mathbf{h}_9^T \cdot \mathbf{s} = 0, \\ \mathbf{h}_{10}^T \cdot \mathbf{s} = 0, & \mathbf{h}_{11}^T \cdot \mathbf{s} = 0, & \mathbf{h}_{12}^T \cdot \mathbf{s} = 0, \\ \mathbf{h}_{13}^T \cdot \mathbf{s} = 0, & \mathbf{h}_{14}^T \cdot \mathbf{s} = 0, & \mathbf{h}_{15}^T \cdot \mathbf{s} = 0, \\ \mathbf{h}_{16}^T \cdot \mathbf{s} = 0 \\ i, j = 1, \cdots, 3 \end{cases} \\ \mathbf{h}_\alpha^T \cdot \mathbf{h}_\beta = \begin{bmatrix} 12 & 0 & 0 & 0 & 0 & 0 & 0 & 0 & 0 & 0 & 0 & 0 & 0 & 0 & 8 & 0 \\ & 12 & 0 & 0 & 0 & 0 & 0 & 0 & 0 & 0 & 0 & 0 & 0 & 8 & 0 & 0 \\ & & 12 & 0 & 0 & 0 & 0 & 0 & 0 & 0 & 0 & 0 & 0 & 0 & 0 & 8 \\ & & & 16 & 12 & 12 & 0 & 0 & 0 & 0 & 0 & 0 & 0 & 0 & 0 & 0 \\ & & & & 16 & 12 & 0 & 0 & 0 & 0 & 0 & 0 & 0 & 0 & 0 & 0 \\ & & & & & 16 & 0 & 0 & 0 & 0 & 0 & 0 & 0 & 0 & 0 & 0 \\ & & & & & & 8 & 0 & 0 & 0 & 0 & 0 & 0 & 0 & 0 & 0 \\ & & & & & & & 12 & 0 & 0 & 0 & 0 & 8 & 0 & 0 & 0 \\ & & & & & & & & 12 & 0 & 8 & 0 & 0 & 0 & 0 & 0 \\ & & & & & & & & & 12 & 0 & 8 & 0 & 0 & 0 & 0 \\ & & & & & & & & & & 12 & 0 & 0 & 0 & 0 & 0 \\ & & & & & & & & & & & 12 & 0 & 0 & 0 & 0 \\ & & & & & & & & & & & & 12 & 0 & 0 & 0 \\ & & & & & & & & & & & & & 8 & 0 & 0 \\ & & & & & & & & & & & & & & 8 & 0 \\ sym & & & & & & & & & & & & & & & 8 \end{bmatrix} \\ \alpha, \beta = 1, \cdots, 16 \end{cases} . \quad \text{(C.5)}$$

Based on the above conditions, the constants a_{ji} and $c_{\alpha i}$ can be determined by the scalar product of Eq. (2.5) by $\mathbf{b}_i^T$, $\mathbf{s}^T$ and $\mathbf{h}_\alpha^T$, successively, which gives:

$$a_{ji} = \mathbf{b}_j^T \cdot \mathbf{d}_i, \qquad c_{\alpha i} = \boldsymbol{\gamma}_\alpha^T \cdot \mathbf{d}_i, \qquad \text{(C.6)}$$

with

$$\begin{aligned}
\boldsymbol{\gamma}_\alpha^T = {} & n_{\alpha 1}\left(\mathbf{h}_1^T - \left(\mathbf{h}_1^T \cdot \mathbf{x}_j\right)\mathbf{b}_j^T\right) + n_{\alpha 2}\left(\mathbf{h}_2^T - \left(\mathbf{h}_2^T \cdot \mathbf{x}_j\right)\mathbf{b}_j^T\right) + n_{\alpha 3}\left(\mathbf{h}_3^T - \left(\mathbf{h}_3^T \cdot \mathbf{x}_j\right)\mathbf{b}_j^T\right) \\
& + n_{\alpha 4}\left[\left(\mathbf{h}_4^T - \frac{4}{5}\mathbf{s}^T\right) - \left(\left(\mathbf{h}_4^T - \frac{4}{5}\mathbf{s}^T\right)\cdot \mathbf{x}_j\right)\mathbf{b}_j^T\right] + n_{\alpha 5}\left[\left(\mathbf{h}_5^T - \frac{4}{5}\mathbf{s}^T\right) - \left(\left(\mathbf{h}_5^T - \frac{4}{5}\mathbf{s}^T\right)\cdot \mathbf{x}_j\right)\mathbf{b}_j^T\right] \\
& + n_{\alpha 6}\left[\left(\mathbf{h}_6^T - \frac{4}{5}\mathbf{s}^T\right) - \left(\left(\mathbf{h}_6^T - \frac{4}{5}\mathbf{s}^T\right)\cdot \mathbf{x}_j\right)\mathbf{b}_j^T\right] + n_{\alpha 7}\left(\mathbf{h}_7^T - \left(\mathbf{h}_7^T \cdot \mathbf{x}_j\right)\mathbf{b}_j^T\right) \\
& + n_{\alpha 8}\left(\mathbf{h}_8^T - \left(\mathbf{h}_8^T \cdot \mathbf{x}_j\right)\mathbf{b}_j^T\right) + n_{\alpha 9}\left(\mathbf{h}_9^T - \left(\mathbf{h}_9^T \cdot \mathbf{x}_j\right)\mathbf{b}_j^T\right) + n_{\alpha 10}\left(\mathbf{h}_{10}^T - \left(\mathbf{h}_{10}^T \cdot \mathbf{x}_j\right)\mathbf{b}_j^T\right) \\
& + n_{\alpha 11}\left(\mathbf{h}_{11}^T - \left(\mathbf{h}_{11}^T \cdot \mathbf{x}_j\right)\mathbf{b}_j^T\right) + n_{\alpha 12}\left(\mathbf{h}_{12}^T - \left(\mathbf{h}_{12}^T \cdot \mathbf{x}_j\right)\mathbf{b}_j^T\right) + n_{\alpha 13}\left(\mathbf{h}_{13}^T - \left(\mathbf{h}_{13}^T \cdot \mathbf{x}_j\right)\mathbf{b}_j^T\right) \\
& + n_{\alpha 14}\left(\mathbf{h}_{14}^T - \left(\mathbf{h}_{14}^T \cdot \mathbf{x}_j\right)\mathbf{b}_j^T\right) + n_{\alpha 15}\left(\mathbf{h}_{15}^T - \left(\mathbf{h}_{15}^T \cdot \mathbf{x}_j\right)\mathbf{b}_j^T\right) + n_{\alpha 16}\left(\mathbf{h}_{16}^T - \left(\mathbf{h}_{16}^T \cdot \mathbf{x}_j\right)\mathbf{b}_j^T\right)
\end{aligned}$$

and

$$\left[n_{\alpha\beta}\right] = \begin{bmatrix}
\frac{1}{4} & 0 & 0 & 0 & 0 & 0 & 0 & 0 & 0 & 0 & 0 & 0 & 0 & -\frac{1}{4} & 0 \\
 & \frac{1}{4} & 0 & 0 & 0 & 0 & 0 & 0 & 0 & 0 & 0 & 0 & -\frac{1}{4} & 0 & 0 \\
 & & \frac{1}{4} & 0 & 0 & 0 & 0 & 0 & 0 & 0 & 0 & 0 & 0 & 0 & -\frac{1}{4} \\
 & & & \frac{3}{8} & \frac{1}{8} & \frac{1}{8} & 0 & 0 & 0 & 0 & 0 & 0 & 0 & 0 & 0 \\
 & & & & \frac{3}{8} & \frac{1}{8} & 0 & 0 & 0 & 0 & 0 & 0 & 0 & 0 & 0 \\
 & & & & & \frac{3}{8} & 0 & 0 & 0 & 0 & 0 & 0 & 0 & 0 & 0 \\
 & & & & & & \frac{1}{8} & 0 & 0 & 0 & 0 & 0 & 0 & 0 & 0 \\
 & & & & & & & \frac{3}{20} & 0 & 0 & 0 & -\frac{1}{10} & 0 & 0 & 0 \\
 & & & & & & & & \frac{3}{20} & 0 & -\frac{1}{10} & 0 & 0 & 0 & 0 \\
 & & & & & & & & & \frac{3}{20} & 0 & -\frac{1}{10} & 0 & 0 & 0 \\
 & & & & & & & & & & \frac{3}{20} & 0 & 0 & 0 & 0 \\
 & & & & & & & & & & & \frac{3}{20} & 0 & 0 & 0 \\
 & & & & & & & & & & & & \frac{3}{20} & 0 & 0 \\
 & & & & & & & & & & & & & \frac{1}{8} & 0 \\
 & & & & & & & & & & & & & & \frac{1}{8} \\
\multicolumn{15}{l}{\textit{sym}}
\end{bmatrix}, \quad \alpha, \beta = 1, \cdots, 16.$$

ÉLÉMENTS FINIS SOLIDE–COQUE POUR L'ANALYSE QUASI-STATIQUE ET DYNAMIQUE DES STRUCTURES MINCES 3D : APPLICATION AUX PROCÉDÉS DE MISE EN FORME

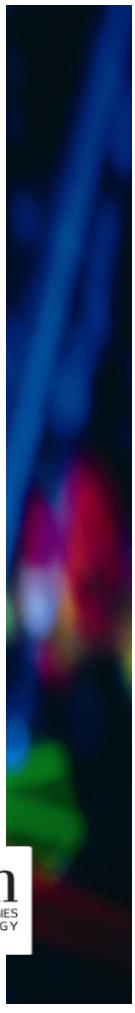
RESUME : La simulation numérique par la méthode des éléments finis (MEF) fournit de nos jours une aide considérable aux ingénieurs dans les processus de conception et d'optimisation des produits. Malgré le développement croissant des ressources de calcul, la fiabilité et l'efficacité des simulations numériques par la MEF restent des qualités importantes à améliorer. Ce travail de thèse consiste à développer une famille d'éléments solide–coque (SHB) pour la modélisation tridimensionnelle des structures minces. Cette famille d'éléments SHB est basée sur une formulation tridimensionnelle en grands déplacements et rotations. La technique dite "d'intégration réduite dans le plan", en utilisant un nombre arbitraire de points d'intégration dans la direction de l'épaisseur, permet de modéliser des structures minces avec une seule couche d'éléments. Dans ce travail de thèse, deux éléments SHB prismatique et hexaédrique linéaires, ainsi que leurs contreparties quadratiques, ont été implantés dans le code de calcul par éléments finis ABAQUS pour l'analyse quasi-statique et dynamique des structures minces. La performance de ces éléments a été validée à travers une série de cas tests académiques, ainsi que sur des problèmes complexes de type impact/crash et des procédés de mise en forme de tôles minces. L'ensemble des résultats numériques obtenus révèle que ces éléments SHB représentent une alternative intéressante aux éléments coques et solides traditionnels dans la modélisation tridimensionnelle des structures minces.

Mots clés : structures minces, élément fini, verrouillage, déformation postulée, solide–coque, quasi-statique, dynamique, mise en forme de tôles

SOLID–SHELL FINITE ELEMENTS FOR QUASI-STATIC AND DYNAMIC ANALYSIS OF 3D THIN STRUCTURES: APPLICATION TO SHEET METAL FORMING PROCESSES

ABSTRACT: Nowadays, the finite element (FE) simulation provides great assistance to engineers in the processes of design and optimization of products. Despite the growing development of computational resources, reliability and efficiency of the FE simulations remain important features that still need to be improved. The current work contributes to the development of a family of solid–shell elements (SHB), for the 3D modeling of thin structures. Based on a 3D formulation, reduced integration and special treatments for the elimination of locking effects and the control of spurious zero-energy modes, the SHB solid–shell elements are capable of modeling thin 3D structural problems with only a single element layer, while accurately describing the various through-thickness phenomena. In the current contribution, a family of prismatic and hexahedral SHB elements, with their linear and quadratic versions, have been implemented into ABAQUS using both standard/quasi-static and explicit/dynamic solvers. The performance of the SHB elements has been evaluated via a series of popular benchmarks as well as impact/crash problems and sheet metal forming processes. All numerical results reveal that these SHB elements represent an interesting alternative to traditional shell and solid elements for the 3D modeling of thin structural problems.

Keywords: thin structures, finite element, locking, assumed strain, solid–shell, quasi-static, dynamic, sheet metal forming



ARTS ET MÉTIERS ParisTech

ParisTech INSTITUT DES SCIENCES ET TECHNOLOGIES PARIS INSTITUTE OF TECHNOLOGY